Universidade de São Paulo
Instituto de Física

Diagramas de fases de modelos microscópicos para misturas nematogênicas

William Gabriel Carreras Oropesa

Orientador: Prof. Dr. André de Pinho Vieira

Tese de doutorado apresentada ao Instituto de Física da Universidade de São Paulo, como requisito parcial para a obtenção do título de Doutor em Ciências.

Banca Examinadora:

Prof. Dr. André de Pinho Vieira - Orientador (IFUSP)

Prof. Dr. Silvio Roberto de Azevedo Salinas (IFUSP)

Prof. Dr. Roberto Fernandes Silva Andrade (UFBA)

Profa. Dra. Maria Socorro Seixas Pereira (UFAL)

Prof. Dr. Daniel Adrián Stariolo (UFF)

São Paulo
2023

FICHA CATALOGRÁFICA
Preparada pelo Serviço de Biblioteca e Informação
do Instituto de Física da Universidade de São Paulo

Carreras Oropesa, William Gabriel

Diagramas de fases de modelos microscópicos para misturas nematogênicas. São Paulo, 2023.

Tese (Doutorado) - Universidade de São Paulo. Instituto de Física. Depto. de Física Geral.

Orientador: Prof. Dr. André de Pinho Vieira

Área de Concentração: Física da Matéria Condensada

Unitermos: 1. Modelos microscópicos; 2. Cristais líquidos; 3. Nanopartículas dipolares; 4. Pontos multicríticos de Landau

USP/IF/SBI-026/2023

University of São Paulo
Physics Institute

Phase diagrams of microscopic models for nematogenic mixtures

William Gabriel Carreras Oropesa

Supervisor: Prof. Dr. André de Pinho Vieira

Thesis submitted to the Physics Institute of the University of São Paulo in partial fulfillment of the requirements for the degree of Doctor of Science.

Examining Committee:
Prof. Dr. André de Pinho Vieira - Supervisor (IFUSP)
Prof. Dr. Silvio Roberto de Azevedo Salinas (IFUSP)
Prof. Dr. Roberto Fernandes Silva Andrade (UFBA)
Profa. Dra. Maria Socorro Seixas Pereira (UFAL)
Prof. Dr. Daniel Adrián Stariolo (UFF)

São Paulo
2023

For Ainhoa, my idea of beautiful.

Acknowledgment

Even at such a delicate moment in human history, this investigation was uninterrupted. My sincere acknowledgment for Malén Ailín Narambuena, Yordana Oropesa Henriquez and André de Pinho Vieira. This is not my investigation, it is our investigation.

- To Eduardo Nascimento for the long hours of talks about nematics liquid crystals. In my head you were always my cosupervisor.
- To Carlos Eduardo Fiore and his research group for the collaborations (especially Carlos Fernandez and Angel Leiva), I always felt like one of you.
- For the Cuban community of Rio Pequeno for the aid received at the birth of my daughter.
- To my family for their unconditional support.
- For the agencies CNPq and FAPESP, and for the INCT-FCx (Instituto Nacional de Ciêntica e Tecnologia de Fluidos Complexos) funded by these agencies.

Abstract

We employ different extensions of the mean-field Maier-Saupe model with discrete orientational states to study the phase behavior of statistical models for nematogenic mixtures. More specifically, we study two problems: (i) dilution effects on liquid crystals and (ii) binary mixtures of nematogens and dipolar nanoparticles. For the dilution problem, the phase behavior of the systems is investigated in terms of the strength of the isotropic interaction between anisotropic objects, as well as the degree of biaxiality and the concentration of those units. We obtain phase diagrams with isotropic phases and stable biaxial and uniaxial nematic structures, various phase coexistences, many types of critical and multicritical behavior, such as ordinary vapor-liquid critical points, critical end points, and tricritical points, as well as distinct Landau-like multicritical points. For the problem involving dipolar nanoparticles, we have an extra parameter, the strength of the interaction between objects of different nature. We obtain phase diagrams with reentrant biaxial structures, ordinary dipolar-rich−dipolar-poor critical points, tricritical points, Landau multicritical points, and various other types of critical behavior. We present a perturbative calculation to study the effects produced in the liquid-crystal host when doping with small amounts of dipolar particles. For both problems, our results widen the possibilities of relating the phenomenological coefficients of the Landau–de Gennes expansion to microscopic parameters, allowing an improved interpretation of theoretical fittings to experimental data.

Keywords: microscopic models; liquid crystals; dipolar nanoparticles; biaxial nematic structures; Landau-like multicritical points

Resumo

Empregamos diferentes extensões do modelo Maier-Saupe de campo médio com estados de orientação discretos para estudar o comportamento de fase de modelos estatísticos para misturas nematogênicas. Especificamente, estudamos dois problemas: (i) efeitos de diluição em cristais líquidos e (ii) misturas binárias de nematógenos e nanopartículas dipolares. No problema da diluição, o comportamento de fase dos sistemas é investigado em termos da interação isotrópica entre objetos anisotrópicos, bem como do grau de biaxialidade e da concentração dessas unidades. Obtemos diagramas com fases isotrópicas e estruturas nemáticas biaxiais e uniaxiais estáveis, várias coexistências de fase, muitos tipos de comportamento crítico e multicrítico, como pontos críticos comuns de vapor-líquido, pontos críticos terminais e pontos tricríticos, bem como distintos pontos multicríticos de Landau. No problema envolvendo nanopartículas dipolares, temos um parâmetro extra, a interação entre objetos de diferentes naturezas. Obtemos diagramas de fase com estruturas biaxiais reentrantes, pontos críticos comuns entre fases ricas e pobres em dipolos, pontos tricríticos, pontos multicríticos de Landau e vários outros tipos de comportamento crítico. Apresentamos um cálculo perturbativo para estudar os efeitos produzidos no cristal líquido hospedeiro ao dopá-lo com pequenas quantidades de partículas dipolares. Para ambos os problemas, nossos resultados ampliam as possibilidades de relacionar os coeficientes fenomenológicos da expansão de Landau–de Gennes a parâmetros microscópicos, permitindo uma melhor interpretação dos ajustes teóricos aos dados experimentais.

Palavras-chave: modelos microscópicos; cristais líquidos; nanopartículas dipolares; estruturas nemáticas biaxiais; pontos multicríticos de Landau

List of Acronyms

LC liquid crystal

NLC nematic liquid crystal

NP nanoparticle

MF mean-field

MSZ Maier-Saupe-Zwanzig

LG lattice-gas

LGMSZ lattice-gas Maier-Saupe-Zwanzig

LGMSZ-B lattice-gas Maier-Saupe-Zwanzig with extra B interaction

ISO isotropic phase

$\mathrm{N_U^+}$ calamitic uniaxial nematic phase

$\mathrm{N_U^-}$ discotic uniaxial nematic phase

$\mathrm{N_B}$ biaxial nematic phase

L multicritical Landau point

CE critical end point

LTC Landau tricritical point

IL isotropic liquid phase

IV isotropic vapor phase

$\mathrm{I_{DP}}$ dipolar-poor isotropic phase

I_{DR}	dipolar-rich isotropic phase
C	critical point
MCE	multicritical end point
TC	tricritical point
LE	Landau critical end point
ML_2	higher-order multicritical point (triple, critical end, tricritical, and Landau point)
ML_3	higher-order multicritical point (critical, critical end, tricritical, and Landau point)
$M_1^{\pm}$	higher-order multicritical points (triple and critical end points)
$M_2^{\pm}$	higher-order multicritical points (triple, tricritical and critical end points)
$M_3^{\pm}$	higher-order multicritical points (critical, triple, tricritical and critical end points)

List of Figures

Contents

Chapter 1

Brief Introduction

Nematic mesophases are probably the simplest states of matter observed in liquid crystals (LCs) that exhibit long-range orientational order in the absence of translational symmetry breaking [1–4]. An uniaxial nematic liquid crystal (NLC) is characterized macroscopically by orientation-dependent physical properties (e.g., optical and magnetic anisotropies), which lead to the definition of the nematic director. Notwithstanding, the breaking of isotropy in the plane perpendicular to the uniaxial director may lead to the elusive biaxial state, whose possibility was theoretically pointed out by Freiser [5], using a generalization of the Maier-Saupe theory [6]. After the paper of Freiser, the characterization of biaxial nematic phases in LCs gained interest, and many of the ideas introduced in uniaxial systems were extended to biaxial systems [7–10]. In 1980 the biaxial nematic phase was finally found experimentally by Yu and Saupe [11] in a lyotropic LC (KL-1-decanol-D2O) and subsequently observed in many other lyotropic systems [12–15]. The observation of biaxial nematic phases in thermotropic LCs is less frequent, but there is experimental evidence of their existence [16, 17].

In recent years, colleagues at the Institute of Physics at the University of São Paulo (IFUSP) have carried out a large number of investigations [18–25] with the aim of studying the stability of biaxial structures in LCs. Many of these works are based on simple statistics lattice models with restrictions on the orientation degrees of freedom, which allows detailed calculations. Despite their simplicity, these models are capable of reproducing the qualitative features of nematic phase diagrams, such as sequences of biaxial-uniaxial-isotropic phase transitions with increasing temperature and a well-defined Landau multicritical point. These investigations make use of a parameter Δ that gauges the degree of biaxiality of the molecules that are the basic units of the system.

The necessity to enhance the properties of NLCs represents a challenge today given its application in different fields (e.g., for liquid-crystal displays, see Refs. [26–28]). A purely physical solution (e.i. without chemical synthesis) to this problem has been the introduction of dipolar nanoparticles (NPs) into a LC host. In particular, NLCs doped with ferroelectric NPs are known to enhance dielectric and optical anisotropy [29, 30]. On the other hand, paramagnetic and fer-

romagnetic NPs in NLCs are promising candidates for magnetically tunable structures. Metal NPs (e.i. Au and Ag-nanoclusters) as well as semiconductor quantum dots (e.i. CdTe nanocrystals) in NLCs enhance the electro-optical response of the system because of reduced threshold voltage [31]. Parallel to the experimental advances, there have been Landau-de Gennes expansions [32, 33], mean-field (MF) calculations [34–36], Monte Carlo simulations [37–39], and molecular dynamics simulations [40] aimed at better understanding this complex problem.

In this doctoral thesis, we address the two problems discussed above: (i) stability of biaxial structures in NLCs and (ii) NLCs doped with dipolar NPs. In Chap. 2 we present a series of tools that will be used throughout this manuscript, such as Gaussian identities, and an overview about the Maier-Saupe-Zwanzig (MSZ) model. Chap. 3 is dedicated to a detailed analysis of the stability of biaxial structures in NLCs. The principal goal of this chapter is the inclusion of dilution in the system. In this problem, the dilution opens the possibility of studying the topological phase behavior of the system as a function of the concentration of nematic molecules. In Chap. 4 we study the problem of dipolar NPs doping NLCs. In this chapter, we do not limit ourselves to studying uniaxial systems (as is generally found in the literature), but we also study systems with intrinsically biaxial molecules. We make no hypotheses about the dipolar nature of the NPs, so our results can be adapted to both ferroelectric and ferromagnetic NPs. In Chap. 5 we present a general conclusion.

Chapter 2

Definitions and concepts

2.1 Introduction

In this chapter we present the basic concepts that will be important for a better understanding of some aspects discussed throughout this manuscript. In Sec. 2.2 we present a molecular idealization as well as a brief introduction to the Zwanzig approximation [41] which plays a fundamental role in obtaining analytical expressions (e.g., Landau-de Gennes free-energy functional). The parameter Δ, which quantifies the degree of biaxiality of the molecules that form the NLC, is introduced from a geometrical and analytical point of view using its analogy with molecular anisotropy, following the same idea of E. S. Nascimento *et al.* at Ref. [22]. In the case of dipolar NPs we present a matrix representation of their state, which will facilitate the calculations in Chap. 4. In Sec. 2.3 we present a discrete version of the Maier-Saupe model which we will call MSZ model. The MSZ model represents the basis of all models for LCs used in this manuscript.

In general, we represent the state of a nematogen by a symmetric traceless tensor $\mathbf{\Omega}$, then it is natural to describe the interaction between two nematogens, labeled 1 and 2, by means of a Frobenius inner product $\mathbf{\Omega}_1 : \mathbf{\Omega}_2 \equiv \mathrm{Tr}\{\mathbf{\Omega}_1\mathbf{\Omega}_2^\top\}$, where $\mathbf{\Omega}_2^\top$ is the transpose of $\mathbf{\Omega}_2$. The norm associated with the Frobenius inner product is $\|\mathbf{\Omega}_1\| = \sqrt{\mathbf{\Omega}_1 : \mathbf{\Omega}_1}$. For more details on Frobenius inner products we recommend the book by Horn and Johnson [42].

2.2 The Zwanzig approximation

Suppose that a nematogen with symmetry point group $\mathrm{D}_{2\mathrm{h}}$, represented by a parallelepiped of mass m, with dimensions a, b and c, can only orient itself with respect to a fixed Cartesian system according to Fig. 2.1. To characterize the orientational state of the molecule we can use the traceless inertia tensor $\mathbf{\Lambda}$, which is defined as

$$\Lambda_{ij} = \mathrm{I}_{ij} - \frac{1}{3}\delta_{ij}, \tag{2.1}$$

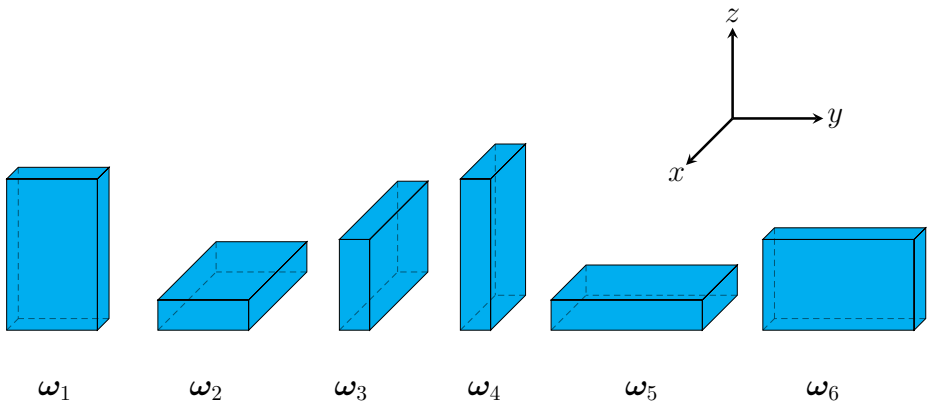

Figure 2.1: Set of states $\{\omega_i\}$ with $i = \overline{1,6}$ is a geometrical representation of the six possible molecular states. In the state $\boldsymbol{\omega}_1$ the parallelepiped has dimensions a, b and c along the axes x, y and z, respectively.

where δ_{ij} is the Kronecker delta function and I_{ij} are entries of the usual inertia tensor. If a molecule is in state $\boldsymbol{\omega}_1$ (see Fig. 2.1), then

$$\boldsymbol{\Lambda} = \frac{m}{36}\begin{pmatrix} \lambda_1 & 0 & 0 \\ 0 & \lambda_2 & 0 \\ 0 & 0 & \lambda_3 \end{pmatrix}, \tag{2.2}$$

where $\lambda_1 = -2a^2 + b^2 + c^2$, $\lambda_2 = a^2 - 2b^2 + c^2$ and $\lambda_3 = -(\lambda_1 + \lambda_2)$. Defining the geometric parameter

$$\Delta = 3\frac{b^2 - a^2}{a^2 + b^2 - 2c^2}, \tag{2.3}$$

we can rewrite $\boldsymbol{\Lambda}$ as

$$\boldsymbol{\Lambda} = \frac{m\lambda_3}{2}\begin{pmatrix} -1+\Delta & 0 & 0 \\ 0 & -1-\Delta & 0 \\ 0 & 0 & 2 \end{pmatrix} \equiv m\lambda_3\boldsymbol{\omega}_1. \tag{2.4}$$

Here we are only interested in orientational order, then the scalar part of the tensor (its trace) plays no role. Assuming $\lambda_3 < 0$, the choice $a = b < c$ would lead to a rod-like molecule with $\Delta = 0$, whereas $a = c > b$ would lead to a disk-like molecule with $\Delta = 3$. For $0 < \Delta < 3$ and $\Delta > 3$ we have a, b, and c different, then the molecules are biaxial objects (e.g., see Fig. 2.2 for a geometrical framework).

Eq. (2.4) indicates a matrix representation of the molecular state $\boldsymbol{\omega}_1$. The other states can be found according to the corresponding symmetry operation, i.e., for state $\boldsymbol{\omega}_4$

$$\boldsymbol{\omega}_4 = \mathbf{R}_z^{\top}(\pi/2)\cdot\boldsymbol{\omega}_1\cdot\mathbf{R}_z(\pi/2) = \frac{1}{2}\begin{pmatrix} -1-\Delta & 0 & 0 \\ 0 & -1+\Delta & 0 \\ 0 & 0 & 2 \end{pmatrix}, \tag{2.5}$$

where $\mathbf{R}_z(\pi/2)$ is a matrix representation of a $\mathrm{C}_4(z)$ rotation and $\mathbf{R}_z^{\top}(\pi/2)$ is the matrix

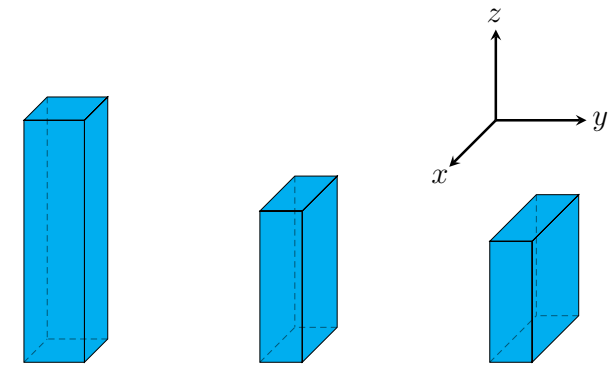

Figure 2.2: Relationship between Δ and the molecular anisotropy. Left figure represents a prolate molecule with $\Delta = 0$ ($a = b < c$). Center figure is an intrinsically biaxial molecule. Right figure is an oblate molecule with $\Delta = 3$ ($a = c > b$). In all three situations the parallelepipeds have dimensions a, b and c along the axes x, y and z, respectively.

transpose. Finally the matrix representation of the possible nematogen states is

$$\boldsymbol{\omega}_1 = \frac{1}{2}\begin{pmatrix} -1+\Delta & 0 & 0 \\ 0 & -1-\Delta & 0 \\ 0 & 0 & 2 \end{pmatrix}, \quad \boldsymbol{\omega}_2 = \frac{1}{2}\begin{pmatrix} 2 & 0 & 0 \\ 0 & -1-\Delta & 0 \\ 0 & 0 & -1+\Delta \end{pmatrix},$$

$$\boldsymbol{\omega}_3 = \frac{1}{2}\begin{pmatrix} 2 & 0 & 0 \\ 0 & -1+\Delta & 0 \\ 0 & 0 & -1-\Delta \end{pmatrix}, \quad \boldsymbol{\omega}_4 = \frac{1}{2}\begin{pmatrix} -1-\Delta & 0 & 0 \\ 0 & -1+\Delta & 0 \\ 0 & 0 & 2 \end{pmatrix}, \tag{2.6}$$

$$\boldsymbol{\omega}_5 = \frac{1}{2}\begin{pmatrix} -1-\Delta & 0 & 0 \\ 0 & 2 & 0 \\ 0 & 0 & -1+\Delta \end{pmatrix}, \quad \boldsymbol{\omega}_6 = \frac{1}{2}\begin{pmatrix} -1+\Delta & 0 & 0 \\ 0 & 2 & 0 \\ 0 & 0 & -1-\Delta \end{pmatrix}.$$

We now consider a lattice where each site is occupied by a nematogen that can only be oriented in states $\{\boldsymbol{\omega}_i\}$ with $i = \overline{1,6}$. If the principal axes point in completely random directions, we are facing a disordered state that we identify as the isotropic phase (ISO). A calamitic uniaxial nematic phase (N_U^+) occurs when the first principal axes are parallel to each other, while the other two principal axes point in arbitrary directions. A discotic uniaxial nematic phase (N_U^-) occurs when the minor principal axes are parallel to each other, while the other two principal axes point in arbitrary directions. A biaxial nematic phase (N_B) occurs when the first principal axes are parallel to each other and the minor principal axes are also parallel to each other. Of course, in this case, the third axes are also parallel to each other.

2.2.1 Gaussian identity

The MF models presented in this manuscript are quadrupolar analogues of the Curie-Weiss infinite-range model. The solution of this class of models is based on determining an integral representation of the partition function or grand partition function depending of the ensemble. In order to obtain this representation we need to use the transformation

$$\exp\left(\frac{\alpha}{N}\sum_{i,j=1}^{N}\boldsymbol{\Omega}_i:\boldsymbol{\Omega}_j\right)=\prod_{\nu\in\{x,y,z\}}\exp\left[\frac{\alpha}{N}\left(\sum_{i=1}^{N}\Omega_i^{\nu\nu}\right)^2\right], \tag{2.7}$$

where $\alpha\in\mathbb{R}_+$, N is a big number and we consider only diagonal tensors. Using

$$\exp\left(\frac{z^2}{2g}\right)=\left(\frac{g}{2\pi}\right)^{1/2}\int_{-\infty}^{+\infty}\exp\left(-\frac{g}{2}x^2+xz\right)\,dx, \tag{2.8}$$

where $\Re\{g\}>0$, and defining $g=\frac{N}{2\alpha}$ and $z=\sum_{i=1}^{N}\Omega_i^{\nu\nu}$, from the right-hand side of Eq. (2.7) we can write [1]

$$\exp\left(\frac{\alpha}{N}\sum_{i,j=1}^{N}\boldsymbol{\Omega}_i:\boldsymbol{\Omega}_j\right)=\left(\frac{N}{4\pi\alpha}\right)^{3/2}\prod_{\nu\in\{x,y,z\}}\int_{\mathbb{R}}\exp\left(-\frac{N}{4\alpha}v_{\nu\nu}^2+v_{\nu\nu}\sum_{i=1}^{N}\Omega_i^{\nu\nu}\right)\,dv_{\nu\nu}, \tag{2.10}$$

and finally, exchanging the order of the product and the integral we get

$$\exp\left(\frac{\alpha}{N}\sum_{i,j=1}^{N}\boldsymbol{\Omega}_i:\boldsymbol{\Omega}_j\right)=\left(\frac{N}{4\pi\alpha}\right)^{3/2}\int_{\mathbb{R}^3}\exp\left(-\frac{N}{4\alpha}\|\mathbf{v}\|^2+\mathbf{v}:\sum_{i=1}^{N}\boldsymbol{\Omega}_i\right)\,d[\mathbf{v}], \tag{2.11}$$

where $\mathbf{v}$ is a 3×3 tracelees diagonal tensor, and $d[\mathbf{v}]=dv_{xx}\,dv_{yy}\,dv_{zz}$. The transformation represented by Eq. (2.11) will be invoked in various parts of this manuscript.

2.2.2 Connection with dipolar nanoparticles

Let us now consider that we have a dipole particle (regardless of its nature) with dipole moment $\mathbf{p}$. Continuing the idea of the Zwanzig approximation, the possible orientational states are represented in Fig. 2.3. In problems associated with nematogenic suspensions, as we want to consider interactions between dipolar NPs and nematogens, it is convenient to define a quadrupolar

[1] In this manuscript we use a compact notation,

$$\int_{\mathbb{R}^n}f(\mathbf{x})\,d[\mathbf{x}]\to\underbrace{\int_{-\infty}^{+\infty}\cdots\int_{-\infty}^{+\infty}}_{n\text{ times}}f(x_1,\cdots,x_n)\,dx_1\cdots dx_n, \tag{2.9}$$

for multiple integrals.

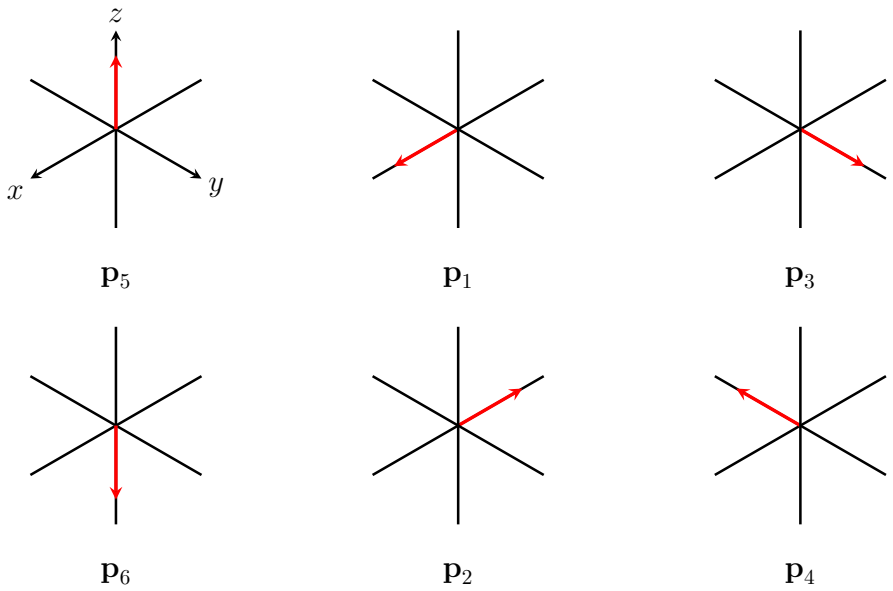

Figure 2.3: Possible dipole states are represented by the small-red arrows. The label at the bottom of each state will be used to identify it in this manuscript.

tensor associated with a dipole particle by

$$\mathbf{\Theta} = \frac{3}{2}(\mathbf{p} \otimes \mathbf{p} - \frac{1}{3}\mathbf{I}), \tag{2.12}$$

where the operation $\otimes$ is the outer product. In this case the six dipolar states represented in Fig. 2.3 give rise to doubly-degenerate tensor states,

$$\mathbf{p}_{1,2} = \begin{pmatrix} \pm 1 \\ 0 \\ 0 \end{pmatrix} \quad \Rightarrow \quad \boldsymbol{\theta}_1 = \frac{1}{2}\begin{pmatrix} 2 & 0 & 0 \\ 0 & -1 & 0 \\ 0 & 0 & -1 \end{pmatrix},$$

$$\mathbf{p}_{3,4} = \begin{pmatrix} 0 \\ \pm 1 \\ 0 \end{pmatrix} \quad \Rightarrow \quad \boldsymbol{\theta}_2 = \frac{1}{2}\begin{pmatrix} -1 & 0 & 0 \\ 0 & 2 & 0 \\ 0 & 0 & -1 \end{pmatrix}, \tag{2.13}$$

$$\mathbf{p}_{5,6} = \begin{pmatrix} 0 \\ 0 \\ \pm 1 \end{pmatrix} \quad \Rightarrow \quad \boldsymbol{\theta}_3 = \frac{1}{2}\begin{pmatrix} -1 & 0 & 0 \\ 0 & -1 & 0 \\ 0 & 0 & 2 \end{pmatrix}.$$

The set of tensors $\{\boldsymbol{\theta}_i\}$ with $i = \overline{1,3}$ will be used to describe the state of dipolar NP in Chap. 4.

2.3 The Maier-Saupe-Zwanzig model

The Maier-Saupe-Zwanzig (MSZ) model or six-states Maier-Saupe model can be considered as a generalization of the three-state Potts model used by de Oliveira and Figueiredo-Neto [43] in the description of the isotropic-nematic transition of lyotropic liquid crystals. In this model we have a lattice system with N sites occupied by asymmetric objects (nematogens). The interaction between nematogens is defined by means of the Hamiltonian

$$\mathcal{H} = -A \sum_{(i,j)} \mathbf{\Omega}_i : \mathbf{\Omega}_j, \tag{2.14}$$

where A is a positive coupling parameter, the sum is performed over pairs (i, j) of neighboring sites i and j in the lattice, and the quantity $\mathbf{\Omega}_j$ is represented by a 3×3 squared matrix with real entries. For nematogens, $\mathbf{\Omega}_i$ is a symmetric traceless matrix.

In order to perform detailed calculations, besides using Eq. (2.14) to describe the system interactions, we also employ a discretizations of directions similar to the one described in Sec. 2.2. We then assume that the principal nematogen axes are restricted to the directions of the Cartesian laboratory axes. Therefore, the second-rank tensor $\mathbf{\Omega}_i$ can assume only six states, represented by $\{\boldsymbol{\omega}_i\}$, see Eq. (2.6). Although it may seem drastic, there is abundant evidence that this approximation does not qualitatively affect the predictions for nematic liquid-crystalline phase diagrams. [2]

Determining the thermodynamic properties of the lattice system defined by Eq. (2.14) is rather intricate, due to the complex interplay between the various interactions. Therefore, we think it is appropriate to study the model in a MF treatment, which is equivalent to considering the fully-connected Hamiltonian

$$\mathcal{H}_{\mathrm{mf}} = -\frac{A}{2N} \sum_{i,j=1}^{N} \mathbf{\Omega}_i : \mathbf{\Omega}_j = -\frac{A}{2N} \sum_{\nu \in \{x,y,z\}} \left(\sum_{i=1}^{N} \Omega^{\nu\nu} \right)^2, \tag{2.15}$$

where the sums over pairs of neighboring sites are replaced by sums over all pairs of sites, and the coupling parameters are replaced by new ones that are inversely proportional to the number of sites to ensure that energy is extensive. Using the Gaussian identity in Eq. (2.11) and defining $\alpha = \beta A/2$ and $\mathbf{v} = \beta A \mathbf{Q}$ we can write

$$\exp\left[\frac{\beta A}{2N} \sum_{i,j=1}^{N} \mathbf{\Omega}_i : \mathbf{\Omega}_j \right] \propto \int_{\mathbb{R}^3} \exp\left(-\frac{\beta A N}{2} \|\mathbf{Q}\|^2 + \beta A \mathbf{Q} : \sum_{i=1}^{N} \mathbf{\Omega}_i \right) d[\mathbf{Q}], \tag{2.16}$$

where $\|\cdot\|$ represents the Frobenius norm, $\mathbf{Q}$ is a symmetric and traceless tensor, and $d[\mathbf{Q}] \equiv$

[2] The exchange of a continuous symmetry for a discrete one would substantially affect the physics of two-dimensional models, due to the Mermin-Wagner theorem [44], but here we restrict ourselves to three-dimensional systems.

$dQ^{xx}\,dQ^{yy}\,dQ^{zz}$. We then obtain an integral representation of the partition function that characterizes the thermodynamic behavior of the system,

$$\mathcal{Z} \propto \int_{\mathbb{R}^3} e^{-N\beta\psi(\mathbf{Q};\Delta,\beta)}\, d[\mathbf{Q}], \tag{2.17}$$

with the Landau-de Gennes free-energy functional

$$\psi(\mathbf{Q};\Delta,\beta) = \frac{A}{2}\|\mathbf{Q}\|^2 - \frac{1}{\beta}\ln\left(\sum_{\mathbf{\Omega}} e^{\beta\mathbf{Q}:\mathbf{\Omega}}\right). \tag{2.18}$$

The traceless condition allows a description of the free energy functional in terms of the scalar parameters S and η that characterize the collective degree of uniaxiality and biaxiality, respectively. The scalar parameters are associated with the tensor $\mathbf{Q}$ [45]

$$\mathbf{Q} = \frac{1}{2}\begin{pmatrix} -S-\eta & 0 & 0 \\ 0 & -S+\eta & 0 \\ 0 & 0 & 2S \end{pmatrix}. \tag{2.19}$$

The equilibrium values of S and η are determined by locating the absolute minima of $\psi(S,\eta)$, leading to the MF equations

$$\frac{\partial\psi}{\partial S} = \frac{\partial\psi}{\partial\eta} = 0, \tag{2.20}$$

which take the self-consistent forms $S = F_1(S,\eta,\Delta,\beta)$ and $\eta = F_2(S,\eta,\Delta,\beta)$. Depending on the solutions to these MF equations, the structure of the eigenvalues q_x, q_y, q_z of $\mathbf{Q}$ may be such that: (i) $q_x = q_y = q_z = 0$, corresponding to the isotropic phase; (ii) $q_x = q_y \neq q_z$ (or similar relations with permutations of the indices x, y and z), corresponding to an uniaxial nematic phase; and (iii) q_x, q_y, and q_z all distinct, corresponding to a biaxial nematic phase. If the eigenvalue with largest absolute value is positive (negative), the nematic solution is calamitic (discotic). In terms of the quantities S and η, the isotropic solution is given by $S = \eta = 0$, and uniaxial solutions are such that $S \neq 0$ with $\eta = 0$ or $\eta = \pm 3S$, while the remaining cases represent biaxial solution.

We emphasize that the values of S and η at the absolute minima of ψ represent thermodynamic equilibrium values for fixed reciprocal temperature β and biaxiality degree Δ. The free-energy $\mathcal{F} = \mathcal{F}(\Delta,\beta)$ of the system corresponds to the convex envelope of ψ determined after inserting values of S and η associated with the minima of the free-energy functional.

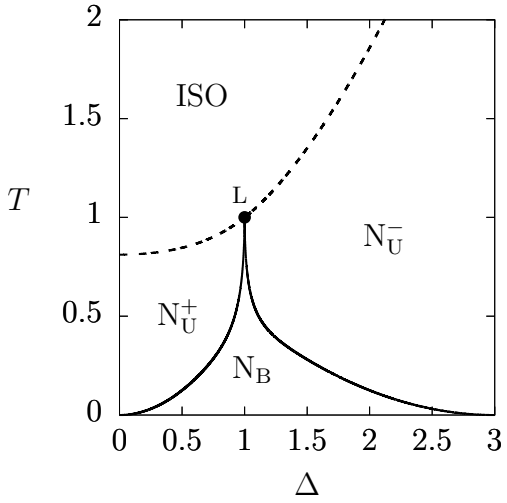

Figure 2.4: Phase diagrams in terms of temperature T and degree of biaxiality Δ, for a system of intrinsically biaxial molecules. $\mathrm{N_U^+}$ and $\mathrm{N_U^-}$ are uniaxial nematic prolate and oblate phases respectively. $\mathrm{N_B}$, is a nematic biaxial phase. L is a multicritical Landau point. ISO, isotropic phase. Solid line represent continuous transitions, and dashed line represent first-order transitions.

The phase diagram of the MSZ model is shown in Fig. 2.4. We have two solid lines representing second-order transitions from a biaxial nematic phase to uniaxial nematic phases $\mathrm{N_U^+}$ and $\mathrm{N_U^-}$. The lines of critical points meet at a multicritical Landau point (L) together with a dotted line that represents a first-order transition between the isotropic and uniaxial nematic phases. In general, the location of the Landau multicritical point is related to the cancellation of higher-order total derivatives,

$$\frac{d^2\psi}{dS^2} = \frac{d^3\psi}{dS^3} = 0, \tag{2.21}$$

evaluated at $(S, \eta) = (0, 0)$. The condition on the third derivative implies that at the Landau point $\Delta = 1$, and the remaining condition implies that $\beta A = 1$. A qualitatively similar phase diagram was obtained by N. Boccara *et al.* [46], for a continuous model with infinite range interactions.

Chapter 3

Effects of dilution

3.1 Introduction

Most theoretical and computational studies looking for biaxial phases focus on the orientational order, leaving aside effects associated with a varying density of nematogens. Approaches based on the phenomenological Landau–de Gennes expansion [45] are able to partially remedy this situation, by exploiting variations in the expansion coefficients, although these are difficult to connect with microscopic parameters. Our aim in this chapter is to investigate the equilibrium phase diagrams of a statistical model in which nematogens with non-cylindrical symmetry can move from site to site in a lattice whose occupation can be controlled. In our model, pairs of nematogens interact via an isotropic potential which can be repulsive or attractive, as well as via an anisotropic potential which favors a biaxial arrangement, leading, at sufficiently high occupation and sufficiently low temperature, to a biaxial phase.

A quite general bilinear anisotropic interaction potential V_{ij} between two nematogens labeled as i and j was proposed by J. P. Straley [47]. In the two-tensor formulation of A. M. Sonnet *et al.* [48], it takes the form

$$V_{ij} = -\frac{9}{4} A \left[\mathbf{q}_i : \mathbf{q}_j + \xi \left(\mathbf{q}_i : \mathbf{b}_j + \mathbf{b}_i : \mathbf{q}_j \right) + \lambda \mathbf{b}_i : \mathbf{b}_j \right]. \tag{3.1}$$

In Eq. (3.1) the parameter A is positive and sets the energy scale. The second-rank tensors $\mathbf{q}$ and $\mathbf{b}$ are defined in terms of mutually orthogonal unit vectors $\hat{n}_1$, $\hat{n}_2$ and $\hat{n}_3$ pointing along the first, second, and third principal axes of each nematogen as

$$\mathbf{q} = \hat{n}_1 \otimes \hat{n}_1 - \frac{1}{3}\mathbf{I} \quad \text{and} \quad \mathbf{b} = \hat{n}_2 \otimes \hat{n}_3 - \hat{n}_3 \otimes \hat{n}_2, \tag{3.2}$$

$\mathbf{I}$ being the 3×3 identity matrix.The adimensional parameters ξ and λ gauge the importance of biaxial couplings. If $\xi = \lambda = 0$, Eq. (3.1) is reduced to the Maier-Saupe interaction energy [6], defined solely by the relative orientation of the first principal axes of both nematogens. This is appropriate when dealing with nematogens whose form may be properly approximated as

uniaxial. Otherwise, if the nematogens are intrinsically biaxial, a proper description of the interaction energy requires setting either ξ or λ to nonzero values, so that the relative orientations of other principal axes are also relevant. Here we work with the condition $\lambda = \xi^2$, corresponding to the London approximation for dispersion forces [48], which allows us to write V_{ij} in the form

$$V_{ij} = -\frac{9}{4}A\left(\mathbf{q}_i + \frac{\Delta}{3}\mathbf{b}_i\right) : \left(\mathbf{q}_j + \frac{\Delta}{3}\mathbf{b}_j\right). \tag{3.3}$$

By resorting to a simplified view of a biaxial nematogen as a parallelepiped, the biaxial parameter $\Delta = 3\xi$ can be interpreted in terms of the sides of a parallelepiped (similar to Chap. 1), so that $\Delta = 0$ would correspond to a "rod-like" object, $\Delta = 3$ to a "disk-like" object, and $\Delta = 1$ to a maximally biaxial object [22].

Using a lattice-gas (LG) extension of the Maier-Saupe-Zwanzig (MSZ) model, in the same spirit of the work of M. Bates [49], we allow each site of a lattice to be empty or occupied by a single nematogen, adding an isotropic interaction to the potential in Eq. (3.3) to obtain the contribution of two neighboring sites i and j to the total interaction energy of the system,

$$V_{ij} = \gamma_i\gamma_j\left[U - \frac{9}{4}A\left(\mathbf{q}_i + \frac{\Delta}{3}\mathbf{b}_i\right) : \left(\mathbf{q}_j + \frac{\Delta}{3}\mathbf{b}_j\right)\right]. \tag{3.4}$$

The occupation variable γ_i is equal to 0 if the site i is empty and 1 if the site is occupied. Here we allow the strength of the isotropic interaction, U, to be either negative, representing attractive interactions, or positive, representing repulsion. This last case could lead to long-range sublattice ordering (e.g., in cubic lattices), an unphysical feature for a fluid phase. At the MF level, however, describing such kind of arrangement would require explicit introduction of sublattices. Instead, we proceed with the simplest MF strategy, which would be appropriate for describing a frustrated lattice or, for that matter, a fluid phase.

In this chapter we investigate the phase diagrams of what may be characterized as a LG extension of the MSZ model, which from now on we will call lattice-gas Maier-Saupe-Zwanzig (LGMSZ) model. The LG extension introduces dilution as an extra ingredient in our model, allowing the study of phenomena such as vapor-liquid, vapor-nematic, and nematic-nematic (low-high concentration) coexistence. The study of such coexistences is not possible if we treat a model based on a fully-occupied lattice.

This chapter is organized as follows. Sec. 3.2 presents the LGMSZ model and sketches its MF solution. In Sec. 3.3 we present a detailed analysis of the dilution effects, in the absence of isotropic interaction for different values of Δ. Sec. 3.4 is dedicated to the study of the effects of isotropic interactions for molecular systems with fixed degrees of biaxiality. In Sec. 3.5 we present an analysis of the effects of the biaxiality degree in the multicritical points present in the phase diagrams. Conclusions are presented in Sec. 3.6.

3.2 The LGMSZ model

Consider a lattice system with N sites and N_m non-spherical objects such that $N \geq N_m$. Each lattice site can be either empty or occupied by an asymmetric object, the state of the site i being described by an occupation variable γ_i taking the values 0 (empty site) or 1 (occupied site). Then, based on Eq. (3.4), we define the LGMSZ model by means of the effective Hamiltonian

$$\mathcal{H} = \sum_{(i,j)} V_{ij} = -A \sum_{(i,j)} \gamma_i \gamma_j \mathbf{\Omega}_i : \mathbf{\Omega}_j + U \sum_{(i,j)} \gamma_i \gamma_j, \tag{3.5}$$

where A and U are coupling parameters, with $A > 0$, the sum is performed over pairs (i, j) of neighboring sites i and j in the lattice, and the quantity $\mathbf{\Omega}_i$ is a second-rank tensor associated with the nematogen at site i. The set $\{\boldsymbol{\omega}_i\}$ with $i = \overline{1,6}$, see Eq. (2.13), represents the possible values of $\mathbf{\Omega}_i$. Note that, for rod-like nematogens ($\Delta = 0$), Eq. (3.5) reduces to a discretized version of the Lebwohl-Laser lattice-gas model introduced by M. Bates [49] (with a rescaling of energy, as our parameter A would be equivalent to $2\epsilon/3$, ϵ being the energy scale of the anisotropic interaction in Ref. [49]).

The first term in Eq. (3.5) represents a diluted version of the MSZ model, and the orientation-dependent interaction may give rise to distinct nematic phases. The second term is the isotropic contribution to the pair potential. For the particular case of $U < 0$, representing attractive isotropic interactions, one can find phase transitions between isotropic fluid states, in analogy with the previous studies [49, 50]. Here we assume that the parameter U can also be positive, representing repulsive interaction. In this latter case, as we are interested in modeling fluid phases only, we refrain from trying to account for any kind of sublattice ordering whatsoever.

For this system, the canonical ensemble is not the more convenient route to investigate the macroscopic behavior because the partition function, which can be written as

$$\mathcal{Z} = {\sum_{\{\gamma_i\}}}' \sum_{\{\mathbf{\Omega}_i\}} \exp\left(\beta A \sum_{(i,j)} \gamma_i \gamma_j \mathbf{\Omega}_i : \mathbf{\Omega}_j - \beta U \sum_{(i,j)} \gamma_i \gamma_j \right), \tag{3.6}$$

presents a restriction on the first sum over the occupation degrees of freedom. The prime above the sum indicates that only configurations that satisfy the constraint

$$\sum_{i=1}^{N} \gamma_i = N_m \tag{3.7}$$

should be considered, which leads to complications in evaluating this function. As a result, it is more convenient to consider the formalism of the grand canonical ensemble, where the number of nematogens may fluctuate due to the coupling to a particle reservoir [19, 22, 25]. Then we

must determine the grand partition function

$$\Xi = \sum_{\{\gamma_i\}} \sum_{\{\mathbf{\Omega}_i\}} \exp\left(\beta A \sum_{(i,j)} \gamma_i \gamma_j \mathbf{\Omega}_i : \mathbf{\Omega}_j - \beta U \sum_{(i,j)} \gamma_i \gamma_j + \beta \mu \sum_i \gamma_i \right), \tag{3.8}$$

where μ is the chemical potential, which controls the number of nematogens. In this ensemble the sum over configurations in Eq. (3.8) is no longer restricted, and MF calculations are feasible.

3.2.1 Molecular field theory

The MF version of the LGMSZ model is obtained by assuming a fully-connected lattice Hamiltonian

$$\mathcal{H}_{\mathrm{mf}} = -\frac{A}{2N} \sum_{i,j=1}^{N} \gamma_i \gamma_j \mathbf{\Omega}_i : \mathbf{\Omega}_j + \frac{U}{2N} \sum_{i,j=1}^{N} \gamma_i \gamma_j, \tag{3.9}$$

where the sums over pairs of neighboring sites are replaced by sums over all pairs of sites, and the coupling parameters are replaced by new ones that are inversely proportional to the number of sites to ensure that energy is extensive. This form of effective, long-range model has been proposed to investigate the phase behavior of statistical models with nematic-like phases [19, 22, 23, 25, 51, 52]. Therefore, our main interest is to study the thermodynamics of phases transitions of the MF model in Eq. (3.9).

The grand partition function of the system can be written as

$$\Xi = \sum_{\{\gamma_i\}} \sum_{\{\mathbf{\Omega}_i\}} \exp\left(\frac{\beta A}{2N} \sum_{i,j=1}^{N} \gamma_i \gamma_j \mathbf{\Omega}_i : \mathbf{\Omega}_j - \frac{\beta U}{2N} \sum_{i,j=1}^{N} \gamma_i \gamma_j + \beta \mu \sum_{i=1}^{N} \gamma_i \right). \tag{3.10}$$

In order to obtain an integral representation of the grand partition function in the MF limit, we can use the restriction in Eq. (3.7) for the number $N_m \equiv \phi N$ of nematogens, and the integral representation of the Dirac delta function,

$$\delta\left(N\phi - \sum_{i=1}^{N} \gamma_i \right) = \frac{1}{2\pi\,\mathrm{i}} \int_{-\mathrm{i}\infty}^{+\mathrm{i}\infty} \exp\left[-\hat{\phi}\left(N\phi - \sum_{i=1}^{N} \gamma_i \right) \right] d\hat{\phi}, \tag{3.11}$$

where $\mathrm{i} = \sqrt{-1}$ represents the imaginary unit. We also have the Gaussian identity in Eq. (2.11) with $\alpha = \beta A/2$, $\mathbf{v} = \beta A \mathbf{Q}$, and $\mathbf{\Omega}_i \to \gamma_i \mathbf{\Omega}_i$,

$$\exp\left(\frac{\beta A}{2N} \sum_{i,j=1}^{N} \gamma_i \gamma_j \mathbf{\Omega}_i : \mathbf{\Omega}_j \right) \propto \int_{\mathbb{R}^3} \exp\left(-\frac{\beta A N}{2} \|\mathbf{Q}\|^2 + \beta A \mathbf{Q} : \sum_{i=1}^{N} \gamma_i \mathbf{\Omega}_i \right) d[\mathbf{Q}], \tag{3.12}$$

where the constant of proportionality is irrelevant, and $\|\cdot\|$ is the Frobenius norm. Using the identities in Eqs. (3.11) and (3.12) and performing the partial trace over the occupation variables

$\{\gamma_i\}$, we can write the grand partition function in the form

$$\Xi \propto \int \mathrm{I}(\mathbf{Q},\phi) e^{-N\beta\Gamma(\mathbf{Q},\phi)}\, d\phi\, d[\mathbf{Q}], \tag{3.13}$$

where

$$\Gamma(\mathbf{Q},\phi) = \frac{A}{2}\|\mathbf{Q}\|^2 + \frac{U}{2}\phi^2 - \mu\phi, \tag{3.14}$$

$$\mathrm{I}(\mathbf{Q},\phi) = \frac{N}{2\pi\,\mathrm{i}} \int_{-\mathrm{i}\infty}^{\mathrm{i}\infty} e^{Nf(\mathbf{Q},\phi,\hat{\phi})}\, d\hat{\phi}, \tag{3.15}$$

and

$$f(\mathbf{Q},\phi,\hat{\phi}) = -\phi\hat{\phi} + \ln\left(6 + e^{\hat{\phi}} \sum_{\mathbf{\Omega}} e^{\beta A \mathbf{Q}:\mathbf{\Omega}}\right). \tag{3.16}$$

In the thermodynamic limit $N \gg 1$, we expect the integral in Eq. (3.15) to be dominated by the highest stationary point of $f(\mathbf{Q},\phi,\hat{\phi})$ with respect to $\hat{\phi}$. As for a complex function the only stationary points are saddle points, the integral is therefore dominated by the highest saddle point. A saddle point $\hat{\phi}_o$, can be determined by the condition $\partial f/\partial\hat{\phi} = 0$ evaluated at $\hat{\phi} = \hat{\phi}_o$. Then

$$\hat{\phi}_o = \ln\left(\frac{6\phi}{1-\phi}\right) + \ln\left(\sum_{\mathbf{\Omega}} e^{\beta A \mathbf{Q}:\mathbf{\Omega}}\right), \tag{3.17}$$

where $\hat{\phi}_o \in \mathbb{R}$, because $0 < \phi < 1$. In a neighborhood of $\hat{\phi}_o$ we can write

$$f(\mathbf{Q},\phi,\hat{\phi}) \approx f(\mathbf{Q},\phi,\hat{\phi}_o) + \frac{1}{2} f''(\mathbf{Q},\phi,\hat{\phi}_o)(\hat{\phi}-\hat{\phi}_o)^2, \tag{3.18}$$

so that the integral $\mathrm{I}(\mathbf{Q},\phi)$ takes the form

$$\mathrm{I}(\mathbf{Q},\phi) \approx \frac{N}{2\pi\,\mathrm{i}} e^{Nf(\mathbf{Q},\phi,\hat{\phi}_o)} \int_{-\mathrm{i}\infty}^{\mathrm{i}\infty} e^{Nf''(\mathbf{Q},\phi,\hat{\phi}_o)(\hat{\phi}-\hat{\phi}_o)^2}\, d\hat{\phi}. \tag{3.19}$$

The integral in Eq. (3.19) can be solved by the method of steepest descents, as long as we deform the integration contour so that it passes through the saddle point, as allowed by Cauchy's theorem. For $\hat{\phi} \approx \hat{\phi}_o$, we write

$$\hat{\phi} - \hat{\phi}_o = \rho e^{i\varphi}, \tag{3.20}$$

in which φ is the angle according to which the integration contour passes through the saddle point $\hat{\phi}_o$ so that, in the complex plane defined by $\hat{\phi}$, $f''(\mathbf{Q},\phi,\hat{\phi}_o)$ is a real number. Taking into account that in this problem $f''(\mathbf{Q},\phi,\hat{\phi}_o) = \phi(1-\phi)$, implying $\varphi = \pi/2$ (see Ref. [53], p. 491), we obtain

$$\mathrm{I}(\mathbf{Q},\phi) \approx \sqrt{\frac{N}{2\pi}} \frac{e^{Nf(\mathbf{Q},\phi,\hat{\phi}_o)}}{\sqrt{\phi(1-\phi)}}. \tag{3.21}$$

Finally, we get an integral representation of the grand partition function,

$$\Xi \propto \int_{\mathbb{R}^4} e^{-N\beta\psi(\mathbf{Q},\phi)} \frac{d\phi\, d[\mathbf{Q}]}{\sqrt{\phi(1-\phi)}}, \tag{3.22}$$

where the Landau-de Gennes (grand canonical) free-energy functional is

$$\psi(\mathbf{Q},\phi) = \frac{A}{2}\|\mathbf{Q}\|^2 + \frac{U}{2}\phi^2 - \mu\phi - \frac{1}{\beta} f(\mathbf{Q},\phi,\hat{\phi}_o), \tag{3.23}$$

with

$$f(\mathbf{Q},\phi,\hat{\phi}_o) = -\phi\ln(\phi) - (1-\phi)\ln\left(\frac{1-\phi}{6}\right) + \phi\ln\left(\sum_{\mathbf{\Omega}} e^{\beta A\mathbf{Q}:\mathbf{\Omega}}\right). \tag{3.24}$$

Note that, from self-consistent MF matrix equations, $\partial\psi/\partial\mathbf{Q} = 0 \Rightarrow \mathrm{Tr}\,\mathbf{Q} = 0$. The symmetric traceless tensor $\mathbf{Q}$ can be parameterized by the scalar quantities S and η, similar to Sec. 2.3. Then we obtain

$$\begin{aligned}\psi(S,\eta,\phi) = \frac{A}{4}(3S^2+\eta^2) + \frac{U}{2}\phi^2 - \mu\phi - \frac{\phi}{\beta}\ln\left[\Lambda(S,\eta)\right] \\ + \frac{1}{\beta}\left[(1-\phi)\ln\left(\frac{1-\phi}{6}\right) + \phi\ln(\phi)\right],\end{aligned} \tag{3.25}$$

where

$$\begin{aligned}\Lambda(S,\eta) = 2\exp\left[-\frac{3\beta A}{4}(S+\eta)\right]\cosh\left[\frac{3\beta A}{4}\left(S-\frac{\eta}{3}\right)\Delta\right] \\ + 2\exp\left[-\frac{3\beta A}{4}(S-\eta)\right]\cosh\left[\frac{3\beta A}{4}\left(S+\frac{\eta}{3}\right)\Delta\right] \\ + 2\exp\left(\frac{3\beta A}{2}S\right)\cosh\left(\frac{\beta A}{2}\eta\Delta\right).\end{aligned} \tag{3.26}$$

Notice that ϕ corresponds to the concentration of nematogens [1].

The equilibrium values of S, η, and ϕ are determined by locating the absolute minima of $\psi(S,\eta,\phi)$, leading to the MF equations

$$\frac{\partial\psi}{\partial S} = \frac{\partial\psi}{\partial\eta} = \frac{\partial\psi}{\partial\phi} = 0, \tag{3.27}$$

[1] In this manuscript, in order not to overload the notation, we will use the same notation for the variables (e.g., S, η, ϕ) and for their statistical average.

which take the self-consistent forms

$$\begin{aligned} S &= F_1(S, \eta, \phi; \beta, \mu, \Delta), \\ \eta &= F_2(S, \eta, \phi; \beta, \mu, \Delta), \\ \phi &= F_3(S, \eta, \phi; \beta, \mu, \Delta). \end{aligned} \tag{3.28}$$

3.3 Phase behavior for $U = 0$

When the isotropic interaction is zero ($U = 0$) the analysis of the phase behavior is less complicated because of the reduction in the number of parameters of the system. Some aspects of this case are analyzed by D. D. Rodrigues *et al.* [25], but only a specific range of parameters is considered. In this section we present a detailed analysis of the ϕ-T phase diagrams with many different topologies by exploring a wider range of values for thermodynamics fields. The results presented in this section are the starting point for the construction of more complex phase diagrams for systems with both isotropic and anisotropic interactions between nematogens, as presented in the next section.

By considering intrinsically uniaxial nematogens, for which $\Delta = 0$, we find the phase diagram shown in Fig. 3.1(a), which is qualitatively equivalent and quantitatively similar to the one obtained by Monte Carlo simulations of the Lebwohl-Lasher lattice-gas model by M. Bates [49], in the absence of isotropic interaction. At high concentration ($\phi \gtrsim 0.75$), as T decreases, the observed phase sequence is isotropic (ISO), followed by a biphasic region of coexisting rod-rich uniaxial nematic ($\mathrm{N_U^+}$) and rod-poor isotropic phase, followed by a pure uniaxial nematic and finally a reentrant coexistence region. At lower rod concentration the coexistence region is stable at low temperatures. The coexistence lines signaling the discontinuous transition from the isotropic phase to the uniaxial nematic phase are determined by Eq. (3.27) evaluated at $(S, \eta, \phi) = (S_\mathrm{U}, 0, \phi_\mathrm{U})$ and at $(S, \eta, \phi) = (0, 0, \phi_\mathrm{I})$, supplemented by $\psi(S_\mathrm{U}, 0, \phi_\mathrm{U}) = \psi(0, 0, \phi_\mathrm{I})$, where ϕ_I and ϕ_U are, respectively, the concentrations of the isotropic and uniaxial phases at the transition point, and S_U is the value of S at that point. Notice that, since the nematogens are intrinsically uniaxial, we can assume $\eta = 0$ without loss of generality. It is worth mentioning that in the uniaxial limit of $\Delta = 0$ we see a single isotropic phase, with no sign of vapor-liquid coexistence, in agreement with Monte Carlo [54] and mean-field [55] calculations for the off-lattice hard-sphere Maier-Saupe model.

For the case of noncylindrical molecules, $\Delta \neq 0$ and $\Delta \neq 3$, it is possible to observe stable biaxial phases ($\mathrm{N_B}$), as shown in Fig. 3.1(b) for biaxiality degree $\Delta = 19/20$. In this diagram, at high concentrations and temperatures, there is a small biphasic region of coexisting uniaxial and isotropic phases. As temperature decreases, we have a second-order transition from the $\mathrm{N_U^+}$ phase to a pure $\mathrm{N_B}$ phase, and finally the biphasic region ISO-$\mathrm{N_B}$ appears. The conditions for determining the first-order transition between ISO and $\mathrm{N_B}$ are given by Eq. (3.27) evaluated at $(S, \eta, \phi) = (S_\mathrm{B}, \eta_\mathrm{B}, \phi_\mathrm{B})$ and at $(S, \eta, \phi) = (0, 0, \phi_\mathrm{I})$, as well as $\psi(S_\mathrm{B}, \eta_\mathrm{B}, \phi_\mathrm{B}) = \psi(0, 0, \phi_\mathrm{I})$,

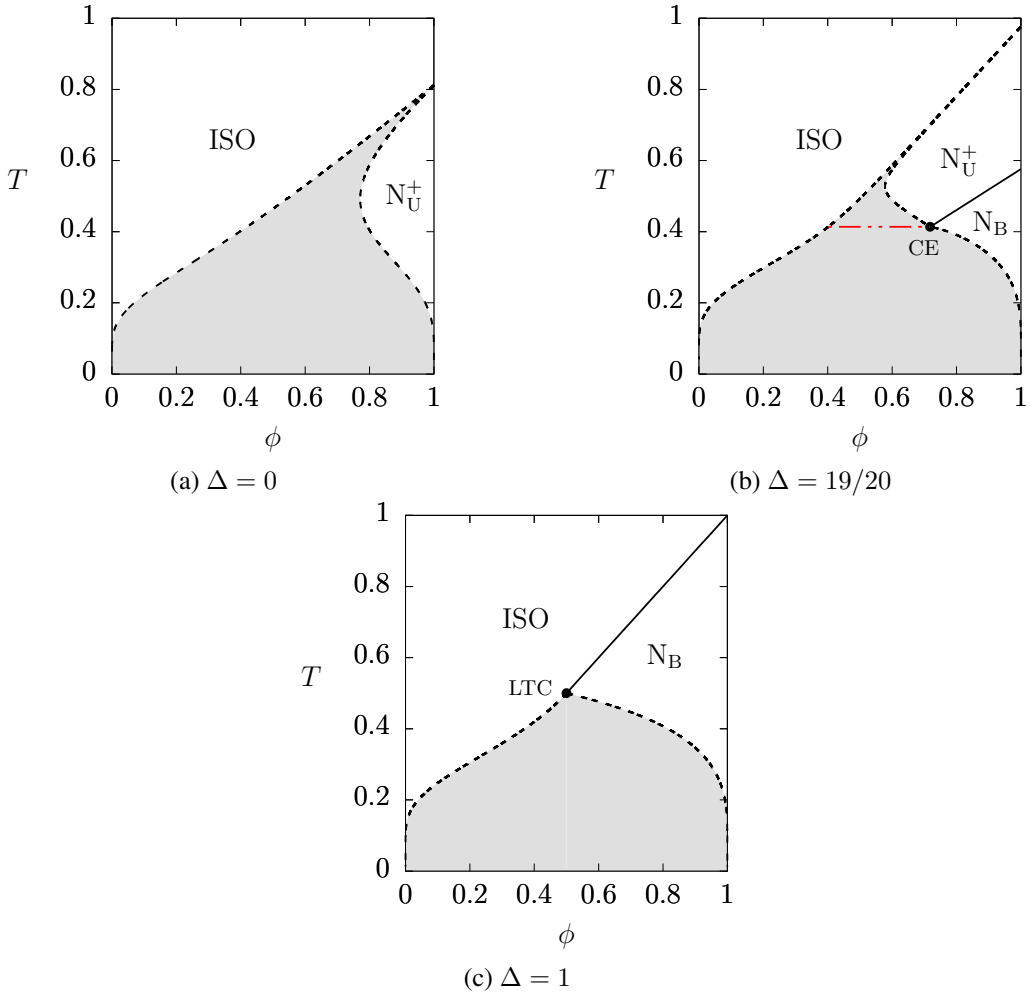

(a) $\Delta = 0$ (b) $\Delta = 19/20$ (c) $\Delta = 1$

Figure 3.1: Phase diagrams in terms of temperature T (in units of A) and concentration ϕ of nematogens, for different values of biaxiality degree and in absence of isotropic interaction ($U = 0$). ISO: isotropic phase. N_U^+: calamitic uniaxial nematic phase. N_B: biaxial nematic phase. Short-dashed lines are the boundaries of biphasic region (gray). Red dot-dashed line: critical end point (CE). LTC is a Landau tricritical point.

where S_B and η_B are the values taken by S and η in the biaxial state at the transition point. On the other hand, the second order transition between uniaxial and biaxial phases is located by Eq. (3.27) and $\partial^2\psi/\partial\eta^2 = 0$, all evaluated at $(S, \eta, \phi) = (S_o, 0, \phi_o)$, where S_o and ϕ_o are the values of S and ϕ at the transition line. We also find that the N_U^+-N_B transition line meets the ISO-N_B biphase region at a critical end point (CE), in which a critical nematic state separating uniaxial and biaxial phases coexists with a noncritical isotropic state. Critical end points are among the various possible multicritical points that can be found in thermodynamic systems with many components [2, 56, 57]. In our case, we have a critical end points related to nematic transitions in a lattice-gas model with orientation-dependent interactions. These kinds of multicritical points were also reported in a Maier-Saupe model that mimics binary mixtures of uniaxial and biaxial nematogens [22].

For anisotropic objects with maximal biaxiality degree, $\Delta = 1$, stable uniaxial phases are absent and the diagrams present the general aspect shown in Fig. 3.1(c). In this case, for high temperatures and concentration, the ISO-N_B transition is continuous and determined by the

conditions

$$\frac{\partial\psi}{\partial\phi} = \frac{\partial\psi}{\partial\eta} = \frac{\partial^2\psi}{\partial\eta^2} = 0, \tag{3.29}$$

evaluated at the transition point $(S, \eta, \phi) = (0, 0, \phi_o)$. This line of continuous transitions is actually a line of multicritical Landau points. On the other hand, for low T and intermediate concentrations, we observe an ISO-$\mathrm{N_B}$ coexistence region associated with a first-order transition at which

$$\frac{\partial\psi}{\partial\eta} = \frac{\partial\psi}{\partial\phi} = 0 \tag{3.30}$$

at $(S, \eta, \phi) = (S_\mathrm{B}, \eta_\mathrm{B}, \phi_\mathrm{B})$ and at $(S, \eta, \phi) = (0, 0, \phi_\mathrm{I})$, supplemented by the continuity condition $\psi(S_\mathrm{B}, \eta_\mathrm{B}, \phi_\mathrm{B}) = \psi(0, 0, \phi_\mathrm{I})$. The discontinuous and continuous transitions meet at a multicritical point which we call Landau tricritical point (LTC). Roughly speaking, according to the solutions of mean-field equations, the multicritical point LTC has properties common to both Landau points [45] and tricritical points [56, 57]. Notice that in the limit of a pure system (i.e., $\phi \to 1$) consisting of a biaxial objects with $\Delta = 1$, our findings are in agreement with earlier mean-field results, which show a direct ISO-$\mathrm{N_B}$ transition through a single, isolated Landau point in the Δ-T phase diagram [22, 23].

It is possible to determine the conditions that characterize a Landau tricritical point by following the discussion presented by D. D. Rodrigues *et al.* [25]. Indeed, in our context, an LTC point is the endpoint of a line of Landau points, and a Landau point happens when the stable solutions of MF equations for ISO, $\mathrm{N_U^+}$, and $\mathrm{N_U^-}$ become degenerate. Each point on a Landau line satisfies

$$\frac{\partial\psi}{\partial\phi} = 0 \quad \text{and} \quad \frac{d^2\psi}{dS^2} = \frac{d^3\psi}{dS^3} = 0, \tag{3.31}$$

evaluated at $(S, \eta, \phi) = (0, 0, \phi_\mathrm{L})$. Observe that these conditions involve partial derivatives as well as total derivatives (with respect to S) of the free-energy functional ψ. We must treat ϕ as an implicit function of S while calculating the total derivative. Thus, we find

$$\begin{aligned} &\Delta = 1, \\ &(\beta A - 1)e^{\beta\mu} - 1 = 0, \\ &\beta A \phi_\mathrm{L} = 1, \end{aligned} \tag{3.32}$$

which are the same results obtained in Ref. [25]. The solution to Eqs. (3.32) defines a line of Landau points, which is represented by a solid line in Fig. 3.1(c). In the limiting case of maximum concentration of biaxial objects, i.e., $\beta\mu \gg 1$ or equivalent $\phi \to 1$, we recover the results obtained in previous treatments [22, 23], apart from differences in the definitions of parameters. Nevertheless, we also have to check whether the solution leading to a Landau point corresponds to a minimum of the free-energy functional. This can be done by analyzing the behavior of the total fourth-order derivative of ψ with respect to η at $(S, \eta, \phi) = (0, 0, \phi_\mathrm{L})$,

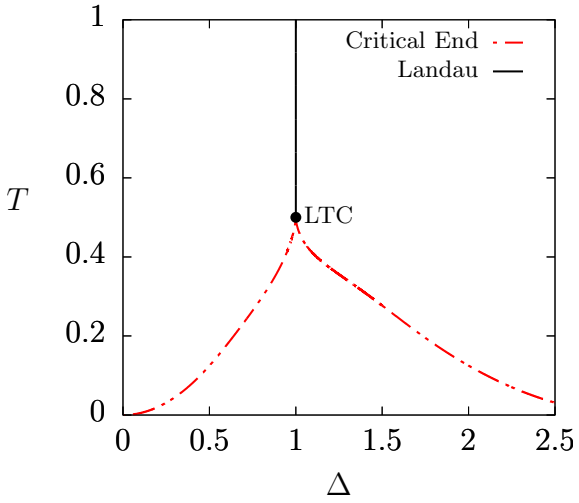

Figure 3.2: Lines of multicritical points in the plane Δ-T for zero isotropic interaction. The line of Landau points (black solid) meets the lines of critical end points (red dot-dashed) at a Landau tricritical (LTC) point, which is present only for maximal biaxiality degree $\Delta = 1$.

which gives

$$\frac{d^4\psi}{d\eta^4} = -\frac{3A^4\beta^3}{8}\phi_L(1-2\phi_{\rm L}). \tag{3.33}$$

This total derivative should be positive for stable states, but we notice that it may change its sign from positive, for $\phi_{\rm L} > 1/2$, to negative, for $\phi_{\rm L} < 1/2$ (implying stable Landau points for $\beta A < 2$). Thus, precisely at $\phi_{\rm L} = 1/2$, both $d^2\psi/\,d\eta^2$ and $d^4\psi/\,d\eta^4$ are zero, setting the conditions for locating a tricritical point that is also a Landau point. The coordinates of the LTC point are $(\beta A)_{\rm LTC} = 2$, $\phi_{\rm LTC} = 1/2$, and $\mu_{\rm LTC} = 0$. The stability of the LTC point can be checked by looking at the sixth-order derivative of ψ with respect to η, which gives $d^6\psi/\,d\eta^6 = 2A > 0$, therefore corresponding to a free-energy minimum.

We plotted all the lines of multicritical points obtained until now in the Δ-T plane shown in Fig. 3.2. It is worth mentioning that, as we are assuming zero isotropic interaction, the space of thermodynamic fields is spanned by temperature T, chemical potential μ, and biaxiality degree Δ. Due to that, the lines presented in Fig. 3.2 are critical solutions of MF equations with varying chemical potential. Besides, although we have focused the discussion on calamitic nematic phases, for which $0 < \Delta < 1$, the results for discotic nematics (see, e.g., Ref. [58]) with $1 < \Delta < 3$ lead to phase diagrams with analogous topologies. Observe that for systems with maximal biaxiality degree, the LTC point occurs when the line of Landau points meets the two lines of critical end points. The Landau tricritical point is present only for maximal biaxiality $\Delta = 1$.

We mention that the sequence of diagrams shown in Figs. 3.1(a)-3.1(c) for increasing biaxility parameter is reminiscent of the diagrams obtained from the mean-field treatment of the off-lattice Krieger-James model for ferronematics as the relative strength of the quadrupolar over dipolar interactions is increased [59]. In the latter model, a ferromagnetic phase replaces the biaxial phase of the LGMSZ model.

3.4 Phase behavior for $U \neq 0$

We now discuss phase diagrams in the presence of an isotropic interaction $U \neq 0$. In addition to uniaxial and biaxial structures, we may observed coexistence between isotropic fluid-like phases, which we call isotropic liquid phase (IL) and isotropic vapor phase (IV), as well as between nematic phases with different nematogen concentrations.

3.4.1 Phase diagrams for $\Delta = 0$

For intrinsically uniaxial, rod-like objects, a sufficiently attractive ($U < 0$) isotropic interaction leads to the appearance of a vapor-liquid (or a high-density−low-density transition) coexistence analogous to the van der Walls condensation; see Fig. 3.3(a), for $U = -3$. The vapor-liquid transition is determined by $\partial\psi/\partial\phi = 0$ at $(S, \eta, \phi) = (0, 0, \phi_{\rm IV})$ and at $(S, \eta, \phi) = (0, 0, \phi_{\rm IL})$, in addition to $\psi(0, 0, \phi_{\rm IV}) = \psi(0, 0, \phi_{\rm IL})$. These first-order lines meet at a simple critical point (C), located at $\phi_{\rm C} = 1/2$, $\beta_{\rm C} = -4/U$, $\mu_{\rm C} = U/2$ with $\psi_{\rm C} = U[2\ln(12) - 1]/8$. We

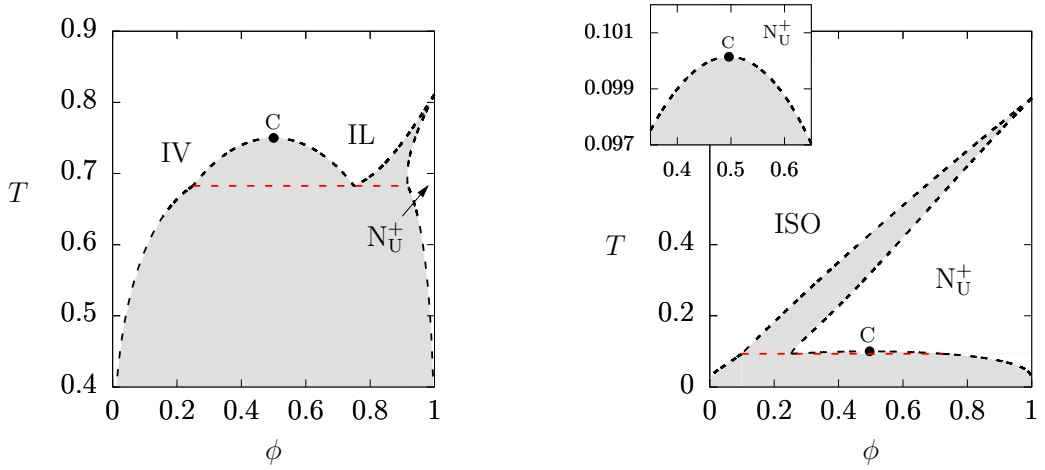

(a) $(A, U) = (1, -3)$ (b) $(A, U) = (1, 11/10)$

Figure 3.3: Phase diagrams in terms of temperature T (in units of A) and concentration ϕ of nematogens, for an intrinsically uniaxial system ($\Delta = 0$). Red long-dashed line: triple point. Black short-dashed line: boundaries of biphasic regions (gray). C is a ordinary critical point.

also find a vapor-liquid-uniaxial triple point, which is determined by evaluating Eq. (3.27) at $(S, \eta, \phi) = (0, 0, \phi_{\rm IV})$, at $(S, \eta, \phi) = (0, 0, \phi_{\rm IL})$ and at $(S, \eta, \phi) = (S_{\rm U}, 0, \phi_{\rm U})$, in addition to imposing $\psi(0, 0, \phi_{\rm IV}) = \psi(0, 0, \phi_{\rm IL}) = \psi(S_{\rm U}, 0, \phi_{\rm U})$. For T values lower than the triple-point temperature, the IV-IL discontinuous transition becomes metastable with respect to the IV-N$_{\rm U}^+$ first-order transition. As the strength $|U|$ of the attractive interaction increases, the region of stability of N$_{\rm U}^+$ decreases and tends to become limited to a very small region near $\phi = 1$; see Fig. 3.3(a). This reduction in the area of the uniaxial phase was observed by M. Bates, using Monte Carlo simulations in a lattice-gas extension of the Lebwohl-Lasher model [49] and later in the model proposed by Humphries *et al.* [50].

For repulsive isotropic interactions ($U > 0$), it is possible to notice the appearance of a very

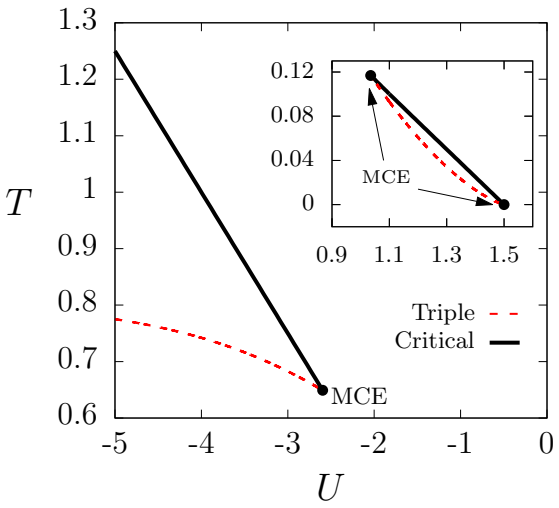

Figure 3.4: Lines of critical and of triple points in the U-T plane, for the case of rod-like nematogens ($\Delta = 0$). We notice that the lines of critical points meet the lines of triple points at higher-order multicritical end points MCEs. The inset shows the case for repulsive isotropic interaction ($U > 0$).

narrow coexistence regions between uniaxial nematic phases, as shown in Fig. 3.3(b). This biphasic coexistence region between uniaxial structures presents an ordinary critical point (C), which can be found by imposing the conditions

$$\frac{\partial \psi}{\partial S} = \frac{\partial \psi}{\partial \phi} = 0 \quad \text{and} \quad \frac{d^2\psi}{d\phi^2} = \frac{d^3\psi}{d\phi^3} = 0, \tag{3.34}$$

evaluated at $(S, \eta, \phi) = (S_{\rm C}, 0, \phi_{\rm C})$.

We plot the lines of critical points and of triple points in the U-T plane in Fig. 3.4. These lines meet at higher-order critical points, which we call multicritical end points (MCEs), in analogy with critical end points appearing when lines of first-order and second-order transitions meet. For $U < U^{(1)}_{\rm MCE} \approx -2.596$, we find phase diagrams with a simple critical point related to an IV-IL biphasic region, in addition to a vapor-liquid-uniaxial triple point. This kind of phase phenomenon is associated with an attractive character of the isotropic interaction. Nevertheless, for $U > U^{(1)}_{\rm MCE}$, it is no longer possible to distinguish between the IV and IL phases, and from a thermodynamic perspective there is a single isotropic phase. Then we have phase diagrams which only show ISO-$\rm N^+_U$ coexistence regions.

In the case of repulsive isotropic interactions with $U < U^{(2)}_{\rm MCE} \approx 1.035$, the phase diagrams also exhibit first-order transitions between isotropic and uniaxial phases. However, for $U^{(2)}_{\rm MCE} < U < U^{(3)}_{\rm MCE} = 3/2$, as illustrated in Fig. 3.3(b), it is possible to find phase diagrams exhibiting a coexistence region between uniaxial structures, with an associated critical point, as well as a triple point connecting one isotropic and two uniaxial states. As U increases, we notice a decrease in the area of the low-temperature isotropic-uniaxial coexistence region, together with the decrease in the temperature of the critical and the triple points, until the ISO-$\rm N^+_U$ coexistence disappears completely as $U \to U^{(3)}_{\rm MCE}$. For this limiting value of U , the temperatures both of the critical point and of the triple point become zero.

The sequence of diagrams in Figs. 3.3(a) and 3.3(b), obtained from the LGMSZ model as the isotropic interaction is tuned from attractive to repulsive, including the phase coexistences, is qualitatively equivalent to the ones obtained from the off-lattice Maier-Saupe model augmented by isotropic interactions [55, 60]. Other systems with similar sequences are mixtures of rod-like colloidal particles and hard-sphere polymers with varying diameters [61], binary mixtures of thermotropic nematogens with increasing dissimilarity [62], and long hard rods with short-range attractions with changing rod length or attraction range [63, 64].

3.4.2 Phase diagrams for $0 < \Delta < 1$

As previously mentioned, the discrete-state Maier-Saupe model presents phase diagrams with stable biaxial structures when the nematogens are intrinsically biaxial [22,23]. Then, we expect that the presence of dilution and isotropic interaction may lead to phase diagrams with more complex topologies. Indeed, for systems with attractive isotropic interactions, we obtain phase diagrams of the type shown in Fig. 3.5(a). In this case, we have a critical point C associated with an IV-IL biphasic region, and an IV-IL-N_U^+ triple point, analogous to those discussed in Sec. 3.4.1 for intrinsically uniaxial nematogens. We also find and IV-$\mathrm{N_B}$ discontinuous transition, determined by the conditions in Eq. (3.27), evaluated at $(S, \eta, \phi) = (0, 0, \phi_\mathrm{IV})$ and at $(S, \eta, \phi) = (S_\mathrm{B}, \eta_\mathrm{B}, \phi_\mathrm{B})$, supplemented by $\psi(0, 0, \phi_\mathrm{IV}) = \psi(S_\mathrm{B}, \eta_\mathrm{B}, \phi_\mathrm{B})$. The coexistence between the biaxial phase and the isotropic vapor is verified at low temperatures, below the temperature of a critical end point CE ($T_\mathrm{CE} \approx 0.56$), whose location is set by Eq. (3.27), evaluated at $(S, \eta, \phi) = (0, 0, \phi_\mathrm{IV})$ and at $(S, \eta, \phi) = (S_\mathrm{CE}, 0, \phi_\mathrm{CE})$ and $d^2\psi/\, d\eta^2 = 0$ at $(S, \eta, \phi) = (S_\mathrm{CE}, 0, \phi_\mathrm{CE})$. The biaxial nematic phase is stable for high concentrations and small temperatures.

Let us now consider repulsive isotropic interactions, $U = 1$, with biaxiality degree $\Delta = 4/5$. The phase diagrams is shown in Fig. 3.5(b), where it is possible to identify a triple point in which isotropic, uniaxial, and biaxial phases coexist, as well as a tricritical point (TC), which satisfies the conditions $\partial\psi/\partial\phi = \partial\psi/\partial S = d^2\psi/\, d\eta^2 = d^4\psi/\, d\psi^4 = 0$, evaluated at $(S, \eta, \phi) = (S_\mathrm{TC}, 0, \phi_\mathrm{TC})$. The total derivatives are determined by treating S and ϕ as implicit functions of η. The boundaries of the coexistence region associated with uniaxial and biaxial phases are determined by Eq. (3.27) evaluated at $(S, \eta, \phi) = (S_\mathrm{U}, 0, \phi_\mathrm{U})$ and at $(S, \eta, \phi) = (S_\mathrm{B}, \eta_\mathrm{B}, \phi_\mathrm{B})$, as well as $\psi(S_\mathrm{U}, 0, \phi_\mathrm{U}) = \psi(S_\mathrm{B}, \eta_\mathrm{B}, \phi_\mathrm{B})$. We also show in Fig. 3.5(c) the phase diagram corresponding to the repulsive case with $\Delta = 19/20$ and $U = 13/10$. There are biphasic regions associated with ISO and N_U^+, N_U^+ and $\mathrm{N_B}$, and ISO and $\mathrm{N_B}$. Beside, there is a triple point marking the coexistence of ISO, N_U^+, and $\mathrm{N_B}$. Finally, we observe the presence of a biaxial-biaxial coexistence region, whose boundaries are determined by Eq. (3.27) evaluated at $(S, \eta, \phi) = (S_1, \eta_1, \phi_1)$ and at $(S, \eta, \phi) = (S_2, \eta_2, \phi_2)$, supplemented by $\psi(S_1, \eta_1, \phi_1) = \psi(S_2, \eta_2, \phi_2)$.

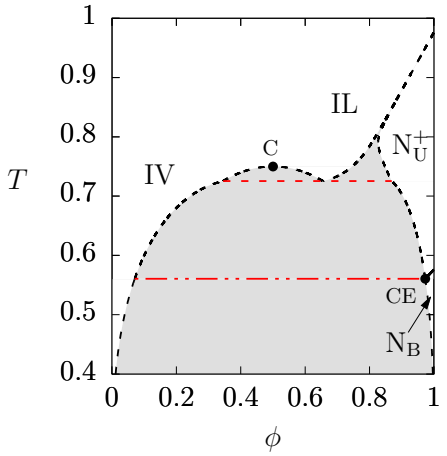

(a) $\Delta = 19/20$ and $(A, U) = (1, -3)$

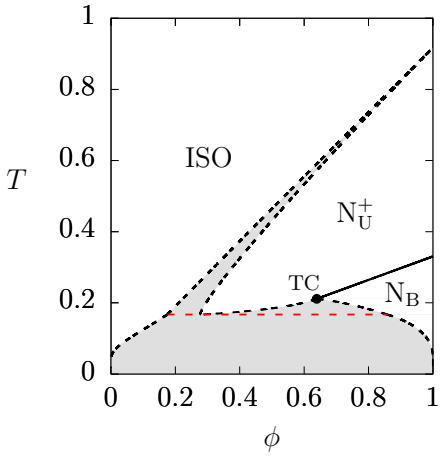

(b) $\Delta = 4/5$ and $(A, U) = (1, 1)$

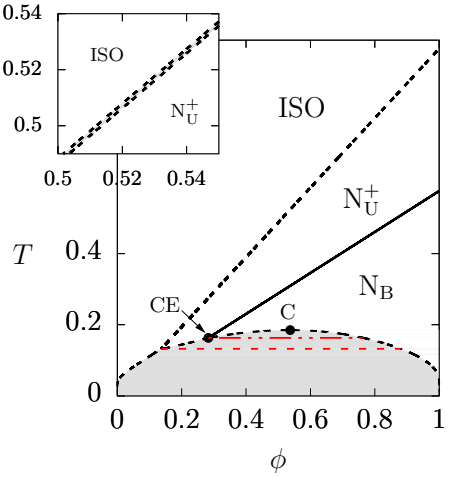

(c) $\Delta = 19/20$ and $(A, U) = (1, 13/10)$

Figure 3.5: Phase diagrams in terms of temperature T (in units of A) and concentration ϕ of nematogens, for different values of biaxiality degree. The red long-dashed line represents a ISO-N_U^+-N_B triple point. The red dot-dashed line is associated with a critical end (CE) point, while C is a ordinary critical point and TC is a tricritical point. The inset shows the ISO-N_U^+ coexistence region.

3.4.3 Phase diagrams for $\Delta = 1$

Following our discussion in Sec. 3.3, we can obtain the conditions leading to Landau points for the maximal biaxiality degree and investigate the possible presence of Landau tricritical points. Indeed, we find analogous features when nonzero isotropic interactions are considered. Nevertheless, the parameter U plays an important role in the criteria for determining the LTC point. After performing the calculation, we find that the coordinates of the Landau point satisfy

$$\begin{aligned} (\beta A - 1)e^{\beta\mu} &= e^{U/A}, \\ \beta A \phi &= 1. \end{aligned} \tag{3.35}$$

For $\mu \to \infty$, i.e., in the limit of a fully occupied lattice, we recover the expected phase diagram with $\beta A = 1$ at the Landau point, whereas for $U/A \to 0$, we obtain the results discussed in Sec. 3.3. As we already know, the stability of a Landau point is related to the existence of an

absolute minimum of the free-energy functional, and higher-order derivatives should be considered because we are dealing with a multicritical point. The fourth-order derivative, evaluated at $(S, \eta, \phi) = (0, 0, \phi_{\rm L})$, is

$$\frac{d^4\psi}{d\eta^4} = -\frac{3}{8}A^3\beta^2\left[\frac{U + A^2\beta - A(2+\beta U)}{A^2\beta + U(\beta A - 1)}\right]. \tag{3.36}$$

This fourth-order derivative changes sign when $\beta A(A-U) = 2A-U$, which sets the condition for a possible LTC point. Notice that, as long as the isotropic interaction is attractive ($U < 0$), there is always a candidate Landau tricritical point (since β must be positive). However, as in the case $U = 0$, the stability of that point for $U \neq 0$ must be checked by looking at the sixth-order derivative of ψ with respect to η evaluated at $(S, \eta, \phi) = (0, 0, \phi_{\rm L})$,

$$\frac{d^6\psi}{d\eta^6} = \frac{(U-2A)^4(8A^2 - 30AU + 15U^2)}{64A(A-U)^4}. \tag{3.37}$$

We then note that, since $A > 0$, any LTC points are locally unstable if the isotropic interaction is repulsive ($U > 0$) and such that $0.32 \lesssim U/A \lesssim 1.68$.

For $U < 0$, the LTC point is always locally stable, although it may not correspond to an absolute minimum of the free-energy functional. This is the case for $U = -5$, as shown by the phase diagram in Fig. 3.6(a). There is a wide coexistence region associated with isotropic phases of vapor and liquid, and an ordinary critical point (C). For high concentrations, as T decreases, there exists a continuous transition from the IL phase to the $\rm N_B$ phase. Additionally, for a fixed sufficiently low temperature, by varying the concentration we enter a coexistence region between the IV and the $\rm N_B$ phases.

The line of continuous transitions consists of Landau points, and that line meets the coexistence regions at a Landau critical end point (LE). On the other hand, for isotropic interaction $U = -3$, we obtain the phase diagram exhibited in Fig. 3.6(b). In this diagram, we now observe an LTC point, i.e., the LE point is not stable, and there also exists a triple point related to the IL, IV, and $\rm N_B$ phases. When the isotropic interaction is sufficiently repulsive, we have a biaxial-biaxial coexistence region, as shown in Fig. 3.6(c). This biphasic region presents a critical point C and a Landau critical end point LE. For phase diagrams with $U > 2$, there are no coexistence regions and we observe only second-order transitions between the ISO and $\rm N_B$ phases; see Appendix A.

Notice that the sequence of phase-diagram topologies shown in Figs. 3.6(a)-3.6(c) as the isotropic interaction is tuned from attractive to repulsive for maximally biaxial nematogens is equivalent to the sequence observed for off-lattice dipolar fluids [65–72], the biaxial phase being replaced by the ferromagnetic or ferroelectric phases.

For the particular case $\Delta = 1$ we can plot a graph in the U-T plane showing the multicritical points found for maximal biaxiality; see Fig. 3.7. The corresponding phase diagrams in the ϕ-T plane present a line of Landau points regardless of the character of the isotropic interaction.

The stability limits of points belonging to these Landau lines are: (i) at high temperatures, the point $(\phi, T) = (1, 1)$ (fully occupied lattice) and (ii) at low temperatures, a multicritical point whose nature depends on the value of U. In the U-T plane, the stable Landau points occupy an extensive region which we call the Landau zone. The boundaries of this region are the line $(\phi, T) = (1, 1)$ and the lines of Landau critical end points and Landau tricritical points, which meet at higher-order multicritical points ML_2 and ML_3. We also find a higher-order multicritical end point MCE related to a line of triple points. These triple points are associated with coexisting vapor, liquid and biaxial phases. Observe that the MCE point occurs when the line of triple points meets a line of critical points.

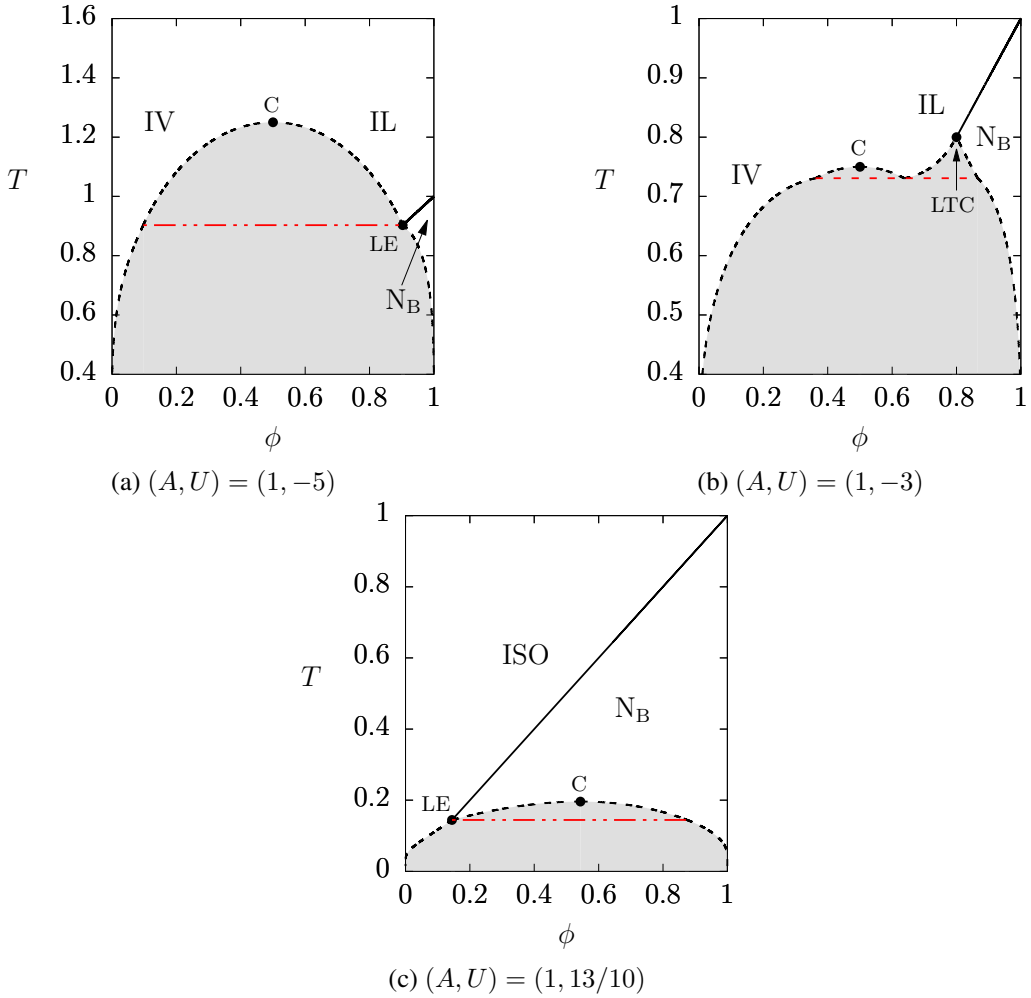

(a) $(A, U) = (1, -5)$

(b) $(A, U) = (1, -3)$

(c) $(A, U) = (1, 13/10)$

Figure 3.6: Phase diagrams in terms of temperature T (in units of A) and concentration ϕ of nematogens, for maximal biaxiality degree $\Delta = 1$. The red long-dashed line represents a IV-IL-$\mathrm{N_B}$ triple point. The red dot-dashed line represents a Landau critical end (LE) point. C is a ordinary critical point.

3.5 Multicritical points

We may summarize the different topologies of the ϕ-T phase diagrams by constructing diagrams of multicritical points in the plane Δ-T for a fixed value of U, as shown in Fig. 3.8. Thus, given

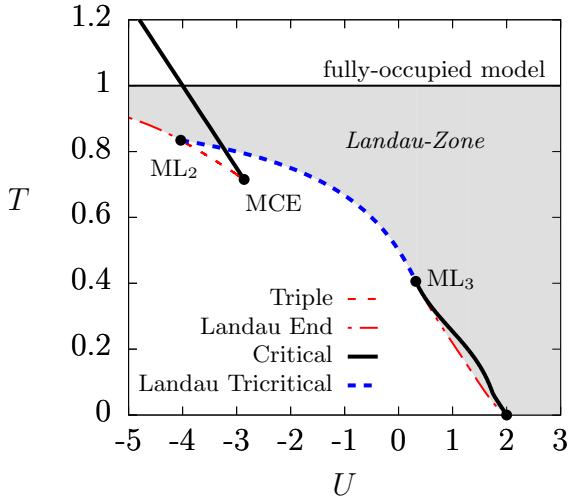

Figure 3.7: Lines of multicritical points in the U-T plane for the case of maximal biaxiality parameter $\Delta = 1$. the gray region marked as "Landau zone" consists of Landau points associated with different concentrations of nematogens. ML_2 and ML_3 are higher-order Landau multicritical points. MCE is a higher-order multicritical end point.

a nematic-like system with parameters (A, U), we can determine the multicritical points in the plane ϕ-T phase diagrams for different values of Δ. Due to the large parameter space, we focus on only some representative values of the isotropic interaction U.

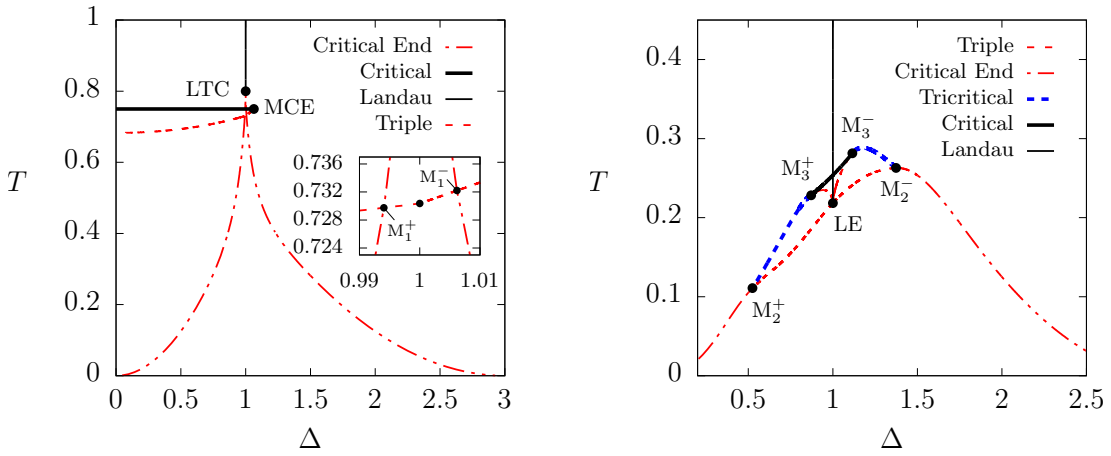

(a) $U = -3$ (b) $U = 1$

Figure 3.8: Lines of multicritical points in the Δ-T plane. MCE: higher-order multicritical end point. $\mathrm{M}_1^{\pm}$, $\mathrm{M}_2^{\pm}$, and $\mathrm{M}_3^{\pm}$ are higher-order multicritical points.

3.5.1 Case with $U < 0$

By assuming attractive isotropic interaction with $(A, U) = (1, -3)$, we obtain the Δ-T diagram shown in Fig. 3.8(a). We notice that the line of triple points meets the lines of critical end points at higher-order multicritical points $\mathrm{M}_1^{\pm}$. Also, the line of ordinary critical points meets the line of triple points at a higher-order multicritical end point MCE. For $\Delta < \Delta_1^+ \approx 0.994$, where $\Delta_1^{\pm}$ are the values of Δ at $\mathrm{M}_1^{\pm}$, phase diagrams in the ϕ-T plane exhibit ordinary critical

points related to the vapor-liquid biphasic regions, critical end points (CEs), and vapor-liquid-uniaxial triple points, a topology exemplified in Fig. 3.5(a). Precisely at $\Delta = \Delta_1^+$, the lines of CE and triple points meet at the temperature $T_1^+ \approx 0.7298$. For values of model parameters corresponding to $\mathrm{M}_1^\pm$, ϕ-T phase diagrams do not exhibit a coexistence region between the isotropic vapor and the uniaxial phases. In the range $\Delta_1^+ < \Delta < 1$, the temperature of the CE point is higher than that of the triple point, which now represents a coexistence of isotropic (vapor and liquid) and biaxial phases. For maximal biaxiality $\Delta = 1$, only isotropic and biaxial phases are stable, and ϕ-T phase diagrams are characterized by an ordinary vapor-liquid critical point, a Landau line, and, depending on the value of $U < 0$, a Landau tricritical point, as in Fig. 3.6(b), or a Landau end point, as in Fig. 3.6(a).

On the other hand, for $1 < \Delta < \Delta_1^- \approx 1.006$, the ϕ-T phase diagrams may exhibit uniaxial discotic phases, whose region of stability increases with Δ. In addition, we have CE points and vapor-liquid-biaxial triple points, producing the same topology as in Fig. 3.5(a). When $\Delta = \Delta_1^-$, the lines of CE and triple points meet at the temperature $T_1^- \approx 0.7322$. For $\Delta_1^- < \Delta < \Delta_{\mathrm{MCE}} \approx 1.063$, the ϕ-T phase diagrams also present CE points and vapor-liquid-biaxial triple points whose temperature approaches that of the vapor-liquid critical point as $\Delta \to \Delta_{\mathrm{MCE}}$. For biaxiality degree $\Delta = \Delta_{\mathrm{MCE}}$, the vapor-liquid-biaxial triple point and the ordinary vapor-liquid critical point meet at the temperature $T_{\mathrm{MCE}} = 3/4$, and we cannot distinguish isotropic vapor and liquid phases. For nematic systems with $\Delta_{\mathrm{MCE}} < \Delta < 3$, the topology of the ϕ-T phase diagrams is the same as the one shown in Fig. 3.1(b), the only multicritical point being a CE point separating regions of coexistence between the low-concentration isotropic phase and the high-concentration biaxial (at low temperatures) or uniaxial (at higher temperatures) phases. For the intrinsically uniaxial cases $\Delta = 0$ or $\Delta = 3$, the phase diagrams exhibit only isotropic and uniaxial phases, as exemplified in Sec. 3.4.1.

3.5.2 Case with $U > 0$

Now, by considering repulsive isotropic interactions with $(A, U) = (1, 1)$, we obtain the multicritical lines shown in Fig. 3.8(b). Here lines of CE, tricritical, and triple points meet at multicritical points $\mathrm{M}_2^\pm$. We also have the multicritical points $\mathrm{M}_3^\pm$, where lines of CE, triple, and ordinary critical points meet. The topology of the ϕ-T phase diagrams is essentially symmetric with respect to the axis $\Delta = 1$, except for the change in character of the uniaxial phases, from calamitic ($0 \leqslant \Delta < 1$) to discotic ($1 < \Delta \leqslant 3$).

In the ranges $0 < \Delta < \Delta_2^+ \approx 0.525$ or $\Delta_2^- \approx 1.3743 < \Delta < 3$, where $\Delta_i^\pm$ is the biaxiality parameter at $\mathrm{M}_i^\pm$, the topology of the ϕ-T phase diagrams is the same as the one shown in Fig. 3.1(b), and the temperature of the CE point increases as the value of Δ becomes closer to 1. For biaxiality degree in the ranges $\Delta_2^+ < \Delta < \Delta_3^+ \approx 0.872$ or $\Delta_3^- \approx 1.115 < \Delta < \Delta_2^-$, there exist isotropic-uniaxial and uniaxial-biaxial coexistence regions, as well as a tricritical (TC) point, as illustrated in Fig. 3.5(b). Finally, for $\Delta_3^+ < \Delta < \Delta_3^-$, the TC point is replaced by

a low-concentration CE point (or Landau end point if $\Delta = 1$) and an ordinary critical point associated with a biaxial-biaxial coexistence region, a topology exemplified in Fig. 3.6(c). For biaxiality exactly equal to Δ_3^+ or Δ_3^-, the lines of critical and CE points meet the line of TC points and the biaxial-biaxial coexistence region is absent.

3.6 Conclusions

We considered a LG version of the MSZ model for biaxial nematics with discrete orientations, in addition to an energetic term that describes an isotropic interaction. The model was investigated in MF theory through a fully-connected spin-like system with inclusion of dilution effects. The free-energy Landau-de Gennes functional and the MF equations were obtained exactly.

For systems without isotropic interaction, $U = 0$, we have drawn phase diagrams in terms of temperature and concentration of nematogens, with fixed values of Δ. The case $\Delta = 1$ is in particular interesting due to the absence of a nematic uniaxial phase, and we find a line of L points which is limited by a LTC point. In the cases $\Delta = 0$ or $\Delta = 3$ the nematogens are intrinsically uniaxial, so that the phase diagram shows no biaxial nematic phase. Any other values of Δ leads to a diagram which present CE points at high concentration.

Systems with $U \neq 0$ present a great variety of multicritical points depending on the character of the isotropic interaction and the biaxiality degree of the nematogens. To clarify this idea, diagrams with multicritical point were constructed in the U-T plane for some fixed values of Δ, and these diagrams show the different multicritical points that can be found in the ϕ-T phase diagrams.

Although our calculations are of MF nature, we do not anticipate much qualitative difference between our results and those which would be obtained from improved approximations from Monte Carlo simulations. Our basis for this is twofold. First, there is a general agreement between our results for limiting cases and those from previous work employing either improved off-lattice approximations (see, e.g., Refs. [59] and [60]) or Monte Carlo simulations (see, e.g., Refs. [49] and [54]). Second, MF calculations for dilute lattice systems are specially sensitive to effects related to percolation, as the infinite range of MF interactions leads to a percolation threshold at an infinitesimal particle concentration, in sharp contrast to the finite percolation threshold of three-dimensional lattices with nearest-neighbor interactions. Therefore, we expect predictions of ordered phases at low concentrations to be MF artifacts. However, except for very strong repulsive isotropic interaction, our calculations do not lead to such predictions. Monte Carlo simulations focusing on both exceptional cases as well as on the predicted multicritical points would be most welcome.

Chapter 4

Weakly-interacting nanoparticles

4.1 Introduction

In the last decade, the need to enhance the physical properties of LCs using physical methods (i.e., without chemical synthesis of new substances) has represented a real challenge. One solution is the introduction of colloidal particles into a LC host. The effects induced by the colloidal particles depend strongly on their size. Microparticles induce elastic distortions in the LC host, and these distortions are responsible for an indirect interaction between them. In this case the microparticles may form a periodic array with potential applications in photonics [73–78]. On the other hand, nanoparticles (NPs) are too small to cause distortion in the LC host. However, NPs can produce significant changes in the effective properties of the LC host. Using low concentration ($\sim 0.2\%$) of $\mathrm{BaTiO_3}$ ferroelectric nanoparticles in the nematic LC MLC-6609, an increase of $\sim 10\%$ at the nematic orientational coupling was reported by F. Li *et al.* [79]. In the same experiment, an increment of 40°C in the clearing point [1], as compared with the value for the pure LC host, was reported. Both increases and decreases in the clearing point have been reported for different experiments [80–88]; see also Refs. [89, 90] and references therein.

In the two-tensor formulation discussed at the beginning of Chap.3 we show that, under certain conditions, Eq. (3.3) represents the interaction potential between two nematogens. In order to describe the anisotropic interaction potential between a nematogen and an uniaxial dipolar NP with dipolar moment represented by the unit vector $\mathbf{p}$, it is necessary to represent the dipolar state by a tensor

$$\mathbf{d} = \mathbf{p} \otimes \mathbf{p} - \frac{1}{3}\mathbf{I}, \tag{4.1}$$

where $\mathbf{I}$ is the 3×3 identity matrix. Then Eq. (3.3), under changes $\mathbf{q}_j \to \mathbf{d}_j$, $\mathbf{b}_j \to \mathbf{0}$, and $A \to B$, takes the form

$$V_{ij} = -\frac{9}{4}B\left(\mathbf{q}_i : \mathbf{d}_j + \xi \mathbf{b}_i : \mathbf{d}_j\right) = -\frac{9}{4}B\left(\mathbf{q}_i + \xi \mathbf{b}_i\right) : \mathbf{d}_j. \tag{4.2}$$

[1] The temperature at which a LC phase is converted to the ISO liquid is called the clearing point.

In this case the adimensional parameter ξ gauges the importance of the coupling between the dipole and the nematogenic biaxial part. For $\xi = 0$ we recover the Maier-Saupe interaction energy which is appropriate only for the description of intrinsically uniaxial nematogens. For intrinsically biaxial nematogens we need to set the parameter ξ to a nonzero value. In the same spirit to the description for the nematogen-nematogen interaction we use $\xi = \Delta/3$, and then

$$V_{ij} = -\frac{9}{4}B\left(\mathbf{q}_i + \frac{\Delta}{3}\mathbf{b}_i\right) : \mathbf{d}_j. \tag{4.3}$$

For a binary mixture of nematogens and dipolar NPs, we allow each lattice site to be occupied by a single object, with no empty sites. In this problem, similar to the dilution problem discussed in Chap. 3, we introduce an isotropic interaction. Under these considerations the contribution of two neighboring sites i and j to the total interaction energy of the system is

$$\begin{aligned} V_{ij} = \gamma_i\gamma_j\left[U - \frac{9}{4}A\left(\mathbf{q}_i + \frac{\Delta}{3}\mathbf{b}_i\right) : \left(\mathbf{q}_j + \frac{\Delta}{3}\mathbf{b}_j\right)\right] \\ - \gamma_i(1-\gamma_j)\frac{9}{4}B\left(\mathbf{q}_i + \frac{\Delta}{3}\mathbf{b}_i\right) : \mathbf{d}_j. \end{aligned} \tag{4.4}$$

In this problem the occupation variable γ_i is equal to 0 if the site i is occupied by a dipolar NP and 1 if the site is occupied by a nematogen. Here we allow the strength of the anisotropic interaction between objects of different nature, B, to be either negative or positive. The case $B > 0$ energetically favors configurations in which a dipole aligns with the first principal axis of a nematogen. On the other hand, the case $B < 0$ energetically favors configurations in which a dipole is perpendicular to the first principal axis of a nematogen. Finally, the case $B = 0$ represents an effective diluted problem similar to the one discussed in Chap.3.

In Chap.3, we presented the LGMSZ model for the description of the effects of dilution in NLCs with intrinsically-biaxial nematogens. Mathematically, the dilution problem can be understood as a binary mixture of nematogens and non-interacting objects (the holes or empty sites). In this chapter the holes are exchanged for dipolar NPs that do not directly interact with each other, but do interact with the nematogens. As the strength of the interaction between nematogens and dipolar NPs is B, see Eq. (4.4), the lattice model used to describe the binary mixture will be called lattice-gas Maier-Saupe-Zwanzig with extra B interaction (LGMSZ-B).

We note that, in principle, neglecting interactions between dipolar nanoparticles is a reasonable approximation only in the limit where the relative concentration of such particles is small. However, in experimental systems there are also ionic impurities which may screen electrostatic interactions (see Ref. [91] and references therein), therefore extending the validity of the approximation to higher concentrations, while at the same time weakening the coupling between NPs and nematogens. For the sake of completeness, we extend the approximation to the full range of possible concentrations, with the warning that results for the highest values should be subject to further checks.

This chapter is organized as follows. Sec. 4.2 presents the LGMSZ-B model and sketches its MF solution. It also discusses the stability of multicritical Landau points for different values of the degree of biaxiality of nematogens. In Sec. 4.3 we present an analysis of the effects of anisotropic interactions between nematogens and dipolar NPs with fixed degree of biaxiality and zero isotropic interaction. Sec. 4.4 is dedicated to LC-based suspensions and the effects of NP on the clearing point as well as on the uniaxial-biaxial second-order transition temperature. In Sec. 4.5 we present a study of the effects of the isotropic interaction for fixed biaxiality degree and anisotropic interaction between objects of different nature. Conclusions are presented in Sec. 4.6.

4.2 The LGMSZ-B model

We consider a system which is a binary mixture consisting of N_m nematogens and N_n dipolar NPs. Each lattice site can be occupied by an asymmetric object or by a dipole, the state of the site i being described by an occupation variable γ_i taking the value 0 (dipole) or 1 (nematogen). Then, we define the LGMSZ-B model by means of the effective Hamiltonian

$$\mathcal{H} = -\sum_{(i,j)} V_{ij} = -A\sum_{(i,j)} \gamma_j\gamma_j \mathbf{\Omega}_i : \mathbf{\Omega}_j - B\sum_{(i,j)} \gamma_i(1-\gamma_j)\mathbf{\Omega}_i : \mathbf{\Theta}_j + U\sum_{(i,j)} \gamma_i\gamma_j, \qquad (4.5)$$

where A, B and U are coupling parameters, with $A > 0$, the sum is performed over pairs (i, j) of neighboring sites i and j in the lattice, and the quantities $\mathbf{\Omega}_i$ and $\mathbf{\Theta}_j$ are second-rank tensors associated with the nematogen at site i and the dipolar at site j respectively. Specifically, the tensor $\mathbf{\Omega}_i$ is the same that was used in Chaps. 1 and 2. For dipolar NPs, we have

$$\mathbf{\Theta}_i = \frac{3}{2}\left(\mathbf{p}_i \otimes \mathbf{p}_i - \frac{1}{3}\mathbf{I}\right), \qquad (4.6)$$

where $\mathbf{p}_i$ is the dipolar moment associated with the NP at i. Instead of working with continuous orientational states, we follow the Zwanzig prescription (see Sec. 2.2) in assuming that the principal axes of a nematogen and the dipolar axes are restricted to align in the directions of the Cartesian axes. Within this approximation the states of a nematogen and of a dipolar NP take values from the sets $\{\boldsymbol{\omega}_i\}$ and $\{\boldsymbol{\theta}_j\}$ with $i = \overline{1,6}$ and $j = \overline{1,3}$ respectively; see Eqs. (2.6) and (2.13). Every state of the set $\{\boldsymbol{\theta}_j\}$ is doubly degenerate. Note that, for zero isotropic interaction ($U = 0$) and intrinsically uniaxial molecules ($\Delta = 0$), Eq. (4.5) reduces to a discretized version of the continuous model introduced by A. N. Zakhlevnykh *et al.* [36] for suspensions of anisometric particles in nematic liquid crystals (with a rescaling of energies, as our parameters A and B would be equivalent to $\sqrt{3/2}A$ and $\sqrt{3/2}B$ in the units of Ref. [36]).

4.2.1 Molecular field theory

In order to make analytic progress in the problem defined by Eq.(4.5), we resort to a MF treatment, which is equivalent to considering the fully-connected Hamiltonian

$$\mathcal{H}_{\rm mf} = -\frac{A}{2N}\sum_{i,j=1}^{N}\gamma_i\gamma_j\mathbf{\Omega}_i:\mathbf{\Omega}_j - \frac{B}{N}\sum_{i,j=1}^{N}\gamma_i(1-\gamma_j)\mathbf{\Omega}_i:\mathbf{\Theta}_j + \frac{U}{2N}\sum_{(i,j)}\gamma_i\gamma_j, \tag{4.7}$$

where the sums over pairs of neighboring sites are replaced by sums over all pairs of sites, and the factor of $1/N$ is included to ensure that energy is extensive. In this problem $N = N_n + N_m$ is the number of objects (nematogens and dipolar NPs) of the binary mixture.

As in Sec. 3.2, it is more convenient to consider the grand canonical formalism. The grand partition function is

$$\Xi = \sum_{\{\gamma_i\}}\sum_{\{\mathbf{\Omega}_i\}}\sum_{\{\mathbf{\Theta}_i\}}\exp\left(\beta\mathcal{H}_{\rm mf} - \beta\mu\sum_{i=1}^{N}\gamma_i\right), \tag{4.8}$$

where μ is the chemical potential, which controls the number of nematogens. In order to obtain an integral representation of the grand partition function in the MF limit, we introduce the two new variables

$$\phi = \frac{1}{N}\sum_{i=1}^{N}\gamma_i \quad \text{and} \quad \mathbf{D} = \frac{1}{N}\sum_{i=1}^{N}(1-\gamma_i)\mathbf{\Theta}_i, \tag{4.9}$$

with the help of Dirac delta functions, and use Gaussian identities similar to that in Eq. (3.12). Finally we obtain

$$\Xi \propto \int_{\mathbb{R}^7} e^{-\beta N\Phi(\mathbf{Q},\mathbf{D},\phi)}\mathcal{D}(\mathbf{Q},\mathbf{D},\phi)\,d[\mathbf{Q}]\,d[\mathbf{D}]\,d\phi, \tag{4.10}$$

with

$$\Phi(\mathbf{Q},\mathbf{D},\phi) = \frac{A}{2}\|\mathbf{Q}\|^2 + \frac{U}{2}\phi^2 - \mu\phi, \tag{4.11}$$

and

$$\begin{aligned}\mathcal{D}(\mathbf{Q},\mathbf{D},\phi) = \sum_{\{\gamma_i\}}\sum_{\{\mathbf{\Omega}_i\}}\sum_{\{\mathbf{\Theta}_i\}}&\delta\left(\phi - \frac{1}{N}\sum_{i=1}^{N}\gamma_i\right)\delta\left(\mathbf{D} - \frac{1}{N}\sum_{i=1}^{N}(1-\gamma_i)\mathbf{\Theta}_i\right)\\ &\times\exp\left[-\beta(A\mathbf{Q}+B\mathbf{D}):\sum_{i=1}^{N}\gamma_i\mathbf{\Omega}_i\right],\end{aligned} \tag{4.12}$$

where the constant of proportionality in Eq. (4.10) is irrelevant. Performing the sum in the exponential in Eq.(4.12) and using integral representations for the Dirac delta functions, we obtain

$$\mathcal{D}(\mathbf{Q},\mathbf{D},\phi) = \left(\frac{N}{2\pi\,\mathrm{i}}\right)^4\int_{\mathcal{C}} e^{-NF(\hat{\mathbf{D}},\hat{\phi})}\,d[\hat{\mathbf{D}}]\,d\hat{\phi} \tag{4.13}$$

where

$$F(\hat{\mathbf{D}},\hat{\phi}) = \hat{\mathbf{D}} : \mathbf{D} + \hat{\phi}\phi - \ln\left[\chi(\hat{\mathbf{D}},\hat{\phi})\right], \tag{4.14}$$

and

$$\chi(\hat{\mathbf{D}},\hat{\phi}) = e^{\hat{\phi}} \sum_{\{\mathbf{\Omega}\}} e^{\beta(A\mathbf{Q}+B\mathbf{D}):\mathbf{\Omega}} + \sum_{\{\mathbf{\Theta}\}} e^{\hat{\mathbf{D}}:\mathbf{\Theta}}. \tag{4.15}$$

In the thermodynamic limit ($N \gg 1$), we can use the multivariable Morse lemma to get an extension of steepest-descent method into complex variables $(\hat{\mathbf{D}},\hat{\phi})$ (see Refs. [92] and [93]). We expect the integral in the Eq. (4.13) to be dominated by the highest saddle point, $(\hat{\mathbf{D}}_o,\hat{\phi}_o) \in \mathcal{M}_3(\mathbb{C}) \times \mathbb{C}$ (see footnote [2]), which can be determined by the conditions

$$\frac{\partial}{\partial\hat{\mathbf{D}}} F(\hat{\mathbf{D}}_o,\hat{\phi}_o) = 0 \quad \Rightarrow \quad \mathbf{D} = \frac{1}{\chi(\hat{\mathbf{D}}_o,\hat{\phi}_o)} \sum_{\{\mathbf{\Theta}\}} e^{\hat{\mathbf{D}}_o:\mathbf{\Theta}}\mathbf{\Theta}, \tag{4.16}$$

and

$$\frac{\partial}{\partial\hat{\phi}} F(\hat{\mathbf{D}}_o,\hat{\phi}_o) = 0 \quad \Rightarrow \quad \phi = \frac{e^{\hat{\phi}_o}}{\chi(\hat{\mathbf{D}}_o,\hat{\phi}_o)} \sum_{\{\mathbf{\Omega}\}} e^{\beta(A\mathbf{Q}+B\mathbf{D}):\mathbf{\Omega}}. \tag{4.17}$$

Under regularity conditions (single non-degenerate saddle point) we have

$$\mathcal{D}(\mathbf{Q},\mathbf{D},\phi) = \left(\frac{2\pi}{N}\right)^2 \frac{e^{-NF(\hat{\mathbf{D}}_o,\hat{\phi}_o)}}{\sqrt{\det \mathbf{H}(\hat{\mathbf{D}}_o,\hat{\phi}_o)}} + \mathcal{O}(1/N), \tag{4.18}$$

where $\det \mathbf{H}(\hat{\mathbf{D}}_o,\hat{\phi}_o)$ is the Hessian matrix having eigenvalues $\{\lambda_i\}$ with $i = \overline{1,4}$ and $|\arg(\lambda_i)| < \pi/2$ [3].

Now the grand partition function can be written as

$$\Xi \propto \int_{\mathbb{R}^7} e^{-\beta N\psi(\mathbf{Q},\mathbf{D},\phi)}\, d[\mathbf{Q}]\, d[\mathbf{D}]\, d\phi, \tag{4.19}$$

where

$$\psi(\mathbf{Q},\mathbf{D},\phi) = \Phi(\mathbf{Q},\mathbf{D},\phi) + \frac{1}{\beta} F(\hat{\mathbf{D}}_o,\hat{\phi}_o) \tag{4.20}$$

is the Landau-de Gennes free-energy functional. Note that Eqs.(4.16) and (4.17) implicitly yield $\hat{\mathbf{D}}_o$ and $\hat{\phi}_o$ as functions of $\mathbf{Q}$, $\mathbf{D}$ and ϕ.

The steepest-descent method can be applied once more, now to Eq.(4.19), yielding the MF equations for the equilibrium values of $\mathbf{Q}$, $\mathbf{D}$ and ϕ given the interactions A, B and U and the

[2] $\mathcal{M}_n(\mathbb{C})$ is the set of square matrices of order n whose elements belong to the set $\mathbb{C}$.

[3] Note that

$$\sqrt{\det \mathbf{H}(\hat{\mathbf{D}}_o,\hat{\phi}_o)} = e^{\mathrm{i}\,\varphi/2} \prod_{k=1}^{4} |\lambda_k|^{1/2} \neq 0, \quad \text{where} \quad \varphi = \sum_{k=1}^{4} \arg(\lambda_k).$$

If $(\hat{\mathbf{D}},\hat{\phi}) \in \mathcal{M}_3(\mathbb{R}) \times \mathbb{R}$ and $\Im[F(\mathbf{Q},\mathbf{D},\phi)] = 0$ then $\varphi = 0$. Also if $(\hat{\mathbf{D}},\hat{\phi}) \in \mathcal{M}_3(\mathbb{R}) \times \mathbb{R}$, $\Re[F(\mathbf{Q},\mathbf{D},\phi)] = 0$ and $|\sqrt{\lambda_k}| < \pi/4$ then $\varphi = \pi m/2$ where m is the number of negative eigenvalues minus the number of positives ones (stationary phase method).

parameters T and μ. These equations are

$$\frac{\partial}{\partial \mathbf{Q}}\psi(\mathbf{Q},\mathbf{D},\phi)=0 \quad \Rightarrow \quad \mathbf{Q}=\frac{e^{\hat{\phi}_o}}{\chi(\hat{\mathbf{D}}_o,\hat{\phi}_o)}\sum_{\{\mathbf{\Omega}\}} e^{\beta(A\mathbf{Q}+B\mathbf{D}):\mathbf{\Omega}}\mathbf{\Omega}, \tag{4.21}$$

$$\frac{\partial}{\partial \mathbf{D}}\psi(\mathbf{Q},\mathbf{D},\phi)=0 \quad \Rightarrow \quad \hat{\mathbf{D}}_o=\frac{Be^{\hat{\phi}_o}}{\chi(\hat{\mathbf{D}}_o,\hat{\phi}_o)}\sum_{\{\mathbf{\Omega}\}} e^{\beta(A\mathbf{Q}+B\mathbf{D}):\mathbf{\Omega}}\mathbf{\Omega}, \tag{4.22}$$

and

$$\frac{\partial}{\partial \phi}\psi(\mathbf{Q},\mathbf{D},\phi)=0 \quad \Rightarrow \quad \hat{\phi}_o=\frac{e^{\hat{\phi}_o}}{\chi(\hat{\mathbf{D}}_o,\hat{\phi}_o)}\sum_{\{\mathbf{\Omega}\}} e^{\beta(A\mathbf{Q}+B\mathbf{D}):\mathbf{\Omega}}, \tag{4.23}$$

From Eq.(4.21), we conclude that the equilibrium value of $\mathbf{Q}$ is associated with the biaxial-nematogen order parameter, and that it is a traceless tensor, which can be parametrized as Eq.(2.19). As Eq.(4.16) implies $\mathrm{Tr}\,\mathbf{D}=0$, we can also parametrize the second-rank tensor associated with the dipolar NP as

$$\mathbf{D}=\frac{1}{2}\begin{pmatrix}-R-\zeta & 0 & 0\\ 0 & -R+\zeta & 0\\ 0 & 0 & 2R\end{pmatrix}. \tag{4.24}$$

Likewise, Eq.(4.22) implies that $\hat{\mathbf{D}}_o$ is a traceless diagonal tensor. Parametrizing it in the same fashion as $\mathbf{D}$, with parameters $\hat{R}_o$ and $\hat{\zeta}_o$, and following a lengthy but straightforward algebraic calculation, we can solve Eqs.(4.16) and (4.17) explicitly for $\hat{R}_o$, $\hat{\zeta}_o$, and $\hat{\phi}_o$ as functions of S, η, R, ζ, and ϕ, allowing us to write the Landau-de Gennes free-energy functional as

$$\begin{aligned}\psi(S,R,\eta,\zeta,\phi)=&\frac{A}{4}(3S^2+\eta^2)+\frac{U}{2}\phi^2-\mu\phi+\frac{\zeta-R}{3\beta}\ln\left[(R-1+\phi)^2-\zeta^2\right]\\ &+\frac{1-\phi}{3\beta}\ln\left\{(1+2R-\phi)\left[(R-1+\phi)^2-\zeta^2\right]\right\}\\ &+\frac{2R}{3\beta}\ln(1+2R-\phi)-\frac{2\zeta}{3\beta}\ln(1-R-\zeta-\phi)\\ &-\frac{\phi}{\beta}\ln[\Lambda(S,R,\eta,\zeta)]+\frac{\phi}{\beta}\ln(6\phi)-\frac{2}{\beta}\ln(6),\end{aligned} \tag{4.25}$$

where

$$\begin{aligned}\Lambda(S,R,\eta,\zeta) = {} & 2\exp\left\{-\frac{3\beta}{4}\left[A(S+\eta)+B(R+\zeta)\right]\right\} \\ & \times\cosh\left\{\frac{3\beta}{4}\left[A\left(S-\frac{\eta}{3}\right)+B\left(R-\frac{\zeta}{3}\right)\right]\Delta\right\} \\ & + 2\exp\left\{-\frac{3\beta}{4}\left[A(S-\eta)+B(R-\zeta)\right]\right\} \\ & \times\cosh\left\{\frac{3\beta}{4}\left[A\left(S+\frac{\eta}{3}\right)+B\left(R+\frac{\zeta}{3}\right)\right]\Delta\right\} \\ & + 2\exp\left[\frac{3\beta}{2}(AS+BR)\right]\cosh\left[\frac{\beta}{2}(A\eta+B\zeta)\Delta\right].\end{aligned} \tag{4.26}$$

The equilibrium values of S, R, η, ζ and ϕ are determined by locating the absolute minima of $\psi(S,R,\eta,\zeta,\phi)$, leading to the MF equations

$$\frac{\partial\psi}{\partial S}=\frac{\partial\psi}{\partial\eta}=\frac{\partial\psi}{\partial R}=\frac{\partial\psi}{\partial\zeta}=\frac{\partial\psi}{\partial\phi}=0, \tag{4.27}$$

which take the self-consistent forms

$$\begin{aligned} S &= F_1(S,R,\eta,\zeta,\phi;\{\alpha\}) \\ \eta &= F_2(S,R,\eta,\zeta,\phi;\{\alpha\}) \\ R &= F_3(S,R,\eta,\zeta,\phi;\{\alpha\}) \\ \zeta &= F_4(S,R,\eta,\zeta,\phi;\{\alpha\}) \\ \phi &= F_5(S,R,\eta,\zeta,\phi;\{\alpha\}) \end{aligned} \tag{4.28}$$

where $\{\alpha\}\equiv\{\beta,\mu,\Delta,\kappa\}$, with $\kappa=B/A$, is a set of parameters.

We emphasize that the values of S, η, R, ζ and ϕ at the absolute minima of ψ represent thermodynamic equilibrium values for fixed reciprocal temperature β, chemical potential μ, parameter κ and biaxiality degree Δ. The free energy $\mathcal{F}=\mathcal{F}(\{\alpha\})$ of the system corresponds to the convex envelope of ψ determined after inserting values of S, η, R, ζ and ϕ associated with the minima of the Landau-de Gennes free-energy functional.

4.2.2 The Landau point

Systems with quadrupole interactions may exhibit Landau (L) multicritical points (see, e.g., Ref [22]), in which the isotropic phase and various nematic phases become identical. To determine the location of a Landau point we must impose certain conditions on the Landau-de Gennes free-energy functional, that is, we need to satisfy Eqs. (4.27) and the extra conditions $d^2\psi/\,dS^2 = d^3\psi/\,dS^3 = 0$ evaluated at $(S,\eta,R,\zeta,\phi)=(0,0,0,0,\phi_{\rm L})$ (similar to the dilution problem in Chap. 3). For intrinsically biaxial nematogens, these conditions lead to

$$\phi_{\rm L}e^{-\beta(\mu-U\phi_{\rm L})}=1-\phi_{\rm L}, \tag{4.29}$$

$$-16+\beta(\Delta^2+3)\left[4A+3B^2\beta(1-\phi_{\rm L})\right]\phi_{\rm L}=0, \tag{4.30}$$

and

$$64(\Delta^2-1)-B^3\beta^3(\Delta^2+3)^3\phi_{\rm L}^2(1-\phi_{\rm L})=0, \tag{4.31}$$

Note that, for $B=0$, Eqs. (4.30) and (4.31) indicate that the Landau point can only exist if $\Delta=1$, and the ϕ-T diagrams present a line of Landau points $A\beta\phi_{\rm L}=1$ (see Refs. [25] and [94]). For $B\neq 0$ we have many candidates for multicritical Landau points, satisfying

$$A\beta^{(1,2)}=\xi_1(\Delta,\kappa)\pm\xi_2(\Delta,\kappa),\quad \text{with}\quad \kappa=\frac{B}{A}, \tag{4.32}$$

these functions $\xi_{1,2}(\Delta,\kappa)$ are

$$\xi_1(\Delta,\kappa)=\frac{2}{9}\left[\frac{9}{3+\Delta^2}-\frac{6}{\kappa^2}+\frac{3+\Delta^2}{(\Delta^2-1)\kappa}\right], \tag{4.33}$$

and

$$\xi_2(\Delta,\kappa)=\sqrt{(\Delta^2+3)-\frac{12}{\kappa}(\Delta^2-1)}\frac{\left|\dfrac{(\Delta^2+3)^2}{\kappa}-9(\Delta^2-1)\right|}{(\Delta^2-1)(\Delta^2+3)^{3/2}}. \tag{4.34}$$

We refrain from writing the lengthy expressions for the concentration values $\phi_{\rm L}^{(1)}$ and $\phi_{\rm L}^{(2)}$ associated with the temperatures $A\beta^{(1)}$ and $A\beta^{(2)}$. Note that the solutions in Eq. (4.32) are invalid for $\Delta=1$ because $\xi_{1,2}(\Delta,\kappa)\to\infty$. The cases $12(\Delta^2-1)/(\Delta^2+3)<\kappa<0$ with $0<\Delta<1$ and $0<\kappa<12(\Delta^2-1)/(\Delta^2+3)$ with $1<\Delta<3$ represent unphysical situations because $\Im\{\xi_2(\Delta,\kappa)\}\neq 0$. From Eqs. (4.29) to (4.31) we can see that for $\Delta=1$ the location of the Landau point is $\phi_{\rm L}=1$, $A\beta=1$, and $\mu\to\infty$.

We emphasize that the solutions in Eq. (4.32) represent candidates for Landau points, but say nothing about whether such points are really stable. However, these solutions indicate where we will not find Landau points. For $\kappa>0$, see Fig. 4.1(a), we can expect the following characteristics in the ϕ-T phase diagrams. (i) For calamitic molecules, $0<\Delta<1$, we find that $\xi_1(\Delta,\kappa)<\xi_2(\Delta,\kappa)$, and as a consequence the solution $A\beta^{(2)}<0$ (is unphysical). The ϕ-T phase diagrams for these values of Δ can present at most one Landau point. (ii) For discotic nematogens, $1<\Delta<3$, both solutions $A\beta^{(1)}$ and $A\beta^{(2)}$ are positive and in this case the ϕ-T phase diagrams can present one or two Landau multicritical points.

On the other hand, if $\kappa<0$ (see Fig. 4.1(b)), for calamitic nematogens we can find ϕ-T phase diagrams with one or two Landau multicritical points. Finally for discotic nematogens $\xi_1(\Delta,\kappa)+\xi_2(\Delta,\kappa)<0$, so that $A\beta^{(1)}<0$, and the ϕ-T phase diagrams can present at most one Landau point.

In the particular case where $\xi_2(\Delta,\kappa)=0$ we have that $\beta^{(1)}=\beta^{(2)}$. The values of κ for

which this occurs are

$$\kappa_1 = \frac{12(\Delta^2-1)}{\Delta^2+3} \quad \Rightarrow \quad A\beta_1 = \frac{(\Delta^2+3)^3+216(\Delta^2-1)^2}{108(\Delta^2-1)^2(\Delta^2+3)} \geqslant 0 \tag{4.35}$$

and

$$\kappa_2 = \frac{(\Delta^2+3)^2}{9(\Delta^2-1)} \quad \Rightarrow \quad A\beta_2 = \frac{4\Delta^2(\Delta^2-9)^2}{(\Delta^2+3)^4} > 0. \tag{4.36}$$

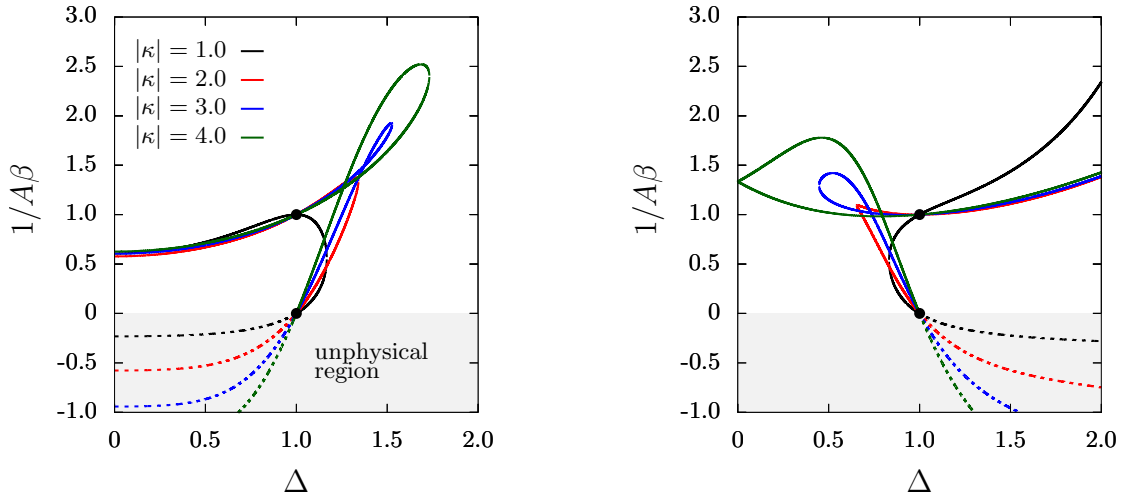

(a) $B > 0$ (b) $B < 0$

Figure 4.1: Candidates for multicritical Landau points, diagram of temperature as function of the molecular degree of biaxiality Δ, for different values of $\kappa = B/A$. Gray region is unphysical.

In order to analyze the stability of a Landau point, we must examine the higher order total derivatives of ψ with respect to η, evaluated at $(S, \eta, R, \zeta, \phi) = (0, 0, 0, 0, \phi_{\rm L})$. At the Landau point we will always have $d^2\psi/\,d\eta^2 = 0$, so that we need to look at the fourth-order derivative

$$\frac{d^4\psi}{d\eta^4} = \varsigma(\beta, \phi_{\rm L}) - \frac{3(1-\phi_{\rm L})\left[16 - 3B^2\beta^2(\Delta^2+3)\phi_{\rm L}^2\right]^2}{64\beta(\Delta^2+3)^2\phi_{\rm L}^3\left[1+U\beta(1-\phi_{\rm L})\phi_{\rm L}\right]}, \tag{4.37}$$

with

$$\varsigma(\beta, \phi_{\rm L}) = -3\left[\frac{9B(\Delta^2-1)+A(\Delta^2+3)^2}{(\Delta^2+3)^3\phi_{\rm L}^2} - 6\frac{18(\Delta^2-1)+(\Delta^2+3)^3}{\beta(\Delta^2+3)^5\phi_{\rm L}^3}\right]. \tag{4.38}$$

If the fourth-order derivative in Eq.(4.37) is negative, then the point does not represent a minimum of the Landau-de Gennes free-energy functional, therefore being unstable. (If the derivative is non-negative, the candidate point represents a minimum, but we must still check whether that minimum is absolute, before we can conclude that it represents a physically realizable Landau point.)

4.3 Phase behavior for $U = 0$

For this binary system, the phase diagrams present a great variety of topologies. This is intuitive when observing the energy levels associated with two nematogens or a nematogen and a dipolar NP, plotted in Fig. 4.2. Depending on the degree of biaxiality, Δ, of the nematogens, we can observe how different energy levels with different degeneracies (12 for red labels and 6 for black labels) intersect. The degeneracies are associated with entropic contributions to the free energy and can produce important effects on the phase behavior of the system, mainly for values of Δ near the points of crossings of energy levels. Another evidence of the large number of topologies that can be found is the dependence of the positions of the crossing points between energy levels with the value of the strength of the interaction between dipolar NPs and nematogens (see differences between Figs. 4.2(a) and 4.2(b)).

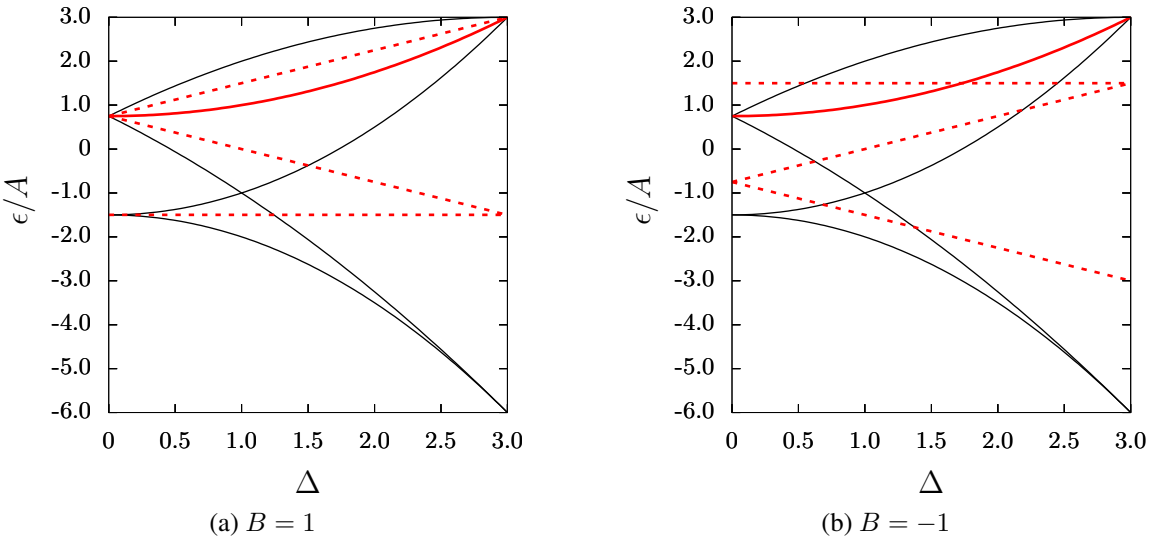

(a) $B = 1$ (b) $B = -1$

Figure 4.2: Energy levels as a function of the degree of biaxiality Δ. Level crossings account for variations in the entropic contributions to the free energy. Solid lines correspond to energy levels associated with interactions between two nematogens, while dashed lines indicate energy levels arising from interactions involving NPs and nematogens. Line thickness is proportional to the degeneracy of the corresponding level.

In this section, we start the investigation of the phase behavior for zero isotropic interaction ($U = 0$), which simplifies the analysis of the system, and $0 \leqslant \Delta \leqslant 3$. Here we discuss both $B > 0$ and $B < 0$ values for the strength of the nematogen-NP interaction, as well as the effect produced by introducing small amounts of dipolar NPs into the LC host.

In the phase diagrams presented that have more than one uniaxial phase of the same type (calamitic or discotic) we will use Roman numerals to distinguish the phases, e.g., $\mathrm{N}^{+}_{\mathrm{U_I}}$, $\mathrm{N}^{+}_{\mathrm{U_{II}}}$, $\mathrm{N}^{+}_{\mathrm{U_{III}}}$, etc.

4.3.1 Phase diagrams for $\Delta = 0$

We find the ϕ-T phase diagrams shown in Fig. 4.3, for different positive values of the strength of the anisotropic interaction between dipolar NPs and nematogens. For high concentration of nematogens, as the temperature decreases, the observed phase sequence in these diagrams is ISO, followed by a narrow ISO-$\mathrm{N_U^+}$ coexistence region, followed by a pure nematogen-rich (or dipolar-poor) $\mathrm{N_U^+}$ phase. At lower concentrations of nematogens, as the temperature decreases, the observed phase sequence in the diagrams is ISO, followed by a ISO-$\mathrm{N_U^+}$ region of coexistence, followed by a pure nematogen-poor (or dipolar-rich) low temperature $\mathrm{N_U^+}$ phase. The coexistence lines signaling the first-order transition from the ISO phase to the $\mathrm{N_U^+}$ phase are determined by the Eq. (4.27) evaluated at $(S, \eta, R, \zeta, \phi) = (S_\mathrm{U}, 0, R_\mathrm{U}, 0, \phi_\mathrm{U})$ and at $(S, \eta, R, \zeta, \phi) = (0, 0, 0, 0, \phi_\mathrm{I})$, supplemented by $\psi(S_\mathrm{U}, 0, R_\mathrm{U}, 0, \phi_\mathrm{U}) = \psi(0, 0, 0, 0, \phi_\mathrm{I})$, where ϕ_I and ϕ_U are, respectively, the nematogen concentration in the ISO and $\mathrm{N_U^+}$ phases at the transition point, while S_U and R_U are the values of S and R at that point. In this case, without loss of generality, we can assume $\eta = \zeta = 0$.

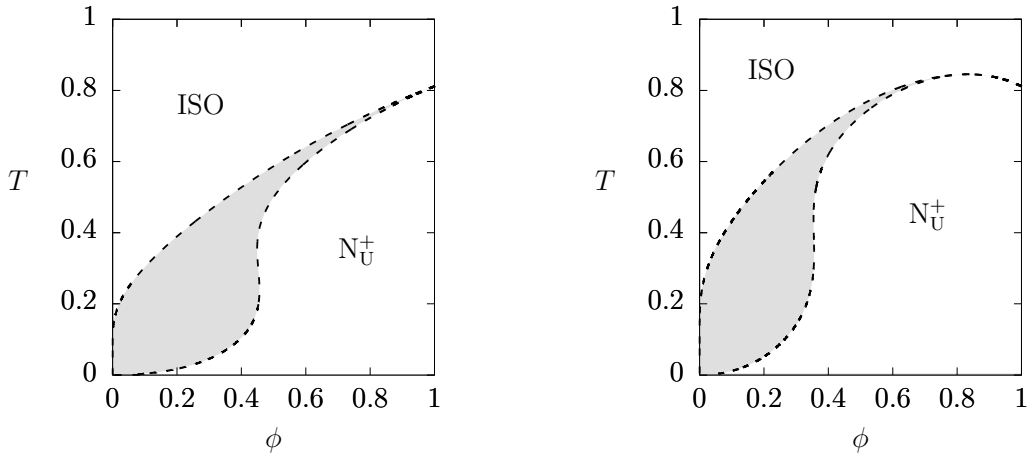

(a) $(A, B) = (1, 3/4)$ (b) $(A, B) = (1, 5/4)$

Figure 4.3: Phase diagrams in terms of temperature T (in units of A) and concentration ϕ of nematogens, for an intrinsically uniaxial system ($\Delta = 0$), different values of anisotropic interaction between nematogens and dipolar NPs and in absence of isotropic interaction ($U = 0$). ISO: isotropic phase. $\mathrm{N_U^+}$: calamitic uniaxial nematic phase. Short-dashed lines are the boundaries of the biphasic region (gray).

The phase diagrams for systems with negative interactions between dipolar nanoparticles and nematogens ($B < 0$) are shown in Fig. 4.4. The ϕ-T phase diagram shown in Fig. 4.4(a) corresponds to a system with $(A, B) = (1, -3/4)$. At lower concentration of nematogens, as the temperature decreases, we observe an ISO phase, followed by an ISO-$\mathrm{N_U^+}$ coexistence region stable at low temperature. At high concentration of nematogens we observe an ISO phase, followed by a narrow ISO-$\mathrm{N_U^+}$ coexistence region, then by a pure $\mathrm{N_U^+}$ phase and finally by a reentrant coexistence region. For $T \to 0$ we have a stable ISO-$\mathrm{N_U^+}$ biphasic region, which becomes metastable with respect to the $\mathrm{N_U^+}$ phase if $B < -A$ or $B > A/2$, as shown in Appendix A. Fig. 4.4(b) represents a situation with strong anisotropic interaction ($B = -3A$) between dipolar NPs and nematogens. In this diagram there is a large stability region for the $\mathrm{N_U^+}$ phase

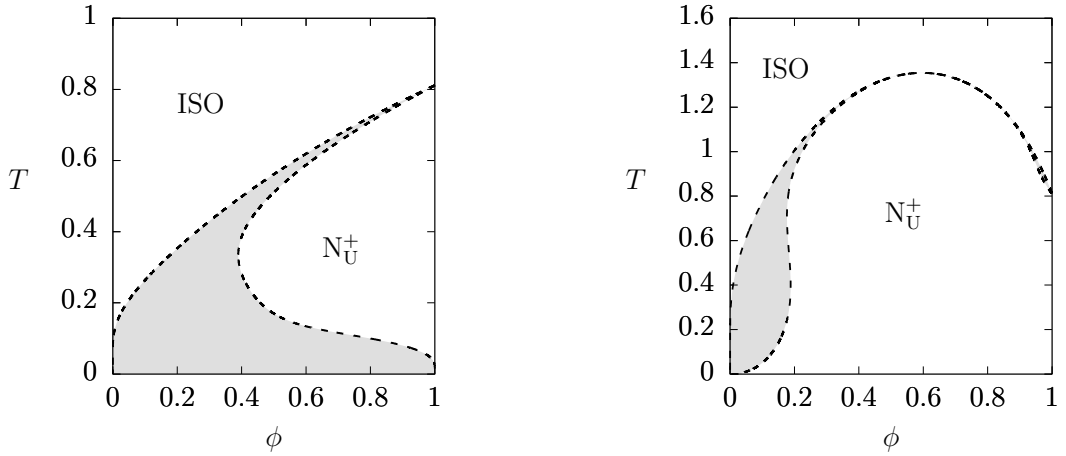

(a) $(A, B) = (1, -3/4)$ (b) $(A, B) = (1, -3)$

Figure 4.4: Phase diagrams in terms of temperature T (in units of A) and concentration ϕ of nematogens, for an intrinsically uniaxial system ($\Delta = 0$), different values of anisotropic interaction between nematogens and dipolar NPs and in absence of isotropic interaction ($U = 0$). ISO: isotropic phase. $\mathrm{N_U^+}$: calamitic uniaxial nematic phase. Short-dashed lines are the boundaries of biphasic region (gray).

and the ISO-$\mathrm{N_U^+}$ coexistence disappears at low temperature. Note that for high concentration of nematogens the addition of dipolar NPs increases the temperature of the first-order ISO-$\mathrm{N_U^+}$ phase transition.

4.3.2 Phase diagrams for $\Delta = 4/5$

For intrinsically biaxial nematogens with $\Delta = 4/5$ we can find a great variety of phase diagrams as a function of the parameter B. For $(A, B) = (1, 1)$ we can see from the phase diagram in Fig. 4.5(a) that, for high concentration of nematogens, the sequence of phases observed, as the temperature decreases, is a nematogen-rich ISO phase, followed by a first-order weak ISO-$\mathrm{N_U^+}$ phase transition, followed by a large temperature range where an $\mathrm{N_U^+}$ phase is stable, limited below by a second-order $\mathrm{N_U^+}$-$\mathrm{N_B}$ phase transition, and finally a low-temperature $\mathrm{N_B}$ phase is stable. The conditions for the second-order $\mathrm{N_U^+}$-$\mathrm{N_B}$ transition are determined by Eqs. (4.27) and the extra condition $d^2\psi/\,d\eta^2 = 0$ evaluated at $(S, \eta, R, \zeta, \phi) = (S_o, 0, R_o, 0, \phi_o)$. In this diagram we have a critical end point (CE), in which the biaxial nematic ($\mathrm{N_B}$) phase becomes identical to the uniaxial nematic ($\mathrm{N_U^+}$) phase, and this resulting nematic state coexists with a noncritical isotropic state. For low concentration of nematogens ($\phi \leqslant \phi_{\mathrm{CE}} \approx 0.1$) and temperature the system presents a dipolar-rich biaxial nematic phase.

When the strength of the anisotropic interaction between dipolar NPs and nematogens is such that it favors dipolar axes perpendicular to the first principal nematogenic axes, we obtain phase diagrams similar to the one shown in Fig. 4.5(b). In this diagram there is a tricritical (TC) point which can be determined by Eqs. (4.27) in addition to $d^2\psi/\,d\eta^2 = d^4\psi/\,d\eta^4 = 0$ evaluated at $(S, \eta, R, \zeta, \phi) = (S_{\mathrm{TC}}, 0, R_{\mathrm{TC}}, 0, \phi_{\mathrm{TC}})$, where S_{TC} and R_{TC} are the values of S and R respectively at the TC point and ϕ_{TC} is the concentration of nematogens. In addition

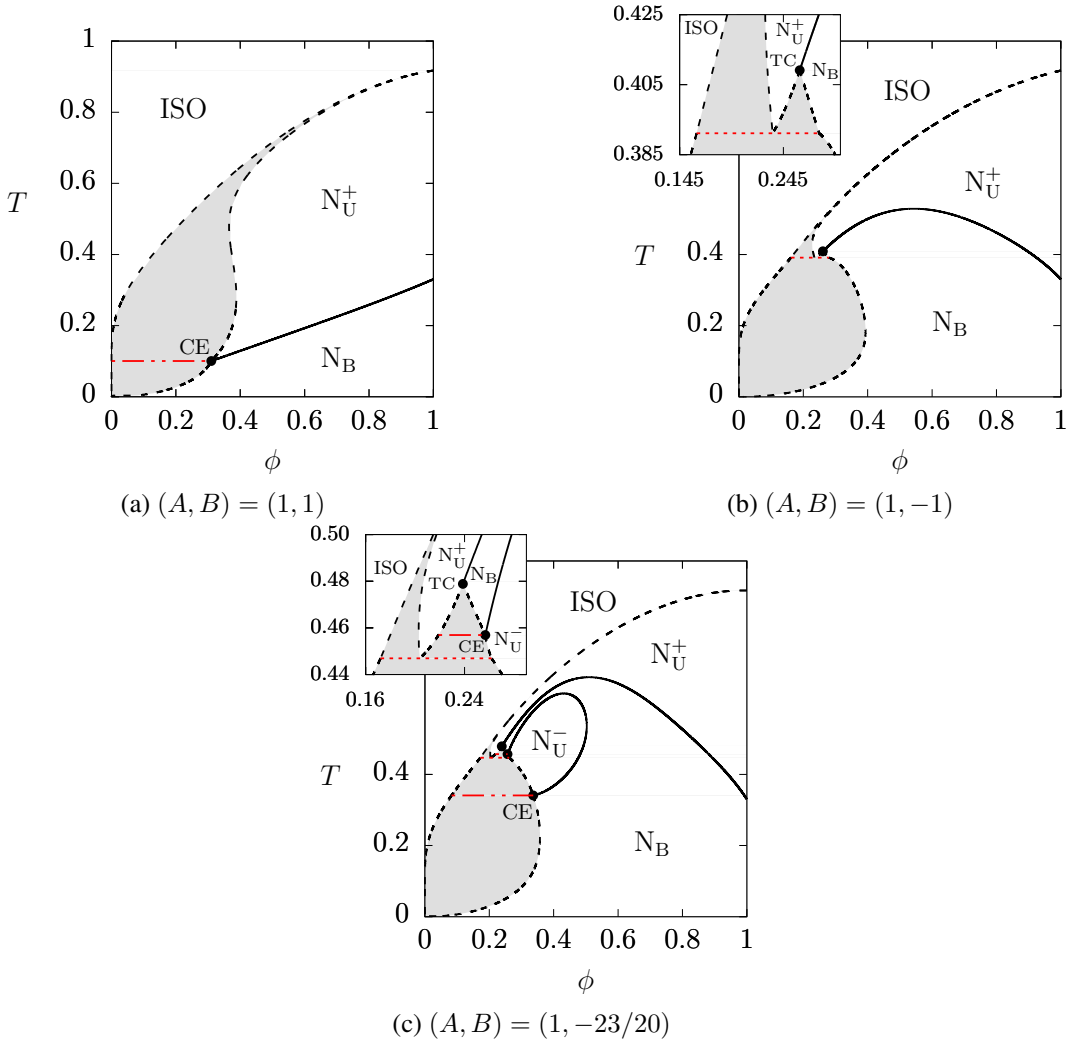

(a) $(A, B) = (1, 1)$

(b) $(A, B) = (1, -1)$

(c) $(A, B) = (1, -23/20)$

Figure 4.5: Phase diagrams in terms of temperature T (in units of A) and concentration ϕ of nematogens, for biaxiality degree $\Delta = 4/5$ and in the absence of isotropic interaction ($U = 0$). ISO: isotropic phase. N_U^+: calamitic uniaxial nematic phase. N_U^-: discotic uniaxial nematic phase. N_B: biaxial nematic phase. Short-dashed lines are the boundaries of biphasic regions (gray). Red dot-dashed line: critical end point (CE). Red dashed line is a triple point. TC is a tricritical point.

to the TC point the diagram presents a triple point (short red line), which indicates an ISO-N_U^+-N_B phase coexistence. To determine the location of the triple point we need the MF equations evaluated at $(S, \eta, R, \zeta, \phi) = (0, 0, 0, 0, \phi_I)$, at $(S, \eta, R, \zeta, \phi) = (S_U, 0, R_U, 0, \phi_U)$, and at $(S, \eta, R, \zeta, \phi) = (S_B, 0, R_B, 0, \phi_B)$, supplemented by $\psi(0, 0, 0, 0, \phi_I) = \psi(S_U, 0, R_U, 0, \phi_U) = \psi(S_B, 0, R_B, 0, \phi_B)$. For T values lower than the triple-point temperature, both ISO-N_U^+ and N_U^+-N_B coexistences become metastable with respect to the ISO-N_B first-order transition. For a fixed temperature at the range $T_{TC} \leqslant T \lessapprox 0.5$, the sequence of phases observed, as the concentration increases, is an ISO phase, followed by a small ISO-N_U^+ coexistence, followed by pure N_B phase limited by dipolar-rich and dipolar-poor N_U^+-N_B second-order transitions at left and right respectively, and finally a stable N_U^+ phase. Upon decreasing the value of B, while T_{TC} increases at the ϕ-T phase diagrams, a small region begins to appear where a N_U^- phase is stable. The small region is delimited by a second-order transition line (to the biaxial phase)

ending in two CE points with temperatures $T_{\rm CE}^{(1)}$ and $T_{\rm CE}^{(2)}$ ($T_{\rm CE}^{(1)} \leqslant T_{\rm CE}^{(2)}$). For $B \approx -1.1313$ the triple point and the CE point with temperature $T_{\rm CE}^{(2)}$ meet at a higher-order multicritical point, while for $-108/91 < B \lessapprox -1.1313$ the phase diagrams are qualitatively similar to that shown in Fig. 4.5(c). This new topology presents a $\rm N_U^+$-$\rm N_U^-$ phase transition limited inferiorly by an ISO-$\rm N_U^+$-$\rm N_U^-$ triple point and superiorly by a CE point (see inset in Fig. 4.5(c)).

The Landau points (discussed in Sec. 4.2.2) are present in the ϕ-T phase diagrams depending of the strength of the anisotropic interaction between dipoles and nematogens. As we discussed for $0 < \Delta < 1$ we can find phase diagrams that can even present two Landau points. Fig. 4.6(a) represents the phase diagram for a system with $(A, B) = (1, -6/5)$ where we find different multicritical points and nematic phases. We can notice a wide region of stability for the $\rm N_B$ phase, bounded at high temperatures by two $\rm N_U^-$-$\rm N_B$ and $\rm N_{U_I}^+$-$\rm N_B$ second-order lines. The two continuous lines meet at a high-concentration L point [4]. At this point the three nematic phases ($\rm N_B$, $\rm N_{U_I}^+$ and $\rm N_U^-$) become identical to each other and to the ISO phase. In the diagram we can see another L point, at low concentration, at which two uniaxial nematic phases ($\rm N_{U_{II}}^+$ and $\rm N_U^-$) become identical to the ISO phase. For temperatures below the low-concentration L point there are two different ISO-$\rm N_{U_{II}}^+$ and $\rm N_{U_{II}}^+$-$\rm N_U^-$ biphasic regions. The $\rm N_{U_{II}}^+$-$\rm N_U^-$ first-order transition can be determined by the Eqs. (4.27) evaluated at $(S, \eta, R, \zeta, \phi) = (S_+, 0, R_+, 0, \phi_+)$ and at $(S, \eta, R, \zeta, \phi) = (S_-, 0, R_-, 0, \phi_-)$, supplemented by $\psi(S_+, 0, R_+, 0, \phi_+) = \psi(S_-, 0, R_-, 0, \phi_-)$, where ϕ_+ and ϕ_- are the nematogen concentrations at the $\rm N_{U_{II}}^+$ and $\rm N_U^-$ phases respectively, while $S_\pm$ and $R_\pm$ are the corresponding values of S and R. Near the low-concentration L point, $\phi_+ \to \phi_-$ and the uniaxial-uniaxial first-order transition is very weak (see the inset Fig. 4.6(a)). There is an ISO-$\rm N_{U_{II}}^+$-$\rm N_U^-$ triple point (short red dashed line) which marks the limit of stability for both ISO-$\rm N_{U_{II}}^+$ and $\rm N_{U_{II}}^+$-$\rm N_U^-$ coexistence regions because for temperatures below the triple point these coexistences become metastable with respect to the ISO-$\rm N_U^-$ coexistence.

In general, for values of $B < -108/91$, the phase diagrams for $\Delta = 4/5$ present a stable high-concentration L point. Nevertheless the low-concentration L point is only stable for $-1.3645 \lessapprox B < -108/91$ because for values of $B < -1.3645$ the low-concentration L point represents a local minimum of the Landau-de Gennes free-energy functional and becomes metastable with respect to the ISO-$\rm N_U^-$ coexistence. The loss of this Landau point obviously implies the disappearance of the region of stability of the $\rm N_{U_{II}}^+$ phase, then the ϕ-T phase diagram adopts a topology similar to that represented in Fig. 4.6(b) for $(A, B) = (1, -3/2)$. If B continually reaches more negative values, an increase in the region where phase $\rm N_U^-$ is stable and a decrease in the stability region of phase $\rm N_U^+$ can be noted, see Fig. 4.6(c). For $|B| \gg A$ the $\rm N_U^+$ phase is stable only very close to the line $\phi = 1$.

[4] For phase diagrams that present two multicritical Landau points, we will refer to these as high-concentration and low-concentration Landau points.

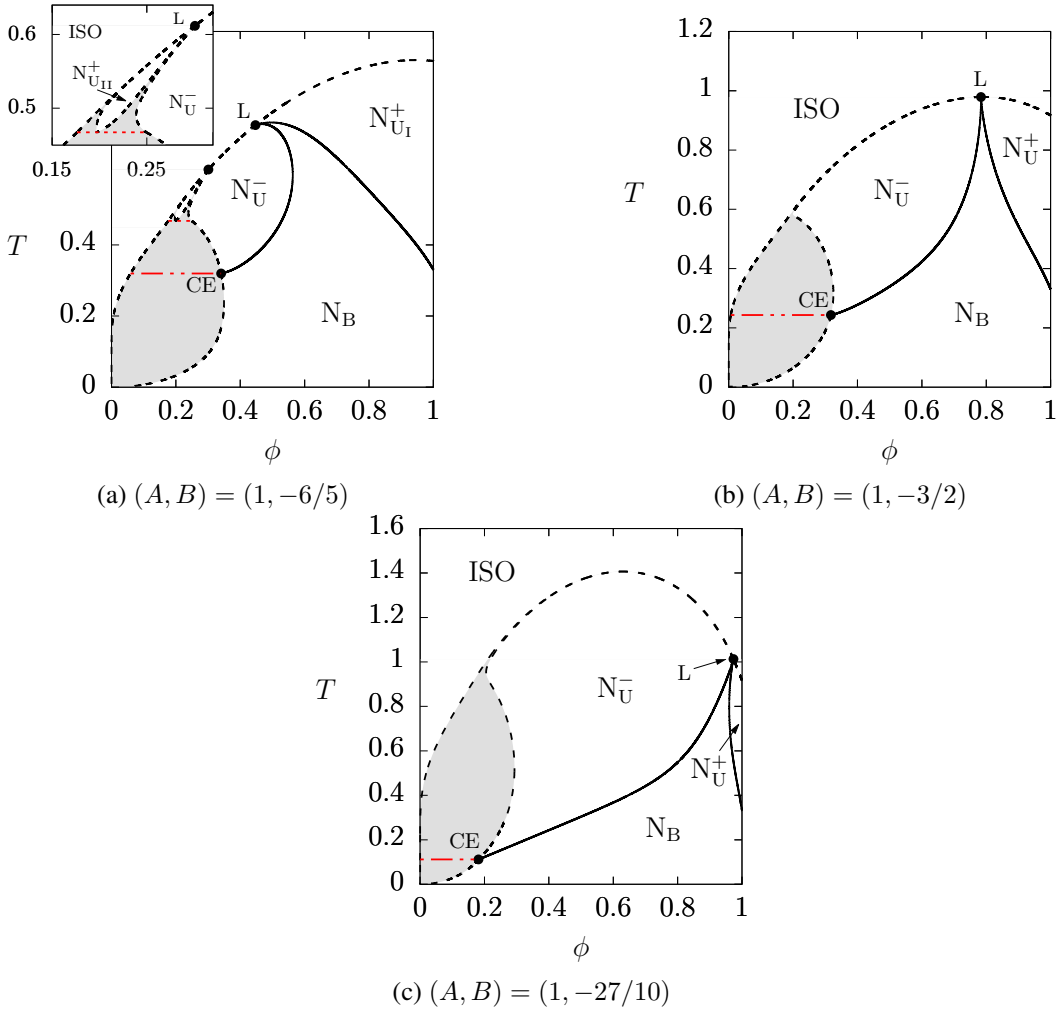

(a) $(A, B) = (1, -6/5)$

(b) $(A, B) = (1, -3/2)$

(c) $(A, B) = (1, -27/10)$

Figure 4.6: Phase diagrams in terms of temperature T (in units of A) and concentration ϕ of nematogens, for biaxiality degree $\Delta = 4/5$ and in the absence of isotropic interaction ($U = 0$). ISO: isotropic phase. N_U^+, $N_{U_I}^+$, and $N_{U_{II}}^+$: calamitic uniaxial nematic phases. N_U^-: discotic uniaxial nematic phase. N_B: biaxial nematic phase. Short-dashed lines are the boundaries of biphasic regions (gray). Red dot-dashed line: critical end point (CE). Red dashed line is a triple point. L is a Landau multicritical point.

4.3.3 Phase diagrams for $\Delta = 1$

If the nematogens present the degree of biaxiality $\Delta = 1$ we can see phase diagrams similar to those shown in Fig. 4.7. Here the diagrams present a single multicritical L point located at $(\phi_L, T_L) = (1, 1)$, as discussed in Sec. 4.2.2. These diagrams present a stable phase N_U^+ whose stability region is strongly dependent on B. We know that for $B = 0$ the system is characterized by the absence of the uniaxial phase because in this case we have a diluted quadrupolar problem (see Chap. 3 and Ref. [94]). For $B \gg A > 0$ we find a large stability region for the N_U^+ phase, see Fig. 4.7(c). In addition to the L point, these diagrams present a CE point that marks the stability limit of an ISO-N_B coexistence region. As discussed in Appendix. A, for $T \to 0$ there is a coexistence region between the ISO and the N_B phases only if $|B| < 2/3$, and outside this range we find a stable N_B phase for all concentrations at zero temperature. Note that, for the sequence of diagrams from 4.7(a) to 4.7(c), increasing B leads to a reduction of the isotropic-

nematic coexistence region.

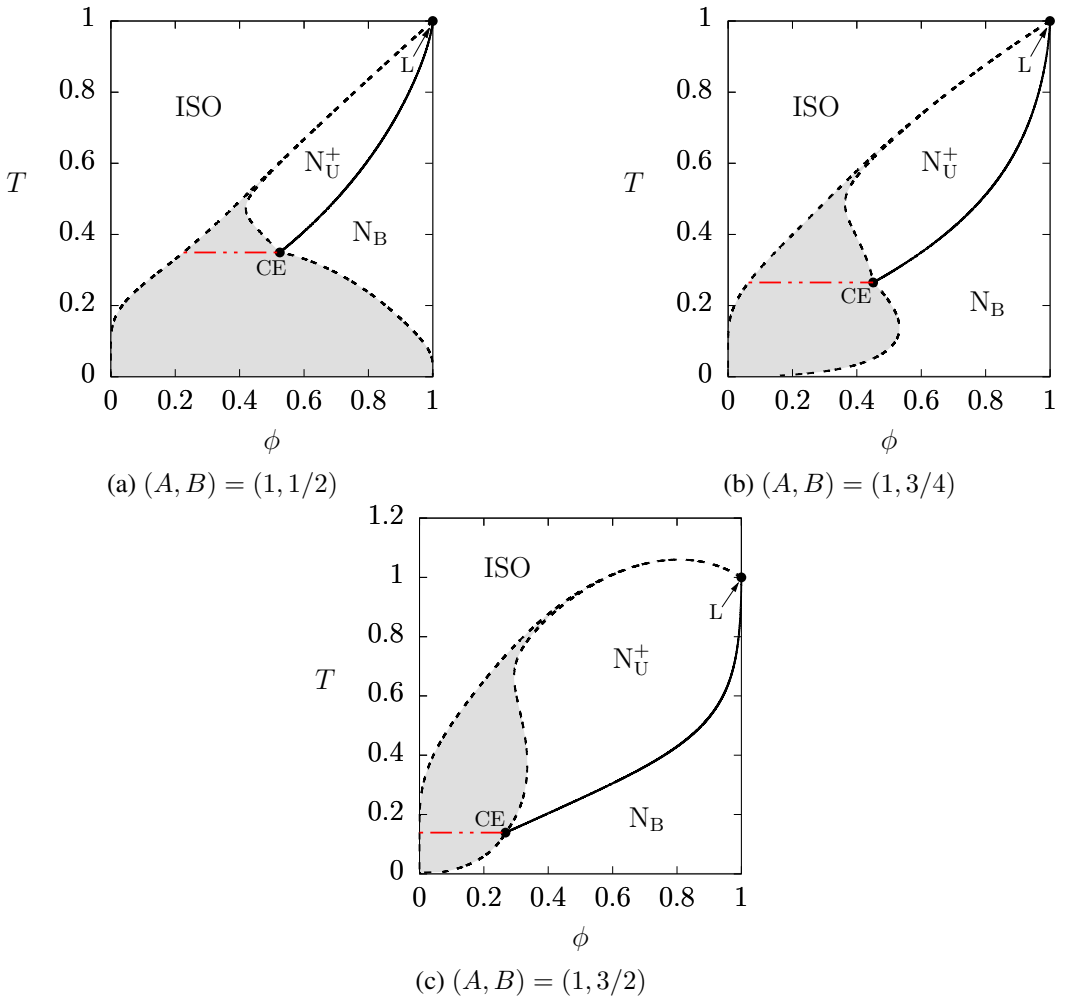

(a) $(A, B) = (1, 1/2)$

(b) $(A, B) = (1, 3/4)$

(c) $(A, B) = (1, 3/2)$

Figure 4.7: Phase diagrams in terms of temperature T (in units of A) and concentration ϕ of nematogens, for biaxiality degree $\Delta = 1$ and in the absence of isotropic interaction ($U = 0$). ISO: isotropic phase. N_U^+: calamitic uniaxial nematic phase. N_B: biaxial nematic phase. Short-dashed lines are the boundaries of biphasic region (gray). Red dot-dashed line: critical end point (CE). L is a Landau multicritical point.

4.4 LC-based suspensions

For high concentration of nematogens ($\phi \to 1$) the role of the dipolar NPs can be favorable or detrimental for the formation of nematic structures [5]. This is strongly dependent of the strength of the anisotropic interaction between dipolar NPs and nematogens. The behavior of the doped transition temperature, $T_{\text{I-N}}$, of the host liquid crystal with respect to the pure liquid crystal transition temperature, $T_{\text{I-N}}^{(0)}$, has been studied using different approaches, mostly for uniaxial systems. In the framework of the molecular MF theory, M. V. Gorkunov and M. A. Osipov [34] predict a softening of the isotropic-uniaxial first-order transition caused by strongly

[5] If the introduction of dipolar NPs in a nematic host produces an increase in the transition temperature between the isotropic and uniaxial phases, then the formation of nematic structures will be favored. If the transition temperature decreases, the formation of nematic structures will be disadvantaged.

anisotropic interaction between nanoparticles and nematogens, together with a shift [6] $\delta T_{\text{I-U}} = T_{\text{I-U}} - T_{\text{I-U}}^{(0)}$ that can be positive or negative depending on the anisotropic interaction between objects of different nature and the concentration of NPs. Similar results are obtained by A. N. Zakhlevnykh *et al.* [36] using the spherical approximation to derive an analytic expression for the free-energy functional. Experimentally, negative and positive shifts in the transition temperature have been reported for various systems [37, 81, 95–98]. Using our LGMSZ-B model we present a detailed analysis of both uniaxial-isotropic and uniaxial-biaxial transitions in the limit of an LC-based suspension ($\phi \geqslant 0.9$).

The simplest situation are the LC-based suspensions with rod-like ($\Delta = 0$) nematogens, which can only present an ISO-N_{U}^{+} first-order phase transition (see Sec. 4.3.1). Fig. 4.8(a) shows the ISO-N_{U}^{+} coexistence region for different values of $\kappa = B/A$ and $\Delta = 0$, with the temperature normalized by $T_{\text{I-U}}^{(0)} = \frac{9}{16\ln(2)}$. We can see a reduction for the coexistence region as

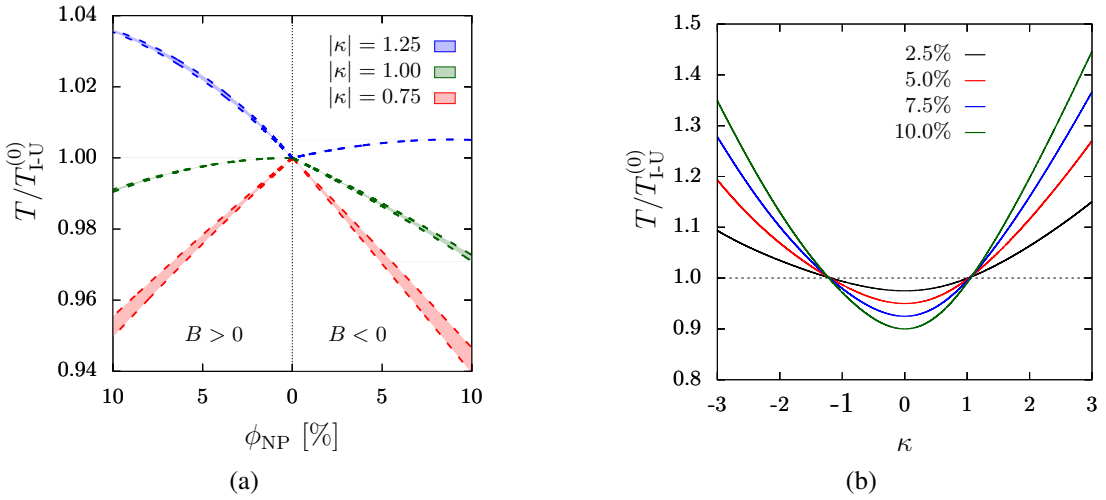

Figure 4.8: (a) Normalized isotropic-uniaxial transition temperature as a function of the concentration of dipolar NPs ϕ_{NP} for intrinsically uniaxial nematogens $\Delta = 0$ and different values of $\kappa = B/A$. (b) Normalized isotropic-uniaxial transition temperature as a function of $\kappa = B/A$ for intrinsically uniaxial nematogens $\Delta = 0$ and different values of ϕ_{NP}. Black thin-dashed line indicates the clearing point ($T = T_{\text{I-U}}^{(0)}$) of the LC host.

$|\kappa|$ increases. This reduction represents a softening of the phase transition.

The relative transition temperature as a function of κ for different values of fixed concentration ϕ_{NP} of dipolar NPs is shown in Fig. 4.8(b). For $\kappa = 0$ we have a diluted problem (see Chap. 3 and Ref. [94]), and in this case $\delta T_{\text{I-U}} < 0$ because the presence of dipolar NPs decreases the effective interaction between nematogens. For $\kappa > 0$ the dipoles tend to align with the first axes of the nematogens, that is, the macroscopic director $\hat{\mathbf{n}}$ corresponds to an *easy axis* for the dipoles. This orientational preference increases the effective interaction between nematogens but implies a decrease in the dipole contribution to the entropy of the system. For $\kappa < 0$ the dipoles tend to arrange themselves perpendicularly to $\hat{\mathbf{n}}$, corresponding to an *easy plane* for the

[6] The change from I-N to I-U refers to an isotropic-uniaxial nematic phase transition. In general we will use the subscripts I, U and B for isotropic, uniaxial and biaxial phases respectively.

dipoles. Naturally, this orientational restriction is less costly, from an entropic point of view, than the one discussed for $\kappa > 0$. The behavior of the system is qualitatively similar to the case $\kappa > 0$, as we can see in Fig. 4.8(b).

For intrinsically biaxial nematogens (e.g., $\Delta = 4/5$), at the limit of LC suspension we will not only have an ISO-N_U^+ first-order transition, but also an N_U^+-N_B second-order transition. In the case of pure LC the transition temperatures are $T_{\mathrm{I\text{-}U}}^{(0)} \approx 0.9171$ and $T_{\mathrm{U\text{-}B}}^{(0)} \approx 0.3304$ for the first-order and second-order transitions respectively. Fig. 4.9 shows the temperatures of the

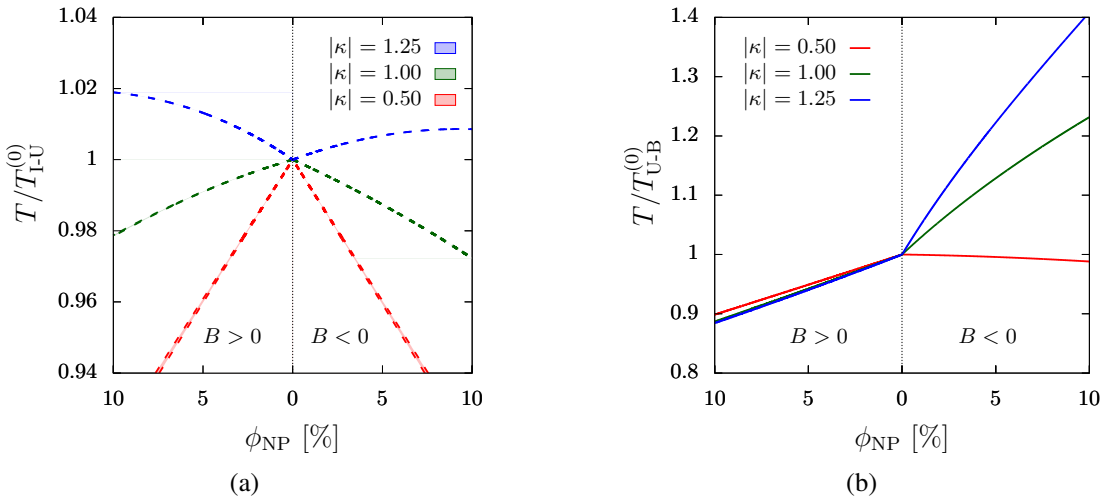

Figure 4.9: (a) Normalized uniaxial-biaxial transition temperature as a function of the concentration of dipolar NPs ϕ_{NP} for intrinsically biaxial nematogens $\Delta = 4/5$ and different values of $\kappa = B/A$. (b) Normalized uniaxial-biaxial transition temperature as a function of ϕ_{NP} for intrinsically biaxial nematogens $\Delta = 4/5$ and different values of $\kappa = B/A$.

two phase transitions for different values of κ. Similar to the case for rod-like nematogens, the ISO-N_U^+ biphasic region is reduced by increasing $|\kappa|$, implying a softening of the first-order transition. For $\kappa > 0$ we can see that $\delta T_{\mathrm{U\text{-}B}} = T_{\mathrm{U\text{-}B}} - T_{\mathrm{U\text{-}B}}^{(0)} < 0$ for the entire range $0 < \phi_{\mathrm{NP}} < 0.1$, while the case $\kappa < 0$ represents a favorable situation for the formation of biaxial structures for $\kappa \lesssim -0.5115$ because $\delta T_{\mathrm{U\text{-}B}} > 0$ (exemplified in Fig. 4.9(b) by the blue and dark-green solid lines for $B < 0$) but this behavior, as we will discuss below, can be affected by the existence of a high-concentration L point.

In Sec. 4.2.2, and more specifically in Sec. 4.3.2 for the case of $\Delta = 4/5$, we discussed the existence of a stable L point at $\Delta \neq 0$. A L point similar to that shown in Fig. 4.6(b) is related to the existence of two converging N_U^--N_B and N_U^+-N_B second-order lines, and two ISO-N_U^- and ISO-N_U^+ first-order transitions. The concentration ϕ_L increases as B decreases (for $\Delta = 4/5$ fixed), and for sufficiently negative values of B this L point can approach the point $(\phi, T) = (1, T_{\mathrm{I\text{-}U}}^{(0)})$ similar to Fig. 4.6(c). As it has been noted throughout this section, we consider a LC suspension limit if nematogens represent at least 90% of the mixture. If the value of B implies that $\phi_\mathrm{L} \geqslant 0.9$, then we will have a suspension that presents a stable L point. Fig. 4.10 shows the κ-T phase diagram for a LC suspension with concentration of

NPs $\phi_{\rm NP} = 0.025$ and nematogens with biaxiality degree $\Delta = 4/5$. In the $\rm N_B$ phase, for $\kappa > 0$ the probability of finding a dipole aligned with the first axes of the nematogens is very high, which increases the effective interaction between nematogens. This alignment implies a decrease in the entropy contribution of the dipoles, but the entropic cost is not very important for small values of κ. If the value of B increases continuously, the increase in the effective interaction between nematogens does not compensate the decrease in the entropy of the system and, as a consequence, the temperature of the $\rm N_U^+$-$\rm N_B$ second-order transition decreases (see inset Fig. 4.10). Note that in the $\rm N_U^+$ phase the suspension exhibits a cylindrical symmetry but this symmetry is broken in the $\rm N_B$ phase, making entropic effects on the free energy more important.

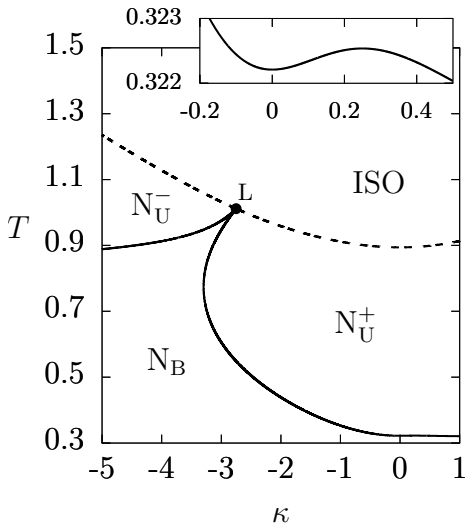

Figure 4.10: Phase diagram in terms of temperature T (in units of A) and $\kappa = B/A$, for biaxiality degree $\Delta = 4/5$, concentration of nematogens $\phi = 0.975$, and in absence of isotropic interaction ($U = 0$). ISO: isotropic phase. $\rm N_U^+$: calamitic uniaxial nematic phase. $\rm N_U^-$: discotic uniaxial nematic phase. $\rm N_B$: biaxial nematic phase. L is a Landau multicritical point.

For values of $\kappa < 0$, the system presents a multicritical L point where four phases ($\rm N_U^+$, $\rm N_U^-$, $\rm N_B$, and ISO) become identical. On the second-order line related to the $\rm N_B$-$\rm N_U^+$ transition there is a point (κ_o, T_o) which satisfies the condition $dT/\,d\kappa \to \infty$. This point implies a reentrance of the $\rm N_B$ phase. For a fixed value of $\kappa_o < \kappa < \kappa_{\rm L}$ the sequence of phases observed, as the temperature decreases, if ISO, followed by a $\rm N_U^-$ phase where $S < 0$ and $R > 0$, followed by a small stability region for the $\rm N_B$ phase which is bounded above and below by two second-order lines, followed by a $\rm N_U^+$ phase where $S > 0$ and $R < 0$, and finally the $\rm N_B$ is one more time stable. This fascinating phase behavior is also reflected in the scalar parameters S, R, η, and ζ as we can see in Fig. 4.11

For values of $\kappa < \kappa_o$ the phase sequence observed, as T decreases is ISO, followed by a small stability region for the $\rm N_U^-$ phase, and finally a long stability region for the $\rm N_B$ phase.

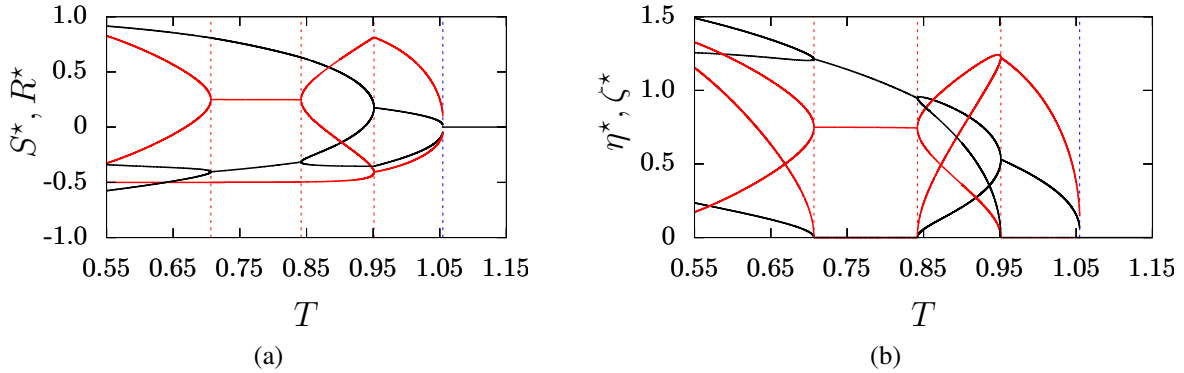

(a) (b)

Figure 4.11: Equilibrium values of $S^\star = S/\phi$ (black-solid line) and $R^\star = R/(1-\phi)$ (red-solid line) (a) and $\eta^\star = \eta/\phi$ (black-solid line) and $\zeta^\star = \zeta/(1-\phi)$ (red-solid line)(b), for $\kappa = -3.25$, as a function of temperature T (in units of A). Red thin-dashed lines are second-order transitions and blue thin-dashed line is a first-order transition.

4.5 Phase behavior for $U \neq 0$

For systems with nonzero isotropic lattice interaction ($U \neq 0$) the phase diagrams can undergo various modifications. For the attractive case, $U < 0$, the regions of phases coexistence are enlarged. For sufficiently attractive values of U we observed low-concentration $-$ high-concentration transitions in the ISO phase.

For $\Delta = 0$ we obtain the sequence of phase diagrams shown in the Fig. 4.12 for fixed values of $(A, B) = (1, -2)$. We can notice a reduction in the stability region of $\mathrm{N_U^+}$ upon increasing the attractive character of U. At $T = 0$, for $U < -3/2$ the $\mathrm{N_U^+}$ phase becomes metastable with respect to the ISO-$\mathrm{N_U^+}$ coexistence. For a fixed temperature $T < 1$, the width of the low-concentration ISO-$\mathrm{N_U^+}$ coexistence region increases with $|U|$, as shown in Figs. 4.12(a)-4.12(c).

For sufficiently attractive values of U we can find a first-order transition between two isotropic phases of high and low concentration of nematogens. Fig. 4.13(a) shows the ϕ-T phase diagram for a system with parameters $(A, B, U) = (1, -1, -3)$ and rod-like molecules. For low temperatures there is a coexistence region between a dipolar-poor isotropic phase ($\mathrm{I_{DP}}$) and a dipolar-rich isotropic phase ($\mathrm{I_{DR}}$). The diagram exhibits a $\mathrm{I_{DR}}$-$\mathrm{I_{DP}}$-$\mathrm{N_U^+}$ triple point (red dashed line) which marks the limit of stability of the $\mathrm{I_{DR}}$-$\mathrm{N_U^+}$ coexistence. The location of the triple point can be determined by the MF equations evaluated at $(S, \eta, R, \zeta, \phi) = (0, 0, 0, 0, \phi_{\mathrm{I_{DR}}})$, at $(S, \eta, R, \zeta, \phi) = (0, 0, 0, 0, \phi_{\mathrm{I_{DP}}})$, and at $(S, \eta, R, \zeta, \phi) = (S_\mathrm{U}, 0, R_\mathrm{U}, 0, \phi_\mathrm{U})$ supplemented by $\psi(0, 0, 0, 0, \phi_{\mathrm{I_{DR}}}) = \psi(0, 0, 0, 0, \phi_{\mathrm{I_{DP}}}) = \psi(S_\mathrm{U}, 0, R_\mathrm{U}, 0, \phi_\mathrm{U})$. There is a simple C point at which the $\mathrm{I_{DR}}$ and $\mathrm{I_{DP}}$ phases become identical. This simple C point can be determined by $\partial\psi/\partial\phi = d^2\psi/\,d\phi^2 = d\psi/\,d\phi^3 = 0$ evaluated at $(S, \eta, R, \zeta, \phi) = (0, 0, 0, 0, \phi_\mathrm{C})$, which leads $\phi_\mathrm{C} = 1/2$, $\beta_\mathrm{C} = -4/U$, and $\mu_\mathrm{C} = U/2$. In the context of the Landau-de Gennes free-energy functional, for attractive isotropic interaction, the simple C point can be either stable (an absolute minimum) or metastable (a local minimum). For repulsive isotropic interaction,

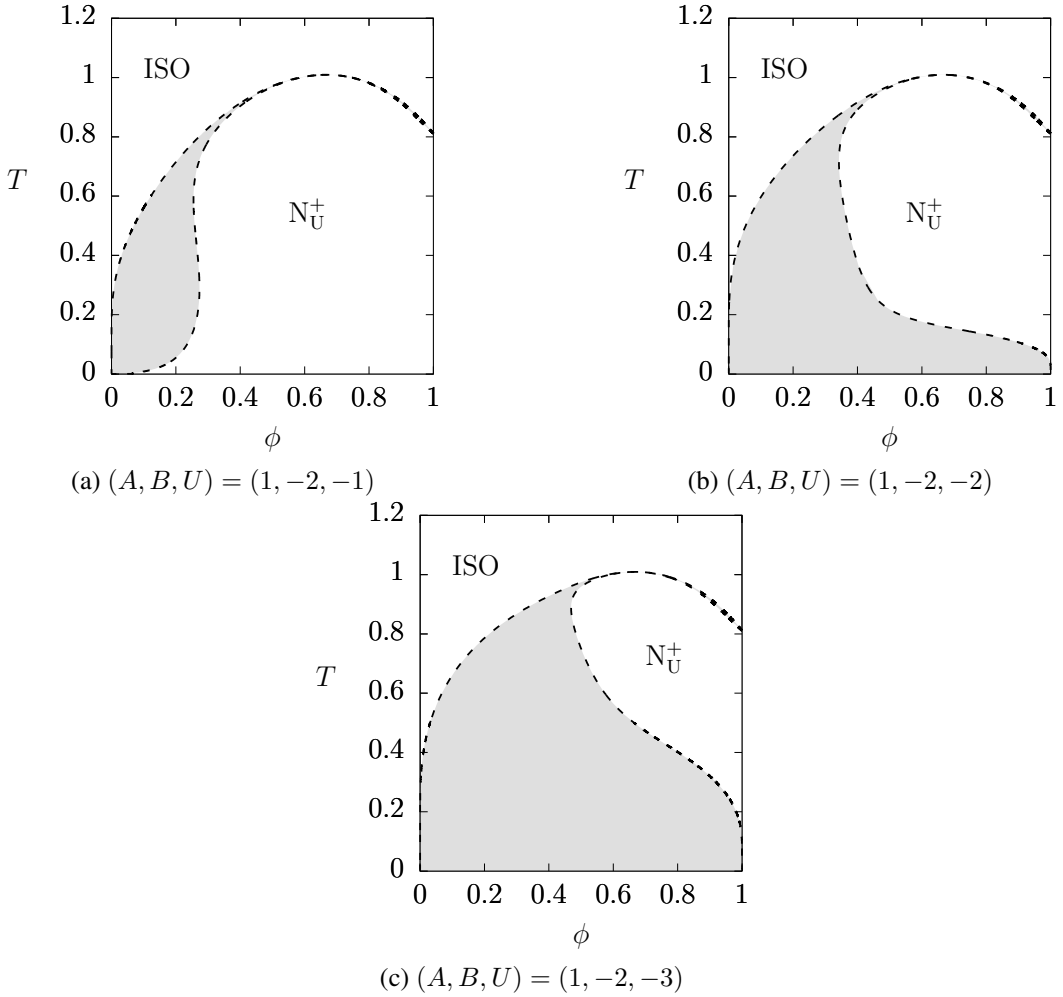

(a) $(A, B, U) = (1, -2, -1)$

(b) $(A, B, U) = (1, -2, -2)$

(c) $(A, B, U) = (1, -2, -3)$

Figure 4.12: Phase diagrams in terms of temperature T (in units of A) and concentration ϕ of nematogens, for intrinsically uniaxial nematogens ($\Delta = 0$) and different values of the isotropic interaction. ISO: isotropic phase. N_U^+: calamitic uniaxial nematic phase. Short-dashed lines are the boundaries of biphasic regions (gray).

C is unstable. Any point on I_{DR}-I_{DP} first-order lines occurs for a chemical potential μ_C. If the isotropic interaction is more attractive (e.g., see Fig. 4.13(b)), there is an increment in the I_{DR}-I_{DP} coexistence region and the simple C point takes a temperature greater than the I_{DP}-N_U^+ transition temperature for the pure LC host.

For intrinsically biaxial nematogens ($\Delta = 19/20$) we show the ϕ-T phase diagram in Fig. 4.14(a) for fixed parameters $(A, B, U) = (1, -3/4, -1)$. This diagram presents a multicritical L point, located at $\phi_L \approx 0.7515$ and $T_L \approx 0.8262$, which signals a direct transition from the N_B phase to the ISO phase. The position of the L point is independent of U. At high concentration of nematogens ($\phi > \phi_L$) the phase sequence observed is ISO, followed by a narrow ISO-N_U^+ coexistence, followed by a pure N_U^+ phase that is bounded from below by a second-order line, followed by a pure N_B phase, and finally a low temperature coexistence between a dipolar-poor N_B and a dipolar-rich ISO phase. For values of $\phi_{CE} < \phi < \phi_L$ the observed phase sequence, as T decreases, is similar but the uniaxial phase is discotic. The ϕ-T phase diagram shown in Fig. 4.14(b) illustrates a similar situation (with respect to Fig. 4.14(a)), but in this case $U = -2$.

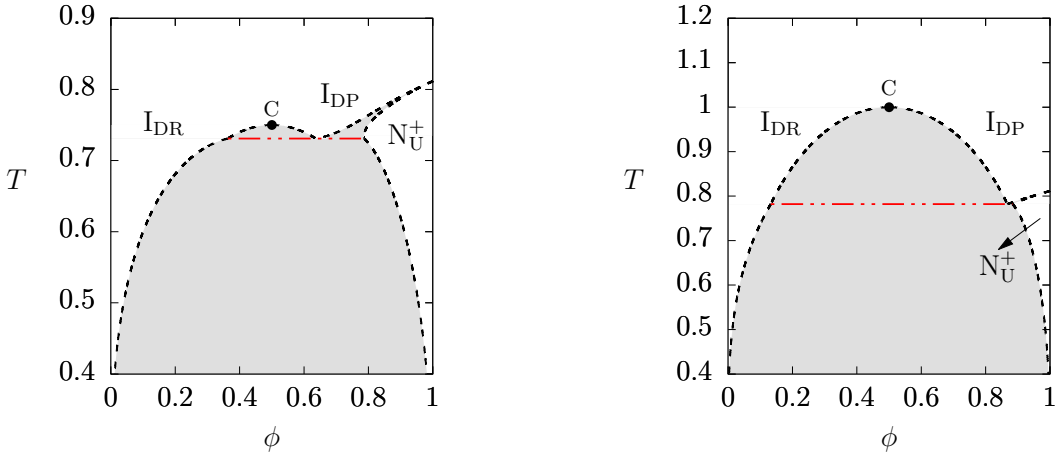

(a) $(A, B, U) = (1, -1, -3)$ (b) $(A, B, U) = (1, -1, -4)$

Figure 4.13: Phase diagrams in terms of temperature T (in units of A) and concentration ϕ of nematogens, for intrinsically uniaxial nematogens ($\Delta = 0$) and for different values of the isotropic interaction. $\mathrm{I_{DR}}$: dipolar-rich isotropic phase. $\mathrm{I_{DP}}$: dipolar-poor isotropic phase. $\mathrm{N_U^+}$: calamitic uniaxial nematic phase. Short-dashed lines are the boundaries of biphasic regions (gray). Red long-dashed line: is an $\mathrm{I_{DR}}$-$\mathrm{I_{DP}}$-$\mathrm{N_U^+}$ triple point. C is a simple critical point.

We can observe that, the increase of the attractiveness of the isotropic interaction reduces the stability of the $\mathrm{N_B}$ and $\mathrm{N_U^-}$ phases.

For nematogens with degree of biaxiality $\Delta = 1$, as we saw in Sec. 4.2.2, the system presents a stable L point at $(\phi, T) = (1, 1)$. In this case, it is impossible for two uniaxial phases to appear in the same phase diagram in the ϕ-T plane, regardless of the value of U. Fig. 4.15 shows a representative sequence of phase diagrams for a molecular system with parameters $(A, B) = (1, 2/\sqrt{3})$ and different values for the strength of the isotropic interaction. The phase diagram in Fig. 4.15(a) exhibits ISO-$\mathrm{N_U^+}$ coexistence that widens as the temperature decreases. There is a CE point, represented by the red dot-dashed line, which is a stability bound because for temperatures below T_{CE} the ISO-$\mathrm{N_U^+}$ coexistence becomes metastable with respect to an ISO-$\mathrm{N_B}$ coexistence. This diagram presents a second-order transition between a $\mathrm{N_U^+}$ and a $\mathrm{N_B}$ phase, represented by the black solid line. The $\mathrm{N_U^+}$-$\mathrm{N_B}$ second-order line is limited at low and at high temperature by CE and L, respectively. The phase diagram shown in Fig. 4.15(b) corresponds to a system with isotropic interaction $U = -2$. This diagram is similar to the one shown in Fig. 4.15(a) with an important difference at low temperatures. The ISO-$\mathrm{N_B}$ is stable, regardless of the concentration of nematogens. This is one more example that shows that the attractive isotropic interaction favors isotropic-nematic phase coexistence.

A sufficiently attractive isotropic interaction gives rise to the occurrence of a high-temperature $\mathrm{I_{DR}}$-$\mathrm{I_{DP}}$ coexistence ending at an ordinary C point, as shown Fig. 4.15(c). This diagram exhibits a $\mathrm{I_{DR}}$-$\mathrm{I_{DP}}$-$\mathrm{N_U^+}$ triple point represented by the red dashed line. At temperatures below the triple point temperature the $\mathrm{I_{DR}}$-$\mathrm{I_{DP}}$ coexistence becomes metastable with respect to $\mathrm{I_{DR}}$-$\mathrm{N_U^+}$ phase coexistence. The red dot-dashed line represents a CE point. The stability region for the $\mathrm{N_B}$ phase is very small because the isotropic interaction is much more important than both

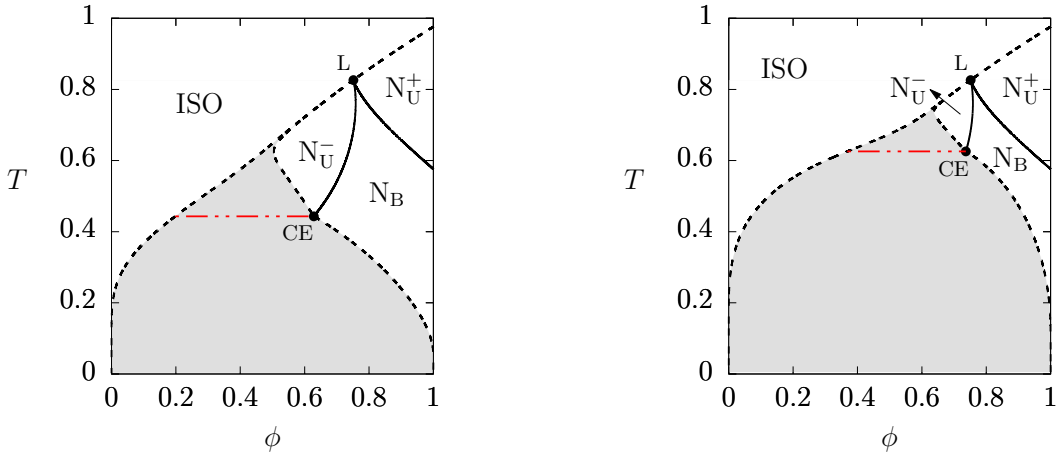

(a) $(A, B, U) = (1, -3/4, -1)$ (b) $(A, B, U) = (1, -3/4, -2)$

Figure 4.14: Phase diagrams in terms of temperature T (in units of A) and concentration ϕ of nematogens, for biaxiality degree $\Delta = 19/20$ and different values of the isotropic interaction ($U = 0$). ISO: isotropic phase. N_U^+: calamitic uniaxial nematic phase. N_U^-: discotic uniaxial nematic phase. N_B: biaxial nematic phase. Short-dashed lines are the boundaries of biphasic regions (gray). Red dot-dashed line: critical end point (CE). L is a Landau point.

the anisotropic interaction between nematogens and the anisotropic interaction between dipolar NPs and nematogens.

4.6 Conclusions

We considered a binary mixture of nematogens and dipolar NPs, whose interaction is given by an adaptation of the Maier-Saupe model with discrete orientations. In addition to the anisotropic nematogen-nematogen and nematogen-NP interactions we considered an isotropic interaction in the same spirit to the dilution problem discussed in Chap. 3. This problem was investigated in the context of MF theory. The Landau-de Gennes functional, the MF equations, and the position of many multicritical point (e.g., Landau points and simple critical points) were obtained exactly.

For systems with $U = 0$, we presented the ϕ-T phase diagrams for fixed values of Δ. In this case we find a large number of different topologies and multicritical points depending on the value of B. For $B \leqslant -108/91$ and $\Delta = 4/5$ the phase diagram may present one or two stable Landau points. Other multicritical points like critical-end or tricritical point are present (see e.g. Figs. 4.5 and 4.6).

We presented a detailed study for LC-based suspensions (i.e. systems with low concentration of dipolar NPs). For rod-like nematogens ($\Delta = 0$) our results are capable of reproducing changes in clearing points, for which there is experimental evidence (see e.g. Refs. [80] and [81]). Our results are also compatible with MF calculations of models with continuous degrees of freedom, based on spherical approximations (see Ref. [63]). For intrinsically biaxial nematogens ($\Delta \neq 0$) we studied the effects of NPs on the uniaxial-biaxial second-order transi-

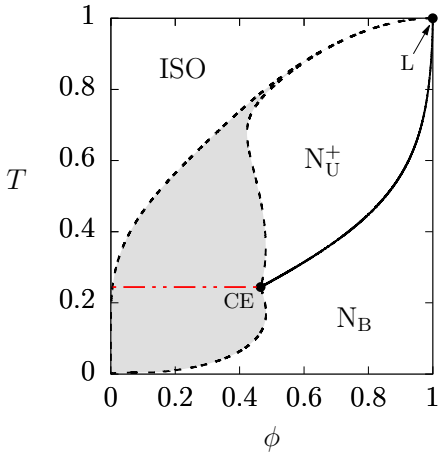

(a) $(A, B, U) = (1, 2/\sqrt{3}, -1)$

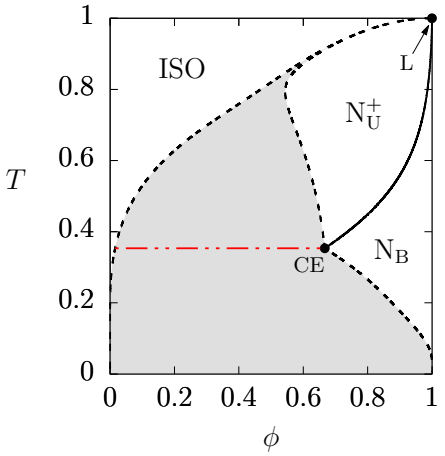

(b) $(A, B, U) = (1, 2/\sqrt{3}, -2)$

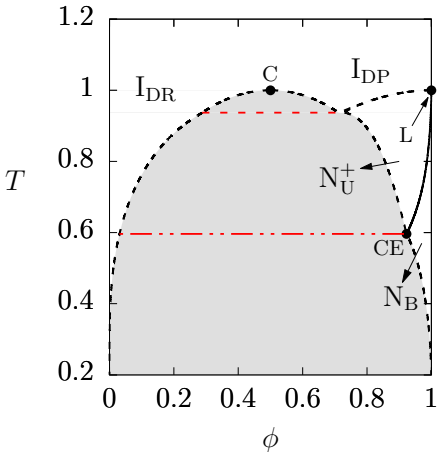

(c) $(A, B, U) = (1, 2/\sqrt{3}, -4)$

Figure 4.15: Phase diagrams in terms of temperature T (in units of A) and concentration ϕ of nematogens, for biaxiality degree $\Delta = 1$ and different values of the isotropic interaction. ISO: isotropic phase. I_{DR}: dipolar-rich isotropic phase. I_{DP}: dipolar-poor isotropic phase. N_U^+: calamitic uniaxial nematic phase. N_B: biaxial nematic phase. Short-dashed lines are the boundaries of biphasic regions (gray). Red dot-dashed line: critical end point (CE). Red dashed line is a triple point. L is a Landau point. C is a simple critical point.

tion. We showed that, depending on the value of B, the isotropic-uniaxial first-order transition and the uniaxial-biaxial second-order transition lines meet at a Landau multicritical point.

Systems with $U \neq 0$ were analyzed and showed to exhibit a great variety of multicritical points depending on the character of the isotropic interaction, the biaxiality degree, and the strength of the anisotropic interaction between objects of different nature.

Chapter 5

Concluding remarks

For this manuscript, different extensions of the mean-field Maier-Saupe model for nematogenic mixtures were studied. The two models presented, the LGMSZ and LGMSZ-B models, were derived from the general bilinear anisotropic interaction potential [47] in the London approximation for the dispersion forces [48]. In order to perform detailed calculations we also employed the Zwanzig approximation [41], which restricts the possible orientations of a microscopic object to the coordinate axes.

The effects of dilution were studied using a lattice-gas extension of the MSZ model and an additional isotropic interaction between nematogens. A large number of ϕ-T phase diagrams were built for fixed values of the degree of biaxiality Δ of the nematogens and of the strength of the isotropic interaction. Many different critical and multicritical points, such as ordinary vapor-liquid critical points, critical end points, triple points, tricritical points as well as Landau multicritical points were found in these diagrams. Many of the ϕ-T phase diagrams that were obtained are equivalent to diagrams obtained in previous works employing either Monte Carlo simulations [49, 50, 54] or improved off-lattice approximations [59, 60].

The phase behavior of a binary mixtures of nematogens and dipolar NPs was investigated in terms of the strength of the isotropic interaction between anisotropic objects, the strength of the interaction between objects of different nature, as well as the degree of biaxiality and the concentration of nematogenic units. A perturbative calculation to study the effects produced in the nematic phases when doping a LC host with small amounts of dipolar NPs was presented. At this limit ($\phi \to 1$), for intrinsically uniaxial systems, our results are compatible with many experimental reports [37, 81, 95–98] and theoretical MF calculations [34, 36]. For intrinsically biaxial nematogens we study the effects of doping with dipolar NPs on the uniaxial-biaxial second-order phase transition.

Despite the simplicity of the models presented in this manuscript, they reproduce previously obtained theoretical and experimental results. However, there are inaccessible situations for these models. For example, the models assume the shape of the basic units to be fixed. This is a reasonable assumption for thermotropic systems, in which the nematogens are asymmetric molecules, but not for lyotropic systems, characterized by mesogens produced by the

aggregation of amphiphilic molecules in solution, forming micelles whose properties can vary with parameters such as temperature and density of solute. In order to alleviate the limitations of assuming a fixed nematogen shape, the models can be augmented by the introduction of an elastic energy term, allowing shape fluctuations around an average value, gauged by an elastic constant setting the corresponding energy scale. This is left for future investigations.

Another limitation of our models is that, in addition to their mean-field character, they focus on bulk properties, and thus do not take into account anchoring effects which are present in many experimental situations. It would certainly be interesting to employ Monte Carlo simulations to study finite-dimensional versions of the models, both under periodic and under fixed boundary conditions, in order to identify the features of the phase diagrams that change with respect to our predictions.

Appendix A

Low-temperature coexistence

A.1 The LGMSZ model

In the isotropic phase, with $T \to 0$, we have $\mathbf{\Omega}_i : \mathbf{\Omega}_j = 0$ for any pair of nematogens (i, j), so the free energy is

$$\mathcal{F}_{\mathrm{ISO}}(\phi) = \frac{U}{2N} \sum_{i,j=1}^{N} \gamma_i \gamma_j = \frac{U}{2N} \left(\sum_{i=1}^{N} \gamma_i \right)^2 = \frac{U}{2N} N_m^2 = \frac{UN}{2} \phi^2, \tag{A.1}$$

where we have used that $\phi = N_m/N$. In the nematic phase (biaxial if $0 < \Delta < 3$ or uniaxial phase if $\Delta = 0$ or $\Delta = 3$), we have if $\mathbf{\Omega}_i : \mathbf{\Omega}_j = (3 + \Delta^2)/2$ for any pair of nematogens (i, j), and free energy in this case is

$$\mathcal{F}_{\mathrm{N}}(\phi) = -\frac{AN}{4}(3 + \Delta^2)\phi^2 + \frac{UN}{2}\phi^2. \tag{A.2}$$

For a isotropic-nematic coexistence, the double-tangent construction (considering the isotropic phase stable only if $\phi = 0$) leads to

$$U - \frac{A}{2}(\Delta^2 + 3) = 0, \tag{A.3}$$

Therefore, if $U/A > (\Delta^2 + 3)/2$ the nematic phase is stable, otherwise there appears an isotropic-nematic coexistence region.

A.2 The LGMSZ-B model

For this model, the free-energy of the system strongly depends on the value of B. In the limit $T \to 0$ the free energy of the isotropic phase is

$$\mathcal{F}_{\mathrm{ISO}}(\phi) = \frac{UN}{2}\phi^2, \tag{A.4}$$

while in the biaxial nematic phase, in which all nematogens are fully aligned with each other, the free energy is

$$\mathcal{F}_{\mathrm{N}}(\phi) = -\frac{AN}{4}(3+\Delta^2)\phi^2 + \frac{3BN}{2}\phi(1-\phi)f(B) + \frac{UN}{2}\phi^2, \tag{A.5}$$

where $f(B)$ takes the value -1 if $B > 0$ or $(1+\Delta)/2$ if $B < 0$. The function $f(B)$ takes different values because different relative orientations between the dipole axes and the first principal nematogen axes are energetically favored, depending on the sign of B. In order to minimize the free energy, for $B > 0$ ($B < 0$), all dipoles have their axes fully aligned with the first (third) principal nematogen axes.

In the interval $0 \leqslant \phi \leqslant 1$, the above equations imply $\mathcal{F}_{\mathrm{N}}(\phi) \leqslant \mathcal{F}_{\mathrm{ISO}}(\phi)$, with the equality valid only at $\phi = 0$. Therefore, the isotropic phase is stable for $\phi = 0$ only. However, $\mathcal{F}''_{\mathrm{N}}(\phi) < 0$ for

$$-\frac{2(2A-U)}{3(\Delta+1)} < B \leqslant 0 \quad \text{or} \quad 0 \leqslant B \leqslant \frac{2A-U}{3}, \tag{A.6}$$

so that, under these conditions, a $\phi = 0$ isotropic phase coexists with a $\phi = 1$ nematic phase. Otherwise, the nematic phase is stable for $0 < \phi \leqslant 1$.

Appendix B

z expansion

In the limit of high concentration of nematogens we have $\phi = 1 - \phi_{\rm NP}$, where $\phi_{\rm NP} \ll 1$ is the concentration of nanoparticles. In this limit, the chemical potential $\mu \to \infty$ and then the fugacity $z \equiv e^{-\beta\mu} \to 0$. If we introduce the scalar functions

$$a(\mathbf{Q}) = \sum_{\{\mathbf{\Theta}\}} e^{\beta B \mathbf{Q}:\mathbf{\Theta}}, \quad b(\mathbf{Q},\mathbf{D}) = \sum_{\{\mathbf{\Omega}\}} e^{\beta(A\mathbf{Q}+B\mathbf{D}):\mathbf{\Omega}}, \tag{B.1}$$

and the tensor functions

$$c(\mathbf{Q},\mathbf{D}) = \frac{1}{\beta A}\cdot\frac{\partial}{\partial \mathbf{Q}} b(\mathbf{Q},\mathbf{D}), \quad d(\mathbf{Q}) = \frac{1}{\beta B}\cdot\frac{\partial}{\partial \mathbf{Q}} a(\mathbf{Q}), \tag{B.2}$$

the mean-field equation related to the concentration can be written as

$$\phi_{\rm NP} = 1 - \left[1 + z\frac{a(\mathbf{Q})}{b(\mathbf{Q},\mathbf{D})} e^{\beta U(1-\phi_{\rm NP})}\right]^{-1} \approx z\frac{a(\mathbf{Q})}{b(\mathbf{Q},\mathbf{D})} e^{\beta U} \tag{B.3}$$

where the second-rank tensors associated with nematogen and dipolar nanoparticles are $\mathbf{Q} = \mathbf{Q}^{(0)} + \delta\mathbf{Q}$ and $\mathbf{D} = \delta\mathbf{D}$ respectively, and $\delta\mathbf{Q}$ and $\delta\mathbf{D}$ are small tensors[1]. The mean-field equations related to the order parameters of nematogens and of dipolar nanoparticles are

$$\mathbf{Q}^{(0)} + \delta\mathbf{Q} = \left[1 + z\frac{a(\mathbf{Q})}{b(\mathbf{Q},\mathbf{D})} e^{\beta U(1-\phi_{\rm NP})}\right]^{-1} \frac{c(\mathbf{Q},\mathbf{D})}{b(\mathbf{Q},\mathbf{D})} = (1-\phi_{\rm NP})\frac{c(\mathbf{Q},\mathbf{D})}{b(\mathbf{Q},\mathbf{D})}, \tag{B.4}$$

$$\delta\mathbf{D} = z e^{\beta U(1-\phi_{\rm NP})}\left[1 + z\frac{a(\mathbf{Q})}{b(\mathbf{Q},\mathbf{D})} e^{\beta U(1-\phi_{\rm NP})}\right]^{-1} \frac{d(\mathbf{Q})}{b(\mathbf{Q},\mathbf{D})} \approx z e^{\beta U}\frac{d(\mathbf{Q})}{b(\mathbf{Q},\mathbf{D})}, \tag{B.5}$$

Eq. (B.3) into Eq. (B.5) we obtain

$$\delta\mathbf{D} \approx \phi_{\rm NP}\frac{d(\mathbf{Q})}{a(\mathbf{Q})}. \tag{B.6}$$

[1]We say that a second-rank tensor $\mathbf{G}$ is small if its entries g_{ij} are small quantities for all pairs ij.

Notice that

$$\frac{a(\mathbf{Q})}{b(\mathbf{Q},\mathbf{D})} = \frac{a^{(0)}(\mathbf{Q}) + \delta a(\mathbf{Q})}{b^{(0)}(\mathbf{Q},\mathbf{D}) + \delta b(\mathbf{Q},\mathbf{D})} \approx \frac{a^{(0)}(\mathbf{Q})}{b^{(0)}(\mathbf{Q},\mathbf{D})}\left[1 + \frac{\delta a(\mathbf{Q})}{a^{(0)}(\mathbf{Q})} - \frac{\delta b(\mathbf{Q},\mathbf{D})}{b^{(0)}(\mathbf{Q}),\mathbf{D})}\right], \tag{B.7}$$

$$\frac{d(\mathbf{Q})}{a(\mathbf{Q})} = \frac{d^{(0)}(\mathbf{Q}) + \delta d(\mathbf{Q})}{a^{(0)}(\mathbf{Q}) + \delta a(\mathbf{Q})} \approx \left\{\mathbf{I} + \delta d(\mathbf{Q})[d^{(0)}(\mathbf{Q})]^{-1} - \frac{\delta a(\mathbf{Q})}{a^{(0)}(\mathbf{Q})}\right\}\frac{d^{(0)}(\mathbf{Q})}{a^{(0)}(\mathbf{Q})}, \tag{B.8}$$

and

$$\begin{aligned}\frac{c(\mathbf{Q},\mathbf{D})}{b(\mathbf{Q},\mathbf{D})} = \frac{c^{(0)}(\mathbf{Q},\mathbf{D}) + \delta c(\mathbf{Q},\mathbf{D})}{b^{(0)}(\mathbf{Q},\mathbf{D}) + \delta b(\mathbf{Q},\mathbf{D})} \approx \\ \left\{\mathbf{I} + \delta c(\mathbf{Q},\mathbf{D})[c^{(0)}(\mathbf{Q},\mathbf{D})]^{-1} - \frac{\delta b(\mathbf{Q},\mathbf{D})}{b^{(0)}(\mathbf{Q}),\mathbf{D})}\right\}\frac{c^{(0)}(\mathbf{Q},\mathbf{D})}{b^{(0)}(\mathbf{Q},\mathbf{D})},\end{aligned} \tag{B.9}$$

where the quantities

$$a^{(0)}(\mathbf{Q}) = \sum_{\{\mathbf{\Theta}\}} e^{\beta^{(0)} B\mathbf{Q}^{(0)}:\mathbf{\Theta}}, \quad b^{(0)}(\mathbf{Q},\mathbf{D}) = \sum_{\{\mathbf{\Omega}\}} e^{\beta^{(0)} A\mathbf{Q}^{(0)}:\mathbf{\Omega}}, \tag{B.10}$$

$$c^{(0)}(\mathbf{Q},\mathbf{D}) = \sum_{\{\mathbf{\Omega}\}} e^{\beta^{(0)} A\mathbf{Q}^{(0)}:\mathbf{\Omega}} \cdot \mathbf{\Omega}, \quad d^{(0)}(\mathbf{Q}) = \sum_{\{\mathbf{\Theta}\}} e^{\beta^{(0)} B\mathbf{Q}^{(0)}:\mathbf{\Theta}} \cdot \mathbf{\Theta}. \tag{B.11}$$

In the limit of pure nematogen host ($\phi = 1$) we have that $\mathbf{Q}^{(0)} \equiv \langle\mathbf{\Omega}\rangle_0 = c^{(0)}(\mathbf{Q},\mathbf{D})/b^{(0)}(\mathbf{Q},\mathbf{D})$, so that the MF equations take the form

$$\mathbf{Q}^{(0)} + \delta\mathbf{Q} = (1 - \phi_{\mathrm{NP}})\left\{\mathbf{I} + \delta c(\mathbf{Q},\mathbf{D})[c^{(0)}(\mathbf{Q},\mathbf{D})]^{-1} - \frac{\delta b(\mathbf{Q},\mathbf{D})}{b^{(0)}(\mathbf{Q}),\mathbf{D})}\right\}\mathbf{Q}^{(0)}. \tag{B.12}$$

Using $[c^{(0)}(\mathbf{Q},\mathbf{D})]^{-1} \cdot \mathbf{Q}^{(0)} = \mathbf{I}/b^{(0)}(\mathbf{Q}),\mathbf{D})$ and ignoring the terms of order $\phi_{NP}\delta c(\mathbf{Q},\mathbf{D})$ and $\phi_{NP}\delta b(\mathbf{Q},\mathbf{D})$ we obtain

$$\delta\mathbf{Q} = \frac{\delta c(\mathbf{Q},\mathbf{D})}{b^{(0)}(\mathbf{Q},\mathbf{D})} - \frac{\delta b(\mathbf{Q},\mathbf{D})}{b^{(0)}(\mathbf{Q},\mathbf{D})}\mathbf{Q}^{(0)} - \phi_{\mathrm{NP}}\mathbf{Q}^{(0)}. \tag{B.13}$$

Note that

$$\delta b(\mathbf{Q},\mathbf{D}) = \alpha_{\mathbf{Q}} : \delta\mathbf{Q} + \alpha_{\mathbf{D}} : \delta\mathbf{D} + \alpha_T\delta T \tag{B.14}$$

with

$$\alpha_{\mathbf{Q}} = \beta^{(0)} B\sum_{\{\mathbf{\Omega}\}} e^{\beta^{(0)} A\mathbf{Q}^{(0)}:\mathbf{\Omega}} \cdot \mathbf{\Omega} = \beta^{(0)} Ac^{(0)}(\mathbf{Q},\mathbf{D}), \tag{B.15}$$

$$\alpha_{\mathbf{D}} = \beta^{(0)} A\sum_{\{\mathbf{\Omega}\}} e^{\beta^{(0)} A\mathbf{Q}^{(0)}:\mathbf{\Omega}} \cdot \mathbf{\Omega} = \beta^{(0)} Bc^{(0)}(\mathbf{Q},\mathbf{D}), \tag{B.16}$$

$$\begin{aligned}\alpha_T &= -(\beta^{(0)})^2 A \sum_{\{\mathbf{\Omega}\}} e^{\beta^{(0)} A \mathbf{Q}^{(0)}:\mathbf{\Omega}} (\mathbf{Q}^{(0)} : \mathbf{\Omega}) \\ &= -(\beta^{(0)})^2 A \mathbf{Q}^{(0)} : \sum_{\{\mathbf{\Omega}\}} e^{\beta^{(0)} A \mathbf{Q}^{(0)}:\mathbf{\Omega}} \cdot \mathbf{\Omega} = -(\beta^{(0)})^2 A \mathbf{Q}^{(0)} : c^{(0)}(\mathbf{Q}, \mathbf{D}),\end{aligned} \tag{B.17}$$

Then we can insert Eqs. (B.15)-(B.17) into the second term on the right-hand side of Eq. (B.13) and obtain

$$\frac{\delta b(\mathbf{Q}, \mathbf{D})}{b(\mathbf{Q}, \mathbf{D})} = \beta^{(0)} A \mathbf{Q}^{(0)} : \delta\mathbf{Q} + \beta^{(0)} B \mathbf{Q}^{(0)} : \delta\mathbf{D} - (\beta^{(0)})^2 A \|\mathbf{Q}^{(0)}\|^2 \delta T. \tag{B.18}$$

On the other hand, we have

$$\delta c(\mathbf{Q}, \mathbf{D}) = \frac{1}{A}\delta\left[\frac{1}{\beta} \cdot \frac{\partial}{\partial \mathbf{Q}} b(\mathbf{Q}, \mathbf{D})\right] = \frac{1}{A}\delta T c^{(0)}(\mathbf{Q}, \mathbf{D}) + \frac{1}{A\beta^{(0)}}\delta\left[\frac{\partial}{\partial \mathbf{Q}} b(\mathbf{Q}, \mathbf{D})\right] \tag{B.19}$$

and

$$\delta\left[\frac{\partial}{\partial \mathbf{Q}} b(\mathbf{Q}, \mathbf{D})\right] = \mathbf{B}_\mathbf{Q} \cdot \delta\mathbf{Q} + \mathbf{B}_\mathbf{D} \cdot \delta\mathbf{D} + b_T \delta T \mathbf{I}, \tag{B.20}$$

with

$$\mathbf{B}_\mathbf{Q} = \beta^{(0)} A \sum_{\{\mathbf{\Omega}\}} e^{\beta^{(0)} A \mathbf{Q}^{(0)}:\mathbf{\Omega}} \cdot \mathbf{\Omega}^2, \tag{B.21}$$

$$\mathbf{B}_\mathbf{D} = \beta^{(0)} B \sum_{\{\mathbf{\Omega}\}} e^{\beta^{(0)} A \mathbf{Q}^{(0)}:\mathbf{\Omega}} \cdot \mathbf{\Omega}^2, \tag{B.22}$$

$$b_T = -(\beta^{(0)})^2 A \sum_{\{\mathbf{\Omega}\}} (\mathbf{Q}^{(0)} : \mathbf{\Omega}) e^{\beta^{(0)} A \mathbf{Q}^{(0)}:\mathbf{\Omega}} \cdot \mathbf{\Omega}. \tag{B.23}$$

Using Eq. (B.19) we obtain

$$\frac{\delta c(\mathbf{Q}, \mathbf{D})}{b(\mathbf{Q}, \mathbf{D})} = \frac{\delta T}{A}\mathbf{Q}^{(0)} + \langle \mathbf{\Omega}^2 \rangle_0 \delta\mathbf{Q} + \kappa \langle \mathbf{\Omega}^2 \rangle_0 \delta\mathbf{D} + \beta^{(0)} \delta T \langle (\mathbf{Q}^{(0)} : \mathbf{\Omega}) \cdot \mathbf{\Omega} \rangle_0, \tag{B.24}$$

$$\delta\mathbf{D} = \phi_{\mathrm{NP}} \frac{d^{(0)}(\mathbf{Q})}{a^{(0)}(\mathbf{Q})}. \tag{B.25}$$

B.1 The ISO-N_U first-order transition

By substituting the MF equations (4.21) and (4.22) into Eq.(4.20), the Landau-de Gennes free-energy functional can be written as

$$\psi(\mathbf{Q}, \mathbf{D}, \phi) = \frac{A}{2}\|\mathbf{Q}\|^2 + B\mathbf{Q} : \mathbf{D} - \frac{U}{2}\phi^2 - \frac{1}{\beta}\ln\left[a(\mathbf{Q}) + \frac{e^{-\beta U \phi}}{z} b(\mathbf{Q}, \mathbf{D})\right]. \tag{B.26}$$

In the limit $z \to 0$ we can write

$$\begin{aligned}\frac{1}{\beta}\ln\left[a(\mathbf{Q})+\frac{e^{-\beta U\phi}}{z}b(\mathbf{Q},\mathbf{D})\right] &= \frac{1}{\beta^{(0)}}\left[\frac{a^{(0)}(\mathbf{Q})}{b^{(0)}(\mathbf{Q},\mathbf{D})}e^{\beta^{(0)}U}z-\ln(z)\right]\\ &-U\phi+\frac{1}{\beta^{(0)}}\ln[b^{(0)}(\mathbf{Q},\mathbf{D})]+\delta\left\{\frac{1}{\beta}\ln[b(\mathbf{Q},\mathbf{D})]\right\}+\mathcal{O}(z).\end{aligned} \tag{B.27}$$

Notice that

$$\delta\left\{\frac{1}{\beta}\ln[b(\mathbf{Q},\mathbf{D})]\right\} = \ln[b^{(0)}(\mathbf{Q},\mathbf{D})]\delta T + T\delta\left\{\ln[b(\mathbf{Q},\mathbf{D})]\right\}, \tag{B.28}$$

with

$$\delta\left\{\ln[b(\mathbf{Q},\mathbf{D})]\right\} = \frac{\delta\{b(\mathbf{Q},\mathbf{D})\}}{b(\mathbf{Q},\mathbf{D})}. \tag{B.29}$$

Using $\delta\{\|\mathbf{Q}\|^2\} = 2\mathbf{Q}^{(0)} : \delta\mathbf{Q}$ and $\delta\{\mathbf{Q}:\mathbf{D}\} = \mathbf{Q}^{(0)} : \delta\mathbf{D}$ in Eq. (B.18) we obtain

$$\begin{aligned}\psi(\mathbf{Q},\mathbf{D},\phi) = \frac{A}{2}\|\mathbf{Q}^{(0)}\|^2 &+ A\mathbf{Q}^{(0)} : \delta\mathbf{Q} + B\mathbf{Q}^{(0)} : \delta\mathbf{D} - \frac{U}{2} - \frac{1}{\beta^{(0)}}\ln[b^{(0)}(\mathbf{Q},\mathbf{D})]\\ &- \ln[b^{(0)}(\mathbf{Q},\mathbf{D})]\delta T - A\mathbf{Q}^{(0)} : \delta\mathbf{Q} - B\mathbf{Q}^{(0)} : \delta\mathbf{D} + \beta^{(0)}A\|\mathbf{Q}^{(0)}\|^2\delta T\\ &- \frac{1}{\beta^{(0)}}\left[\frac{a^{(0)}(\mathbf{Q})}{b^{(0)}(\mathbf{Q},\mathbf{D})}e^{\beta^{(0)}U}z-\ln(z)\right]+\mathcal{O}(z),\end{aligned} \tag{B.30}$$

which is equivalent to

$$\begin{aligned}\psi(\mathbf{Q},\mathbf{D},\phi) = \frac{A}{2}\|\mathbf{Q}^{(0)}\|^2 &- \frac{U}{2} - \frac{1}{\beta^{(0)}}\ln[b^{(0)}(\mathbf{Q},\mathbf{D})]\\ &- \ln[b^{(0)}(\mathbf{Q},\mathbf{D})]\delta T + \beta^{(0)}A\|\mathbf{Q}^{(0)}\|^2\delta T\\ &- \frac{1}{\beta^{(0)}}\left[\frac{a^{(0)}(\mathbf{Q})}{b^{(0)}(\mathbf{Q},\mathbf{D})}e^{\beta^{(0)}U}z-\ln(z)\right]+\mathcal{O}(z).\end{aligned} \tag{B.31}$$

We know that for the ISO-N_U^+ first-order transition $\psi(\mathbf{0},\mathbf{0},\phi_\mathrm{I}) = \psi(\mathbf{Q}_\mathrm{U},\mathbf{D}_\mathrm{U},\phi_\mathrm{U})$, then for the ISO phase we have that $a^{(0)}(\mathbf{Q}) = a^{(0)}(\mathbf{0}) = 6$ and $b^{(0)}(\mathbf{Q},\mathbf{D}) = b^{(0)}(\mathbf{0},\mathbf{0}) = 6$, so that

$$\psi(\mathbf{0},\mathbf{0},\phi_\mathrm{I}) = -\frac{U}{2} - \frac{1}{\beta^{(0)}}\ln(6) - \ln(6)\delta T - \frac{1}{\beta^{(0)}}\left[e^{\beta^{(0)}U}z-\ln(z)\right]+\mathcal{O}(z). \tag{B.32}$$

A comparison between Eq. (B.32) and Eq. (B.31) yields

$$\begin{aligned}-\frac{1}{\beta^{(0)}}\ln(6) - \ln(6)\delta T - \frac{1}{\beta^{(0)}}\left[e^{\beta^{(0)}U}z\right] &= \frac{A}{2}\|\mathbf{Q}_\mathrm{U}^{(0)}\|^2 - \frac{1}{\beta^{(0)}}\ln[b^{(0)}(\mathbf{Q}_\mathrm{U},\mathbf{D}_\mathrm{U})]\\ -\ln[b^{(0)}(\mathbf{Q}_\mathrm{U},\mathbf{D}_\mathrm{U})]\delta T + \beta^{(0)}A\|\mathbf{Q}_\mathrm{U}^{(0)}\|^2\delta T &- \frac{1}{\beta^{(0)}}\left[\frac{a^{(0)}(\mathbf{Q})}{b^{(0)}(\mathbf{Q},\mathbf{D})}e^{\beta^{(0)}U}z\right],\end{aligned} \tag{B.33}$$

but for the pure nematic we have (see Sec. 2.3)

$$\frac{A}{2}\|\mathbf{Q}_\mathrm{U}^{(0)}\|^2 - \frac{1}{\beta^{(0)}}\ln[b^{(0)}(\mathbf{Q}_\mathrm{U},\mathbf{D}_\mathrm{U})] = -\frac{1}{\beta^{(0)}}\ln(6), \tag{B.34}$$

so that

$$-\beta^{(0)}\frac{A}{2}\|\mathbf{Q}_{\mathrm{U}}^{(0)}\|^2\delta T=\frac{e^{\beta^{(0)}U}}{\beta^{(0)}}\left[1-\frac{a^{(0)}(\mathbf{Q}_{\mathrm{U}})}{b^{(0)}(\mathbf{Q}_{\mathrm{U}},\mathbf{D}_{\mathrm{U}})}\right]z. \tag{B.35}$$

Using Eq. (B.3) we have $ze^{\beta^{(0)}U}=\phi_{\mathrm{NP}}b^{(0)}(\mathbf{Q}_{\mathrm{U}},\mathbf{D}_{\mathrm{U}})/a^{(0)}(\mathbf{Q}_{\mathrm{U}})$, then

$$\frac{dT_{\mathrm{I-U}}}{d\phi_{\mathrm{NP}}}=\frac{\delta T_{\mathrm{I-U}}}{\phi_{\mathrm{NP}}}=\frac{2}{A}\left[1-\frac{b^{(0)}(\mathbf{Q}_{\mathrm{U}},\mathbf{D}_{\mathrm{U}})}{a^{(0)}(\mathbf{Q}_{\mathrm{U}})}\right]\left(\frac{T_{\mathrm{I-U}}^{(0)}}{\|\mathbf{Q}_{\mathrm{U}}^{(0)}\|}\right)^2. \tag{B.36}$$

Notice that for $a^{(0)}(\mathbf{Q}_{\mathrm{U}})=b^{(0)}(\mathbf{Q}_{\mathrm{U}},\mathbf{D}_{\mathrm{U}})$ this derivative is zero.

B.2 The $\mathrm{N_U}$-$\mathrm{N_B}$ second-order transition

The perturbative calculations for the $\mathrm{N_U}$-$\mathrm{N_B}$ second-order transition are more complicated from an algebraic point of view. The conditions for the second-order transition are the MF equations supplemented by $d^2\psi/\,d\eta^2=0$. In this case we solve the problem computationally using Wolfram Mathematical, see [99].

Appendix C

Published articles

In this appendix we present the articles published throughout the doctorate.

Journal of Magnetism and Magnetic Materials 503 (2020) 166614

Contents lists available at ScienceDirect

Journal of Magnetism and Magnetic Materials

journal homepage: www.elsevier.com/locate/jmmm

Minimal model for the magnetic phase diagram of $CeTi_{1-x}Sc_xGe$, $GdFe_{1-x}Co_xSi$, and related materials

William Gabriel Carreras Oropesa[a,b], Sergio Encina[a], Pablo Pedrazzini[a,c], Víctor F. Correa[a,c], Julián G. Sereni[a,c], Verónica Vildosola[c,d], Daniel J. García[a,c], Pablo S. Cornaglia[a,c,*]

[a] Centro Atómico Bariloche and Instituto Balseiro, CNEA, 8400 Bariloche, Argentina
[b] Instituto de Física, Universidade de São Paulo, Caixa Postal 66318, 05314-970 São Paulo, SP, Brazil
[c] Consejo Nacional de Investigaciones Científicas y Técnicas (CONICET), Argentina
[d] Centro Atómico Constituyentes, CNEA, Buenos Aires, Argentina

ARTICLE INFO

Keywords:
Magnetism
RTX

ABSTRACT

We present a theoretical analysis of the magnetic phase diagram of $CeTi_{1-x}Sc_xGe$ and $GdFe_{1-x}Co_xSi$ as a function of the temperature and the Sc and Co concentration x, respectively. CeScGe and GdCoSi, as many other RTX (R = rare earth, T = transition metal, X = p-block element) compounds, present a tetragonal crystal structure where bilayers of R are separated by layers of T and X. While GdFeSi and $CeTi_{0.75}Sc_{0.25}Ge$ are ferromagnetic, CeScGe and GdCoSi order antiferromagnetically with the R 4f magnetic moments on the same bilayer aligned ferromagnetically and magnetic moments in nearest neighbouring bilayers aligned antiferromagnetically. The antiferromagnetic transition temperature T_N decreases with decreasing concentration x in both compounds and for low enough values of x the compounds show a ferromagnetic behavior. Based on these observations we construct a simplified model Hamiltonian that we solve numerically for the specific heat and the magnetization. We find a good qualitative agreement between the model and the experimental data. Our results show that the main magnetic effect of the Sc → Ti and Co → Fe substitution in these compounds is consistent with a change in the sign of the exchange coupling between magnetic moments in neighbouring bilayers. We expect a similar phenomenology for other magnetic RTX compounds with the same type of crystal structure.

1. Introduction

Several compounds of the RTX (R = rare earth, T = transition metal, X = p-block element) family crystalize in the CeFeSi-type or CeScSi-type structures [1]. These tetragonal structures can be described as stackings of R bilayers separated by layers of T and X. Neutron scattering experiments have found that the magnetically ordered state can generally be described as a stacking of ferromagnetic bilayers coupled ferromagnetically or antiferromagnetically between them, depending on the compound [2,3].

Among these compounds, CeScGe crystallizes in the CeScSi-type structure (I4/mmm, N 139, tI12) and has attracted considerable attention because of its surprisingly large (for Ce compounds) transition temperature $T_N \simeq 47$ K [4]. CeTiGe, however, crystalizes in the CeFeSi-type structure (P4/nmm, N 129, tP6) and does not present a magnetically ordered state at low temperatures. In recent works, Sereni et al. studied the evolution of the thermodynamic and transport properties of $CeTi_{1-x}Sc_xGe$ for samples with $0.25 \lesssim x \leqslant 1$ [4–6]. A continuous reduction of T_N with decreasing Sc content was observed for x down to ~ 0.5 and ferromagnetic behavior for lower values of x down to ~ 0.25 where there is a change in the crystal structure to CeFeSi-type with no magnetic order.

The interest in the RTX family has also been fueled by the large magnetocaloric effect (MCE) in the R = Gd compounds. The MCE is generally maximal at temperatures near to the Curie temperature. This makes it attractive for applications to be able to set the transition temperature near the target operation temperature, e.g. by tuning the magnetic exchange couplings. As in the R = Ce compounds, the transition metal T plays an essential role determining the magnetic properties: while GdFeSi and GdCoSi have the same CeFeSi-type structure,

* Corresponding author.
E-mail address: pablo.cornaglia@cab.cnea.gov.ar (P.S. Cornaglia).

https://doi.org/10.1016/j.jmmm.2020.166614
Received 10 December 2019; Received in revised form 5 February 2020; Accepted 11 February 2020
Available online 12 February 2020

GdFeSi is a ferromagnet with $T_C = 118$ K and GdCoSi is an antiferromagnet with $T_N = 220$ K[1]. The substitution of Co by Fe reduces T_N and leads to a ferromagnetic behavior in $GdFe_{1-x}Co_xSi$ for $x \lesssim 0.4$ [11]. Since other RTX compounds like the RFeSi with R = Nd,Sm,Tb also show a change in the nature of the magnetic ground state compared to RCoSi, and all have a CeFeSi-type structure, we would expect for those compounds a qualitatively similar phase diagram to the one observed for $GdFe_{1-x}Co_xSi$.

In this work we propose a model to describe the effect of the replacement of the transition metal T by an element in an adjacent column in the periodic table. Based on previous results we assume (see Ref. [12]) that this T replacement produces a local change in the sign of the inter-bilayer exchange coupling. More precisely, that the main effect in the magnetic interactions when a transition metal atom is replaced, is a change in the sign of the magnetic coupling between the two magnetic moments which are closer to the transition metal atom and in different bilayers.

2. Model

To analyze the main effects of the transition metal replacement we construct a simplified magnetic model that takes into account the layered structure of the CeScSi-type and CeFeSi-type crystals. The nature of the local magnetic moments can vary widely from one rare earth compound to the other. In CeScGe the transition temperature is high enough ($T_N \sim 47$ K) that the first excited crystal split doublet of the Ce 4*f* orbital cannot be ignored for a detailed description [13]. In the Gd compounds the crystal field is generally very small [14,15], and an isotropic spin 7/2 describes accurately the physics [16]. Note, however, that a simple de Gennes scaling is nicely followed by the transition temperature for several of the RTX compounds [2], which signals the possibility of a common description.

In constructing the simplified model we do not attempt to reproduce the precise spin arrangement nor the complexity of the rare earth magnetic moments for each compound, but to account for the main parameters driving the magnetic characteristics. We consider a cubic array of Ising magnetic moments with a first neighbour ferromagnetic coupling $J^{\parallel}$ inside the $\hat{x} - \hat{y}$ planes and a coupling $J^{\perp}$ for nearest neighbours in the $\hat{z}$ direction. For a description of the GdCoSi and CeScGe compounds, $J^{\perp}$ is chosen antiferromagnetic which leads to an A-type antiferromagnetic ground state as observed experimentally. To describe the ferromagnetic GdFeSi a ferromagnetic $J^{\perp}$ needs to be considered. In agreement with the double exchange mechanism for the magnetic couplings across the TX layer described in the Appendix, we assume that the most relevant effect of the replacement of a T atom in a TX layer is a change in the coupling between the nearest neighbour R 4*f* magnetic moments to the T ion across the TX layer. For the Co → Fe and the Sc → Ti replacements (which change the parity of the T 3*d* level occupancy) it can even be associated with a sign change in the interplane coupling $J^{\perp}$ (see also Ref. [12]). For a compound where a proportion x of the T atoms have been replaced, we expect an equal proportion of interplane couplings to change. We assume the replaced T atoms to be randomly distributed throughout the sample which leads to a uniform random distribution in the location of the modified couplings (see Fig. 1).

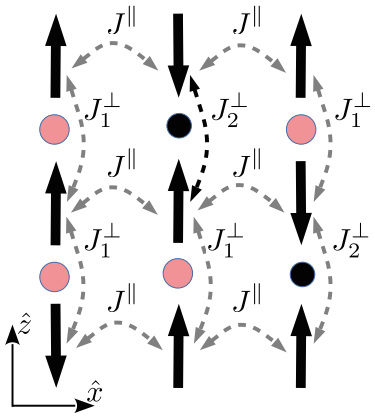

Fig. 1. Schematic representation of the model used in the simulations for a $0 < x < 1$ situation. The Ising spins form a cubic lattice with ferromagnetic nearest-neighbour couplings $J^{\parallel}$ in the $\hat{x} - \hat{y}$ plane. The magnetic couplings in the $\hat{z}$-axis ($J_1^{\perp}$ or $J_2^{\perp}$) depend on the type of transition metal atom (represented by filled circles) between the magnetic moments. The thick arrows represent the Gd^{3+} magnetic moments, and the thin dashed style arrows indicate the magnetic couplings.

2.1. Ising model

For a cubic lattice with magnetic moments at positions (i, j, k) with i,j, and k natural numbers in the range $[1, L]$ the model Hamiltonian reads

$$H = J^{\parallel} \sum_{\langle (i,j),(i',j') \rangle} \sum_{k} S(i,j,k)S(i',j',k) \tag{1}$$

$$+ \sum_{i} \sum_{j} \sum_{k} J^{\perp}(i,j,k)S(i,j,k)S(i,j,k+1) \tag{2}$$

$$+ \frac{\Delta}{2} \sum_{i,j,k} S(i,j,k) \tag{3}$$

where $S(i, j, k) = \{-1, 1\}$ represents an Ising spin, Δ is a Zeeman energy splitting due to an external magnetic field, $\langle , \rangle$ indicates nearest neighbors and $J^{\perp}(i, j, k)$ can take two different values: $J_1^{\perp}$ with probability x and $J_2^{\perp}$ with probability $1 - x$. For fixed $J^{\perp}(i, j, k)$ the model can be analyzed as a function of the temperature using Monte Carlo simulations.

3. Results

We first perform a mean field analysis averaging over disorder realizations of the couplings. This leads to a uniform $J_{eff}^{\perp}(x) = xJ_1^{\perp} + (1 - x)J_2^{\perp}$ coupling in the $\hat{z}$ direction. The effective interplane coupling $J_{eff}^{\perp}(x)$ changes sign for $x = x_c \equiv \frac{1}{1 - \frac{J_1^{\perp}}{J_2^{\perp}}}$, with $0 \leqslant x_c \leqslant 1$ provided $J_1^{\perp}$ and $J_2^{\perp}$ have opposite sign. At x_c the ground state changes from FM to A-type AFM. In what follows we take[2] $J_2^{\perp} = 4J^{\parallel} < 0$ and $J_1^{\perp} = -3J_2^{\perp}$ which leads to $x_c = 0.25$.

The magnetic transition temperature in the mean field approximation is given by

$$T_{crit}(x) = \frac{2}{k_B}[2|J^{\parallel}| + |J_{eff}^{\perp}(x)|] \tag{4}$$

which for $x \leqslant x_c$ is a Curie temperature to a ferromagnetic ground state and for $x > x_c$ corresponds to a Néel temperature.

To describe the effect of disorder in a more realistic way we perform

[1] There have been several conflicting reports in the literature on the nature of the magnetic order of GdCoSi and its transition temperature. Some authors report a ferromagnetic order with a low magnetization (roughly an order of magnitude lower than the expected for the Gd^{3+} ion) which could be non-collinear [7–9] while density functional theory calculations and magnetocaloric measurements indicate an antiferromagnetic order[10–12].

[2] We obtained qualitatively similar results for different values of the ratio between $J_2^{\perp}$ and $J^{\parallel}$.

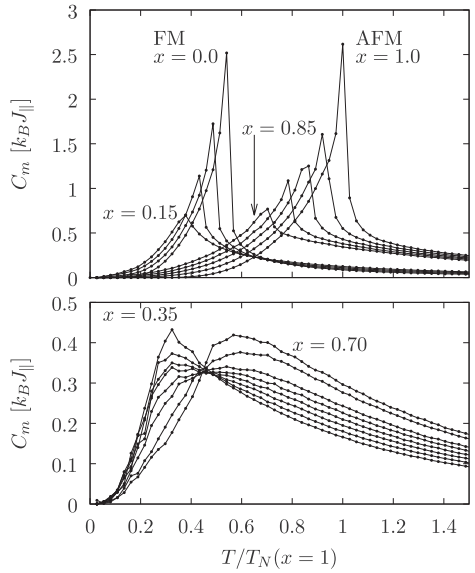

Fig. 2. Specific heat C_m of the disordered Ising model as a function of the temperature for different proportions x of modified couplings in the $\hat{z}$ direction. Upper panel: For two sets of values of x: {0, 0.05, 0.1, 0.15} and {0.85, 0.9, 0.95, 1} a sharp peak can be observed in C_m which can be associated with a ferromagnetic and an antiferromagnetic transition, respectively. Lower panel: for $0.35 \lesssim x \lesssim 0.7$ the peak in C_m is rounded and no clear signature of a sharp transition is observed.

Monte Carlo simulations as a function of the temperature and external magnetic field for systems with sizes up to $N = 32 \times 32 \times 32$ magnetic moments in a cubic lattice with periodic boundary conditions, and average the results over three realizations of the disorder [3]. The results for the specific heat as a function of the temperature and different values of the concentration $x \sim 1$ and to $x \sim 0$ are presented in the upper panel of Fig. 2. The sharp peak in C_m at the transition temperature obtained for $x = 1$ and $x = 0$ shifts to lower temperatures as x departs from stoichiometry. A broadening of the peaks is also observed, in agreement with the reported specific heat experimental data for $CeTi_{1-x}Sc_xGe$ and $x \sim 1$. In the intermediate regime of values of x, a broad peak is observed in the specific heat (see lower panel of Fig. 2).

We also calculate the magnetization as a function of the temperature using a field cooling (FC) and a zero-field cooling protocol. The results of the Monte Carlo simulation and the experimental results for $CeTi_{1-x}Sc_xSi$ are presented in Fig. 3. The numerical calculations and the experiment present a similar qualitative behavior for all values of x, except for $x = 0.4$ where the FC experimental results present a peak in the magnetization. The observed reduction of the magnetization at low temperatures may be due to a dipolar interaction between ferromagnetic clusters which is not included in the model. For values of $x \sim 0$ ($x \sim 1$), the peak in the specific heat is concomitant with an increase (decrease) in the magnetization which signals a ferromagnetic (antiferromagnetic) transition. In the intermediate range of values of x, although there is a clear change in the behavior of the magnetization at temperatures where a peak in the specific heat is observed, it is not apparent from these quantities what the nature of the magnetic ground state is and whether there is a sharp transition.

Finally, we use the peaks in the specific heat C_m and in C_m/T as criteria to determine the transition (or crossover) temperature T_{crit}. In the intermediate regime of values of x, the two criteria do not coincide and we use this difference to estimate the "error" in the determination

[3] The specific heat and the magnetization show little dependence on the disorder realization for the system sizes considered. We performed numerical calculations from $N = 8 \times 8 \times 8$ up to $N = 32 \times 32 \times 32$ lattice sites to rule out finite size effects in the reported quantities.

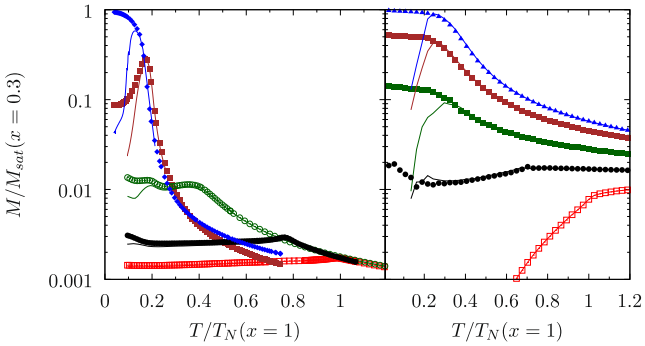

Fig. 3. Magnetization as a function of the temperature for the transition metal concentration values $x = \{0.3, 0.4, 0.6, 0.8, 1.0\}$ from top to bottom at low temperatures using a field cooling (symbols) and zero field cooling (solid lines) schemes. Left panel: experimental data for $CeTi_{1-x}Sc_xSi$ and $H = 100$Oe. Right panel: Monte Carlo data for a Zeeman splitting $\Delta = 0.02J^{\parallel}$.

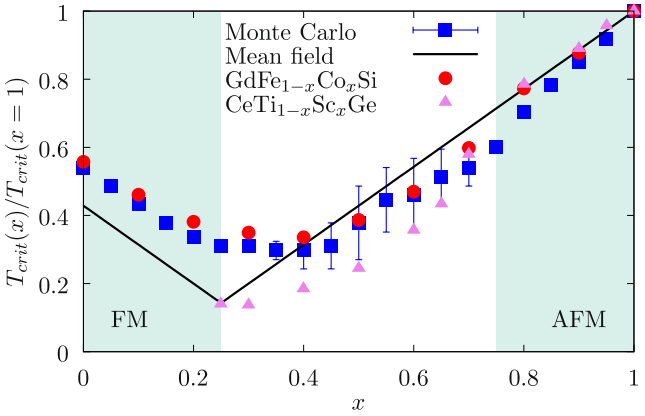

Fig. 4. Experimental transition temperatures for $CeTi_{1-x}Sc_xGe$ (from Ref. [11]) and $GdFe_{1-x}Co_xSi$ (from Ref. [4]) as a function of x. The solid line is the mean-field transition temperature for disorder-averaged couplings, to an FM ground state for $0 \leqslant x \leqslant 0.25$ and an AFM ground state for $0.25 < x \leqslant 1$. The Monte Carlo values are the average of the temperatures for the maximum values of C_m and C_m/T, the error bars are estimated from the difference of the values obtained by the two criteria.

of T_{crit}. The resulting T_{crit}, which is the average of the value obtained using the two criteria, is presented in Fig. 4 as a function of x, together with the experimental values for $CeTi_{1-x}Sc_xGe$ and $GdFe_{1-x}Co_xSi$. In spite of the simplicity of the model, a good agreement is obtained between the Monte Carlo and the experimental results. The mean field results (using an effective disorder-averaged interplane coupling) deviate significantly from the numerical results in the range of intermediate values of x, but provide a qualitative correct picture with a linear behavior in x, for $x \sim 0$ and $x \sim 1$.

4. Conclusions

We present a minimal model to describe the magnetic properties of $CeTi_{1-x}Sc_xGe$ and $GdFe_{1-x}Co_xSi$, which provides a qualitative description of the magnetic specific heat and the magnetization as a function of the temperature. Using Monte Carlo simulations we obtain a magnetic phase diagram which shows a good agreement with those observed experimentally. The proposed model captures the most relevant effect of the Sc → Ti and Co → Fe replacements in these materials, which is a change in the sign of the exchange coupling between R 4f magnetic moments in neighbouring bilayers. Although a material specific model is probably needed to describe the detailed physics of other compounds with the same type of crystal structure but different rare earth ions with their corresponding multiplet structures, we expect the present model

to serve as a base to include these type of features. This analysis could also be extended to analyze other RTX materials with hexagonal crystal structure [17].

The similarity of the current model to the Anderson model (see e.g. Ref. [18]), which presents a spin glass phase, suggests that this type of physics could be expected for $CeTi_{1-x}Sc_xGe$ and $GdFe_{1-x}Co_xSi$ and $x \sim 0.5$.

This work opens the possibility to analyze the properties of the low temperature state in the intermediate range of values of the transition metal concentration x using a simple model.

CRediT authorship contribution statement

William Gabriel Carreras Oropesa: Software, Investigation. **Sergio Encina:** Investigation. **Pablo Pedrazzini:** Conceptualization, Writing - review & editing. **Víctor F. Correa:** Conceptualization, Writing - review & editing. **Julián G. Sereni:** Conceptualization, Writing - review & editing. **Verónica Vildosola:** Investigation, Writing - review & editing. **Daniel J. García:** Conceptualization, Writing - review & editing. **Pablo S. Cornaglia:** Conceptualization, Writing - original draft, Writing - review & editing.

Declaration of Competing Interest

The authors declare that they have no known competing financial interests or personal relationships that could have appeared to influence the work reported in this paper.

Acknowledgement

We acknowledge insightful discussions with A. Kolton and financial support from PICT 2016–0204.

Appendix A. Simplified model for the interplane R-R exchange coupling

We present here a simplified local model for the exchange coupling of nearest-neighbouring R magnetic moments in different bilayers. As discussed for R = Gd compounds in Ref. [12], the most relevant effect in the magnetic couplings when the transition metal is replaced (Ti → Sc or Fe → Co), is a significant modification, that can even lead to a sign change, of the exchange couplings between the magnetic moments of nearest-neighbour Gd^{3+} ions in different bilayers. A DFT analysis indicates an important overlap of the T 3d, Gd 5d and X p wavefunctions, which leads to an indirect magnetic exchange mechanism via delocalized 5d rare earth electrons [8] (see also Ref. [16]). Additionally, the R 4f electrons couple with the R 5d conduction electrons with a magnetic exchange coupling J_{fd} and the almost empty R 5d orbitals have a small hybridization with the partially occupied transition metal d orbitals.

With these ingredients we construct a simplified model to describe qualitatively the behavior of interlayer exchange coupling. We consider two R ions (1 & 2) separated by a transition metal ion and consider a single level with energy $E_{\alpha,\sigma}$ for the each of the R 5d orbitals $\alpha = 1, 2$. The R 5d orbitals are hybridized with a single effective level with energy E_d that models the transition metal d orbitals.

While the Si or Ge p orbitals contribute to the conduction electron bands, and to the R-R exchange couplings, we focus here in the role of the TM and do not include the p orbitals in the model. The energy of an electron in the 5d orbital depends on the relative orientation of its spin σ w.r.t. the R 4f magnetic moment: $E_{d\sigma} = E_d \pm \sigma\delta$, where the - (+) sign corresponds to parallel (antiparallel) configurations. The R-R coupling is estimated as $K_\perp \sim (E_{AP} - E_P)/2J^2$, where E_P is the electronic energy when the 4f spins of the two R are parallel, and E_{AP} the corresponding to the antiparallel configuration. The model Hamiltonian is

$$H_{eff} = \sum_{\alpha,\sigma} E_{\alpha\sigma} c^\dagger_{\alpha,\sigma} c_{\alpha,\sigma} + E_d \sum_\sigma d^\dagger_\sigma d_\sigma + t \sum_{\alpha,\sigma} (c^\dagger_{\alpha,\sigma} d_\sigma + h.\,c.\,) \tag{5}$$

where $c^\dagger_{\alpha,\sigma}$ ($d^\dagger_\sigma$) creates an electron with spin projection $\sigma = \pm$ along the z-axis on the R 5d (T 3d) effective orbital. The model can be readily diagonalized and for a single electron occupancy to lowest order in t and δ it gives an R-R coupling:

$$K_\perp \sim \frac{8\delta^2 t^4}{J^2(E_c - E_d)^5} < 0 \tag{6}$$

where we have assumed that t is a small parameter. This corresponds to a ferromagnetic interaction.

For an occupancy of two electrons there is a qualitative change. The two electrons are antiparallel to satisfy Pauli exclusion principle and the minimal energy for the conduction band electrons is obtained when the R 4f magnetic moments are antiparallel. This leads to an effective antiferromagnetic exchange coupling between the R magnetic moments in adjacent layers,

$$K_\perp \sim \frac{|\delta| t^2}{J^2(E_c - E_d)^2} > 0. \tag{7}$$

References

[1] S. Gupta, K. Suresh, Review on magnetic and related properties of RTX compounds, J. Alloy. Compd. 618 (2015) 562–606.

[2] R. Welter, A. Vernire, G. Venturini, B. Malaman, High rare earth sublattice ordering temperatures in new CeFeSi-type RTiGe (R = La-Nd, Sm) compounds, J. Alloy. Compd. 283 (1) (1999) 54–58, https://doi.org/10.1016/S0925-8388(98)00904-9 URL: http://www.sciencedirect.com/science/article/pii/S0925838898009049.

[3] R. Welter, G. Venturini, B. Malaman, Magnetic properties of RFeSi (R = La-Sm, Gd-Dy) from susceptibility measurements and neutron diffraction studies, J. Alloy. Compd. 189 (1) (1992) 49–58, https://doi.org/10.1016/0925-8388(92)90045-B URL: http://www.sciencedirect.com/science/article/pii/092583889290045B.

[4] J.G. Sereni, P. Pedrazzini, M. Gómez Berisso, A. Chacoma, S. Encina, T. Gruner, N. Caroca-Canales, C. Geibel, Local character of the highest antiferromagnetic temperature of Ce systems in Sc-rich $CeTi_{1-x}Sc_xGe$, Phys. Rev. B 91 174408 (2015), https://doi.org/10.1103/PhysRevB.91.174408.

[5] J. Sereni, P. Pedrazzini, M.G. Berisso, A. Chacoma, S. Encina, T. Gruner, N. Caroca-Canales, C. Geibel, Exploring high temperature magnetic order in $CeTi_{1-x}Sc_xGe$, J. Phys.: Conf.Series 592 (2015) 012005 IOP Publishing.

[6] S. Encina, P. Pedrazzini, J. Sereni, C. Geibel, Low temperature thermopower and magnetoresistance of Sc-rich $CeSc_{1-x}Ti_xGe$, Physica B 536 (2018) 133–136.

[7] H. Kido, M. Shimada, M. Koizumi, Synthesis and magnetic properties of GdCoSi and GdMnSi, Physica Status Solidi. A, Appl. Res. 70 (1) (1982) K23–K26.

[8] S. Nikitin, T. Ivanova, I. Makhro, Y.A. Tskhadadze, Itinerant magnetism of GdxLa1-xMSi (M = Fe, Co) compounds, J. Magn. Magn. Mater. 157 (1996) 387–388.

[9] W. Qin, F. Yang, J. Wang, N. Tang, J. Hu, X. Zhong, F. De Boer, Structure and magnetic properties of $GdMn_{1-x}CoxSi$ compounds, J. Alloys Compounds 265 (1–2) (1998) 26–28.

[10] R. Welter, G. Venturini, E. Ressouche, B. Malaman, Magnetic properties of RCoSi (R≡ La-Sm, Gd, Tb) compounds from susceptibility measurements and neutron diffraction studies, J. Alloys Compounds 210 (1–2) (1994) 279–286.

[11] P. Wlodarczyk, L. Hawelek, P. Zackiewicz, T.R. Roy, A. Chrobak, M. Kaminska, A. Kolano-Burian, J. Szade, Characterization of magnetocaloric effect, magnetic ordering and electronic structure in the $GdFe_{1-x}Co_xSi$ intermetallic compounds, Mater. Chem. Phys. 162 (2015) 273–278, https://doi.org/10.1016/j.matchemphys.2015.05.067 URL: http://www.sciencedirect.com/science/article/pii/S0254058415301280.

[12] D.J. García, V. Vildosola, P.S. Cornaglia, Magnetic couplings and magnetocaloric effect in the Gd(T = Sc, Ti)(X = Si, Ge) compounds, (unpublished), 2019.
[13] C. Ritter, A. Provino, P. Manfrinetti, A. Pathak, Tetragonal to triclinic structural transition in the prototypical CeScSi induced by a two-step magnetic ordering: a temperature-dependent neutron diffraction study of CeScSi, CeScGe and LaScSi, J. Phys.: Condens. Matter 29 (4) (2016) 045802 .
[14] D. Betancourth, V. Correa, D. García, Evidence of a low energy anisotropy in $GdCoIn_5$, J. Low Temp. Phys. 179 (1–2) (2015) 90–93.
[15] D. Betancourth, V. Correa, J.I. Facio, J. Fernández, V. Vildosola, R. Lora-Serrano, J. Cadogan, A. Aligia, P.S. Cornaglia, D. García, Magnetostriction reveals orthorhombic distortion in tetragonal gd compounds, Phys. Rev. B 99 (13) (2019) 134406 .
[16] J.I. Facio, D. Betancourth, P. Pedrazzini, V.F. Correa, V. Vildosola, D.J. García, P.S. Cornaglia, Why the Co-based 115 compounds are different: the case study of $GdMIn_5$ (M = Co, Rh, Ir), Phys. Rev. B 91 (2015) 014409, https://doi.org/10.1103/PhysRevB.91.014409.
[17] S. Gupta, K. Suresh, A. Das, A. Nigam, A. Hoser, Effects of antiferro-ferromagnetic phase coexistence and spin fluctuations on the magnetic and related properties of NdCuSi, APL Mater. 3 (6) (2015) 066102 .
[18] H. Nishimori, Statistical Physics of Spin Glasses and Information Processing: An Introduction, Clarendon Press, 2001.

Thermodynamics of collisional models for Brownian particles: General properties and efficiency

Angel L. L. Stable, C. E. Fernández Noa, William G. C. Oropesa, and C. E. Fiore
Universidade de São Paulo, Instituto de Física, Rua do Matão, 1371, 05508-090 São Paulo, São Paulo, Brasil

(Received 1 May 2020; accepted 2 September 2020; published 2 October 2020)

We introduce the idea of *collisional models* for Brownian particles, in which a particle is sequentially placed in contact with distinct thermal environments and external forces. Thermodynamic properties are exactly obtained, irrespective of the number of reservoirs involved. In the presence of external forces, the entropy production presents a bilinear form in which Onsager coefficients are exactly calculated. Analysis of Brownian engines based on sequential thermal switchings is proposed and considerations about their efficiencies are investigated, taking into account distinct external forces protocols. Our results shed light to an alternative route for obtaining efficient thermal engines based on finite times Brownian machines.

DOI: 10.1103/PhysRevResearch.2.043016

I. INTRODUCTION

Stochastic thermodynamics has proposed a general and unified scheme for addressing central issues in thermodynamics [1–5]. It includes not only an extension of concepts from equilibrium to nonequilibrium systems but also it deals with the existence of new definitions and bounds [6–9], general considerations about the efficiency of engines at finite time operations [1–3], and others aspects. In all cases, the concept of entropy production [1,4,10] plays a central role, being a quantity continuously produced in nonequilibrium steady states (NESS), whose main properties and features have been extensively studied in the last years, including its usage for typifying phase transitions [11–14].

Basically, a NESS can be generated under two fundamental ways: From fixed thermodynamic forces [15,16] or from time-periodic variation of external parameters [17–20]. In this contribution, we address a different kind of periodic driving, suitable for the description of engineered reservoirs, at which a system interacts sequentially and repeatedly with distinct environments [21–23]. Commonly referred as *collisional models*, they have been inspired by the assumption that in many cases (e.g., the original Brownian motion) a particle collides only with few molecules of the environment and then the subsequent collision will occur with another fraction of uncorrelated molecules. Collisional models have been viewed as more realistic frameworks in certain cases, encompassing not only particles interacting with a small fraction of the environment but also those presenting distinct drivings over each member of system [24–27] or even species yielding a weak coupling with the reservoir. More recently, they have been (broadly) extended for quantum systems for mimicking the environment, represented by a weak interaction between the system and a sequential collection of uncorrelated particles [28–30].

With the above in mind, we introduce the concept of repeated interactions for Brownian particles. More specifically, a particle under the influence of a given external force is placed in contact with a reservoir during the time interval and afterwards it is replaced by an entirely different (and independent) set of interactions. Exact expressions for thermodynamic properties are derived and the entropy production presents a bilinear form, in which Onsager coefficients are obtained as function of period. Considerations about the efficiency are undertaken and a suited regime for the system operating as an efficient thermal machine is investigated.

The present study sheds light for fresh perspectives in nonequilibrium thermodynamics, including the possibility of experimental buildings of heat engines based on Brownian dynamics [31–36] with sequential reservoirs. Also, they provide us the extension and validation of recent bounds between currents and entropy production, the so called thermodynamic uncertainty relations (TURs) [8,9,37–41], which has aroused a recent and great interest.

This paper is organized as follows: Secs. II and III present the model description and its exact thermodynamic properties. In Sec. IV we extend analysis for external forces and considerations about efficiency are performed in Sec. V. Conclusions and perspectives are drawn in Sec. VI.

II. MODEL AND FOKKER-PLANCK EQUATION

We are dealing with a Brownian particle with mass m sequentially placed in contact with N different thermal reservoirs. Each contact has a duration of τ/N and occurs during the intervals $\tau_{i-1} \leqslant t < \tau_i$, where $\tau_i = i\tau/N$ for $i = 1, .., N$, in which the particle evolves in time according to the following Langevin equation:

$$m\frac{dv_i}{dt} = -\alpha_i v_i + F_i(t) + B_i(t), \tag{1}$$

where quantities v_i, α_i, and $F_i(t)$ denote the particle velocity, the viscous constant and external force, respectively. From

now on, we shall express them in terms of reduced quantities: $\gamma_i = \alpha_i/m$ and $f_i(t) = F_i(t)/m$. The stochastic force $\zeta_i(t) = B_i(t)/m$ accounts for the interaction between particle and the ith environment and satisfies the properties

$$\langle \zeta_i(t) \rangle = 0 \tag{2}$$

and

$$\langle \zeta_i(t)\zeta_{i'}(t') \rangle = 2\gamma_i T_i \delta_{ii'} \delta(t - t'), \tag{3}$$

respectively, where T_i is the bath temperature. Let $P_i(v, t)$ be the velocity probability distribution at time t, its time evolution is described by the Fokker-Planck (FP) equation [3,16,42]

$$\frac{\partial P_i}{\partial t} = -\frac{\partial J_i}{\partial v} - f_i(t)\frac{\partial P_i}{\partial v}, \tag{4}$$

where J_i is given by

$$J_i = -\gamma_i v P_i - \frac{\gamma_i k_B T_i}{m}\frac{\partial P_i}{\partial v}. \tag{5}$$

It is worth mentioning that above equations are formally identical to description of the overdamped harmonic oscillator subject to the harmonic force $f_h = -\bar{k}x$ just by replacing $x \to v$, $\bar{k}/\alpha \to \gamma_i$, $1/\alpha \to \gamma_i/m$.

From the FP equation and by performing appropriate partial integrations together boundary conditions in which both $P_i(v, t)$ and $J_i(v, t)$ vanish at extremities, the time variation of the energy system $U_i = \langle E_i \rangle$ in contact with the ith reservoir is given by

$$\frac{dU_i}{dt} = -\frac{m}{2}\int v^2 \left[\frac{\partial J_i}{\partial v} + f_i(t)\frac{\partial P_i}{\partial v}\right] dv. \tag{6}$$

The right side of Eq. (6) can be rewritten as $dU_i/dt = -(\dot{W}_i + \dot{Q}_i)$, where $\dot{W}_i$ and $\dot{Q}_i$ denote the work per unity of time and heat flux from the system to the environment (thermal bath) given by

$$\dot{W}_i = -m\langle v_i \rangle f_i(t) \quad \text{and} \quad \dot{Q}_i = \gamma_i\big(m\langle v_i^2 \rangle - k_B T_i\big), \tag{7}$$

respectively. In the absence of external forces $\dot{W}_i = 0$ and all heat flux comes from/goes to the thermal bath.

By assuming the system entropy S is given by $S_i(t) = -k_B \int P_i(v, t) \ln[P_i(v, t)] dv$ and from the expression for J_i, one finds that its time derivative is given by

$$\frac{dS_i}{dt} = -k_B \int \left(\frac{J_i}{P_i}\right)\left(\frac{\partial P_i}{\partial v}\right) dv. \tag{8}$$

As for the mean energy, above expression can be rewritten in the following form:

$$\frac{dS_i}{dt} = \frac{m}{\gamma_i T_i}\left(\int \frac{J_i^2}{P_i} dv + \gamma_i \int v J_i dv\right). \tag{9}$$

Equation (9) can be interpreted according to the following form: $dS_i/dt = \Pi_i(t) - \Phi_i(t)$ [16,42], where the former term corresponds to the entropy production rate $\Pi_i(t)$ and it is strictly positive (as expected). The second term is the the flux of entropy and can also be rewritten more conveniently as

$$\Phi_i(t) = \frac{\dot{Q}_i}{T_i} = \gamma_i\left(\frac{m}{T_i}\langle v_i^2 \rangle - k_B\right). \tag{10}$$

If external forces are null and the particle is placed in contact to a single reservoir, then the probability distribution approaches for large times the Gibbs (equilibrium) distribution $P_i^{\text{eq}}(v) = e^{-E/k_B T_i}/Z$, with $E = mv^2/2$ its kinetic energy and Z the partition function. In such case, $\langle v_i^2 \rangle = k_B T_i/m$ and therefore $\Pi_{\text{eq}} = \Phi_{\text{eq}} = 0$ (as expected). Conversely, it will evolve to a nonequilibrium steady state (NESS) when placed in contact with sequential and distinct reservoirs, in which heat is dissipated and the entropy is produced and hence $\Pi_{\text{NESS}} = \Phi_{\text{NESS}} > 0$.

III. EXACT SOLUTION FOR ARBITRARY SET OF SEQUENTIAL RESERVOIRS

From now on, quantities will be expressed in terms of the "reduced temperature" $\Gamma_i = 2\gamma_i k_B T_i/m$ and $k_B = 1$. Since we are dealing with a linear force on the velocity, the NESS will also be characterized by a Gaussian probability distribution $P_i(v, t) = e^{-(v-\langle v_i \rangle)^2/2b_i(t)}/\sqrt{2\pi b_i(t)}$ in which both mean $\langle v_i \rangle(t)$ and the variance $b_i(t) \equiv \langle v_i^2 \rangle(t) - \langle v_i \rangle^2(t)$ will be in general time-dependent. Their expressions can be calculated from Eqs. (4) and (5) and read

$$\frac{d}{dt}\langle v_i \rangle = -\gamma_i \langle v_i \rangle + f_i(t) \tag{11}$$

and

$$\frac{d}{dt} b_i(t) = -2\gamma_i b_i(t) + \Gamma_i, \tag{12}$$

respectively, where appropriate partial integrations were performed. Their solutions are given by the following expressions:

$$\langle v_i \rangle(t) = e^{-\gamma_i(t-\tau_{i-1})}\left[v'_{i-1} + \int_{\tau_{i-1}}^{t} e^{\gamma_i(t'-\tau_{i-1})} f_i(t') dt'\right] \tag{13}$$

and

$$b_i(t) = A_{i-1} e^{-2\gamma_i(t-\tau_{i-1})} + \frac{\Gamma_i}{2\gamma_i}, \tag{14}$$

respectively, where quantities $v'_{i-1} \equiv \langle v_i \rangle(\tau_{i-1})$ and A_i's are evaluated by taking into account the set of continuity relations for the averages and variances, $\langle v_i \rangle(\tau_i) = \langle v_{i+1} \rangle(\tau_i)$ and $b_i(\tau_i) = b_{i+1}(\tau_i)$ (for all $i = 1, ..., N$), respectively. Since the system returns to the initial state after a complete period, $\langle v_1 \rangle(0) = \langle v_N \rangle(\tau)$ and $b_1(0) = b_N(\tau)$, all coefficients can be solely calculated in terms of model parameters, temperature reservoirs and the period. Also, the above conditions state that the probability at each point returns to the same value after every period.

For simplicity, from now on we shall assume the same viscous constant $\gamma_i = \gamma$ for all i's. In the absence of external forces, all v'_i's vanish and the entropy production only depends on the coefficients A_i's and Γ_i's. Hence, the coefficient A_i becomes

$$A_{i+1} = xA_i + \frac{1}{2\gamma}(\Gamma_i - \Gamma_{i+1}), \tag{15}$$

where $x = e^{-2\gamma\tau/N}$ and all of them can be found from a linear recurrence relation

$$A_i = x^{i-1}A_1 + \frac{1}{2\gamma}\sum_{l=2}^{i} x^{i-l}(\Gamma_{l-1} - \Gamma_l), \tag{16}$$

for $i = 2, ...N$. As the particle returns to the initial configuration after a complete period, A_N then reads

$$A_N = x^{-1}A_1 + \frac{x^{-1}}{2\gamma}(\Gamma_1 - \Gamma_N). \tag{17}$$

By equaling Eqs. (16) and (17) for $i = N$, all coefficients A_i's can be finally calculated and are given by

$$A_1 = \frac{1}{2\gamma}\frac{x^N}{1-x^N}\sum_{l=1}^{N} x^{-l}(\Gamma_l - \Gamma_{l+1}) \tag{18}$$

and

$$A_i = \frac{1}{2\gamma}\frac{x^{i-1}}{1-x^N}\left[\sum_{l=1}^{i-1} x^{-l}(\Gamma_l - \Gamma_{l+1}) + \sum_{l=i}^{N} x^{N-l}(\Gamma_l - \Gamma_{l+1})\right], \tag{19}$$

for $i = 1$ and $i > 1$, respectively. As we are focusing on the steady-state time-periodic regime, thermodynamic quantities can be averaged over one period τ. The mean entropy production $\overline{\Pi}$ then reads

$$\overline{\Pi} = \frac{1}{\tau}\sum_{i=1}^{N}\int_{\tau_{i-1}}^{\tau_i}\Phi_i(t)\,dt = \frac{(1-e^{-2\gamma\tau/N})}{2\gamma\tau}\sum_{i=1}^{N}\frac{A_i}{\Gamma_i}. \tag{20}$$

From Eqs. (18) and (19), it follows that

$$\sum_{i=1}^{N}\frac{A_i}{\Gamma_i} = \frac{x^N}{1-x^N}\sum_{i,l=1}^{N} x^{-l}\left(\frac{\Gamma_{i+l-1} - \Gamma_{i+l}}{\Gamma_i}\right), \tag{21}$$

and we arrive at an expression for $\overline{\Pi}$ solely dependent on the model parameters

$$\overline{\Pi} = -\frac{N}{2\gamma\tau}\left(\frac{1-x}{x}\right) + \frac{1}{2\gamma\tau}\cdot\frac{x^{N-1}(1-x)^2}{1-x^N}\sum_{i,l=1}^{N} x^{-l}\frac{\Gamma_{i+l}}{\Gamma_i}. \tag{22}$$

To show that $\overline{\Pi} \geqslant 0$, we resort to the inequality $\sum_{i=1}^{N}\Gamma_{i+l}/\Gamma_i \geqslant N\sqrt[N]{\prod_{i=1}^{N}\Gamma_{i+l}/\Gamma_i}$ for showing that $\sum_{i=1}^{N}\Gamma_{i+l}/\Gamma_i \geqslant N$, and hence Eq. (22) fulfills the condition

$$\overline{\Pi} \geqslant -\frac{N}{2\gamma\tau}\left(\frac{1-x}{x}\right) + \frac{N}{2\gamma\tau}\left(\frac{1-x}{x}\right) = 0, \tag{23}$$

in consistency with the second law of thermodynamics.

As an concrete example, we derive explicit results for the two sequential reservoirs case. From Eqs. (13) and (14), coefficients A_1 and A_2 reduce to the following expressions:

$$A_1 = \frac{\Gamma_2 - \Gamma_1}{2\gamma}\left(\frac{1-e^{-\gamma\tau}}{1-e^{-2\gamma\tau}}\right) = \frac{\Gamma_2 - \Gamma_1}{2\gamma}\left(\frac{1}{1+e^{\gamma\tau}}\right), \tag{24}$$

where $A_2 = -A_1$ and hence

$$\Phi_1(t) = \gamma\left(\frac{\Gamma_2 - \Gamma_1}{\Gamma_1}\right)\left(\frac{1}{1+e^{2\gamma\tau}}\right)e^{-2\gamma t}, \tag{25}$$

for $0 \leqslant t < \tau/2$ and

$$\Phi_2(t) = \gamma\left(\frac{\Gamma_1 - \Gamma_2}{\Gamma_2}\right)\left(\frac{1}{1+e^{2\gamma\tau}}\right)e^{-2\gamma(t-\frac{\tau}{2})}, \tag{26}$$

$\tau/2 \leqslant t < \tau$, respectively, whose average entropy production reads

$$\overline{\Pi} = \left[\frac{\Gamma_1\Gamma_2}{2\tau}\tanh\left(\frac{\gamma\tau}{2}\right)\right]\left(\frac{1}{\Gamma_1} - \frac{1}{\Gamma_2}\right)^2. \tag{27}$$

Note that $\overline{\Pi} \geqslant 0$ and it vanishes when $\Gamma_1 = \Gamma_2$. In the limit of slow ($\tau \gg 1$) and fast ($\tau << 1$) oscillations, $\overline{\Pi}$ approaches to the following asymptotic expressions:

$$\overline{\Pi} \approx \frac{\Gamma_1\Gamma_2}{2\tau}\left(\frac{1}{\Gamma_1} - \frac{1}{\Gamma_2}\right)^2 \quad \text{and} \quad \frac{\Gamma_1\Gamma_2\gamma}{4}\left(\frac{1}{\Gamma_1} - \frac{1}{\Gamma_2}\right)^2, \tag{28}$$

respectively, and such a latter expression is independent on the period.

Equation (27) can be conveniently written down as a flux-times-force expression, where the thermodynamic force attempts to the difference of temperatures of reservoirs. Given that the viscous coefficient is the same for all switchings, the thermodynamic force can be more conveniently expressed in terms of difference of Γ_i's. More specifically, we have that $\overline{\Pi} = \mathcal{J}_T f_T$, where $f_T = (1/\Gamma_2 - 1/\Gamma_1)$ and $\mathcal{J}_T$ can also be rewritten as $\mathcal{J}_T = L_{TT} f_T$, where L_{TT} is the Onsager coefficient given by

$$L_{TT} = \frac{\Gamma_1\Gamma_2}{2\tau}\tanh\left(\frac{\gamma\tau}{2}\right). \tag{29}$$

Note that $L_{TT} \geqslant 0$ (as expected).

Figure 1 depicts the average entropy production $\overline{\Pi}$ versus τ for distinct values of Γ_2 and $\Gamma_1 = 1, \gamma = 1$. Note that it is monotonically increasing with f_T and reproduces above asymptotic limits.

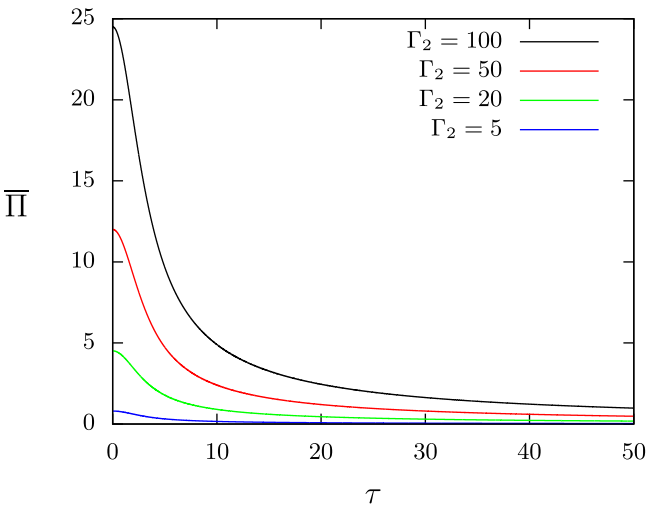

FIG. 1. Mean entropy production $\overline{\Pi}$ versus τ for distinct temperature sets $\Gamma_1 = 1$ and Γ_2 and $\gamma = 1$.

IV. FORCED BROWNIAN AND SEQUENTIAL RESERVOIRS

Next, we extend analysis for the case of a Brownian particle in contact with sequential reservoirs and external forces. We shall focus on the two stage case and two simplest external forces protocols: constant and linear drivings. More specifically, the former is given by

$$f_i(t) = \begin{cases} f_1; & 0 \leqslant t < \tau/2, \\ f_2; & \tau/2 \leqslant t < \tau, \end{cases} \tag{30}$$

where f_1 and f_2 denote their strengths in the first and second half period, respectively, whereas the latter case accounts for forces evolving linearly over the time according to the slopes:

$$\frac{f_i(t)}{\gamma} = \begin{cases} \lambda_1 t; & 0 \leqslant t < \tau/2, \\ \lambda_2(\frac{\tau}{2} - t), & \tau/2 \leqslant t < \tau, \end{cases} \tag{31}$$

with λ_1 and λ_2 being their amplitudes. It has been considered in Ref. [41] to compare the performance of distinct bounds between currents and the entropy production (TURs). In the presence of external forces, FP equation has the same form of Eq. (14), but now $\langle v_i\rangle(t)$'s will be different from zero.

A. Constant external forces

From Eq. (13), the expressions for $\langle v_i\rangle(t)$'s are given by

$$\langle v\rangle = \begin{cases} \langle v_1\rangle(t) = \frac{e^{\gamma\tau/2}}{\gamma}\left(\frac{f_2-f_1}{1+e^{\gamma\tau/2}}\right)e^{-\gamma t} + \frac{f_1}{\gamma}, \\ \langle v_2\rangle(t) = \frac{e^{\gamma\tau/2}}{\gamma}\left(\frac{f_1-f_2}{1+e^{\gamma\tau/2}}\right)e^{-\gamma(t-\tau/2)} + \frac{f_2}{\gamma}, \end{cases} \tag{32}$$

for the first or second half of each period, respectively.

The average work and heat per time are given by $\overline{\dot{W}} = \overline{\dot{W}}_1 + \overline{\dot{W}}_2$ and $\overline{\dot{Q}} = \overline{\dot{Q}}_1 + \overline{\dot{Q}}_2$, respectively, and straightforwardly evaluated from Eq. (7), whose $\overline{\dot{W}}_1$ and $\overline{\dot{Q}}_1$ read

$$\begin{aligned} \overline{\dot{W}}_1 &= -\frac{mf_1}{\tau}\int_0^{\tau/2}\langle v_1\rangle\, dt \\ &= \frac{mf_1}{\gamma^2\tau}(f_1 - f_2)\tanh\left(\frac{\gamma\tau}{4}\right) - \frac{mf_1^2}{2\gamma} \end{aligned} \tag{33}$$

and

$$\begin{aligned} \overline{\dot{Q}}_1 = \frac{m}{4\gamma\tau}(\Gamma_2 - \Gamma_1)\tanh\left(\frac{\gamma\tau}{2}\right) + \frac{m}{2\gamma^2\tau}(f_1+f_2)^2 \\ \times \tanh\left(\frac{\gamma\tau}{4}\right) + \frac{2mf_1^2}{\gamma^2\tau}\left[\frac{\gamma\tau}{4} - \tanh\left(\frac{\gamma\tau}{4}\right)\right], \end{aligned} \tag{34}$$

respectively. Analogous expressions are obtained for $\overline{\dot{W}}_2$ and $\overline{\dot{Q}}_2$ just by exchanging $1 \leftrightarrow 2$. Note that $\overline{\dot{Q}}_1 + \overline{\dot{Q}}_2 + \overline{\dot{W}}_1 + \overline{\dot{W}}_2 = 0$, in consistency with the first law of thermodynamics.

In the same way as before, the steady entropy production per period $\overline{\Pi}$ can be evaluated from Eq. (10) (by taking $k_B = 1$) and reads

$$\overline{\Pi} = \frac{2\gamma}{m}\left(\frac{\overline{\dot{Q}}_1}{\Gamma_1} + \frac{\overline{\dot{Q}}_2}{\Gamma_2}\right), \tag{35}$$

and we arrive at the following expression

$$\begin{aligned} \overline{\Pi} = \frac{1}{2\tau}\frac{(\Gamma_2-\Gamma_1)^2}{\Gamma_1\Gamma_2}\tanh\left(\frac{\gamma\tau}{2}\right) + \frac{1}{\gamma\tau}\left(\frac{1}{\Gamma_1}+\frac{1}{\Gamma_2}\right) \\ \times \tanh\left(\frac{\gamma\tau}{4}\right)(f_1+f_2)^2 \\ + \left(\frac{f_1^2}{\Gamma_1} + \frac{f_2^2}{\Gamma_2}\right)\left[1 - \frac{4}{\gamma\tau}\tanh\left(\frac{\gamma\tau}{4}\right)\right]. \end{aligned} \tag{36}$$

Since $\gamma\tau \geqslant 0$ and $1 - \tanh(x)/x \geqslant 0$, it follows that $\overline{\Pi} \geqslant 0$. Note that $\overline{\Pi}$ reduces to Eq. (27) as $f_1 = f_2 = 0$.

Bilinear form and Onsager coefficients

The shape of Eq. (36) is similar to the linear irreversible thermodynamics [18,19,43], in which the entropy production is written down as a sum of flux-times-force expression. This similarity provides to reinterpret Eq. (36) in the following form:

$$\overline{\Pi} = \mathcal{J}_T f_T + \mathcal{J}_1 f_1 + \mathcal{J}_2 f_2, \tag{37}$$

where forces $f_T = (1/\Gamma_1 - 1/\Gamma_2)$ and $f_{1(2)}$ have associated fluxes $\mathcal{J}_T$, $\mathcal{J}_{1(2)}$ given by $\mathcal{J}_T = L_{TT} f_T$ [identical to Eq. (29)],

$$\mathcal{J}_1 = L_{11} f_1 + L_{12} f_2 \quad \text{and} \quad \mathcal{J}_2 = L_{21} f_1 + L_{22} f_2, \tag{38}$$

respectively, where L_{11}, L_{12}, L_{21}, and L_{22} denote their Onsager coefficients given by

$$L_{11} = \frac{1}{\Gamma_1}\left[1 - \frac{3}{\gamma\tau}\tanh\left(\frac{\gamma\tau}{4}\right)\right] + \frac{1}{\gamma\tau\Gamma_2}\tanh\left(\frac{\gamma\tau}{4}\right) \tag{39}$$

and

$$L_{12} = L_{21} = \frac{1}{\gamma\tau}\left(\frac{1}{\Gamma_1}+\frac{1}{\Gamma_2}\right)\tanh\left(\frac{\gamma\tau}{4}\right), \tag{40}$$

respectively. Coefficients L_{22} and L_{21} have the same shape of L_{11} and L_{12} by replacing $1 \leftrightarrow 2$, respectively. Besides, L_{11} and $L_{22} \geqslant 0$ (as should be) and they satisfy the inequality $4L_{11}L_{22} - (L_{12}+L_{21})^2 \geqslant 0$, in consistency with the positivity of the entropy production.

B. Time-dependent external forces

By repeating the previous calculations for linear external forces the mean velocities $\langle v_i\rangle(t)$'s are given by

$$\langle v\rangle = \begin{cases} \langle v_1\rangle(t) = \frac{1}{\gamma}\{\lambda_1(\gamma t - 1) \\ \quad + e^{-\gamma t}[\lambda_1 + (\lambda_2 e^{\frac{\gamma\tau}{2}} - \lambda_1)\alpha(\gamma,\tau)]\}, \\ \langle v_2\rangle(t) = \frac{1}{\gamma}\{-\lambda_2\left[\gamma\left(t - \frac{\tau}{2}\right) - 1\right] \\ \quad + e^{-\gamma(t-\frac{\tau}{2})}[(\lambda_1 e^{\frac{\gamma\tau}{2}} - \lambda_2)\alpha(\gamma,\tau) - \lambda_2]\}, \end{cases} \tag{41}$$

where

$$\alpha(\gamma,\tau) = \frac{2 - e^{\frac{\gamma\tau}{2}}(\gamma\tau - 2)}{2(e^{\gamma\tau} - 1)},$$

respectively. Although more complex than the previous case, the mean work and heat per time are evaluated analogously

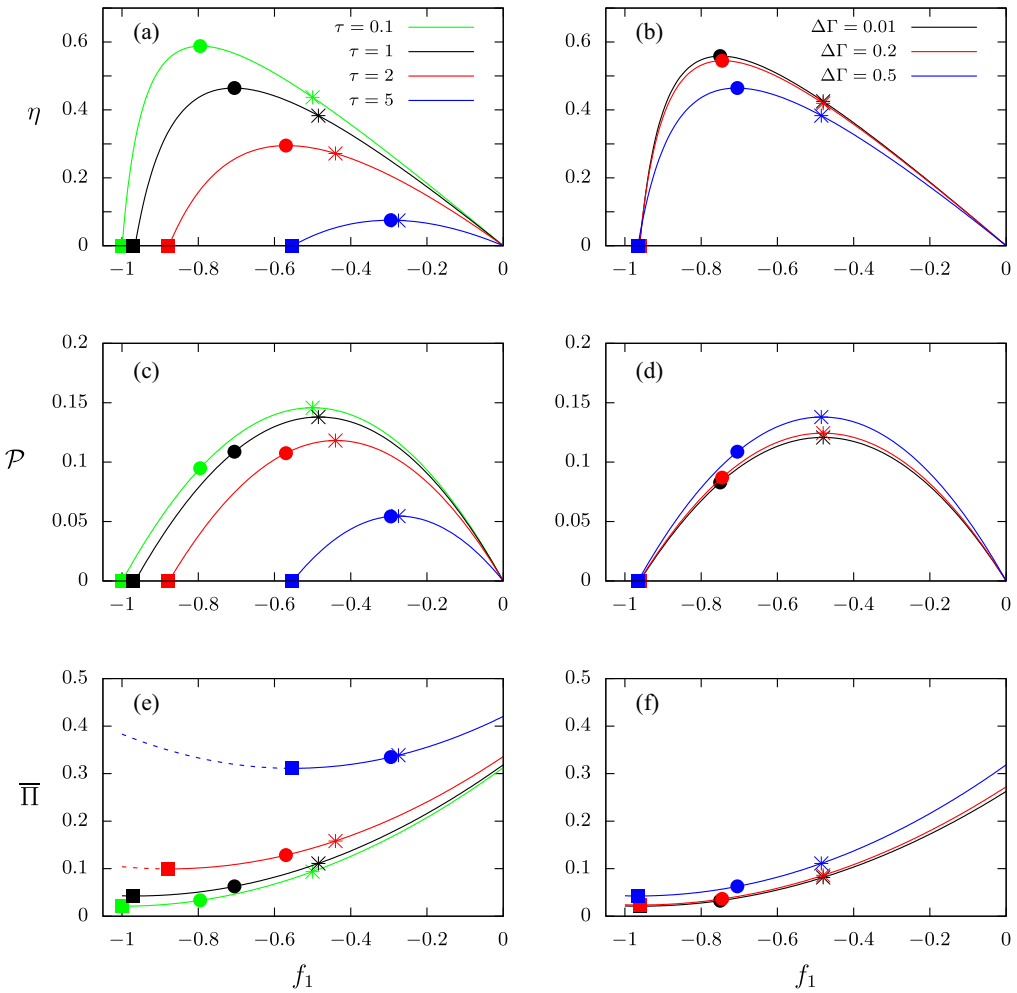

FIG. 2. Panels (a) and (b) depict the efficiency η versus f_1 for distinct periods τ (for $\Delta\Gamma = 0.5$) and $\Delta\Gamma$'s (for $\tau = 1$), respectively. In both cases, $\Gamma_1 = 2$ and $f_2 = 1$. Symbols •, "stars," and "squares" denote the f_{1mE}, f_{1mP}, and f_{1mS}, respectively. Panels (c) and (d) show the corresponding power $\mathcal{P}$, whereas (e) and (f) the average entropy production rate $\overline{\Pi}$. Dashed lines show the values of f_1 the system can not be operated as a thermal machine.

from expressions for $\langle v_i\rangle(t)$'s and $b_i(t)$'s, whose values averaged over a cycle read

$$\overline{\dot{W}} = -\overline{\dot{Q}} = -\mathcal{A}\{e^{\gamma\tau}\varphi_+(\gamma,\tau,\xi) + 12e^{\frac{\gamma\tau}{2}}(\gamma^2\tau^2\xi - 4) + \varphi_-(\gamma,\tau,\xi)\}, \quad (42)$$

where parameters $\mathcal{A}$, ξ and $\varphi_\pm(\gamma,\tau,\xi)$ read

$$\mathcal{A} = \frac{m(\lambda_1+\lambda_2)^2}{24\gamma^2\tau(e^{\gamma\tau}-1)}, \quad \xi = \frac{\lambda_1\lambda_2}{(\lambda_1+\lambda_2)^2},$$

and

$$\varphi_\pm(\gamma,\tau,\xi) = \gamma^2\tau^2(2\xi-1)(3\pm\gamma\tau) + 24(1\pm\gamma\tau\xi),$$

respectively.

Bilinear form and Onsager coefficients

As in the previous case, the entropy production has also the shape of Eqs. (37) and (38) given by $\overline{\Pi} = \mathcal{J}_T f_T + \mathcal{J}_1\lambda_1 + \mathcal{J}_2\lambda_2$, being L_{TT} the same to Eq. (29), whereas the other Onsager coefficients read

$$L_{11} = \frac{1}{\Gamma_1}\left[\frac{\gamma^2\tau^2}{12} - \frac{\gamma\tau(2e^{\gamma\tau}+1)}{4(e^{\gamma\tau}-1)} + \frac{1}{1+e^{-\frac{\gamma\tau}{2}}} + \frac{1}{\gamma\tau}\tanh\left(\frac{\gamma\tau}{4}\right)\right] + \frac{1}{\Gamma_2}\frac{\left[e^{\frac{\gamma\tau}{2}}(\gamma\tau-2)+2\right]^2}{4\gamma\tau(e^{\gamma\tau}-1)}, \quad (43)$$

and

$$L_{12} = \frac{\left(2e^{\frac{\gamma\tau}{2}} - \gamma\tau - 2\right)\left(2e^{\frac{\gamma\tau}{2}} - \gamma\tau e^{\frac{\gamma\tau}{2}} - 2\right)(\Gamma_1+\Gamma_2)}{4\gamma\tau(e^{\gamma\tau}-1)\Gamma_1\Gamma_2}, \quad (44)$$

respectively. Coefficients L_{22} and L_{21} are again identical to L_{11} and L_{12} by exchanging $1 \leftrightarrow 2$. Also, it is straightforward to verify that L_{11} and L_{22} are strictly positive and $4L_{11}L_{22} - (L_{12}+L_{21})^2 \geqslant 0$.

V. EFFICIENCY

Distinct works have tackled the conditions in which periodically driven systems can operate as thermal machines

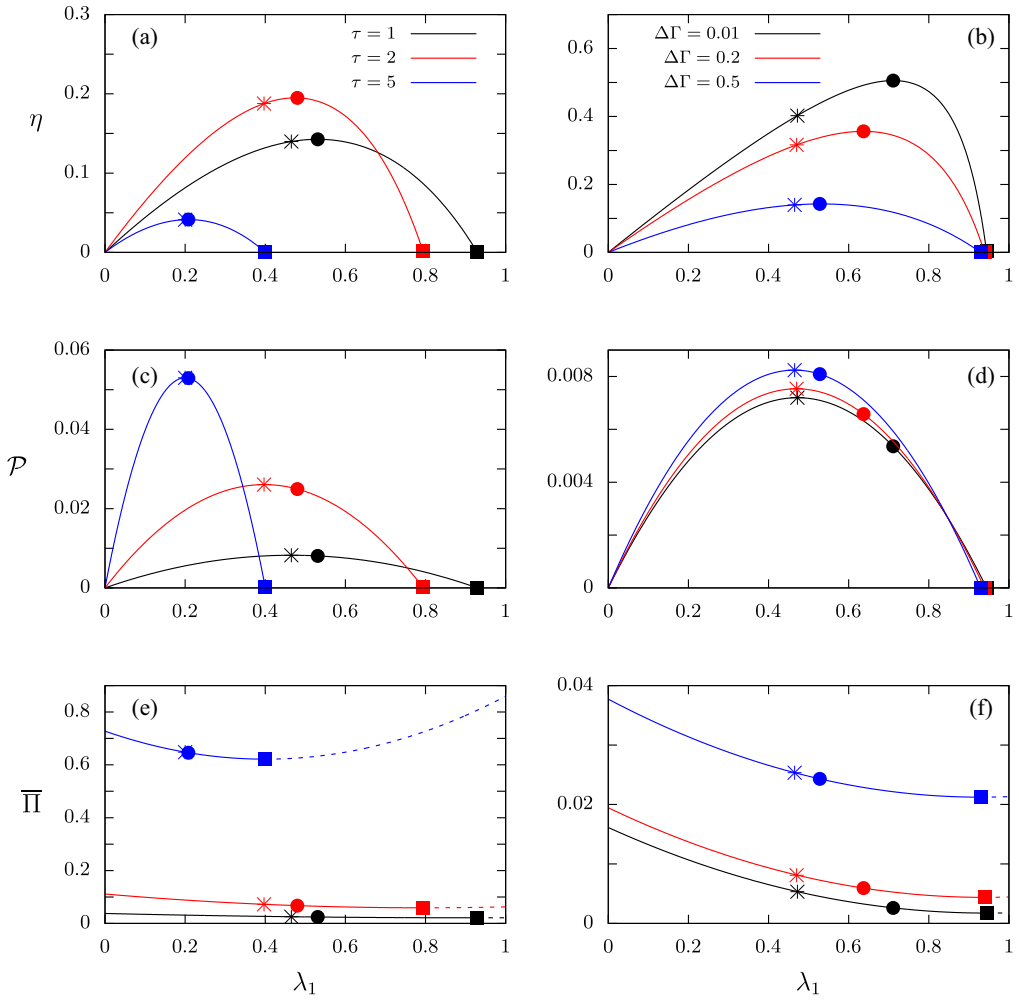

FIG. 3. Panels (a) and (b) depict the efficiency η versus λ_1 for distinct periods τ (for $\Delta\Gamma = 0.5$) and $\Delta\Gamma$'s (for $\tau = 1$), respectively. In both cases, $\Gamma_1 = 2$ and $\lambda_2 = 1$. Symbols •, "stars," and "squares" denote the λ_{1mE}, λ_{1mP}, and λ_{1mS}, respectively. Panels (c) and (d) show the corresponding power $\mathcal{P}$, whereas (e) and (f) the average entropy production rate $\overline{\Pi}$. Dashed lines show the values of λ_1 the system can not be operated as a thermal machine.

[18,43–47]. The conversion of a given type of energy into another one requires the existence of a generic force X_1 operating against its flux $J_1X_1 \leqslant 0$ counterbalancing with driving forces X_2 and X_T in which $J_2X_2 + J_TX_T \geqslant 0$. A measure of efficiency η is given by

$$\eta = -\frac{\mathcal{J}_1X_1}{\mathcal{J}_2X_2 + \mathcal{J}_TX_T} = -\frac{L_{11}X_1^2 + L_{12}X_1X_2}{L_{21}X_2X_1 + L_{22}X_2^2 + L_{TT}X_T^2}, \tag{45}$$

where in such case $X_T = f_T$ and we have taken into account Eq. (37) for relating fluxes and Onsager coefficients. Taking into account that the best machine aims at maximizing the efficiency and minimizing the dissipation $\overline{\Pi}$ for a given power output $\mathcal{P} = -\Gamma_1\mathcal{J}_1X_1$, it is important to analyze the role of three load forces, X_{1mP}, X_{1mE}, and X_{1mS}, in which the power output and efficiency are maximum and the dissipation is minimum, respectively [18]. Their values can be obtained straightforwardly from expressions for $\mathcal{P}$ and Eq. (45), respectively. Due to the present symmetric relation between Onsager coefficients $L_{12} = L_{21}$ (in both cases), they acquire simpler forms and read $2X_{1mP} = -L_{12}X_2/L_{11}$,

$$X_{1mE} = \frac{1}{L_{11}L_{12}X_2}\big[-L_{11}\big(L_{22}X_2^2 + L_{TT}X_T^2\big) + A(X_2, X_T)\big], \tag{46}$$

with $A(X_2, X_T)$ being given by

$$A(X_2, X_T) = \sqrt{L_{11}\big(L_{22}X_2^2 + L_{TT}X_T^2\big)} \times \sqrt{\big[L_{11}\big(L_{22}X_2^2 + L_{TT}X_T^2\big) - L_{12}^2X_2^2\big]}, \tag{47}$$

and $X_{1mS} = -L_{12}X_2/L_{11} = 2X_{1mP}$, respectively, where $X_i = f_i$ and λ_i for the constant and linear drivings, respectively. The efficiencies at minimum dissipation, maximum power and its maximum value become $\eta_{mS} = 0$,

$$\eta_{mP} = \frac{L_{12}^2X_2^2}{2\big(2L_{22}L_{11} - L_{12}^2\big)X_2^2 + 4L_{TT}L_{11}X_{TT}^2}, \tag{48}$$

and

$$\eta_{mE} = \frac{1}{L_{12}^2 X_2^2}\left[2L_{11}\left(L_{22}X_2^2 + L_{TT}X_T^2\right) - L_{12}^2X_2^2 - 2A(X_2, X_T)\right], \tag{49}$$

respectively, and finally their associated power outputs read $\mathcal{P}_{mS} = 0$, $\mathcal{P}_{mP} = \Gamma_1 L_{12}^2 X_2^2/4L_{11}$, and

$$\begin{aligned}\mathcal{P}_{mE} = &\frac{\Gamma_1}{L_{11}L_{12}^2X_2^2} \\ &\times \left[L_{11}\left(L_{22}X_2^2 + L_{TT}X_T^2\right) - A(X_2, X_T) - L_{12}^2X_2^2\right] \\ &\times \left[L_{11}\left(L_{22}X_2^2 + L_{TT}X_T^2\right) - A(X_2, X_T)\right],\end{aligned} \tag{50}$$

respectively. We pause to make a few comments: First, above expressions extend the findings from Ref. [18] for a couple of driving forces. Second, both efficiency and power vanish when $X_1 = X_{1mS}$ and $X_1 = 0$ and are strictly positive between those limits. Hence the physical regime in which the system can operate as an engine is bounded by the lowest entropy production $\overline{\Pi}_{mS} = L_{TT}X_T^2 + (L_{22} - L_{12}^2/L_{11})X_2^2$ and the value $\overline{\Pi}^* = L_{TT}X_T^2 + L_{22}X_2^2$. Third, despite the long expressions for Eqs. (49) and (50), powers $\mathcal{P}_{mP}, \mathcal{P}_{mE}$ and efficiencies η_{mP}, η_{mE} are linked through a couple of simple expressions (in similarity with Refs. [18,46]):

$$\eta_{mP} = \frac{\eta_{mE}}{1 + \eta_{mE}^2} \quad \text{and} \quad \frac{\mathcal{P}_{mE}}{\mathcal{P}_{mP}} = 1 - \eta_{mE}^2, \tag{51}$$

and they imply that $0 \leqslant \eta_{mP} < \eta_{mE}$ (with $0 \leqslant \eta_{mE} \leqslant 1$ and $0 \leqslant \eta_{mP} \leqslant 1/2$) and $0 \leqslant \mathcal{P}_{mE} \leqslant \mathcal{P}_{mP}$. Fourth and last, the achievement of most efficient machine $\eta_{mE} = 1$ implies that the system has to be operated at null power $\mathcal{P}_{mE} = 0$ and hence the projection of a machine operating for finite $\mathcal{P}_{mP}/\mathcal{P}_{mE}$ will imply at a loss of its efficiency.

Our purpose here aims at not only extending relevant concepts about efficiency for Brownian particles in contact with sequential reservoirs, but also to show that a desired compromise between maximum power and maximum efficiency can be achieved by adjusting conveniently the model parameters (such as the period and the driving). From expressions for Onsager coefficients, aforementioned quantities are evaluated, as depicted in Figs. 2 and 3 for distinct periods τ and temperature differences $\Delta\Gamma$'s for constant and linear drivings, respectively. In both cases, quantities follow theoretical predictions and exhibit similar portraits, in which efficiencies and power outputs present maximum values at $f_{1mE}(\lambda_{1mE})$ and $f_{1mP}(\lambda_{1mP})$, respectively. The loss of efficiency from the maximum η_{mE} as $f_1(\lambda_1)$ goes up (down) is signed by the increase of dissipation (as expected) until vanishing when $\overline{\Pi} = \overline{\Pi}^*$. For the constant driving, absolute values of forces and efficiencies increase as the period τ [see, e.g., panels (a)] and/or temperature differences [see, e.g., panels (b)] are lowered. In such a case, $\Gamma_1 \approx \Gamma_2 = \Gamma$, $\Delta\Gamma = \Gamma_1 - \Gamma_2 << 1$ and the thermodynamic force f_T approaches to $f_T \approx \Delta\Gamma/\Gamma^2$. Onsager coefficients become simpler in the limit of fast switchings, $\tau \to 0$ and L_{11}, L_{22}, L_{12} approach to $(\Gamma_1 + \Gamma_2)/(4\Gamma_1\Gamma_2)$. Some remarkable quantities then approach to the asymptotic values $f_{1mS} \to -f_2 = 2f_{1mP}$ and

$$\eta_{mP} \to \frac{f_2^2(\Gamma_1 + \Gamma_2)}{2\left[f_2^2(\Gamma_1 + \Gamma_2) + 2\Delta\Gamma^2\right]}, \tag{52}$$

respectively. For $\Gamma_1 \approx \Gamma_2$, $\eta_{mP} \to 1/2$, $\eta_{mE} \to 1$, and $\mathcal{P}_{mP}$ reads $\mathcal{P}_{mP} \to f_2^2/8$ and thereby the limit of an ideal machine is achieved for low periods and equal temperatures. Similar features are verified for the linear driving, including increasing efficiencies as both τ and $\Delta\Gamma$ decreases. However, they are marked by a reentrant behavior for $\tau << 1$ and $\Delta\Gamma \neq 0$ [see, e.g., Figs. 3(a) and 5]. It moves for lower τ's as $\Delta\Gamma$ goes down and the limit of ideal machine, $\eta_{mP} \to 1/2$ and $\eta_{mE} \to 1$, is also recovered when both $\tau \to 0$ for $\Delta\Gamma \to 0$.

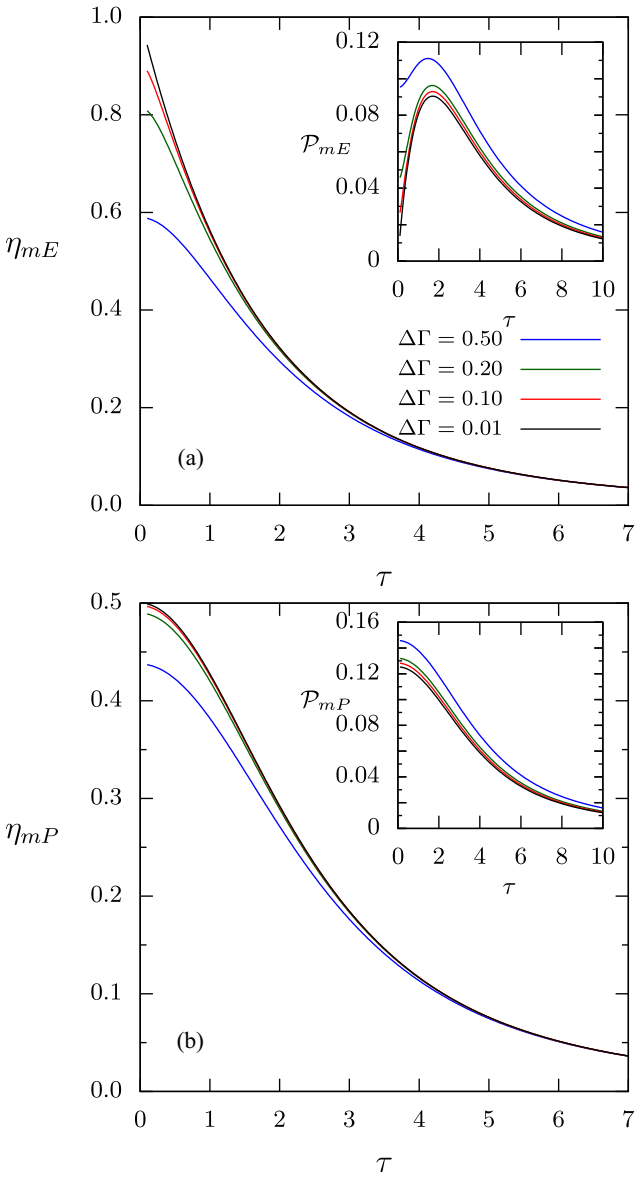

FIG. 4. For $\Gamma_1 = 2$, $f_2 = 1$ and distinct $\Delta\Gamma$'s, the comparison between maximum efficiency [panel (a)] and efficiency at maximum power [panel (b)] for constant drivings. Insets: The corresponding power outputs $\mathcal{P}$'s versus τ.

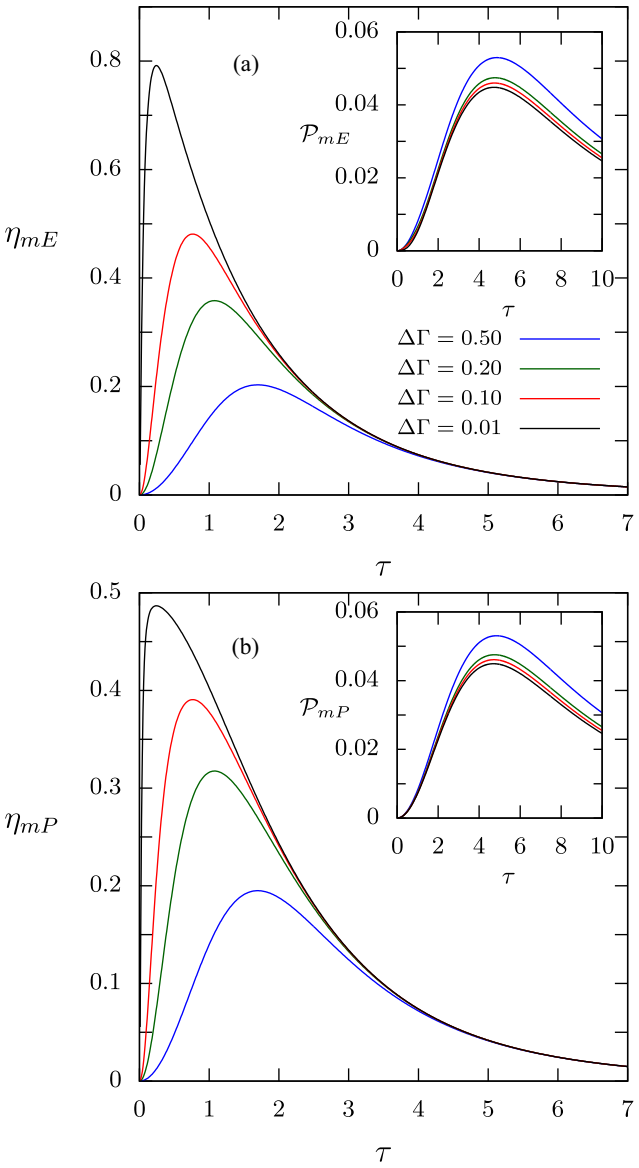

FIG. 5. For $\Gamma_1 = 2$, $\lambda_2 = 1$, and distinct $\Delta\Gamma$'s, the comparison between maximum efficiency [panel (a)] and efficiency at maximum power [panel (b)] for linear drivings. Insets: The corresponding power outputs $\mathcal{P}$'s versus τ.

Other differences between protocols are appraised in Figs. 4 and 5. For finite difference of temperatures, the constant driving is always more efficient than the linear one and their power outputs are also superior. The maximum efficiency curves (linear drivings) are also reentrant, whose maxima values increase and deviate for lower τ's as $\Delta\Gamma$ decreases.

We close this section by remarking that although short periods indicates a general route for optimizing the efficiency of thermal machines in contact to sequential reservoirs, the present description provides to properly tune the period and forces to obtain the desirable compromise between maximum efficiency and power.

VI. CONCLUSIONS

The thermodynamics of a Brownian particle periodically placed in contact with sequential thermal reservoirs is introduced. We have obtained explicit (exact) expressions for relevant quantities, such as heat, work, and entropy production. Generalization for an arbitrary number of sequential reservoirs and the influence of external forces were considered. Considerations about the efficiency were undertaken, in which Brownian machines can be properly operated ensuring the reliable compromise between efficiency and power for small switching periods.

As a final comment, we mention the several perspectives to be addressed. First, it might be very interesting to extend such a study for other external forces protocols (e.g., sinusoidal time-dependent ones) as well as for time asymmetric switchings, to compare their efficiencies, mainly with the linear driving case. Finally, it would be remarkable to verify the validity of recent proposed uncertainties relations (TURs) for Fokker-Planck equations [39,41], in such a class of systems.

ACKNOWLEDGMENTS

We acknowledge Karel Proesmans and Mário J. de Oliveira for careful readings of the manuscript and useful suggestions. C.E.F. acknowledges the financial support from Fundação de Amparo à Pesquisa do estado de São Paulo (FAPESP) under Grant No. 2018/02405-1. Authors also acknowledge the financial support from Brazilian Agencies CAPES and CNPq.

[1] I. Prigogine, *Introduction to Thermodynamics of Irreversible Processes* (Interscience, New York, 1965).
[2] S. R. De Groot and P. Mazur, *Non-Equilibrium Thermodynamics* (North-Holland, Amsterdam, 1962).
[3] T. Tomé and M. J. De Oliveira, *Stochastic Dynamics and Irreversibility* (Springer, Berlin, 2015).
[4] U. Seifert, Rep. Prog. Phys. **75**, 126001 (2012).
[5] C. Van den Broeck and M. Esposito, Physica A **418**, 6 (2015).
[6] C. Jarzynski, Phys. Rev. Lett. **78**, 2690 (1997).
[7] O.-P. Saira, Y. Yoon, T. Tanttu, M. Möttönen, D. V. Averin, and J. P. Pekola, Phys. Rev. Lett. **109**, 180601 (2012).
[8] K. Proesmans and C. Van den Broeck, Europhys. Lett. **119**, 20001 (2017).
[9] A. C. Barato and U. Seifert, Phys. Rev. Lett. **114**, 158101 (2015).
[10] J. Schnakenberg, Rev. Mod. Phys. **48**, 571 (1976).
[11] C. E. Fernández Noa, P. E. Harunari, M. J. de Oliveira, and C. E. Fiore, Phys. Rev. E **100**, 012104 (2019).
[12] T. Herpich, J. Thingna, and M. Esposito, Phys. Rev. X **8**, 031056 (2018).
[13] T. Herpich and M. Esposito, Phys. Rev. E **99**, 022135 (2019).
[14] B. O. Goes, C. E. Fiore, and G. T. Landi, Phys. Rev. Res. **2**, 013136 (2020).
[15] H. Ge, M. Qian, and H. Qian, Phys. Rep. **510**, 87 (2012).
[16] T. Tomé and M. J. de Oliveira, Phys. Rev. E **91**, 042140 (2015).

[17] K. Brandner, K. Saito, and U. Seifert, Phys. Rev. X **5**, 031019 (2015).
[18] K. Proesmans, B. Cleuren, and C. Van den Broeck, Phys. Rev. Lett. **116**, 220601 (2016).
[19] K. Proesmans and C. E. Fiore, Phys. Rev. E **100**, 022141 (2019).
[20] B. Cleuren and K. Proesmans, Physica A **552**, 122789 (2020).
[21] M. Pezzutto, M. Paternostro, and Y. Omar, New J. Phys. **18**, 123018 (2016).
[22] M. Pezzutto, M. Paternostro, and Y. Omar, Quant. Sci. Technol. **4**, 025002 (2019).
[23] G. T. Landi, E. Novais, M. J. de Oliveira, and D. Karevski, Phys. Rev. E **90**, 042142 (2014).
[24] C. H. Bennett, Int. J. Theor. Phys. **21**, 905 (1982).
[25] K. Maruyama, F. Nori, and V. Vedral, Rev. Mod. Phys. **81**, 1 (2009).
[26] T. Sagawa, J. Stat. Mech.: Theory Exp. (2014) P03025.
[27] J. M. Parrondo, J. M. Horowitz, and T. Sagawa, Nat. Phys. **11**, 131 (2015).
[28] V. Giovannetti and G. M. Palma, Phys. Rev. Lett. **108**, 040401 (2012).
[29] P. Strasberg, G. Schaller, T. Brandes, and M. Esposito, Phys. Rev. X **7**, 021003 (2017).
[30] F. L. S. Rodrigues, G. De Chiara, M. Paternostro, and G. T. Landi, Phys. Rev. Lett. **123**, 140601 (2019).
[31] C. Van den Broeck, Phys. Rev. Lett. **95**, 190602 (2005).
[32] T. Schmiedl and U. Seifert, Europhys. Lett. **83**, 30005 (2008).
[33] F. Berger, T. Schmiedl, and U. Seifert, Phys. Rev. E **79**, 031118 (2009).
[34] A. Dechant, N. Kiesel, and E. Lutz, Europhys. Lett. **119**, 50003 (2017).
[35] Y. Izumida and K. Okuda, Eur. Phys. J. B **77**, 499 (2010).
[36] D. Abreu and U. Seifert, Europhys. Lett. **94**, 10001 (2011).
[37] A. C. Barato and U. Seifert, J. Phys. Chem. B **119**, 6555 (2015).
[38] T. R. Gingrich, J. M. Horowitz, N. Perunov, and J. L. England, Phys. Rev. Lett. **116**, 120601 (2016).
[39] Y. Hasegawa and T. Van Vu, Phys. Rev. E **99**, 062126 (2019).
[40] T. Van Vu and Y. Hasegawa, Phys. Rev. E **100**, 012134 (2019).
[41] T. Van Vu and Y. Hasegawa, Phys. Rev. Res. **2**, 013060 (2020).
[42] T. Tomé and M. J. de Oliveira, Phys. Rev. E **82**, 021120 (2010).
[43] K. Proesmans and C. Van den Broeck, Phys. Rev. Lett. **115**, 090601 (2015).
[44] M. Bauer, K. Brandner, and U. Seifert, Phys. Rev. E **93**, 042112 (2016).
[45] A. Rosas, C. Van den Broeck, and K. Lindenberg, Phys. Rev. E **94**, 052129 (2016).
[46] K. Proesmans and C. Van den Broeck, Chaos: Interdiscip. J Nonlin. Sci. **27**, 104601 (2017).
[47] A. Rosas, C. Van den Broeck, and K. Lindenberg, Phys. Rev. E **96**, 052135 (2017).

Efficient asymmetric collisional Brownian particle engines

C. E. Fernández Noa,[1] Angel L. L. Stable,[1] William G. C. Oropesa,[1] Alexandre Rosas,[2] and C. E. Fiore[1]
[1]*Instituto de Física da Universidade de São Paulo, 05508-090 São Paulo, São Paulo, Brazil*
[2]*Departamento de Física, CCEN, Universidade Federal da Paraíba, Caixa Postal 5008, 58059-900 João Pessoa, Brazil*

(Received 2 August 2021; accepted 15 November 2021; published 2 December 2021)

The construction of efficient thermal engines operating at finite times constitutes a fundamental and timely topic in nonequilibrium thermodynamics. We introduce a strategy for optimizing the performance of Brownian engines, based on a collisional approach for unequal interaction times between the system and thermal reservoirs. General (and exact) expressions for thermodynamic properties and their optimized values are obtained, irrespective of the driving forces, asymmetry, temperatures of reservoirs, and protocol to be maximized. Distinct routes for the engine optimization, including maximizations of output power and efficiency with respect to the asymmetry, the force, and both of these, are investigated. For the isothermal work-to-work converter and/or a small difference in temperature between reservoirs, they are solely expressed in terms of Onsager coefficients. Although the symmetric engine can operate very inefficiently depending on the control parameters, the usage of distinct contact times between the system and each reservoir not only can enhance the machine performance (signed by an optimal tuning ensuring the largest gain) but also enlarges substantially the machine regime operation. The present approach can pave the way for the construction of efficient Brownian engines operating at finite times.

DOI: 10.1103/PhysRevResearch.3.043152

I. INTRODUCTION

A long-standing dilemma in thermodynamics and related areas concerns the issue of mitigating the impact of thermal noise or wasted heat in order to improve the machine performance. This constitutes a highly relevant problem, not only for theoretical purposes but also for the construction of experimental setups [1–3]. Giving that the machine performance is commonly dependent on particular chemical compositions and operation conditions, notably for small-scale engines, the role of fluctuations being crucial for such engines, distinct approaches have been proposed and investigated in the realm of stochastic and quantum thermodynamics [4,5]. A second fundamental point concerns the fact that, even if all sources of dissipation could be mitigated, the performance of any thermal machine would still be limited by Carnot efficiency, which requires the occurrence of infinitely slow quasistatic processes, and consequently the engine operates at null power. In contrast, realistic systems operate at finite time and power. Such a conundrum (control or mitigation of dissipation and engine optimization) has contributed to the discovery of several approaches based on the maximization of power output instead of the efficiency [4–20].

Thermal machines based on Brownian particles have been successfully studied not only for theoretical purposes [6,7,15,21] but also for the building of reliable experimental setups [22–27]. They are also remarkable for depicting the limitations of classical thermodynamics and disclose the scales at which thermal fluctuations become relevant. In several situations, thermal machines involve isothermal transformations [22,23,25]. Such a class of processes are fundamental in thermodynamics since they are minimally dissipative. However, isothermal transformations are slow, demanding a sufficiently large number of stages for achieving the desired final state. For this reason, distinct protocols, such as increasing the coupling between the system and the thermal bath, have been undertaken for speeding it up and simultaneously controlling the increase in dissipation [28–32].

Here, we introduce a strategy for optimizing the performance of irreversible Brownian machines operating in isothermal parts via control of the interaction time between the system and the environment. Our approach is based on a Brownian particle sequentially placed in contact with distinct thermal baths and subject to external forces [33] for unequal times. Such a description, also referred to as collisional, has been successfully employed in different contexts, such as systems that interact only with a small fraction of the environment and those presenting distinct drivings over each member of the system [34–37]. Depending on the parameters of the model (period, driving, and difference of temperatures), the symmetric version can operate very inefficiently. Our aim is to show that the machine performance improves substantially by tuning properly the interaction time between the particle and each reservoir. Besides the increase in the power and/or efficiency, the asymmetry in the contact time also enlarges the regime of operation of the machine substantially. Contrasting with previous works [29–32], the optimization is solely

obtained via the control of interaction time, and no external parameters are considered. We derive general relations for distinct kinds of maximization, including the maximization of the efficiency and power with respect to the force, the asymmetry, and both of these. For the isothermal work-to-work converter and/or a small difference in temperature between reservoirs, they are solely expressed in terms of Onsager coefficients. The present approach can pave the way for the construction of efficient Brownian engines operating at finite times.

This paper is organized as follows: In Sec. II we present the thermodynamics of Brownian particles subject to asymmetric time switching. In Sec. III, the efficiency is analyzed for two cases: the work-to-work converter processes and distinct temperature reservoirs. Optimization protocols are presented and exemplified for distinct drivings. Finally, conclusions are drawn in Sec. IV, and explicit calculations of the Onsager coefficients and linear regimes are presented in Appendixes A–C.

II. THERMODYNAMICS OF ASYMMETRIC INTERACTION TIMES

We consider a Brownian particle with mass m sequentially and cyclically placed in contact with different thermal reservoirs, each at a temperature T_i for time interval τ_i. Here, $i = 1, \ldots, N$ label the reservoirs and also the order of contact between the reservoirs and the particle. While in contact with the ith reservoir, the velocity $v_i(t)$ of the particle evolves in time according to the Langevin equation

$$\frac{dv_i}{dt} = -\gamma_i v_i + f_i(t) + \zeta_i(t), \tag{1}$$

where γ_i, $f_i(t)$, and $\zeta_i(t)$ denote the viscous constants, external forces, and stochastic forces (interaction between the particle and the ith reservoir), respectively, all divided by the mass of the particle. Stochastic forces are assumed to satisfy the white noise properties

$$\langle \zeta_i(t) \rangle = 0 \tag{2}$$

and

$$\langle \zeta_i(t)\zeta_{i'}(t') \rangle = 2\gamma_i T_i \delta_{ii'} \delta(t - t'). \tag{3}$$

The system evolves to a nonequilibrium steady-state regime (NESS) characterized by a nonvanishing production of entropy. The time evolution of the velocity probability distribution at time t, $P_i(v, t)$, is described by the Fokker-Planck equation [38–40]

$$\frac{\partial P_i}{\partial t} = -\frac{\partial J_i}{\partial v} - f_i(t)\frac{\partial P_i}{\partial v}, \tag{4}$$

where J_i is the probability current

$$J_i = -\gamma_i v P_i - \frac{\gamma_i k_B T_i}{m}\frac{\partial P_i}{\partial v}. \tag{5}$$

As can be verified by direct substitution, the NESS is characterized by a Gaussian probability distribution $P_i(v, t)$:

$$P_i(v, t) = \frac{1}{\sqrt{2\pi b_i(t)}} e^{-\frac{(v-\langle v_i \rangle)^2}{2b_i(t)}}, \tag{6}$$

for which the mean $\langle v_i \rangle(t)$ and the variance $b_i(t) \equiv \langle v_i^2 \rangle(t) - \langle v_i \rangle^2(t)$ are time dependent and obey the following equations of motion:

$$\frac{d}{dt}\langle v_i \rangle(t) = -\gamma_i \langle v_i \rangle(t) + f_i(t) \tag{7}$$

and

$$\frac{d}{dt} b_i(t) = -2\gamma_i b_i(t) + \Gamma_i, \tag{8}$$

where $\Gamma_i = 2\gamma_i k_B T_i/m$. Obviously, the continuity of the probability distribution must be assured, and we will use it to calculate $b_i(t)$ and $\langle v_i \rangle(t)$ in the following sections.

In order to derive explicit expressions for macroscopic quantities, we start from the definitions of the average energy $U_i = m\langle v_i^2 \rangle/2$ and entropy $S_i(t) = -k_B \langle \ln[P_i(v, t)] \rangle$, respectively. In both cases, the time variation can be straightforwardly obtained from the Fokker-Planck equation, applying vanishing boundary conditions for both $P_i(v, t)$ and $J_i(v, t)$ in the infinity-speed limit [38]. The former is related to the average power dissipated $\dot{W}_i$ and the heat dissipation during the same period $\dot{Q}_i$ through the first law of thermodynamics relation

$$\frac{dU_i}{dt} = -[\dot{W}_i(t) + \dot{Q}_i(t)], \tag{9}$$

where $\dot{W}_i(t)$ and $\dot{Q}_i(t)$ are given by the following expressions:

$$\dot{W}_i(t) = -m\langle v_i \rangle(t) f_i(t) \tag{10}$$

and

$$\dot{Q}_i(t) = m\gamma_i \left(\langle v_i^2 \rangle(t) - \frac{\Gamma_i}{2\gamma_i} \right). \tag{11}$$

Similarly, the rate of variation of the entropy can be written as [39,40]

$$\frac{dS_i}{dt} = \Pi_i(t) - \Phi_i(t), \tag{12}$$

where $\Pi_i(t)$ and $\Phi_i(t)$ denote the entropy production rate and the flux of entropy, respectively, which expressions are given by

$$\Pi_i(t) = \frac{2k_B}{\Gamma_i} \int_{\tilde{\tau}_{i-1}}^{t} \frac{J_i^2}{P_i} dv \tag{13}$$

and

$$\Phi_i(t) = -\frac{2\gamma_i k_B}{\Gamma_i} \int_{\tilde{\tau}_{i-1}}^{t} v J_i dv = \frac{2\gamma_i k_B \dot{Q}_i(t)}{m\Gamma_i} = \frac{\dot{Q}_i(t)}{T_i}, \tag{14}$$

respectively, where $\tilde{\tau}_i = \sum_{j=1}^{i} \tau_j$ (with $\tau_0 \equiv 0$). Both expressions are valid during the contact of the Brownian particle with the ith reservoir.

As stated before, the present collisional approach for Brownian machines can be considered for an arbitrary set of reservoirs and external forces, whose generic solutions $\langle v_i \rangle(t)$ and $b_i(t)$ in the nonequilibrium steady-state regime are

$$\langle v_i \rangle(t) = e^{-\gamma_i(t-\tilde{\tau}_{i-1})} a_i + e^{-\gamma_i t} F_i(t) \tag{15}$$

and

$$b_i(t) = A_i e^{-2\gamma_i(t-\tilde{\tau}_{i-1})} + \frac{\Gamma_i}{2\gamma_i}, \tag{16}$$

where a_i and A_i are integration constants to be determined from the boundary conditions and $F_i(t)$ can be viewed as a "time-integrated force," which is related to the external forces through the expression

$$F_i(t) = \int_{\tilde{\tau}_{i-1}}^{t} e^{\gamma_i t'} f_i(t') dt'. \tag{17}$$

Here, the variable t is interpreted as the time modulus the period $\tau = \tilde{\tau}_N$.

Since the probability distribution is continuous, the conditions $\langle v_i\rangle(\tau_i) = \langle v_{i+1}\rangle(\tau_i)$ and $b_i(\tau_i) = b_{i+1}(\tau_i)$ must hold for $i = 1, \ldots, N-1$. In addition, the steady-state condition (periodicity) implies that $\langle v_1\rangle(0) = \langle v_N\rangle(\tau)$ and $b_1(0) = b_N(\tau)$. Hence the a_i and A_i can be determined as the solution of two uncoupled linear systems of N equations each. Here, we shall focus on the case of $N = 2$ reservoirs—the simplest case for tackling the efficiency of a thermal engine, in which the interaction with the first and second reservoirs occurs during τ_1 and $\tau_2 = \tau - \tau_1$, respectively. For simplicity, from now on, we consider that the viscous constants are equal $\gamma_1 = \gamma_2 = \gamma$. Therefore the average velocities and their variances are

$$\langle v_1\rangle(t) = \frac{(e^{\gamma\tau} - 1)F_1(t) + F_1(\tau_1) + F_2(\tau)}{e^{\gamma t}(e^{\gamma\tau} - 1)}, \tag{18}$$
$$\langle v_2\rangle(t) = \frac{e^{\gamma\tau}F_1(\tau_1) + (e^{\gamma\tau} - 1)F_2(t) + F_2(\tau)}{e^{\gamma t}(e^{\gamma\tau} - 1)},$$

and

$$b_1(t) = -\frac{(\Gamma_1 - \Gamma_2)(1 - e^{-2\gamma\tau_2})}{2\gamma(1 - e^{-2\gamma\tau})} e^{-2\gamma t} + \frac{\Gamma_1}{2\gamma}, \tag{19}$$
$$b_2(t) = \frac{(\Gamma_1 - \Gamma_2)(1 - e^{-2\gamma\tau_1})}{2\gamma(1 - e^{-2\gamma\tau})} e^{-2\gamma(t-\tau_1)} + \frac{\Gamma_2}{2\gamma},$$

respectively. The expressions for $\langle v_1\rangle(t)$ and $b_1(t)$ hold for $0 \leqslant t \leqslant \tau_1$, while the expressions for $\langle v_2\rangle(t)$ and $b_2(t)$ are valid for $\tau_1 \leqslant t \leqslant \tau$. It is worth pointing out that the particle will be exposed to the contact with reservoir 1 and force $f_1(t)$ for a longer (shorter) time than with reservoir 2 and force $f_2(t)$ if $\tau_1 \geqslant \tau_2$ ($\tau_1 \leqslant \tau_2$). Furthermore, while the average velocities $\langle v_i\rangle(t)$ depend on the external force (but not on the temperature of the reservoirs), its variances $b_i(t)$ depend on the temperatures (but not on the external forces).

Having the expressions for the mean velocities and variances, thermodynamic quantities of interest can be directly obtained. The average work in each part of the cycle is given by

$$\overline{\dot{W}}_1 = \frac{1}{\tau}\int_0^{\tau_1} \langle v_1\rangle(t) f_1(t) dt, \tag{20}$$
$$\overline{\dot{W}}_2 = \frac{1}{\tau}\int_{\tau_1}^{\tau} \langle v_2\rangle(t) f_2(t) dt. \tag{21}$$

Using Eq. (18) and expressing each external force as $f_i(t) = X_i g_i(t)$, with X_i and $g_i(t)$ denoting force strength and its driving, respectively, we finally arrive at the following expressions:

$$\overline{\dot{W}}_1 = -\frac{m}{\tau(e^{\gamma\tau} - 1)}\Bigg[X_1^2\Bigg((e^{\gamma\tau} - 1)\int_0^{\tau_1} g_1(t)e^{-\gamma t}\,dt \int_0^{t} g_1(t')e^{\gamma t'}\,dt' + \int_0^{\tau_1} g_1(t)e^{-\gamma t}\,dt \int_0^{\tau_1} g_1(t')e^{\gamma t'}\,dt'\Bigg)$$
$$+ X_1X_2\int_0^{\tau_1} g_1(t)e^{-\gamma t}\,dt \int_{\tau_1}^{\tau} g_2(t')e^{\gamma t'}\,dt'\Bigg], \tag{22}$$
$$\overline{\dot{W}}_2 = -\frac{m}{\tau(e^{\gamma\tau} - 1)}\Bigg[X_2^2\Bigg(\int_{\tau_1}^{\tau} g_2(t)e^{-\gamma t}\,dt \int_{\tau_1}^{\tau} g_2(t')e^{\gamma t'}\,dt' + (e^{\gamma\tau} - 1)\int_{\tau_1}^{\tau} g_2(t)e^{-\gamma t}dt \int_{\tau_1}^{t} g_2(t')e^{\gamma t'}\,dt'\Bigg)$$
$$+ X_1X_2e^{\gamma\tau}\int_{\tau_1}^{\tau} g_2(t)e^{-\gamma t}\,dt \int_0^{\tau_1} g_1(t')e^{\gamma t'}\,dt'\Bigg]. \tag{23}$$

The expressions above, Eqs. (22) and (23), are exact and are valid for any kind of drivings $g_1(t)$ and $g_2(t)$ and stage duration τ_1 and τ_2. Usually, in the linear regime, $\overline{\dot{W}}_i$ is written as the product of a flux $\mathcal{J}_i = L_{ii}X_i + L_{ij}X_j$ by a force X_i; that is, $\overline{\dot{W}}_i = -k_B T_i \mathcal{J}_i X_i$. Since in the present case $\overline{\dot{W}}_i$ is always bilinear in the forces X_i, such an expression is also valid even far from the linear regime. Thus the Onsager coefficients L_{ij} may be written as

$$L_{11} = \frac{2\gamma}{\Gamma_1\tau(e^{\gamma\tau} - 1)}\Bigg[(e^{\gamma\tau} - 1)\int_0^{\tau_1} g_1(t)e^{-\gamma t}dt \int_0^{t} g_1(t')e^{\gamma t'}\,dt' + \int_0^{\tau_1} g_1(t)e^{-\gamma t}\,dt \int_0^{\tau_1} g_1(t')e^{\gamma t'}\,dt'\Bigg],$$
$$L_{22} = \frac{2\gamma}{\Gamma_2\tau(e^{\gamma\tau} - 1)}\Bigg[\int_{\tau_1}^{\tau} g_2(t)e^{-\gamma t}\,dt \int_{\tau_1}^{\tau} g_2(t')e^{\gamma t'}\,dt' + (e^{\gamma\tau} - 1)\int_{\tau_1}^{\tau} g_2(t)e^{-\gamma t}dt \int_{\tau_1}^{t} g_2(t')e^{\gamma t'}\,dt'\Bigg],$$
$$L_{12} = \frac{2\gamma}{\Gamma_1\tau(e^{\gamma\tau} - 1)}\int_0^{\tau_1} g_1(t)e^{-\gamma t}\,dt \int_{\tau_1}^{\tau} g_2(t')e^{\gamma t'}\,dt', \tag{24}$$
$$L_{21} = \frac{2\gamma e^{\gamma\tau}}{\Gamma_2\tau(e^{\gamma\tau} - 1)}\int_0^{\tau_1} g_1(t')e^{\gamma t'}\,dt' \int_{\tau_1}^{\tau} g_2(t)e^{-\gamma t}\,dt.$$

Reciprocal relations are verified as follows: Since forces $f_1(t)$ and $f_2(t)$ solely act from 0 to τ_1 and τ_1 to τ, respectively, both upper and lower integral limits in Eqs. (20) and (21) can be replaced for τ and 0, respectively, and hence all expressions from Eq. (20) to Eq. (24) can be evaluated over a complete cycle. By exchanging the indexes $1 \leftrightarrow 2$, we verify that $L_{ij} \leftrightarrow L_{ji}$.

Similarly, general expressions can be obtained for the average heat dissipation during the contact of the Brownian particle with each reservoir. Since the heat is closely related to the entropy production rate [see, e.g., Eq. (14)], we curb our discussion to the latter quantity. The average entropy production over a complete cycle is then given by

$$\overline{\Pi} = \frac{1}{\tau}\left[\int_0^{\tau_1} \Phi_1(t)\,dt + \int_{\tau_1}^{\tau} \Phi_2(t)\,dt\right]. \tag{25}$$

By inserting Eq. (14) into Eq. (25) and using Eq. (11), $\overline{\Pi}$ can be decomposed into two terms: one associated with the difference in temperature of the reservoirs

$$\overline{\Pi}_T = \frac{k_B}{\tau}\left[\frac{2\gamma^2}{\Gamma_1}\int_0^{\tau_1} b_1(t)\,dt + \frac{2\gamma^2}{\Gamma_2}\int_{\tau_1}^{\tau} b_2(t)\,dt - \gamma\tau\right], \tag{26}$$

and the other coming from the external forces

$$\overline{\Pi}_F = \frac{k_B}{\tau}\left[\frac{2\gamma^2}{\Gamma_1}\int_0^{\tau_1} \langle v_1\rangle^2(t)\,dt + \frac{2\gamma^2}{\Gamma_2}\int_{\tau_1}^{\tau} \langle v_2\rangle^2(t)\,dt\right]. \tag{27}$$

Now, from Eqs. (19) and (26), one obtains the general form for $\overline{\Pi}_T$:

$$\overline{\Pi}_T = k_B\frac{\Gamma_1\Gamma_2}{\tau}\frac{\sinh(\gamma\tau_1)\sinh(\gamma\tau_2)}{\sinh(\gamma\tau)}\left(\frac{1}{\Gamma_1} - \frac{1}{\Gamma_2}\right)^2, \tag{28}$$

which is strictly positive (as expected). The component $(1/\Gamma_1 - 1/\Gamma_2)$ can be regarded as the "thermodynamic force" f_Γ associated with the difference in temperature of the reservoirs. Particularly, in the linear regime ($\Gamma_2 \simeq \Gamma_1 = \Gamma$), $\overline{\Pi}_T$ can be conveniently written down in terms of Onsager coefficient $\overline{\Pi}_T = L_{\Gamma\Gamma} f_\Gamma$, where $L_{\Gamma\Gamma}$ is given by

$$L_{\Gamma\Gamma} = k_B\frac{\Gamma^2}{\tau}\frac{\sinh(\gamma\tau_1)\sinh(\gamma\tau_2)}{\sinh(\gamma\tau)}. \tag{29}$$

Note that $L_{\Gamma\Gamma}$ is strictly positive and it reduces to $k_B\Gamma^2\tanh[\frac{\gamma\tau}{2}]/2\tau$ for $\tau_1 = \tau_2$ (symmetric case). Furthermore, it is straightforward to verify that the dissipation term Π_T is a monotonous decreasing function of τ and it is always larger for the symmetric case ($\tau_1 = \tau_2$). Both properties of $\overline{\Pi}_T$ are illustrated in Fig. 1, where $\overline{\Pi}_T$ is shown as a function of τ for various values of the asymmetry parameter $\kappa = \tau_1/\tau_2$ (notice that $\overline{\Pi}_T$ is invariant over the switch of the interaction times $\tau_1 \leftrightarrow \tau_2$ or, equivalently, $\kappa \leftrightarrow 1/\kappa$). There is one caveat which concerns the validity of the results of Fig. 1. Collisional models usually neglect the time for changing the contact between the system and thermal baths. However, if τ is very small, such an approximation can no longer hold. We shall assume throughout this paper that τ is large enough for the collisional approximation to be valid.

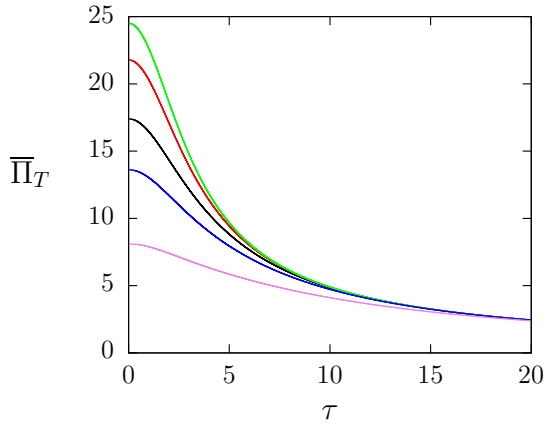

FIG. 1. Mean entropy production component $\overline{\Pi}_T$ as a function of the period τ for $\gamma = 1$, $\Gamma_1 = 1$, and $\Gamma_2 = 100$ and distinct asymmetries. From top to bottom: $\kappa = 1.0$, 0.5, 0.3, 0.2, and 0.1.

The entropy production component coming from external forces also assumes a general (bilinear) form given by

$$\overline{\Pi}_F = \tilde{L}_{11}X_1^2 + (\tilde{L}_{12} + \tilde{L}_{21})X_1X_2 + \tilde{L}_{22}X_2^2. \tag{30}$$

The coefficients $\tilde{L}_{ij}$ are shown in Appendix A, Eq. (A2). It should be noticed that Eq. (30) is exact for all force regimes (not only in the linear regime). For equal temperatures, they coincide with the Onsager coefficients [Eq. (24)]. A detailed analysis for distinct linear regimes (low temperature difference and/or low forces) is undertaken in Appendix A. Furthermore, since $\tau_2 = \tau - \tau_1$, the coefficients above fulfill the reciprocal relations $\tilde{L}_{11} \leftrightarrow \tilde{L}_{22}$ and $\tilde{L}_{12} \leftrightarrow \tilde{L}_{21}$ by exchanging $1 \leftrightarrow 2$ for the generic drivings $g_i(t)$, the interaction times τ_i, and the temperature of the reservoirs T_i.

III. EFFICIENCY

The optimization of engines, which converts energy (usually heat or chemical work) into mechanical work, constitutes one of the main issues in thermodynamics, engineering, chemistry, and other fields. Here, we exploit the role of asymmetric contact times between the Brownian particle and the thermal reservoirs as a reliable strategy for optimizing the machine performance. More specifically, the amount of energy (heat and work) received by the particle is partially converted into output work (or, equivalently, the output power per cycle) $\mathcal{P} = \overline{\dot{W}_2} \geqslant 0$ during the second half stage. A measure of efficiency is given by the ratio of the amount of output work to the total energy injected:

$$\eta = -\frac{\mathcal{P}}{\overline{\dot{W}_1} + \overline{\dot{Q}_i}}, \tag{31}$$

where $\overline{\dot{Q}_i}$ is the average heat extracted from the reservoir i ($i = 1$ or 2 depending on whether reservoir 1 or 2 delivers heat to the Brownian particle), whereas for the other way round (both reservoirs absorbing energy from the particle), $\overline{\dot{Q}_i}$ does not appear in Eq. (31), as shall be discussed in Sec. III A. It is worth mentioning that in the case of more than two reservoirs, the numerator of the efficiency should be the total

power extracted from the systems (sum of all $\overline{\dot{W}_i} > 0$) and the denominator is the total power injected into the system (sum of all $\overline{\dot{W}_i} < 0$) plus the total heat injected into the system (sum of all $\overline{\dot{Q}_i} < 0$).

Below, we are going to investigate the machine optimization with respect to the loading force X_2 and asymmetry coefficient $\kappa = \tau_1/\tau_2$ for two distinct scenarios: equal and different temperatures.

A. Isothermal work-to-work converter

Many processes in nature, such as biological systems, operate at homogeneous (or approximately equal) temperatures, in which an amount of chemical work or energy is converted into mechanical work and vice versa (see, e.g., Refs. [41,42]). This highlights the importance of searching for optimized protocols operating at equal temperatures. Here, we exploit the present Brownian machine operating at equal temperatures, but subject to distinct external forces. From Eqs. (11) and (19), it follows that $\overline{\dot{Q}_1} \geqslant 0$ and $\overline{\dot{Q}_2} \geqslant 0$, and therefore no heat is delivered to the particle. Such an engine reduces to a work-to-work converter: The particle receives input power $\overline{\dot{W}_1} < 0$ which is partially converted into output power $\mathcal{P} \geqslant 0$. From Eq. (24), the output power and efficiency can be expressed in terms of the Onsager coefficients according to the following expressions:

$$\mathcal{P} = \overline{\dot{W}}_2 = -k_{\mathrm{B}}T\left[L_{22}(\kappa)X_2^2 + L_{21}(\kappa)X_1X_2\right] \tag{32}$$

and

$$\eta = -\frac{L_{21}X_1X_2 + L_{22}X_2^2}{L_{11}X_1^2 + L_{12}X_1X_2}. \tag{33}$$

Both of them can be expressed in terms of the ratio X_2/X_1 between forces, the output power being a function of such a ratio multiplied by X_1^2. As mentioned previously, there are three routes to be considered with respect to the engine optimization (holding X_1 and τ fixed): the time asymmetry optimization (conveniently carried out in terms of the ratio $\kappa = \tau_1/\tau_2$), the output force X_2 optimization, and both optimizations together. We shall analyze all cases in Secs. III A 1 to III A 4.

1. Maximization with respect to the asymmetry

Since the Brownian particle must be in contact with the first reservoir long enough for the injected energy to be larger than the energy dissipated by the viscous force, for any set of X_1 and X_2 there is a minimum value κ_m for which $\mathcal{P} \geqslant 0$. On the other hand, depending on the kind of driving, it can extend up $\kappa \to \infty$, for which L_{21} and L_{22} vanish [see Eq. (24)].

The choice of optimal asymmetries is expected to be dependent on the quantity chosen to be maximized. Usually, there are two quantities of interest: maximum efficiency or maximum power output. Starting with the latter case, the optimal asymmetry κ_{MP} which maximizes $\mathcal{P}$ is the solution of the following equation:

$$\frac{L'_{21}(\kappa_{MP})}{L'_{22}(\kappa_{MP})} = -\frac{X_2}{X_1}, \tag{34}$$

where $L'_{ij}(\kappa) \equiv \partial L_{ij}(\kappa)/\partial\kappa$. In this section, L_{ij}'s (together with their derivatives) have been expressed in terms of κ to specify which quantity ($\mathcal{P}$ or η) has been maximized. In general, Eq. (34) may have more than one solution for each choice of the ratio X_2/X_1, and one should be careful to identify the global maximum. However, in the following discussion (as in the examples presented in Sec. III A 3), we consider the cases which present a single maximum.

Similarly, from Eq. (33), we obtain the value of the asymmetry that maximizes the efficiency $\kappa_{M\eta}$ from the transcendental equation

$$\begin{aligned}\Delta_{2212}(\kappa_{M\eta})X_2^2 + \Delta_{2111}(\kappa_{M\eta})X_1^2 \\ + [\Delta_{2211}(\kappa_{M\eta}) + \Delta_{2112}(\kappa_{M\eta})]X_1X_2 = 0,\end{aligned} \tag{35}$$

where $\Delta_{ijkl}(\kappa) = L'_{ij}(\kappa)L_{kl}(\kappa) - L'_{kl}(\kappa)L_{ij}(\kappa)$. Although exact, for a given choice of the drivings $g_i(t)$ and the strengths X_i, Eqs. (34) and (35), in general, have to be solved numerically for κ_{MP} and $\kappa_{M\eta}$, respectively. After these values are obtained, we can evaluate the power $\mathcal{P}_{MP,\kappa}$ and efficiency $\eta_{MP,\kappa}$ at maximum power as

$$\begin{aligned}\mathcal{P}_{MP,\kappa} = \frac{k_{\mathrm{B}}TL'_{21}(\kappa_{MP})}{L'^2_{22}(\kappa_{MP})}[L_{21}(\kappa_{MP})L'_{22}(\kappa_{MP}) \\ - L_{22}(\kappa_{MP})L'_{21}(\kappa_{MP})]X_1^2\end{aligned} \tag{36}$$

and

$$\eta_{MP,\kappa} = \frac{L'_{21}(\kappa_{MP})[L'_{22}(\kappa_{MP})L_{21}(\kappa_{MP}) - L_{22}(\kappa_{MP})L'_{21}(\kappa_{MP})]}{L'_{22}(\kappa_{MP})[L_{11}(\kappa_{MP})L'_{22}(\kappa_{MP}) - L_{12}(\kappa_{MP})L'_{21}(\kappa_{MP})]}. \tag{37}$$

Analogously, we can write the power at maximum efficiency $\mathcal{P}_{M\eta,\kappa}$ and maximum efficiency $\eta_{M\eta,\kappa}$ as

$$\mathcal{P}_{M\eta,\kappa} = -k_{\mathrm{B}}T\left[L_{22}(\kappa_{M\eta})X_2^2 + L_{21}(\kappa_{M\eta})X_1X_2\right] \tag{38}$$

and

$$\eta_{M\eta,\kappa} = -\frac{L_{22}(\kappa_{M\eta})X_2^2 + L_{21}(\kappa_{M\eta})X_1X_2}{L_{11}(\kappa_{M\eta})X_1^2 + L_{12}(\kappa_{M\eta})X_1X_2}, \tag{39}$$

respectively. In Sec. III A 3, we will exemplify our exact expressions for maximum efficiencies and powers for two kinds of drivings.

2. Maximization with respect to the output force

For given asymmetry and drivings, the Onsager coefficients are constant. Hence the maximization of the output power and the efficiency turns out to be similar to the approach from Refs. [16,33]. Below, we recast the main results.

As previously, the engine regime ($\mathcal{P} > 0$) also imposes boundaries to optimization with respect to the force strength. Here, the output force X_2 must lie in the interval $X_m \leqslant X_2 \leqslant 0$, where $X_m = -L_{21}X_1/L_{22}$. In general, X_m is different from the value of the output force that minimizes the entropy production X_{2mS} (for X_1 and κ constants). According to Eq. (30), such a difference is given by $X_{2m} - X_{2mS} = (L_{12} - L_{21})X_1/2L_{22}$. Note that they coincide, $X_m = X_{2mS}$, for symmetric Onsager coefficients $L_{12} = L_{21}$, but they are different when $L_{12} \neq L_{21}$. Similarly to Sec. III A 1, the optimization can be performed to ensure maximum power $\mathcal{P}_{MP,X_2}$ (with efficiency η_{MP,X_2}) or maximum efficiency $\eta_{M\eta,X_2}$ (with power $\mathcal{P}_{M\eta,X_2}$), by adjusting

the output forces to optimal values X_{2MP} and $X_{2M\eta}$, respectively. These optimal output forces can be expressed in terms of the Onsager coefficients as

$$X_{2M\eta} = \frac{L_{11}}{L_{12}}\left(-1+\sqrt{1-\frac{L_{12}L_{21}}{L_{11}L_{22}}}\right)X_1 \tag{40}$$

and

$$X_{2MP} = -\frac{1}{2}\frac{L_{21}}{L_{22}}X_1, \tag{41}$$

respectively. Hence the maximum efficiency $\eta_{M\eta,X_2}$ and the efficiency at maximum power η_{MP,X_2} are given by

$$\eta_{M\eta,X_2} = -\frac{L_{21}}{L_{12}} + \frac{2L_{11}L_{22}}{L_{12}^2}\left(1-\sqrt{1-\frac{L_{12}L_{21}}{L_{11}L_{22}}}\right) \tag{42}$$

and

$$\eta_{MP,X_2} = \frac{L_{21}^2}{4L_{11}L_{22}-2L_{12}L_{21}}, \tag{43}$$

while the power at maximum efficiency $\mathcal{P}_{M\eta,X_2}$ and the maximum power $\mathcal{P}_{MP,X_2}$ can obtained by inserting $X_{2M\eta}$ or X_{2MP} into the expression for $\mathcal{P}$. In fact, these quantities are not independent of each other; instead they are related as

$$\eta_{MP,X_2} = \frac{P_{MP,X_2}}{2P_{MP,X_2}-P_{M\eta,X_2}}\eta_{M\eta,X_2}. \tag{44}$$

Furthermore, for symmetric Onsager coefficients $L_{12}=L_{21}$, there are two additional simple relations given by

$$\eta_{MP,X_2} = \frac{\eta_{M\eta,X_2}}{1+\eta_{M\eta,X_2}^2} \quad \text{and} \quad \frac{\mathcal{P}_{M\eta,X_2}}{\mathcal{P}_{MP,X_2}} = 1-\eta_{M\eta,X_2}^2. \tag{45}$$

As shown in Appendix B, $L_{12}=L_{21}$ for constant drivings for any value of κ. Conversely, they are in general different ($L_{12}\neq L_{21}$) for linear drivings (see Appendix C). For the symmetric time case ($\kappa=1$), however, the equality holds also for linear drivings [33].

3. Constant and linear drivings

In order to access the advantages of the asymmetry in the time spent by the Brownian particle in contact with each reservoir, we consider two different driving models. In the first model, the drivings are constant, and the external forces can be written as

$$f_1(t) = X_1, \quad \text{for } 0 \leqslant t < \tau_1, \tag{46}$$

$$f_2(t) = X_2, \quad \text{for } \tau_1 \leqslant t < \tau. \tag{47}$$

In Appendix B, we present explicit expressions for the average velocities $\langle v_i\rangle(t)$ and Onsager coefficients L_{ij} (which coincide with the coefficients $\tilde{L}_{ij}$ for isothermal reservoirs). The second class of Brownian engines deals with drivings evolving linearly in time and given by the following expressions:

$$f_1(t) = X_1\gamma t, \quad \text{for } 0 \leqslant t < \tau_1, \tag{48}$$

$$f_2(t) = X_2\gamma(t-\tau_1), \quad \text{for } \tau_1 \leqslant t < \tau. \tag{49}$$

The main expressions for such a case are listed in Appendix C. Figures 2 and 3 depict typical plots of the efficiency and power

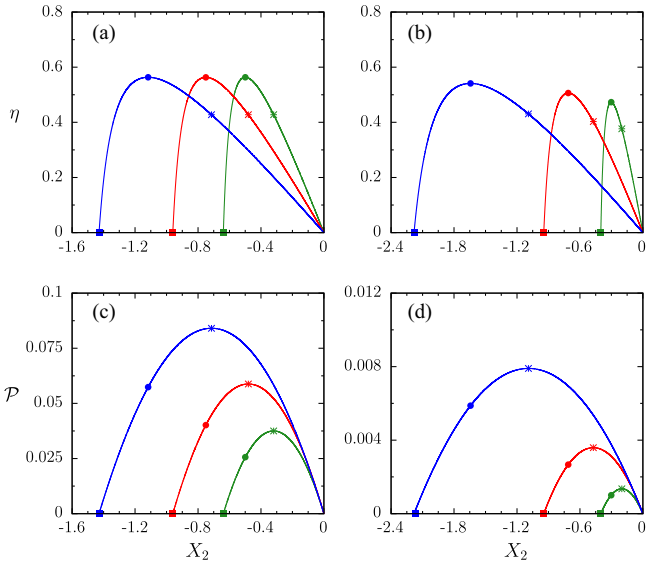

FIG. 2. Efficiency [(a) and (b)] and output power [(c) and (d)] (averaged over one period) for the isothermal work-to-work converter with $X_1=1$, $\tau=1$, $\gamma=1$, and different asymmetries κ (from left to right, $\kappa=1.50$, 1.00, and 0.67). (a) and (c) depict the results for constant drivings, whereas (b) and (d) depict those for linear drivings model. In all panels, squares, circles, and stars denote X_{2mS}, $X_{2M\eta}$, and X_{2MP}, respectively.

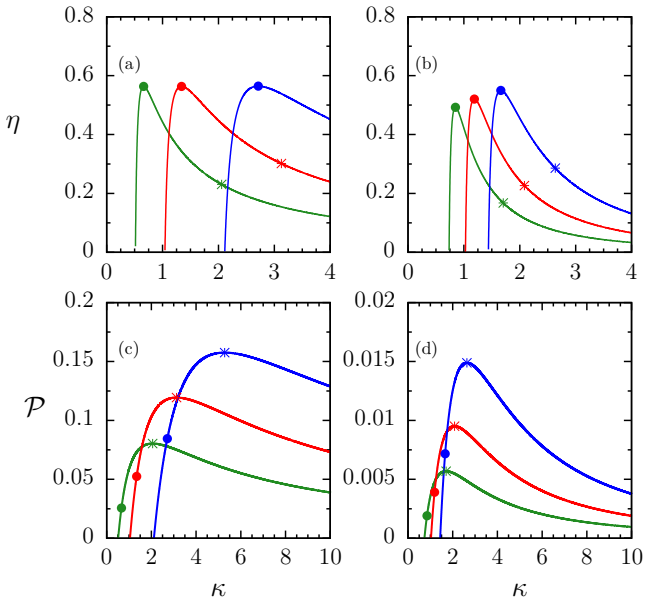

FIG. 3. Efficiency [(a) and (b)] and output power [(c) and (d)] (averaged over one period) for the isothermal work-to-work converter with $X_1=1$, $\tau=1$, $\gamma=1$, and different values of X_2 (from left to right, $X_2=-0.5$, -1.0, and -2.0). (a) and (c) depict the main results for the constant drivings model, while (b) and (d) depict those for the linear drivings model. In all panels, circles and stars denote $\kappa_{2M\eta}$ and κ_{2MP}, respectively. For such a set of parameters, the associated κ_{2mS}'s are out of the engine regime.

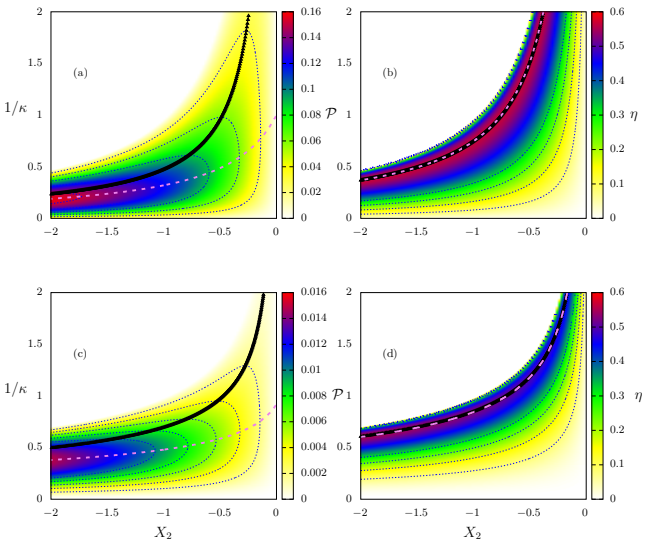

FIG. 4. For the isothermal work-to-work converter, the output power (left panels) and efficiency (right panels) for the constant [(a) and (b)] and linear [(c) and (d)] drivings models as a function of the inverse of the asymmetry parameter κ and loading forces X_2. Dotted lines represent constant value loci; dashed and solid lines represent maximization with respect to κ and X_2, respectively. Parameters: $\tau = 1,\ \gamma = 1,\ X_1 = 1$.

output for both force models as a function of the output force X_2 and asymmetry κ, respectively.

As discussed above, the engine regime operates for $X_{2m} < X_2 < 0$. An immediate advantage of the time asymmetry concerns the minimum output force X_{2m}, which decreases with κ, implying that the engine regime interval increases with the asymmetry (see Fig. 2). Such a trend is consistent with the absorption of energy (average work rate $\overline{W}_1$) for longer and longer times as κ increases. Furthermore, the minimum entropy production (represented by the squares in Fig. 2) coincides with the minimum loading force (vanishing power output and efficiency) for constant drivings, but not for the linear case (although, for the values of the parameters used in Fig. 2, X_{2mS} is so close to X_m that the difference is not discernible—it is of the order of 10^{-3}).

The maximum efficiencies are almost constant for the constant force model [Fig. 2(a)] and slightly increase with κ [Fig. 2(b)] for the linear force model. However, for small $|X_2|$, the efficiency is larger for the smaller values of κ. The effect of the time asymmetry on the output power is more pronounced. For both force models, the maximum power output clearly increases with κ.

Figure 4 depicts, for constant and linear drivings, a heat map for the power output and efficiency as a function of both the asymmetry and loading forces. For aesthetic reasons, they have been expressed in terms of $1/\kappa$ (instead of κ) in the vertical axis. It is noteworthy that the maximum efficiency curves, represented by the dashed (solid) lines for the maximization with respect to κ (loading force), are close to each other. Consequently, the choice of the parameter to maximize the efficiency is not important for either of the models presented here. Moreover, as previously discussed, the maximum efficiency is almost constant for the constant drivings model but increases with κ for the linear drivings one. In contrast to the maximum efficiencies, the maximum power curves [Figs. 4(a) and 4(c) for constant and linear drivings, respectively] present rather different behaviors depending on the optimization parameter. The $\mathcal{P}_{MP,\kappa}$ curves (dashed lines) always lie below the $\mathcal{P}_{MP,X_2}$ (solid lines) ones, and they approach each other as $\kappa \to \infty$.

Finally, it is worth pointing out that while both drivings provide similar efficiencies, the constant driving case is clearly more advantageous than the linear one in terms of the output power.

4. Simultaneous maximization of the asymmetry and the force

One may also raise the relevant issue of maximizing the power output and efficiency with respect to the asymmetry and output force strength simultaneously. Although this is not possible in some cases (as explained below), we will proceed with presenting the framework assuming that such maximization is possible. As before, we shall restrict the analysis to drivings presenting a single physical solution for Eqs. (34) and (35). If this is not the case, each maximum of these equations should be analyzed individually to assert which is the global maximum in each case.

Under the assumption above, the maximum power output must satisfy simultaneously Eqs. (34) and (41), that is, we must find the optimal value of the asymmetry κ^*_{MP} which satisfies the following condition:

$$\frac{L'_{21}(\kappa^*_{MP})}{L'_{22}(\kappa^*_{MP})} = \frac{1}{2}\frac{L_{21}(\kappa^*_{MP})}{L_{22}(\kappa^*_{MP})}. \tag{50}$$

Once the optimal asymmetry κ^*_{MP} is obtained, the optimal force X^*_{2MP} is calculated from Eq. (41) and given by

$$X^*_{2MP} = -\frac{1}{2}\frac{L_{21}(\kappa^*_{MP})}{L_{22}(\kappa^*_{MP})}X_1. \tag{51}$$

Graphically, the condition above is precisely the crossing point between lines for which the power (or efficiency) is maximized with respect to X_2 and κ. However, in some cases (as illustrated by the constant and linear drivings presented above) these two lines do not cross at all. The physical reason is that the power output keeps growing as $\kappa \to \infty$ (with an appropriate choice of value of X_2 for each κ). In other words, for such models, it is advantageous to apply a very large output force (in modulus) for a short period. Conversely, if the force model involves a rapidly decaying input driving $g_1(t)$ and growing output driving $g_2(t)$, an optimal output power may be found. In such a case, the power and efficiency at maximum power are readily evaluated as

$$\mathcal{P}^* = \frac{k_B T}{4}\frac{L^2_{21}(\kappa^*_{MP})}{L_{22}(\kappa^*_{MP})}X_1^2 \tag{52}$$

and

$$\eta^* = \frac{L^2_{21}(\kappa^*_{MP})}{4L_{11}(\kappa^*_{MP})L_{22}(\kappa^*_{MP}) - 2L_{21}(\kappa^*_{MP})L_{12}(\kappa^*_{MP})}. \tag{53}$$

Thereby, the optimal output power increases quadratically with the input force while the efficiency is completely determined by the driving force model. It is noteworthy that,

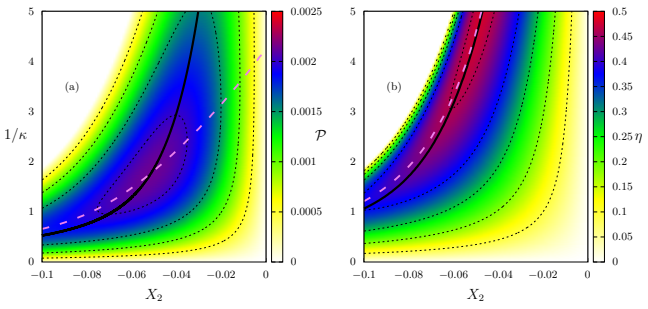

FIG. 5. For the exponential driving, depiction of output power (a) and efficiency (b) vs the inverse of the asymmetry coefficient κ and the output force X_2 for $\tau = 1$, $\gamma = 1$, and $X_1 = 1$. Dotted lines represent constant value loci; dashed and solid lines represent maximization with respect to κ and X_2, respectively.

despite the apparent temperature dependency of the power output in Eq. (52), the temperature cancels out when we use the expressions for the Onsager coefficients [see, e.g., Eq. (24)]. Similar expressions can be obtained for the simultaneous maximization of efficiency [by equaling the ratio X_2/X_1 from Eqs. (35) and (40)]. Since the expressions are more involved, we abstain from presenting them here. In order to illustrate the previous ideas, we consider an exponential driving given by

$$f_1(t) = X_1 e^{-9\gamma t}, \quad \text{for } 0 \leqslant t < \tau_1, \tag{54}$$

$$f_2(t) = X_2 e^{\gamma(t-\tau_1)}, \quad \text{for } \tau_1 \leqslant t < \tau. \tag{55}$$

Figures 5(a) and 5(b) depict, for the above exponential drivings, the heat maps of the output power and efficiency as functions of κ and X_2, respectively. Contrasting to the previous models, the crossing between maximum power curves is evident for the exponential drivings model above, and thereby the global optimization is possible. Although for the exponential model given by Eqs. (54) and (55) the crossing between maximum efficiency curves is absent, it does appear for other exponential driving choices [e.g., for $f_1(t) = X_1 e^{-7\gamma t}$ and $f_2(t) = X_2 e^{3\gamma(t-\tau_1)}$] and follow the theoretical prescription above.

B. Thermal engine

In this section, we derive general findings for thermal engines in which the particle is also exposed to distinct thermal baths in each stage. Although the power output $\mathcal{P}$ is the same as before (it does not depend on the temperatures), the efficiency may change because of the appearance of heat flow. Hence, in addition to the input energy received as work, the engine may also receive energy from the hot reservoir. Consequently, the maximization of power output with respect to the output force X_{2MP} or the asymmetry κ_{MP} is the same as before, but the corresponding efficiencies may differ (if $\overline{\dot{Q}}_1 < 0$ or $\overline{\dot{Q}}_2 < 0$) from such a case, following Eq. (31) instead. Anyhow, the efficiency of the engine for reservoirs with different temperatures is always smaller than or equal to that for isothermal reservoirs.

From Eq. (11), the average heat dissipated by the Brownian particle per cycle while in contact with the i reservoir $\overline{\dot{Q}}_i$ can be obtained as

$$\overline{\dot{Q}}_1 = \frac{m\gamma}{\tau}\left[\int_0^{\tau_1} \langle v_1\rangle^2 dt - C(\tau_1)(\Gamma_1 - \Gamma_2)\right], \tag{56}$$

$$\overline{\dot{Q}}_2 = \frac{m\gamma}{\tau}\left[\int_{\tau_1}^{\tau} \langle v_2\rangle^2 dt + C(\tau_1)(\Gamma_1 - \Gamma_2)\right], \tag{57}$$

where $C(\tau_1) = \operatorname{csch}(\gamma\tau)\sinh(\gamma\tau_1)\sinh(\gamma\tau_2)/2\gamma^2$ is strictly positive. Therefore, since the first term on the right-hand side of Eqs. (56) and (57) is positive, heat always flows into the colder reservoir. As with the hot reservoir, the heat may flow from or into the reservoir. For simplicity, we shall restrict our analysis to the case $\Gamma_1 > \Gamma_2$, that is, the first reservoir being the hot one, but it is worth pointing out that all of the discussion below is valid for $\Gamma_1 < \Gamma_2$ if we analyze Eq. (57) instead of Eq. (56).

For $\Gamma_1 > \Gamma_2$, Eq. (56) ensures that heat flows into the system if $\int_0^{\tau_1}\langle v_1\rangle^2 dt < C(\tau_1)(\Gamma_1 - \Gamma_2)$. Physically, this condition is a balance between kinetic energy that flows into the system due to the forces and the dissipation. If X_1 is strong enough (or if the difference in temperature of the reservoirs is small enough), energy flows into both reservoirs. Thereby, the engine effectively reduces to an isothermal work-to-work converter, so that the efficiency is still described by Eq. (33) and all results and findings from Sec. III A regarding the efficiency optimization hold. Moreover, for small enough temperature differences, the engine efficiency is larger than the Carnot efficiency. This is possible because work-to-work conversion is not bounded by the thermodynamics laws the same way heat-to-work conversion is [43]. Otherwise, the inequality above is satisfied, and energy flows from the first reservoir into the engine. For $\Gamma_1 < \Gamma_2$, the same energy balance occurs, but we need to assert the positiveness or negativeness of Eq. (57).

Furthermore, although exact, the achievement of general expressions for optimized efficiencies outside the isothermal work-to-work regime is more cumbersome than achieving the ones obtained for such a regime, making a general analysis unfeasible. Nevertheless, the discussion of a simple asymptotic limit is instructive. If the second term on the right-hand side of Eq. (56) [or Eq. (57)] is the dominant one, $|\Gamma_1 - \Gamma_2| \gg 1$ and $|\overline{\dot{Q}}_1| \gg |\overline{\dot{W}}_1|$ (or $|\overline{\dot{Q}}_2| \gg |\overline{\dot{W}}_1|$). Therefore the efficiency becomes $\eta \approx -\mathcal{P}/\overline{\dot{Q}}_1$ (or $\eta \approx -\mathcal{P}/\overline{\dot{Q}}_2$), which maximization, with respect to X_2, yields $X_{2M\eta} \approx X_{2MP}$ and follows Eq. (41). Hence the corresponding $\eta_{M\eta}$ approaches to the following expression:

$$\eta_{M\eta,X_2} \approx \frac{T_2}{8\gamma^2 T_i C(\tau_1)}\frac{L_{21}^2}{L_{22}}\tau X_1^2 \ll 1, \tag{58}$$

where T_i is the temperature of the hot reservoir. When the hot bath is the first reservoir, the fact that the efficiency is small is directly observable since the factor $T_2/T_1 \ll 1$. However, when the second reservoir is the hotter one, the temperature ratio becomes 1, and the smallness of the efficiency comes from the Onsager coefficients: $L_{21}^2/L_{22} \propto 1/T_2$. It is also worth mentioning that the apparent dependence on the period cancels out because the Onsager coefficients are proportional to $1/\tau$ [see Eq. (24)]. Therefore, for high

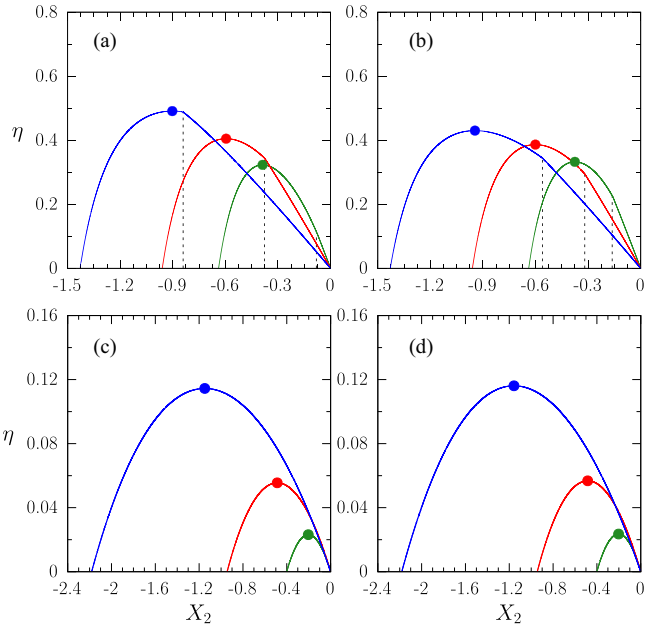

FIG. 6. Efficiency as a function of the force strength X_2 for the constant [(a) and (b)] and linear [(c) and (d)] drivings, respectively. Parameters: $\tau = 1$, $\gamma = 1$, and $X_1 = 1$ and distinct temperatures [$\Gamma_1 = 2.0$ and $\Gamma_2 = 1.5$ in (a) and (c) and $\Gamma_1 = 1.5$ and $\Gamma_2 = 2.0$ in (b) and (d)]. Circles denote maximum efficiencies, and their X_{2MP}'s are the same as in Fig. 2. From left to right, $\kappa = 1.50$, 1.00, and 0.67). Dashed vertical lines stand for the values of X_2 for which $\bar{Q}_i$ changes sign (i being the index of the hot reservoir).

temperature differences, the engine efficiency is very small for any value of the asymmetry.

In order to illustrate our findings for reservoirs with different temperatures, we consider the constant and linear drivings models presented above. Figure 6 exemplifies, for distinct temperature reservoirs, the efficiency for the same values of κ used in Fig. 2 for constant [Figs. 6(a) and 6(b)] and linear drivings [Figs. 6(c) and 6(d)], respectively. In Figs. 6(a) and 6(c) the temperature of the first reservoir is larger than that of the second reservoir, while Figs. 6(b) and 6(d) depict the other way around.

In accordance with general findings from Sec. III B, for constant drivings there are two regimes (the vertical lines in Fig. 6 denote the values of X_2 which separate them) for which the heat exchanged between the Brownian particle and the hot reservoir changes sign. Conversely, they are not present for the linear drivings model [Figs. 6(c) and 6(d)] because the heat exchange with the hot reservoir does not change sign for the parameters used in the figures. Since $\langle v_i \rangle^2$ increases with X_2^2, the term coming from the difference of temperatures in Eq. (56) dominates over it when $|X_2|$ is small, and hence the machine is less efficient than the isothermal work-to-work converter. Conversely, for large $|X_2|$ the engine may become as efficient as the isothermal work-to-work converter if the exchanged heat with the hot reservoir changes sign [left of the lines in Figs. 6(a) and 6(b)]. Anyhow, by comparing the performance of the isothermal case with the different-temperature case, we see that the decay in efficiency for linear drivings is more pronounced than that for constant drivings.

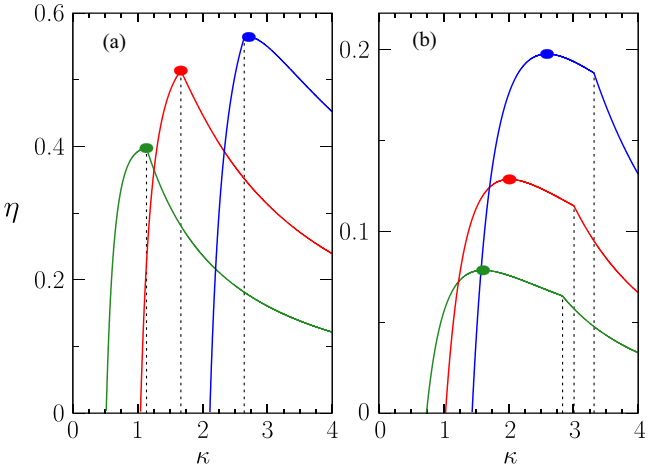

FIG. 7. Efficiency vs the time asymmetry κ for the (a) constant and (b) linear drivings, respectively, for $\tau = 1$, $\gamma = 1$, $X_1 = 1$, and different temperatures ($\Gamma_1 = 2.0$ and $\Gamma_2 = 1.5$). Circles denote maximum efficiencies, and their X_{2MP}'s are the same as in Fig. 3. From left to right, $X_2 = -0.5$, -1.0, and -2.0. Dashed vertical lines stand for the values of κ for which $\bar{Q}_1$ changes sign. For such a set of parameters, κ_{2mS} are out of the engine regime.

As for isothermal reservoirs, the machine performance always improves as κ increases, encompassing not only an extension of its operation regime X_{2m} but also a more pronounced increase in efficiencies, again, more substantial for linear drivings. Moreover, the asymmetry may be used to mitigate the drop in the efficiency produced by the different temperatures of the thermal reservoirs.

In Fig. 7, we show the efficiency as a function of the asymmetry for various values of X_2. Similarly to the previous figure, the vertical lines denote the values of κ for which the heat from the hot reservoir changes sign and delimit the isothermal work-to-work converter regime. The discussion of whether the isothermal work-to-work converter regime lies to the left or right of the vertical lines is not so obvious because both $C(\tau_1)$ and $\langle v_1 \rangle$ depend on the asymmetry. However, the work-to-work regime lies to the right of the lines, since the function $C(\tau_1)$ reaches its maximum for $\kappa = 1$ ($\tau_1 = \tau/2$) and the first term on the right-hand side of Eq. (56) is expected to increase given that its limit of integration increases with κ.

Figure 8 presents heat maps of the efficiency for different temperature reservoirs as a function of the output force and asymmetry. By drawing a comparison with the isothermal work-to-work converter (Fig. 4), it reveals that the difference in temperature makes the choice of the optimization parameter (force strength or time asymmetry) more relevant. While both optimized lines lie almost on top of each other for the isothermal case, Fig. 8 shows that they are clearly distinct, particularly for the linear drivings. Another point to be addressed concerns that high efficiencies are restricted to larger $|X_2|$'s for constant drivings when temperatures are different. This contrasts to its extension to smaller values for isothermal reservoirs [the hot (red) region in Fig. 4(b) has more spread than that in Fig. 8(a)]. Conversely, for linear drivings, the decrease in the efficiency extends for all values of κ and X_2 when compared with the isothermal work-to-work converter

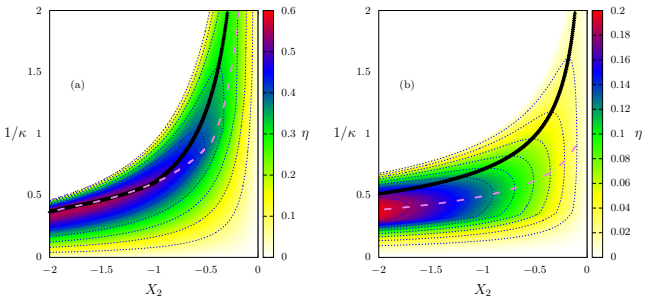

FIG. 8. Depiction of efficiency as a function of the inverse of the asymmetry coefficient κ and the output force X_2, for (a) constant and (b) linear drivings, respectively. Solid and dashed lines denote the maximization with respect to X_2 and κ, respectively. Parameters: $\Gamma_1 = 2.0$ and $\Gamma_2 = 1.5$, $\tau = 1$, $\gamma = 1$, and $X_1 = 1$.

[note that efficiency in Fig. 4(d) is three times larger than that in Fig. 8(b)]. However, larger efficiencies in such a case are obtained solely for larger values of $|X_2|$ in a certain range of κ.

Lastly, we draw a comparison between the efficiency given by Eq. (31) with Eq. (45) from Ref. [33], which is based on the ratio between the entropy production fluxes. Although both expressions behave similarly and approach each other as $\Delta\Gamma \to 0$ (or $\Delta\Gamma \ll 1$), it is worth mentioning that the latter overestimates the efficiency as $\Delta\Gamma$ increases.

IV. CONCLUSIONS

We introduced an alternative strategy for optimizing the performance of Brownian engines, based on the idea of asymmetric interaction time between the system (Brownian particle) and the thermal baths. Exact expressions for thermodynamic quantities and their maximized values were obtained, irrespective of the kind of driving and asymmetry. The time asymmetry can always be tuned to obtain a gain larger than in the symmetric case. In addition to the improvement of the power output and efficiency, the time asymmetry also enlarges the range of forces for which the system operates as an engine. Another advantage of asymmetric times is that they can be conveniently chosen for compensating part of the limitations due to the machine design, such as its operation period and the driving considered. Results for constant and linear drivings confirm that the appropriate tuning of the asymmetry produces gains for the efficiency substantially larger than those achieved for the symmetric case. It is important to point out that the symmetric engine does not necessarily operate inefficiently, as exemplified in Fig. 2. However, the tuning of the asymmetry, for given values of the other parameters (output force and period), provides a reliable route for enhancing the engine performance.

Contrariwise to usual machines, for which the heat flow due to the gradient of temperature is fundamental for the power extraction and enhancing the efficiency, in the present case the efficiency is higher for isothermal reservoirs. The reason for such behavior concerns that the energy exchange between the Brownian particle and the different thermal reservoirs occurs in different stages. Since the heat transfer and the output force are uncoupled, the heat flux cannot be converted into useful work. For instance, one would require drivings dependent on the velocity in order to be able to extract work from heat in the present model. Although the robustness of our findings has been verified for a few examples of drivings, our approach can be straightforwardly extended for other thermal machines, where in principle similar findings are expected. This is reinforced by recent results unveiling the importance of asymmetric times for optimizing the efficiency at maximum power of a quantum-dot thermal machine, which gain provides efficiencies larger than the Curzon-Ahlborn efficiency [44].

We finish this paper highlighting a couple of perspectives. While in this paper we analyzed the maximization of the output power and efficiency with respect to the time asymmetry and the output force strength, keeping the other parameters of the machine fixed, it might be worthwhile to study the maximization under different physical conditions, such as holding the dissipation or efficiency fixed. Finally, it might also be interesting to extend the role of asymmetric times for other kinds of drivings (e.g., velocity-dependent drivings providing extraction of useful work from heat) as well as for massive Brownian particles (underdamped case) in order to compare their performances.

ACKNOWLEDGMENTS

C.E.F. acknowledges the financial support from São Paulo Research Foundation (FAPESP) under Grants No. 2018/02405-1, No. 2021/05503-7, and No. 2021/03372-2. A.R. thanks Pronex/Fapesq-PB/CNPq (Grant No. 151/2018) and CNPq (Grant No. 308344/2018-9). The financial support from Coordenação de Aperfeiçoamento de Pessoal de Nível Superior, Brasil (CAPES) and CNPq are also acknowledged.

APPENDIX A: ONSAGER COEFFICIENTS AND LINEAR REGIMES

In this Appendix, we address the relation between coefficients $\tilde{L}_{ij}$ and Onsager coefficients L_{ij}. Our starting point is the steady-state entropy production averaged over one period, which is given by

$$\overline{\Pi} = \frac{2\gamma k_{\mathrm{B}}}{m}\left(\frac{\overline{\dot{Q}}_1}{\Gamma_1} + \frac{\overline{\dot{Q}}_2}{\Gamma_2}\right) = \overline{\Pi}_F + \overline{\Pi}_T. \tag{A1}$$

The coefficients $\tilde{L}_{ij}$ are straightforwardly obtained from $\overline{\Pi}_F$ performing the integration in Eq. (27) [in which the $\langle v_i\rangle(t)$'s

are given by Eq. (18)] as

$$\begin{aligned}
\tilde{L}_{11} &= \frac{\gamma}{\tau}\left[\frac{(e^{2\gamma(\tau-\tau_1)}-1)\hat{G}_1(\tau_1)^2}{\Gamma_2(e^{\gamma\tau}-1)^2}+\frac{\gamma}{\Gamma_1}\int_0^{\tau_1}\frac{2e^{-2\gamma t}\left[(e^{\gamma\tau}-1)\hat{G}_1(t)+\hat{G}_1(\tau_1)\right]^2}{(e^{\gamma\tau}-1)^2}\,dt\right],\\
\tilde{L}_{22} &= \frac{\gamma}{\tau}\left[\frac{(1-e^{-2\gamma\tau_1})\hat{G}_2(\tau)^2}{\Gamma_1(e^{\gamma\tau}-1)^2}+\frac{\gamma}{\Gamma_2}\int_{\tau_1}^{\tau}\frac{2e^{-2\gamma t}\left[(e^{\gamma\tau}-1)\hat{G}_2(t)+\hat{G}_2(\tau)\right]^2}{(e^{\gamma\tau}-1)^2}\,dt\right],\\
\tilde{L}_{12}+\tilde{L}_{21} &= \frac{2\gamma e^{-\gamma\tau_1}\hat{G}_1(\tau_1)\hat{G}_2(\tau)}{\tau(e^{\gamma\tau}-1)^2}\left[\frac{\sinh(\gamma\tau_1)}{\Gamma_1}+\frac{\sinh(\gamma(\tau-\tau_1))}{\Gamma_2}\right]\\
&\quad+\frac{2\gamma^2}{\Gamma_1\Gamma_2\tau(e^{\gamma\tau}-1)}\left[\Gamma_2\hat{G}_2(\tau)\int_0^{\tau_1}\hat{G}_1(t)e^{-2\gamma t}\,dt+\Gamma_1\hat{G}_1(\tau_1)\int_{\tau_1}^{\tau}\hat{G}_2(t)e^{\gamma(\tau-2t)}\,dt\right],
\end{aligned}\tag{A2}$$

where $\hat{G}_i(t)=\int_{\tau_{i-1}}^{t}g_i(t')dt'$. For equal temperatures $\Gamma_1=\Gamma_2=\Gamma$, $\overline{\Pi}$ reduces to the following expression:

$$\begin{aligned}
\overline{\Pi}=\overline{\Pi}_F &= -\frac{2\gamma k_{\mathrm{B}}}{m\Gamma}(\overline{\dot{W}}_1+\overline{\dot{W}}_2)\\
&= L_{11}X_1^2+(L_{12}+L_{21})X_1X_2+L_{22}X_2^2.
\end{aligned}\tag{A3}$$

Hence, for isothermal reservoirs, the entropy production can be written in terms of the Onsager coefficients even in the nonlinear (force) regime and thereby $\tilde{L}_{ij}=L_{ij}$. Conversely, for the thermal linear regime, it is convenient to express Γ_1 and Γ_2 in terms of the difference of temperatures $\Gamma_1=\Gamma-\Delta\Gamma$ and $\Gamma_2=\Gamma+\Delta\Gamma$. In such a case, Eq. (A1) becomes

$$\overline{\Pi}\approx\frac{2\gamma k_{\mathrm{B}}}{m\Gamma}\left[-(\overline{\dot{W}}_1+\overline{\dot{W}}_2)+(\overline{\dot{Q}}_1-\overline{\dot{Q}}_2)\frac{\Delta\Gamma}{\Gamma}\right].\tag{A4}$$

Let us assume that $\tilde{L}_{ij}$ can be expanded in a power series of the temperature difference, $\tilde{L}_{ij}=L_{ij}^{(0)}+L_{ij}^{(c)}\Delta\Gamma$, where $L_{ij}^{(0)}$ is the coefficient for $\Gamma_1=\Gamma_2=\Gamma$ and $L_{ij}^{(c)}$ is the first-order correction. In terms of such coefficients, the average entropy production $\overline{\Pi}$ is given by

$$\begin{aligned}
\overline{\Pi} &= \overline{\Pi}_F+\overline{\Pi}_T\\
&= \left[L_{11}^{(0)}X_1^2+\left(L_{12}^{(0)}+L_{21}^{(0)}\right)X_1X_2+L_{22}^{(0)}X_2^2\right]\\
&\quad+\left[L_{11}^{(c)}X_1^2+\left(L_{12}^{(c)}+L_{21}^{(c)}\right)X_1X_2+L_{22}^{(c)}X_2^2\right]\Delta\Gamma\\
&\quad+\frac{4L_{\Gamma\Gamma}}{\Gamma^2}(\Delta\Gamma)^2.
\end{aligned}\tag{A5}$$

By comparing Eqs. (A4) and (A5), it follows that

$$L_{11}^{(0)}X_1^2+\left(L_{12}^{(0)}+L_{21}^{(0)}\right)X_1X_2+L_{22}^{(0)}X_2^2=-\frac{2\gamma k_{\mathrm{B}}}{m\Gamma}(\overline{\dot{W}}_1+\overline{\dot{W}}_2),\tag{A6}$$

and hence Onsager coefficients L_{ij} correspond to zeroth-order coefficients $L_{ij}^{(0)}$ evaluated from $\overline{\Pi}_F$. Once again, they do not depend on $\Delta\Gamma$, since $\overline{\dot{W}}_i$ does not depend on the temperature at all.

In the true linear regime (both temperature gradient and force strength are small), the correction of $\overline{\Pi}_F$ is of third order $(X_iX_j\Delta\Gamma)$; thus it can be neglected. Hence the entropy production components $\overline{\Pi}_F$ and $\overline{\Pi}_T$ are approximately

$$\overline{\Pi}_F\approx-\frac{2\gamma k_{\mathrm{B}}}{m\Gamma}(\overline{\dot{W}}_1+\overline{\dot{W}}_2)\tag{A7}$$

and

$$\overline{\Pi}_T\approx\frac{4L_{\Gamma\Gamma}}{\Gamma^2}(\Delta\Gamma)^2,\tag{A8}$$

respectively. In addition, the coefficients $\tilde{L}_{ij}$ and L_{ij} are approximately equal, $\tilde{L}_{ij}\approx L_{ij}$.

APPENDIX B: CONSTANT DRIVINGS

For the machine operating at constant drivings, defined by the forces from Eqs. (46) and (47), the velocities $\langle v_i\rangle(t)$ are given by

$$\langle v_1\rangle(t)=\frac{X_1}{\gamma}+\frac{e^{-\gamma(t-\tau_1)}-e^{-\gamma(t-\tau)}}{e^{\gamma\tau}-1}\frac{X_1-X_2}{\gamma},\tag{B1}$$

$$\langle v_2\rangle(t)=\frac{X_2}{\gamma}+\frac{e^{-\gamma(t-\tau-\tau_1)}-e^{-\gamma(t-\tau)}}{e^{\gamma\tau}-1}\frac{X_1-X_2}{\gamma},\tag{B2}$$

for $i=1$ and 2, respectively. The associated Onsager coefficients are straightforwardly obtained from Eq. (24) and are given by

$$\begin{aligned}
L_{11} &= \frac{2\tau_1}{\Gamma_1\tau}-L_{12},\\
L_{22} &= \frac{2\tau_2}{\Gamma_2\tau}-L_{21},\\
L_{12} &= \frac{4\mathrm{csch}\left(\frac{\gamma\tau}{2}\right)\sinh\left(\frac{\gamma\tau_1}{2}\right)\sinh\left(\frac{1}{2}\gamma\tau_2\right)}{\gamma\Gamma_1\tau},\\
L_{21} &= \frac{4\mathrm{csch}\left(\frac{\gamma\tau}{2}\right)\sinh\left(\frac{\gamma\tau_1}{2}\right)\sinh\left(\frac{1}{2}\gamma\tau_2\right)}{\gamma\Gamma_2\tau}.
\end{aligned}\tag{B3}$$

Furthermore, for isothermal reservoirs, L_{12} and L_{21} are equal for any value of asymmetry parameter $\kappa=\tau_1/\tau_2$.

APPENDIX C: LINEAR DRIVINGS

Similarly to the constant drivings model, the average velocities for the linear driving model [defined by Eqs. (48) and

(49)] are obtained from Eq. (18) and are given by

$$\langle v_1\rangle(t) = \frac{1}{\gamma}\left\{X_1(\gamma t-1)+\frac{e^{-\gamma t}}{e^{\gamma\tau}-1}\left\{X_1\left[e^{\gamma\tau}+e^{\frac{\gamma\kappa\tau}{1+\kappa}}\left(\frac{\gamma\kappa\tau}{1+\kappa}-1\right)\right]-X_2\left[e^{\frac{\gamma\kappa\tau}{1+\kappa}}+e^{\gamma\tau}\left(\frac{\gamma\tau}{1+\kappa}-1\right)\right]\right\}\right\} \tag{C1}$$

and

$$\langle v_2\rangle(t) = \frac{1}{\gamma}\left\{X_2\left[1-\gamma\left(t-\frac{\kappa\tau}{1+\kappa}\right)\right]+\frac{e^{-\gamma\left(t-\frac{\kappa\tau}{1+\kappa}\right)}}{e^{\gamma\tau}-1}\left\{X_1\left[e^{\frac{\gamma\tau}{1+\kappa}}+e^{\gamma\tau}\left(\frac{\gamma\kappa\tau}{1+\kappa}-1\right)\right]-X_2\left[e^{\frac{\gamma\tau}{1+\kappa}}\left(\frac{\gamma\tau}{1+\kappa}-1\right)+e^{\gamma\tau}\right]\right\}\right\}. \tag{C2}$$

Likewise, Onsager coefficients L_{ij} are also straightforwardly calculated from Eq. (24) and read

$$\begin{aligned}
L_{11} &= \frac{2\gamma^3\tau_1^3+\left[6-3\gamma^2\tau_1^2\right]\coth\left(\frac{\gamma\tau}{2}\right)+6\mathrm{csch}\left(\frac{\gamma\tau}{2}\right)\left[\gamma\tau_1\sinh\left(\frac{\gamma(\tau_1-\tau_2)}{2}\right)-\cosh\left(\frac{\gamma(\tau_1-\tau_2)}{2}\right)\right]}{3\gamma\Gamma\tau},\\
L_{22} &= \frac{2\gamma^3\tau_2^3+\left[6-3\gamma^2\tau_2^2-6\cosh(\gamma\tau_1)\right]\coth\left(\frac{\gamma\tau}{2}\right)+6\gamma\tau_2\mathrm{csch}\left(\frac{\gamma\tau}{2}\right)\sinh\left(\frac{\gamma(\tau_2-\tau_1)}{2}\right)+6\sinh(\gamma\tau_1)}{3\gamma\Gamma\tau},\\
L_{12} &= \frac{2}{\gamma\tau\Gamma_1(1-e^{\gamma\tau})}[1+\gamma\tau_1-e^{\gamma\tau_1}][1-e^{\gamma\tau_2}(1-\gamma\tau_2)],\\
L_{21} &= \frac{2}{\gamma\tau\Gamma_2(1-e^{\gamma\tau})}[1+\gamma\tau_2-e^{\gamma\tau_2}][1-e^{\gamma\tau_1}(1-\gamma\tau_1)].
\end{aligned} \tag{C3}$$

Notably, contrasting to the constant drivings case, coefficients L_{12} and L_{21} are different from each other when $\Gamma_1=\Gamma_2$. Only for symmetric switching times ($\tau_1=\tau_2$) does it turn out that $L_{12}=L_{21}$.

[1] H. B. Callen, *Thermodynamics and an Introduction to Thermostatistics* (Wiley, New York, 1998).

[2] I. Prigogine, *Introduction to Thermodynamics of Irreversible Processes* (Interscience, New York, 1965).

[3] S. R. De Groot and P. Mazur, *On the Theory of the Refractive Index of Non-polar Gases. II. Statistical Part* (North-Holland, Amsterdam, 1962).

[4] U. Seifert, Stochastic thermodynamics, fluctuation theorems and molecular machines, Rep. Prog. Phys. **75**, 126001 (2012).

[5] C. Van den Broeck, Thermodynamic Efficiency at Maximum Power, Phys. Rev. Lett. **95**, 190602 (2005).

[6] G. Verley, M. Esposito, T. Willaert, and C. Van den Broeck, The unlikely Carnot efficiency, Nat. Commun. **5**, 4721 (2014).

[7] T. Schmiedl and U. Seifert, Efficiency at maximum power: An analytically solvable model for stochastic heat engines, EPL (Europhys. Lett.) **81**, 20003 (2007).

[8] M. Esposito, K. Lindenberg, and C. Van den Broeck, Universality of Efficiency at Maximum Power, Phys. Rev. Lett. **102**, 130602 (2009).

[9] B. Cleuren, B. Rutten, and C. Van den Broeck, Universality of efficiency at maximum power, Eur. Phys. J.: Spec. Top. **224**, 879 (2015).

[10] M. Esposito, R. Kawai, K. Lindenberg, and C. Van den Broeck, Quantum-dot Carnot engine at maximum power, Phys. Rev. E **81**, 041106 (2010).

[11] U. Seifert, Efficiency of Autonomous Soft Nanomachines at Maximum Power, Phys. Rev. Lett. **106**, 020601 (2011).

[12] Y. Izumida and K. Okuda, Efficiency at maximum power of minimally nonlinear irreversible heat engines, EPL (Europhys. Lett.) **97**, 10004 (2012).

[13] N. Golubeva and A. Imparato, Efficiency at Maximum Power of Interacting Molecular Machines, Phys. Rev. Lett. **109**, 190602 (2012).

[14] V. Holubec, An exactly solvable model of a stochastic heat engine: optimization of power, power fluctuations and efficiency, J. Stat. Mech.: Theory Exp. (2014) P05022.

[15] M. Bauer, K. Brandner, and U. Seifert, Optimal performance of periodically driven, stochastic heat engines under limited control, Phys. Rev. E **93**, 042112 (2016).

[16] K. Proesmans, B. Cleuren, and C. Van den Broeck, Power-Efficiency-Dissipation Relations in Linear Thermodynamics, Phys. Rev. Lett. **116**, 220601 (2016).

[17] Z. C. Tu, Efficiency at maximum power of Feynman's ratchet as a heat engine, J. Phys. A: Math. Theor. **41**, 312003 (2008).

[18] S. Ciliberto, Experiments in Stochastic Thermodynamics: Short History and Perspectives, Phys. Rev. X **7**, 021051 (2017).

[19] M. V. S. Bonança, Approaching Carnot efficiency at maximum power in linear response regime, J. Stat. Mech.: Theory Exp. (2019) 123203.

[20] B. Rutten, M. Esposito, and B. Cleuren, Reaching optimal efficiencies using nanosized photoelectric devices, Phys. Rev. B **80**, 235122 (2009).

[21] K. Proesmans and C. Van den Broeck, The underdamped Brownian duet and stochastic linear irreversible thermodynamics, Chaos **27**, 104601 (2017).

[22] I. A. Martínez, É. Roldán, L. Dinis, D. Petrov, J. M. R. Parrondo, and R. A. Rica, Brownian Carnot engine, Nat. Phys. **12**, 67 (2016).

[23] K. Proesmans, Y. Dreher, M. Gavrilov, J. Bechhoefer, and C. Van den Broeck, Brownian Duet: A Novel Tale of Thermodynamic Efficiency, Phys. Rev. X **6**, 041010 (2016).

[24] S. Krishnamurthy, S. Ghosh, D. Chatterji, R. Ganapathy, and A. K. Sood, A micrometre-sized heat engine operating between bacterial reservoirs, Nat. Phys. **12**, 1134 (2016).

[25] V. Blickle and C. Bechinger, Realization of a micrometre-sized stochastic heat engine, Nat. Phys. **8**, 143 (2012).

[26] P. A. Quinto-Su, A microscopic steam engine implemented in an optical tweezer, Nat. Commun. **5**, 5889 (2014).

[27] A. Kumar and J. Bechhoefer, Nanoscale virtual potentials using optical tweezers, Appl. Phys. Lett. **113**, 183702 (2018).

[28] M. Esposito, R. Kawai, K. Lindenberg, and C. Van den Broeck, Efficiency at Maximum Power of Low-Dissipation Carnot Engines, Phys. Rev. Lett. **105**, 150603 (2010).

[29] T. Schmiedl and U. Seifert, Optimal Finite-Time Processes in Stochastic Thermodynamics, Phys. Rev. Lett. **98**, 108301 (2007).

[30] N. Pancotti, M. Scandi, M. T. Mitchison, and M. Perarnau-Llobet, Speed-ups to Isothermality: Enhanced Quantum Thermal Machines through Control of the System-Bath Coupling, Phys. Rev. X **10**, 031015 (2020).

[31] N. Piccione, G. De Chiara, and B. Bellomo, Power maximization of two-stroke quantum thermal machines, Phys. Rev. A **103**, 032211 (2021).

[32] P. Abiuso and M. Perarnau-Llobet, Optimal Cycles for Low-Dissipation Heat Engines, Phys. Rev. Lett. **124**, 110606 (2020).

[33] A. L. L. Stable, C. E. F. Noa, W. G. C. Oropesa, and C. E. Fiore, Thermodynamics of collisional models for Brownian particles: General properties and efficiency, Phys. Rev. Research **2**, 043016 (2020).

[34] C. H. Bennett, The thermodynamics of computation—a review, Int. J. Theor. Phys. **21**, 905 (1982).

[35] K. Maruyama, F. Nori, and V. Vedral, Colloquium: The physics of Maxwell's demon and information, Rev. Mod. Phys. **81**, 1 (2009).

[36] T. Sagawa, Thermodynamic and logical reversibilities revisited, J. Stat. Mech.: Theory Exp. (2014) P03025.

[37] J. M. R. Parrondo, J. M. Horowitz, and T. Sagawa, Thermodynamics of information, Nat. Phys. **11**, 131 (2015).

[38] T. Tomé and M. J. De Oliveira, *Stochastic Dynamics and Irreversibility* (Springer, Cham, Switzerland, 2015).

[39] T. Tomé and M. J. de Oliveira, Entropy production in irreversible systems described by a Fokker-Planck equation, Phys. Rev. E **82**, 021120 (2010).

[40] T. Tomé and M. J. de Oliveira, Stochastic approach to equilibrium and nonequilibrium thermodynamics, Phys. Rev. E **91**, 042140 (2015).

[41] S. Liepelt and R. Lipowsky, Operation modes of the molecular motor kinesin, Phys. Rev. E **79**, 011917 (2009).

[42] B. Altaner, A. Wachtel, and J. Vollmer, Fluctuating currents in stochastic thermodynamics. II. Energy conversion and nonequilibrium response in kinesin models, Phys. Rev. E **92**, 042133 (2015).

[43] J. M. Horowitz and M. Esposito, Work producing reservoirs: Stochastic thermodynamics with generalized Gibbs ensembles, Phys. Rev. E **94**, 020102(R) (2016).

[44] P. E. Harunari, F. S. Filho, C. E. Fiore, and A. Rosas, Maximal power for heat engines: Role of asymmetric interaction times, Phys. Rev. Research **3**, 023194 (2021).

Phase behavior of a lattice-gas model for biaxial nematics

William G. C. Oropesa,[1,*] Eduardo S. Nascimento,[2,†] and André P. Vieira[1,‡]
[1]*Universidade de São Paulo, Instituto de Fisica, Rua do Matao, 1371, 05508-090, São Paulo, SP, Brazil*
[2]*Department of Physics, PUC-Rio, Rua Marquês de São Vicente 225, 22453-900 Rio de Janeiro, Rio de Janeiro, Brazil*

(Received 1 February 2022; accepted 4 April 2022; published 20 April 2022)

We employ a lattice-gas extension of the Maier-Saupe model with discrete orientation states to study the phase behavior of a statistical model for biaxial nematogenic units in mean-field theory. The phase behavior of the system is investigated in terms of the strength of isotropic interaction between anisotropic objects, as well as the degree of biaxiality and the concentration of those units. We obtain phase diagrams with isotropic phases and stable biaxial and uniaxial nematic structures, various phase coexistences, many types of critical and multicritical behaviors, such as ordinary vapor-liquid critical points, critical end points, and tricritical points, and distinct Landau-like multicritical points. Our results widen the possibilities of relating the phenomenological coefficients of the Landau–de Gennes expansion to microscopic parameters, allowing an improved interpretation of theoretical fittings to experimental data.

DOI: 10.1103/PhysRevE.105.044705

I. INTRODUCTION

Nematic mesophases are probably the simplest states of matter observed in liquid-crystalline systems that exhibit long-range orientational order in the absence of translational symmetry breaking [1–4]. Indeed, uniaxial nematic structures are characterized macroscopically by the existence of orientation-dependent physical properties (for example, optical or magnetic anisotropies), which lead to the definition of the director of a nematic phase. Notwithstanding, the breaking of isotropy in the plane perpendicular to the uniaxial director may lead to the elusive biaxial state, whose possibility was theoretically pointed out by Freiser [5] about 50 years ago. Experimentally, the existence of the biaxial phase was initially confirmed for lyotropic systems [6]. More recently, there have been claims of the identification of the phase in thermotropic systems composed of bent-core molecules, although this remains debatable (see Ref. [7] and references therein). In any case, these claims catalyzed various experimental, computational, and theoretical investigations [8,9] of candidate biaxial systems.

Most theoretical and computational studies looking for biaxial phases focus on the orientational order, leaving aside effects associated with a varying density of nematogens. Approaches based on the phenomenological Landau–de Gennes expansion [10] are able to partially remedy this situation by exploiting variations in the expansion coefficients, although these are difficult to connect with microscopic parameters. Our aim in this paper is to investigate the equilibrium phase diagrams of a statistical model in which nematogens with noncylindrical symmetry can move from site to site in a lattice whose occupation can be controlled. In our model, pairs of nematogens interact via an isotropic potential which can be repulsive or attractive, as well as via an anisotropic potential which favors a biaxial arrangement, leading, at sufficiently high occupation and sufficiently low temperature, to a biaxial phase.

Lattice models of nematic order have a long history in the literature. For uniaxial systems, the pioneering work of Lebwohl and Lasher [11] inspired a number of other investigations, including a lattice-gas extension by Bates [12,13]. For biaxial systems, the Luckhurst-Romano model [14], based on the truncation of an anisotropic potential to second-rank terms, has been likewise influential. As a rule, Monte Carlo calculations for nearest-neighbor versions of these models on fully occupied cubic lattices lead to the same qualitative predictions as those obtained from mean-field versions [15,16], despite sometimes substantial quantitative discrepancies [11,17].

A quite general bilinear anisotropic interaction potential V_{12} between two nematogens labeled as 1 and 2 was proposed by Straley [18]. In the two-tensor formulation of Sonnet *et al.* [19], it takes the form

$$V_{12} = -\tfrac{9}{4}A\{\mathbf{q}_1{:}\mathbf{q}_2 + \zeta(\mathbf{q}_1{:}\mathbf{b}_2 + \mathbf{b}_1{:}\mathbf{q}_2) + \lambda\mathbf{b}_1{:}\mathbf{b}_2\}. \quad (1)$$

In Eq. (1), $A > 0$ sets the energy scale, while the second-rank tensors $\mathbf{q}$ and $\mathbf{b}$ are defined in terms of mutually orthogonal unit vectors $\hat{n}_1$, $\hat{n}_2$, and $\hat{n}_3$ pointing along the first, second, and third principal axes of each nematogen as

$$\mathbf{q} = \hat{n}_1 \otimes \hat{n}_1 - \tfrac{1}{3}\mathbf{I} \quad \text{and} \quad \mathbf{b} = \hat{n}_2 \otimes \hat{n}_2 - \hat{n}_3 \otimes \hat{n}_3, \quad (2)$$

$\mathbf{I}$ being the 3×3 identity matrix. The operation $\mathbf{q}_1{:}\mathbf{q}_2$ is the Frobenius inner product [20], given by $\mathrm{Tr}(\mathbf{q}_1\mathbf{q}_2)$, where $\mathrm{Tr}\mathbf{M}$ is the trace of matrix $\mathbf{M}$. The adimensional parameters ζ and λ gauge the importance of biaxial couplings. If $\zeta = \lambda = 0$, Eq. (1) is reduced to the Maier-Saupe interaction energy [15],

*carreras@if.usp.br
†edusantos18@esp.puc-rio.br
‡apvieira@if.usp.br

defined solely by the relative orientation of the first principal axes of both nematogens. This is appropriate when dealing with nematogens whose form may be properly approximated as uniaxial. Otherwise, if the nematogens are intrinsically biaxial, a proper description of the interaction energy requires setting either ζ or λ to nonzero values, so that the relative orientations of other principal axes are also relevant. Here we work with the condition $\lambda = \zeta^2$, corresponding to the London approximation for dispersion forces [19], which allows us to write V_{12} in the form

$$V_{12} = -\frac{9}{4}A\left(\mathbf{q}_1 + \frac{\Delta}{3}\mathbf{b}_1\right):\left(\mathbf{q}_2 + \frac{\Delta}{3}\mathbf{b}_2\right). \tag{3}$$

By resorting to a simplified view of a biaxial nematogen as a rectangular platelet, the biaxiality parameter $\Delta = 3\zeta$ can be interpreted in terms of the sides of the platelet, so that $\Delta = 0$ would correspond to a "rodlike" object, $\Delta = 3$ to a "disklike" object, and $\Delta = 1$ to a maximally biaxial object [21].

In the same spirit as the lattice-gas version of the Lebwohl–Lasher model investigated by Bates [12], we allow each site of a regular lattice to be empty or occupied by a single nematogen, adding an isotropic interaction to the potential in Eq. (3) to obtain the contribution of two neighboring sites i and j to the total interaction energy of the system,

$$V_{ij} = \gamma_i\gamma_j\left\{U - \frac{9}{4}A\left(\mathbf{q}_i + \frac{\Delta}{3}\mathbf{b}_i\right):\left(\mathbf{q}_j + \frac{\Delta}{3}\mathbf{b}_j\right)\right\}. \tag{4}$$

The occupation variable γ_i is equal to 0 if site i is empty and to 1 if the site is occupied. In this work we allow the isotropic interaction parameter U to be either negative, representing attractive interactions, or positive, representing repulsion. This last case could lead to long-range sublattice ordering in cubic lattices, an unphysical feature for a fluid phase. At the mean-field level, however, describing such kind of arrangement would require the explicit introduction of sublattices. Instead, we proceed with the simplest mean-field strategy, which would be appropriate for describing a frustrated lattice or, for that matter, a fluid phase.

In order to perform detailed calculations, besides using Eq. (4) to describe the pair interactions, we also employ the Zwanzig approximation [22], which restricts the possible orientations of a nematogen to the coordinate axes. This approximation has been applied in different contexts [21,23–31], always leading to qualitative results which fully agree with continuous versions of the corresponding models when a comparison is possible. In particular, when dealing with intrinsically biaxial nematogens, these models are capable of reproducing the qualitative characteristics of nematic phase diagrams, such as sequences of biaxial-uniaxial-isotropic phase transitions with increasing temperature, and a well-defined Landau multicritical point, which signals a direct transition between the isotropic and the biaxial phases [28,31].

Therefore, in this work we investigate the phase diagrams of what may be characterized as a lattice-gas (LG) extension of the Maier-Saupe-Zwanzig model (MSZ), which from now on we will call the LGMSZ model. The LG extension introduces dilution as an extra ingredient in our model, allowing the study of phenomena such as vapor-liquid, vapor-nematic, and nematic-nematic (low-high concentration) coexistence. The study of such coexistences is not possible if we treat a model based on a fully occupied lattice.

This paper is organized as follows. Section II presents the model description and sketches its mean-field solution. In Sec. III we present a detailed analysis of the dilution effects, in the absence of isotropic interactions. Section IV is dedicated to the study of the effects of isotropic interactions for molecular systems with fixed degrees of biaxiality. In Sec. V we present an analysis of the effects of the biaxiality degree in the multicritical points present in the phase diagrams. Conclusions are drawn in Sec. VI. A few technical details are relegated to Appendices A and B.

II. THE LGMSZ MODEL

We consider a lattice system with N sites and N_m nonspherical objects such that $N \geqslant N_m$. Each lattice site can be either empty or occupied by an asymmetric object, the state of site i being described by an occupation variable γ_i taking the values 0 (empty site) or 1 (occupied site). Then, based on Eq. (4), we define the LGMSZ model by means of the effective Hamiltonian

$$\mathcal{H} = \sum_{(i,j)} V_{ij} = -A\sum_{(i,j)} \gamma_i\gamma_j \mathbf{\Omega}_i:\mathbf{\Omega}_j + U\sum_{(i,j)} \gamma_i\gamma_j, \tag{5}$$

where A and U are coupling parameters, with $A > 0$, the sum is performed over pairs (i, j) of neighboring sites i and j in the lattice, and the quantity $\mathbf{\Omega}_i$ is a second-rank tensor associated with the nematogen at site i. Specifically, $\mathbf{\Omega}_i$ is represented by a 3×3 square matrix with real entries. For nematogens, $\mathbf{\Omega}_i$ is a symmetric traceless matrix, its eigenvalues ω_i are real, and their sum is zero [1,8]. Then we can assume that $\omega_1 = (-1 + \Delta)/2$, $\omega_2 = (-1 - \Delta)/2$, and $\omega_3 = 1$, where the parameter Δ gauges the asymmetry or biaxiality degree of the object [21]: $\Delta = 0$ for rodlike shapes, $\Delta = 3$ for platelike shapes, and $\Delta \neq 0, 3$ for bricklike shapes. Biaxial objects with $\Delta = 1$ present a maximal degree of asymmetry. Instead of working with continuous orientational states, we follow the Zwanzig prescription [22] in assuming that the principal axes of a nematogen are restricted to align in the directions of the Cartesian axes, which leads to an effective spinlike model with six states described by diagonal matrices $\mathbf{\Omega}_i$ [21]. Notice that, in the limit $\Delta = 0$, Eq. (5) reduces to a discretized version of the Lebwohl-Lasher lattice-gas model introduced by Bates [12] (with a rescaling of energy, as our parameter A would be equivalent to $2\epsilon/3$, ϵ being the energy scale of the anisotropic interaction in Ref. [12]).

The first term in Eq. (5) represents a dilute version of the MSZ model, and the orientation-dependent interaction may give rise to distinct nematic phases. The second term is the isotropic contribution to the pair potential. For the particular case of $U < 0$, representing attractive isotropic interactions, one can find phase transitions between isotropic fluid states, in analogy with previous studies [12,13]. In the present work we assume that the parameter U can also be positive, representing repulsive interactions. In this latter case, as we are interested in modeling fluid phases only, we refrain from trying to account for any kind of sublattice ordering whatsoever.

Determining the thermodynamic properties of the lattice system defined by Eq. (5) is rather intricate, due to the

complex interplay between the various interactions. Therefore, we think it is appropriate to study the model in a mean-field treatment, which is equivalent to considering the fully connected Hamiltonian

$$\mathcal{H}_{\rm mf} = -\frac{A}{2N}\sum_{i,j=1}^{N}\gamma_i\gamma_j\mathbf{\Omega}_i{:}\mathbf{\Omega}_j + \frac{U}{2N}\sum_{i,j=1}^{N}\gamma_j\gamma_j, \tag{6}$$

where the sums over pairs of neighboring sites are replaced by sums over all pairs of sites, and the coupling parameters are replaced by new ones that are inversely proportional to the number of sites to ensure that energy is extensive. This form of effective, long-range model has been proposed to investigate the phase behavior of statistical models with nematic-like phases [21,24,28–30,32]. Therefore, our main interest is to study the thermodynamics of phases transitions of the mean-field model in Eq. (6).

The canonical ensemble is the usual route to investigate the macroscopic behavior of Hamiltonian systems in statistical mechanics. Nevertheless, because of its lattice-gas character, the configurations of microscopic variables of our model are subject to the restriction that the sum of γ_i over all lattice sites should be equal to N_m, which leads to complications in evaluating the canonical partition function. As a result, it is more convenient to consider the formalism of the grand canonical ensemble, where the number of nematogens may fluctuate due to the coupling to a particle reservoir [21,24,30]. Then we must determine the grand partition function

$$\Xi = \sum_{\{\gamma_i\}}\sum_{\{\mathbf{\Omega}_i\}}\exp\left(\beta\mathcal{H}_{\rm mf} + \beta\mu\sum_i\gamma_i\right), \tag{7}$$

where $\beta = 1/k_BT$, k_B is the Boltzmann constant (which we take to be equal to 1 in suitable units), T is the temperature, and μ is the chemical potential. In this ensemble, the sum over configurations in Eq. (7) is no longer restricted, and mean-field calculations are feasible, as indicated in Appendix A.

As a result, we obtain the Landau–de Gennes (grand-canonical) free-energy functional

$$\begin{aligned}\psi(S,\eta,\phi) = {}& \frac{A}{4}(3S^2+\eta^2) + \frac{U}{2}\phi^2 - \mu\phi \\ & + \frac{1}{\beta}\left[(1-\phi)\ln\left(\frac{1-\phi}{6}\right) + \phi\ln(\phi)\right] \\ & - \frac{\phi}{\beta}\ln[\Lambda(S,\eta)],\end{aligned} \tag{8}$$

where

$$\begin{aligned}\Lambda(S,\eta) = {}& 2\exp\left[-\frac{3\beta A}{4}(S+\eta)\right]\cosh\left[\frac{3\beta A}{4}\left(S-\frac{\eta}{3}\right)\Delta\right] \\ & + 2\exp\left[-\frac{3\beta A}{4}(S-\eta)\right]\cosh\left[\frac{3\beta A}{4}\left(S+\frac{\eta}{3}\right)\Delta\right] \\ & + 2\exp\left(\frac{3\beta A}{2}S\right)\cosh\left(\frac{\beta A}{2}\eta\Delta\right),\end{aligned} \tag{9}$$

ϕ is the concentration of nematogens,

$$\phi = \frac{1}{N}\left\langle\sum_{i=1}^{N}\gamma_i\right\rangle, \tag{10}$$

and the scalar parameters S and η are associated with the symmetric and traceless tensor order parameter [10]

$$\mathbf{Q} = \langle\mathbf{\Omega}\rangle = \frac{1}{2}\begin{pmatrix}-S-\eta & 0 & 0\\ 0 & -S+\eta & 0\\ 0 & 0 & 2S\end{pmatrix}, \tag{11}$$

in which $\langle\cdot\rangle$ denotes the ensemble average.

The equilibrium values of S, η, and ϕ are determined by locating the absolute minima of $\psi(S,\eta,\phi)$, leading to the mean-field (MF) equations

$$\frac{\partial\psi}{\partial S} = \frac{\partial\psi}{\partial\eta} = \frac{\partial\psi}{\partial\phi} = 0, \tag{12}$$

which take the self-consistent forms $S = F_1(S,\eta,\phi;\beta,\mu,\Delta)$, $\eta = F_2(S,\eta,\phi;\beta,\mu,\Delta)$, and $\phi = F_3(S,\eta,\phi;\beta,\mu,\Delta)$. Depending on the solutions to these mean-field equations, the structure of the eigenvalues Q_x, Q_y, Q_z of $\mathbf{Q}$ may be such that (1) $Q_x = Q_y = Q_z = 0$, corresponding to the isotropic phase; (2) $Q_x = Q_y \neq Q_z$ (or similar relations with permutations of the indices x, y and z), corresponding to an uniaxial nematic phase; and (3) Q_x, Q_y, and Q_z all distinct, corresponding to a biaxial nematic phase. If the eigenvalue with the largest absolute value is positive (negative), the nematic solution is calamitic (discotic). We use this terminology for both uniaxial and biaxial cases throughout the paper. In terms of the quantities S and η, the isotropic solution is given by $S = \eta = 0$, and uniaxial solutions are such that $S \neq 0$ with $\eta = 0$ or $\eta = \pm 3S$, while the remaining cases represent biaxial solutions.

We emphasize that the values of S, η, and ϕ at the absolute minima of ψ represent thermodynamic equilibrium values for fixed reciprocal temperature β, chemical potential μ, and biaxiality degree Δ. The (grand-canonical) free-energy $\mathcal{F} = \mathcal{F}(\beta,\mu,\Delta)$ of the system corresponds to the convex envelope of ψ determined after inserting values of S, η and ϕ associated with the minima of the free-energy functional.

III. BEHAVIOR IN THE ABSENCE OF THE ISOTROPIC INTERACTION

We start the investigation by assuming zero isotropic interaction, $U = 0$, which simplifies the analysis of the problem by reducing the number of parameters. Some aspects of this case were discussed by Rodrigues *et al.* [30], but taking into account only a specific range of model parameters. Here we will present phase diagrams with many distinct topologies by exploring a wider range of values of thermodynamic fields. The results with zero isotropic interaction are helpful in understanding the situation involving both isotropic and anisotropic couplings, to be analyzed in the next section.

By considering intrinsically rodlike nematogens, for which $\Delta = 0$, we find the phase diagram shown in Fig. 1(a), which is qualitatively equivalent and quantitatively similar to the one obtained by Monte Carlo simulations for the Lebwohl-Lasher lattice-gas model of Ref. [12], in the absence of isotropic interactions. At high concentration ($\phi \gtrsim 0.75$), as T decreases, the observed phase sequence is isotropic (ISO), followed by a biphasic region of coexisting rod-rich uniaxial nematic (N_U^+) and rod-poor isotropic phases, followed by a pure uniaxial nematic and finally a reentrant coexistence

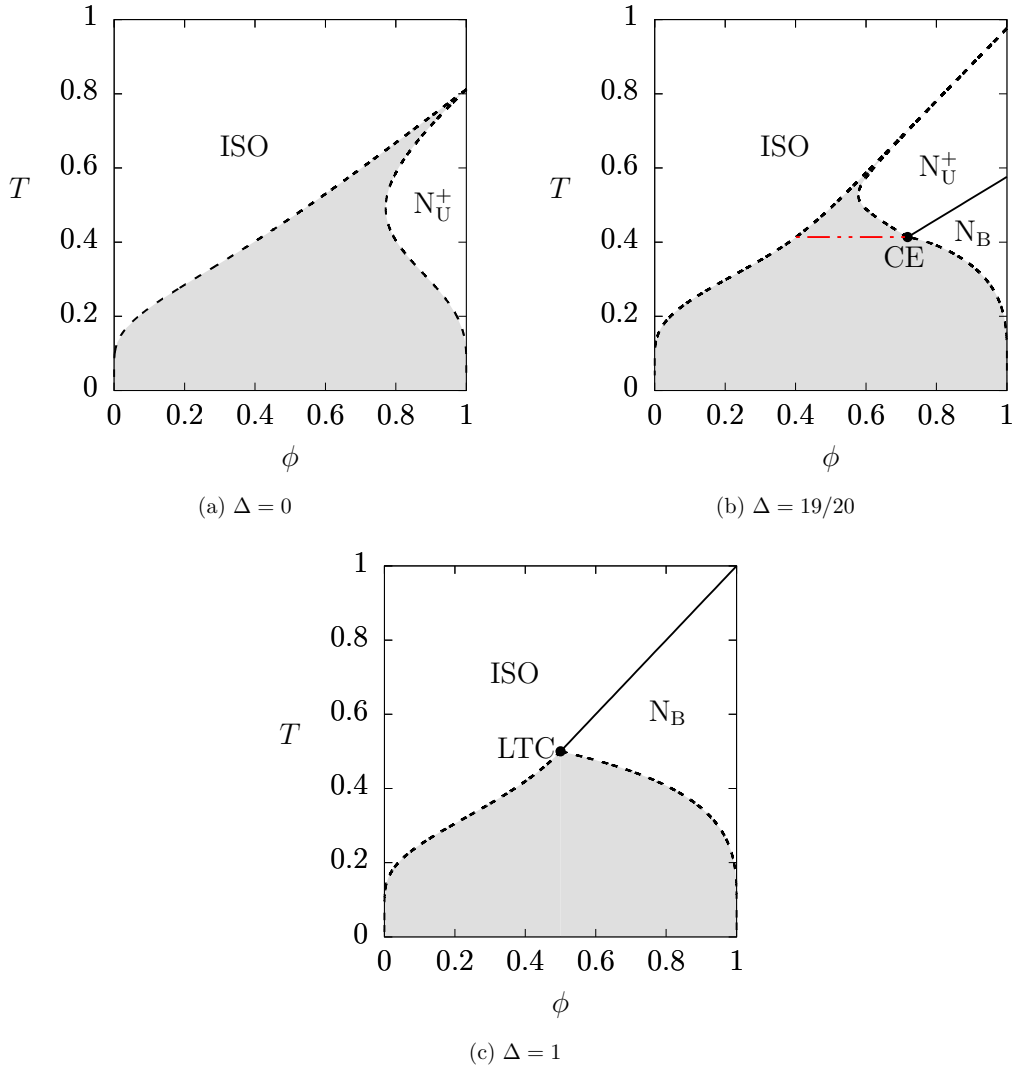

(a) $\Delta = 0$ (b) $\Delta = 19/20$ (c) $\Delta = 1$

FIG. 1. Phase diagram in terms of temperature T (in units of A) and concentration ϕ of nematogens, for different values of biaxiality degree and in the absence of isotropic interactions ($U = 0$). ISO: isotropic phase. N_U^+: calamitic uniaxial nematic phase. N_B: biaxial nematic phase. Short-dashed lines are the boundaries of biphasic region (gray). Red dot-dashed line: critical end point (CE). LTC is a Landau tricritical point.

region. At lower rod concentration the coexistence region is stable at low temperatures. The coexistence lines signaling the discontinuous transition from the isotropic phase to the uniaxial nematic phase are determined by Eq. (12) evaluated at $(S, \eta, \phi) = (S_U, 0, \phi_U)$ and at $(S, \eta, \phi) = (0, 0, \phi_I)$, supplemented by $\psi(S_U, 0, \phi_U) = \psi(0, 0, \phi_I)$, where ϕ_I and ϕ_U are, respectively, the concentrations of the isotropic and uniaxial phases at the transition point, and S_U is the value of S at that point. Notice that, since the nematogens are intrinsically uniaxial, we can assume $\eta = 0$ without loss of generality. It is worth mentioning that in the uniaxial limit of $\Delta = 0$ we see a single isotropic phase, with no sign of vapor-liquid coexistence, in agreement with Monte Carlo [33] and mean-field [34] calculations for the off-lattice hard-sphere Maier-Saupe model.

For the case of objects that are noncylindrical, $\Delta \neq 0$ and $\Delta \neq 3$, it is possible to observe stable biaxial phases (N_B), as shown in Fig. 1(b) for biaxiality degree $\Delta = 19/20$. In this diagram, at high concentrations and high temperatures, there is a small biphasic region of coexisting uniaxial and isotropic phases. As temperature decreases, we have a second-order transition from the N_U^+ phase to a pure N_B phase, and finally the biphasic region ISO-N_B appears. The conditions for determining the first-order transition between ISO and N_B are given by Eq. (12) evaluated at $(S, \eta, \phi) = (S_B, \eta_B, \phi_B)$ and at $(S, \eta, \phi) = (0, 0, \phi_I)$, as well as $\psi(S_B, \eta_B, \phi_B) = \psi(0, 0, \phi_I)$, where S_B and η_B are the values taken by S and η in the biaxial state at the transition point. On the other hand, the second-order transition between uniaxial and biaxial phases is located by Eq. (12) and $\partial^2\psi/\partial\eta^2 = 0$, all evaluated at $(S, \eta, \phi) = (S_o, 0, \phi_o)$, where S_o and ϕ_o are the values of S and ϕ at the transition point. We also find that the N_U^+-N_B transition line meets the ISO-N_B biphase region at a critical end point (CE), in which a critical nematic state separating uniaxial and biaxial phases coexists with a noncritical isotropic state. Critical end points are among the various possible multicritical points that can be found in thermodynamic systems with many components [2,35–37]. In our case, we have

critical end points related to nematic transitions in a lattice-gas model with orientation-dependent interactions. These kinds of multicritical points were also reported in a Maier-Saupe model that mimics binary mixtures of uniaxial and biaxial nematogens [21].

For anisotropic objects with maximal biaxiality degree, $\Delta = 1$, stable uniaxial phases are absent and the phase diagrams present the general aspect shown in Fig. 1(c). In this case, for high temperatures and high concentration, the ISO-N_B transition is continuous and determined by the conditions $\partial\psi/\partial\phi = \partial\psi/\partial\eta = \partial^2\psi/\partial\eta^2 = 0$, evaluated at the transition point $(S, \eta, \phi) = (0, 0, \phi_o)$. This line of continuous transitions is actually a line of multicritical Landau points. On the other hand, for low T and intermediate concentrations, we observe an ISO-N_B coexistence region associated with a first-order transition at which $\partial\psi/\partial\eta = \partial\psi/\partial\phi = 0$ at $(S, \eta, \phi) = (S_B, \eta_B, \phi_B)$, $\partial\psi/\partial\phi = 0$ at $(S, \eta, \phi) = (0, 0, \phi_I)$, and $\psi(S_B, \eta_B, \phi_B) = \psi(0, 0, \phi_I)$. The discontinuous and continuous transitions meet at a multicritical point which we call Landau tricritical (LTC) point. Roughly speaking, according to the solutions of mean-field equations, the multicritical point LTC has properties common to both Landau points [10] and tricritical points [35,36]. Notice that in the limit of a pure system (i.e., $\phi \to 1$) consisting of biaxial objects with $\Delta = 1$, our findings are in agreement with earlier mean-field results, which shown a direct ISO-N_B transition through a single, isolated Landau point in the Δ-T phase diagram [21,28].

It is possible to determine the conditions that characterize a Landau tricritical point by following the discussion presented by Rodrigues *et al.* [30]. Indeed, in our context, an LTC point is the endpoint of a line of Landau points, and a Landau point happens when the stable solutions of MF equations for ISO and $N_U^{\pm}$ become degenerate. Each point on a Landau line satisfies $\partial\psi/\partial\phi = d^2\psi/dS^2 = d^3\psi/dS^3 = 0$, evaluated at $(S, \eta, \phi) = (0, 0, \phi_L)$. Observe that these conditions involve partial derivatives as well as total derivatives (with respect to S) of the free-energy functional ψ. We must treat ϕ as an implicit function of S while calculating the total derivatives. Thus, one can find $\Delta = 1$, $(\beta A - 1)e^{\beta\mu} - 1 = 0$, and $\beta A\phi_L = 1$, which are the same results obtained in Ref. [30]. The solutions to these equations define a line of Landau points, which is represented by a solid line in Fig. 1(c). In the limiting case of maximum concentration of biaxial objects, i.e., $\beta\mu \gg 1$ or equivalently $\phi_L \to 1$, we recover the results obtained in previous treatments [21,28], apart from differences in the definitions of parameters. Nevertheless, we also have to check whether the solution leading to a Landau point corresponds to a minimum of the free-energy functional. This can be done by analyzing the behavior of the total fourth-order derivative of ψ with respect to η at $(S, \eta, \phi) = (0, 0, \phi_L)$, which gives $d^4\psi/d\eta^4 = -3A^4\beta^3\phi_L(1 - 2\phi_L)/8$. This total derivative should be positive for stable states, but we notice that it may change its sign from positive, for $\phi_L > 1/2$, to negative, for $\phi_L < 1/2$, indicating that the Landau point is stable only if $\phi_L > 1/2$ (implying $\beta A < 2$). Thus, precisely at $\phi_L = 1/2$, both $d^2\psi/d\eta^2$ and $d^4\psi/d\eta^4$ are zero, setting the conditions for locating a tricritical point that is also a Landau point. The coordinates of the LTC point are $(\beta A)_{LTC} = 2$, $\phi_{LTC} = 1/2$, and $\mu_{LTC} = 0$. The stability of the LTC point can be checked by looking at the sixth-order derivative of ψ with respect to η, which gives $d^6\psi/d\eta^6 = 2A > 0$, therefore corresponding to a free-energy minimum.

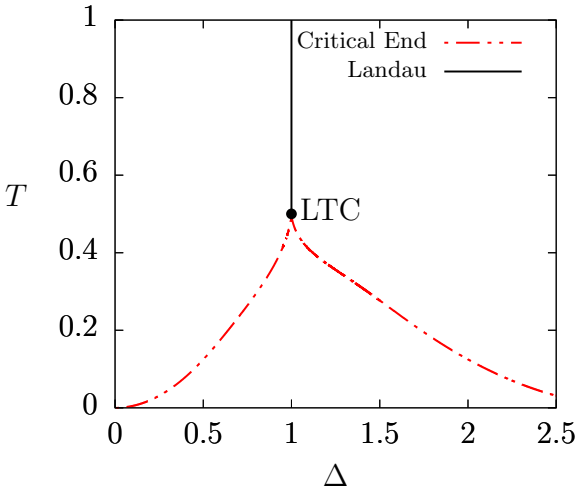

FIG. 2. Lines of multicritical points in the plane Δ-T for zero isotropic interaction. The line of Landau points (black solid) meets the lines of critical end points (red dot-dashed) at a Landau tricritical (LTC) point, which is present only for maximal biaxiality degree $\Delta = 1$.

We plotted all the lines of multicritical points obtained until now in the Δ-T plane shown in Fig. 2. It is worth mentioning that, as we are assuming zero isotropic interaction, the space of thermodynamic fields is spanned by temperature T, chemical potential μ, and biaxiality Δ. Due to that, the lines presented in Fig. 2 are critical solutions of MF equations with varying chemical potential. Besides, although we have focused the discussion on calamitic nematic phases, for which $0 < \Delta < 1$, the results for discotic nematics (see, e.g., Ref. [38]) with $1 < \Delta < 3$ lead to phase diagrams with analogous topologies. Observe that for systems with maximal biaxiality degree, the LTC point occurs when the line of Landau points meets the two lines of critical end points. The Landau tricritical point is present only for maximal biaxiality $\Delta = 1$.

We mention that the sequence of diagrams shown in Figs. 1(a)–1(c) for increasing biaxility parameter is reminiscent of the diagrams obtained from the mean-field treatment of the off-lattice Krieger-James model for ferronematics as the relative strength of the quadrupolar over dipolar interactions is increased [39]. In the latter model, a ferromagnetic phase replaces the biaxial phase of the LGMSZ model.

IV. BEHAVIOR IN THE PRESENCE OF THE ISOTROPIC INTERACTION

We now discuss phase diagrams in the presence of an isotropic interaction $U \neq 0$. In addition to uniaxial and biaxial structures, we may observe coexistence between isotropic fluid-like phases, which we call isotropic liquid (IL) and isotropic vapor (IV), as well as between nematic phases with different nematogen concentrations.

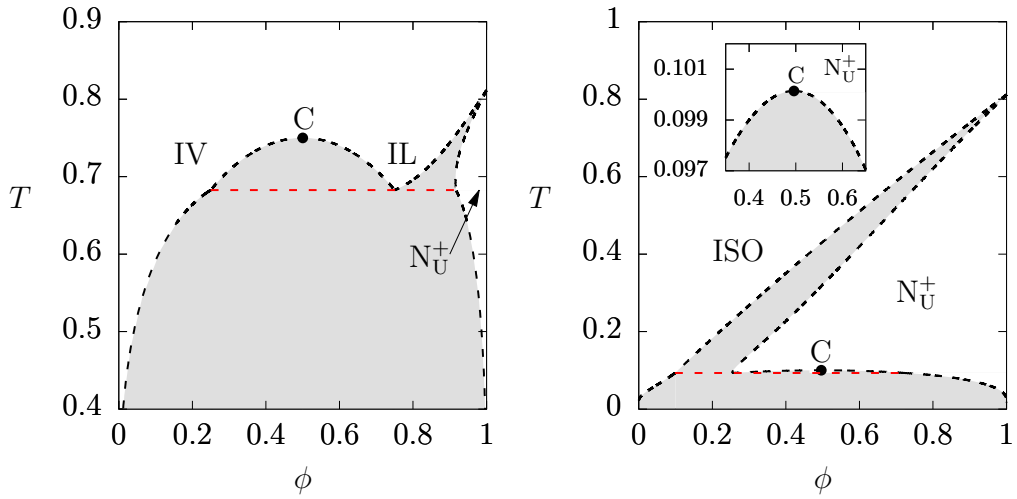

(a) $(A, U) = (1, -3)$ (b) $(A, U) = (1, 11/10)$

FIG. 3. Phase diagrams in terms of temperature T and concentration ϕ of nematogens, for an intrinsically uniaxial system ($\Delta = 0$). Red long-dashed line: triple point. Black short-dashed line: first-order transitions. C is a simple critical point.

A. Phase diagrams for uniaxial prolate nematogens ($\Delta = 0$)

For intrinsically uniaxial, rodlike objects, a sufficiently attractive ($U < 0$) isotropic interaction leads to the appearance of a vapor-liquid (or a high-density–low-density transition) coexistence analogous to the van der Walls condensation; see Fig. 3(a). The vapor-liquid transition is determined by $\partial\psi/\partial\phi = 0$ at $(S, \eta, \phi) = (0, 0, \phi_{\rm IV})$ and at $(S, \eta, \phi) = (0, 0, \phi_{\rm IL})$, in addition to $\psi(0, 0, \phi_{\rm IV}) = \psi(0, 0, \phi_{\rm IL})$. These first-order lines meet at a simple critical point (C), located at $\phi_{\rm C} = 1/2$, $\beta_{\rm C} = -4/U$, $\mu_{\rm C} = U/2$ with $\psi_{\rm C} = U[2\ln(12) - 1]/8$.

We also find a vapor-liquid-uniaxial triple point, which is determined by evaluating Eq. (12) at $(S, \eta, \phi) = (0, 0, \phi_{\rm IV})$, at $(S, \eta, \phi) = (0, 0, \phi_{\rm IL})$ and at $(S, \eta, \phi) = (S_{\rm U}, 0, \phi_{\rm U})$, in addition to imposing $\psi(0, 0, \phi_{\rm IV}) = \psi(0, 0, \phi_{\rm IL}) = \psi(S_{\rm U}, 0, \phi_{\rm U})$. For T values lower than the triple-point temperature, the IV-IL discontinuous transition becomes metastable with respect to the IV-N_U^+ first-order transition. As the strength $|U|$ of the attractive interaction increases, the region of stability of N_U^+ decreases and tends to become limited to a very small region near $\phi = 1$; see Fig. 3(a). This reduction in the area of the uniaxial phase was observed by Bates, using Monte Carlo simulations, in a lattice-gas extension of the Lebwohl-Lasher model [12] and later in the model proposed by Humphries *et al.* [13].

For repulsive isotropic interactions ($U > 0$), it is possible to notice the appearance of a very narrow coexistence region between uniaxial nematic phases, as shown in Fig. 3(b). This biphasic coexistence region between uniaxial structures presents an ordinary critical point C, which can be found by imposing the conditions $\partial\psi/\partial S = \partial\psi/\partial\phi = d^2\psi/d\phi^2 = d^3\psi/d\phi^3 = 0$, evaluated at $(S, \eta, \phi) = (S_{\rm C}, 0, \phi_{\rm C})$.

We plot the lines of critical points and of triple points in the U-T plane in Fig. 4. These lines meet at higher-order critical points, which we call multicritical end points (MCEs), in analogy with critical end points appearing when lines of first-order and second-order transitions meet. For $U < U^{(1)}_{\rm MCE} \approx -2.596$, we find phase diagrams with a simple critical point related to an IV-IL biphase region, in addition to a vapor-liquid-uniaxial triple point. This kind of phase phenomenon is associated with an attractive character of the isotropic interaction. Nevertheless, for $U > U^{(1)}_{\rm MCE}$, it is no longer possible to distinguish between the IV and IL phases, and from a thermodynamic perspective there is a single isotropic phase. Then we have phase diagrams which only show ISO-N_U coexistence regions.

In the case of repulsive isotropic interactions with $U < U^{(2)}_{\rm MCE} \approx 1.035$, the phase diagrams also exhibit first-order

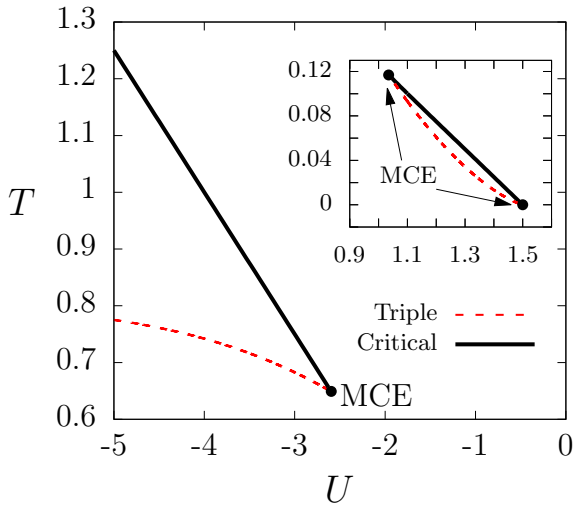

FIG. 4. Lines of critical and of triple points in the U-T plane, for the case of rodlike nematogens ($\Delta = 0$). We notice that the lines of critical points meet the lines of triple points at higher-order multicritical end points (MCEs). The inset shows the case for repulsive isotropic interaction ($U > 0$).

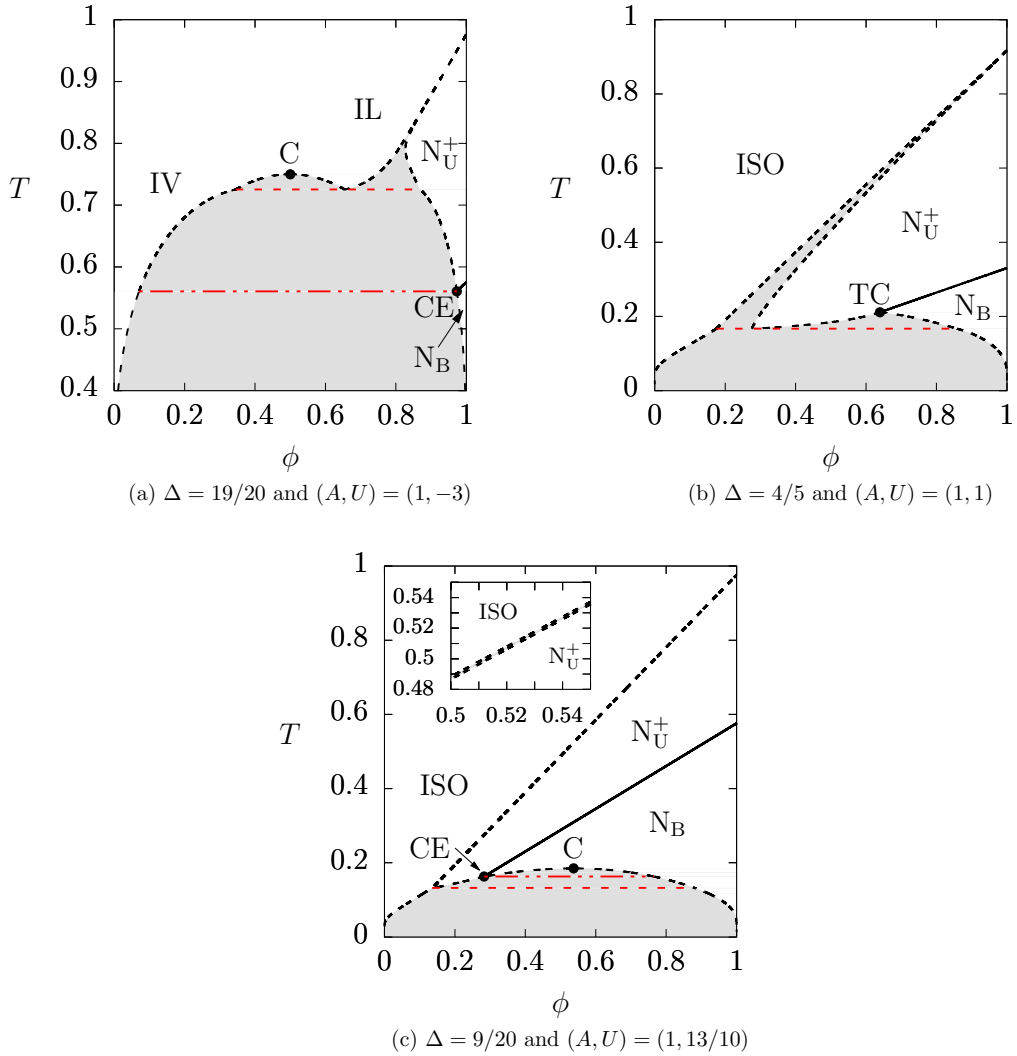

(a) $\Delta = 19/20$ and $(A, U) = (1, -3)$

(b) $\Delta = 4/5$ and $(A, U) = (1, 1)$

(c) $\Delta = 9/20$ and $(A, U) = (1, 13/10)$

FIG. 5. Phase diagrams in terms of temperature T (in units of A) and concentration ϕ of nematogens, for different values of the biaxiality degree. The red long-dashed line represents a triple point. The red dot-dashed line is associated with a critical end point (CE), while C is a critical point and TC is a tricritical point. The inset shows the isotropic-uniaxial coexistence region.

transitions between isotropic and uniaxial phases. However, for $U_{\mathrm{MCE}}^{(2)} < U < U_{\mathrm{MCE}}^{(3)} = 3/2$, as illustrated in Fig. 3(b), it is possible to find phase diagrams exhibiting a coexistence region between uniaxial structures, with an associated critical point, as well as a triple point connecting one isotropic and two uniaxial states. As U increases, we notice a decrease in the area of the low-temperature isotropic-uniaxial coexistence region, together with the decrease in the temperature of the critical and the triple points, until the ISO-N_U coexistence disappears completely as $U \to U_{\mathrm{MCE}}^{(3)}$. For this limiting value of U, the temperatures both of the critical point and of the triple point become zero.

The sequence of diagrams in Figs. 3(a) and 3(b) obtained from the LGMSZ model as the isotropic interaction is tuned from attractive to repulsive, including the phase coexistences, is qualitatively equivalent to the ones obtained from the off-lattice Maier-Saupe model augmented by isotropic interactions [34,40]. Other systems with similar sequences are mixtures of rodlike colloidal particles and hard-sphere polymers with varying diameters [41], binary mixtures of thermotropic nematogens with increasing dissimilarity [42], and long hard rods with short-range attractions with changing rod length or attraction range [43,44].

B. Phase diagrams for $0 < \Delta < 1$

As previously mentioned, the discrete-state Maier-Saupe model presents phase diagrams with stable biaxial structures when the nematogens are intrinsically biaxial [21,28]. Then, we expect that the presence of dilution and isotropic interactions may lead to phase diagrams with more elaborate topologies. Indeed, for systems with attractive isotropic interactions, we obtain phase diagrams of the type shown in Fig. 5(a). In this case, we have a critical point C associated with an IV-IL biphasic region, and an IV-IL-N_U^+ triple point, analogous to those discussed in Sec. IV A for intrinsically uniaxial nematogens. We also find an IV-N_B discontinuous transition, determined by the conditions in Eq. (12), evaluated at $(S, \eta, \phi) = (0, 0, \phi_{\mathrm{IV}})$ and at $(S, \eta, \phi) = (S_B, \eta_B, \phi_B)$, supplemented by $\psi(0, 0, \phi_{\mathrm{IV}}) = \psi(S_B, \eta_B, \phi_B)$.

The coexistence between the biaxial phase and the isotropic vapor is verified at low temperatures, below the temperature of a critical end point CE ($T_{CE} \approx 0.56$ in the figure), whose location is set by Eq. (12), evaluated at $(S, \eta, \phi) = (0, 0, \phi_{IV})$ and at $(S, \eta, \phi) = (S_{CE}, 0, \phi_{CE})$, supplemented by $\psi(0, 0, \phi_{IV}) = \psi(S_{CE}, 0, \phi_{CE})$ and $\partial^2\psi/\partial\eta^2 = 0$ at $(S, \eta, \phi) = (S_{CE}, 0, \phi_{CE})$. The biaxial nematic phase is stable for high concentrations and small temperatures.

Let us now consider repulsive isotropic interactions, $(A, U) = (1, 1)$, with biaxiality degree $\Delta = 4/5$. The phase diagram is shown in Fig. 5(b), where it is possible to identify a triple point in which isotropic, uniaxial, and biaxial phases coexist, as well as a tricritical point (TC), which satisfies the conditions $\partial\psi/\partial\phi = \partial\psi/\partial S = d^2\psi/d\eta^2 = d^4\psi/d\eta^4 = 0$, evaluated at $(S, \eta, \phi) = (S_{TC}, 0, \phi_{TC})$. The total derivatives are determined by treating S and ϕ as implicit functions of η. The boundaries of the coexistence region associated with uniaxial and biaxial phases are determined by Eq. (12) evaluated at $(S, \eta, \phi) = (S_U, 0, \phi_U)$ and at $(S, \eta, \phi) = (S_B, \eta_B, \phi_B)$, as well as $\psi(S_U, 0, \phi_U) = \psi(S_B, \eta_B, \phi_B)$. We also show in Fig. 5(c) the phase diagram corresponding to the repulsive case with $\Delta = 19/20$ and $(A, U) = (1, 13/10)$. There are biphasic regions associated with ISO and N_U^+, N_U^+, and N_B, and ISO and N_B. Besides, there is a triple point marking the coexistence of ISO, N_U^+ and N_B. Finally, we observe the presence of a biaxial-biaxial coexistence region, whose boundaries are determined by Eq. (12) evaluated at $(S, \eta, \phi) = (S_1, \eta_1, \phi_1)$ and at $(S, \eta, \phi) = (S_2, \eta_2, \phi_2)$, supplemented by $\psi(S_1, \eta_1, \phi_1) = \psi(S_2, \eta_2, \phi_2)$.

C. Phase diagrams for $\Delta = 1$

Following our discussion in Sec. III, we can obtain the conditions leading to Landau points for the maximal biaxiality degree and investigate the possible presence of Landau tricritical points. Indeed, we find analogous features when nonzero isotropic interactions are considered. Nevertheless, the parameter U plays an important role in the criteria for determining the LTC point. After performing the calculation, we find that the coordinates of the Landau point satisfy $(\beta A - 1)e^{\beta\mu} = e^{U/A}$ and $\beta A\phi = 1$. For $\mu \to \infty$, i.e., in the limit of a fully occupied lattice, we recover the expected phase diagram with $\beta A = 1$ at the Landau point, whereas for $U/A \to 0$, we obtain the results discussed in Sec. III. As we already know, the stability of a Landau point is related to the existence of an absolute minimum of the free-energy functional, and high-order derivatives should be considered because we are dealing with a multicritical point. The fourth-order derivative is

$$\left.\frac{d^4\psi}{d\eta^4}\right|_{(0,0,\phi)} = -\frac{3}{8}A^3\beta^2\left[\frac{U + A^2\beta - A(2 + \beta U)}{A^2\beta + U(\beta A - 1)}\right]. \quad (13)$$

This fourth-order derivative changes sign when $A(A - U)\beta = 2A - U$, which sets the condition for a possible LTC point. Notice that, as long as the isotropic interaction is attractive ($U < 0$), there is always a candidate Landau tricritical point (since β must be positive). However, as in the case $U = 0$, the stability of that point for $U \neq 0$ must be checked by looking at the sixth-order derivative of ψ with respect to η,

$$\left.\frac{d^6\psi}{d\eta^6}\right|_{(0,0,\phi)} = \frac{(U - 2A)^4(8A^2 - 30AU + 15U^2)}{64A(A - U)^4}. \quad (14)$$

We then note that, since $A > 0$, any LTC points are locally unstable if the isotropic interaction is repulsive ($U > 0$) and such that $0.32 \lesssim U/A \lesssim 1.68$.

For $U < 0$, the LTC point is always locally stable, although it may not correspond to an absolute minimum of the free-energy functional. This is the case for $U = -5$, as shown by the phase diagram in Fig. 6(a). There is a wide coexistence region associated with isotropic phases of vapor and liquid, and an ordinary critical point (C). For high concentrations, as T decreases, there exists a continuous transition from the IL phase to the N_B phase. Additionally, for a fixed sufficiently low temperature, by varying the concentration we enter a coexistence region between the IV and the N_B phases. The line of continuous transition consists of Landau points, and that line meets the coexistence regions at a Landau critical end point (LE). On the other hand, for isotropic interaction $U = -3$, we obtain the phase diagram exhibited in Fig. 6(b). In this diagram, we now observe an LTC point, i.e., the LE point is not stable, and there also exists a triple point related to the IL, IV, and N_B phases. When the isotropic interaction is sufficiently repulsive, we have a biaxial-biaxial coexistence region, as shown in Fig. 6(c). This biphasic region presents a critical point C and a Landau critical end point LE. For phase diagrams with $U > 2$, there are no coexistence regions and we observe only second-order transitions between the ISO and N_B phases; see Appendix B.

Notice that the sequence of phase-diagram topologies shown in Figs. 6(a)–6(c) as the isotropic interaction is tuned from attractive to repulsive for maximally biaxial nematogens is equivalent to the sequence observed for off-lattice dipolar fluids [45–52], the biaxial phase being replaced by the ferromagnetic or ferroelectric phases.

For the particular case $\Delta = 1$ we can plot a graph in the U-T plane showing the multicritical points found for maximal biaxiality; see Fig. 7. The corresponding phase diagrams in the ϕ-T plane present a line of Landau points regardless of the character of the isotropic interaction. The stability limits of points belonging to these Landau lines are (1) at high temperatures, the point $(\phi, T) = (1, 1)$ (fully occupied lattice) and (2) at low temperatures, a multicritical point whose nature depends on the value of U. In the U-T plane, the stable Landau points occupy an extensive region which we call the Landau zone. The boundaries of this region are the line $(\phi, T) = (1, 1)$ and the lines of Landau critical end points and Landau tricritical points, which meet at multicritical Landau points ML_2 and ML_3. We also find a higher-order multicritical end point MCE related to a line of triple points. These triple points are associated with coexisting vapor, liquid and biaxial phases. Observe that the MCE point occurs when the line of triple points meets a line of critical points.

V. MULTICRITICAL POINTS IN THE BIAXIALITY-TEMPERATURE PLANE

We may summarize the different topologies of the ϕ-T phase diagrams of the model by constructing diagrams of

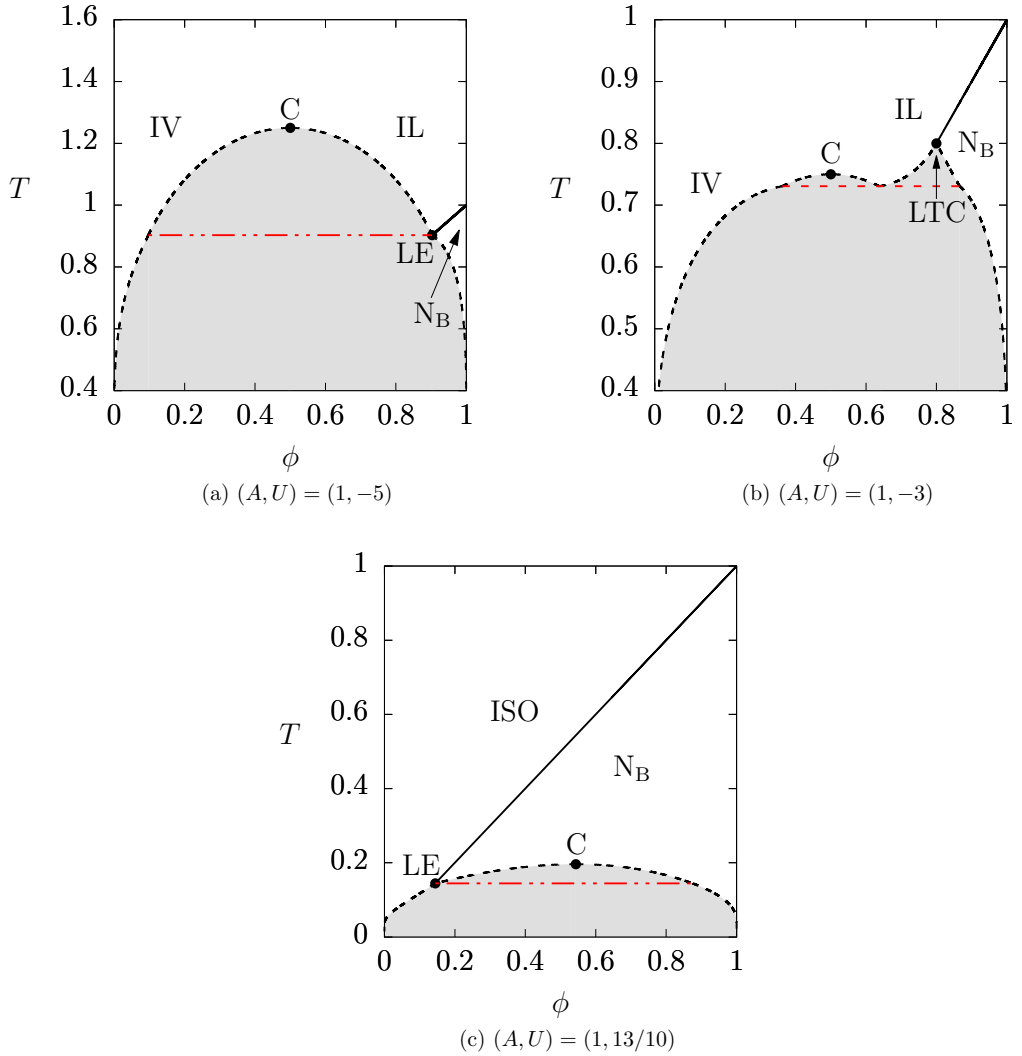

(a) $(A, U) = (1, -5)$ (b) $(A, U) = (1, -3)$

(c) $(A, U) = (1, 13/10)$

FIG. 6. Phase diagram in terms of temperature T (in units of A) and concentration ϕ of nematogens, for maximal biaxiality degree $\Delta = 1$. The red long-dashed line represents a triple point. The red dot-dashed line represents a Landau critical end point (LE). C is a critical point.

multicritical points in the plane Δ-T for a fixed value of U, as shown in Fig. 8. Thus, given a nematic-like system with parameters (A, U), we can determine the multicritical points in the ϕ-T phase diagrams for different values of Δ. Due to the large parameter space, we focus on only some representative values of the isotropic interaction U.

A. Case with $U < 0$

By assuming attractive isotropic interactions with $(A, U) = (1, -3)$, we obtain the Δ-T diagram shown in Fig. 8(a). We notice that the line of triple points meets the lines of critical end points at higher-order multicritical points $M_1^{\pm}$. Besides, the line of ordinary critical points meets the line of triple points at the higher-order multicritical end point MCE. For $\Delta < \Delta_1^+ \approx 0.994$, where $\Delta_1^{\pm}$ are the values of Δ at $M_1^{\pm}$, phase diagrams in the ϕ-T plane exhibit ordinary critical points related to vapor-liquid biphasic regions, critical end points (CEs), and vapor-liquid-uniaxial triple points, a topology exemplified in Fig. 5(a). Precisely at $\Delta = \Delta_1^+$, the lines of CE and triple points meet at the temperature $T_1^+ \approx 0.7298$. For values of model parameters corresponding to $M_1^{\pm}$, ϕ-T phase diagrams do not exhibit a coexistence region between the isotropic vapor and the uniaxial phases. In the range $\Delta_1^+ < \Delta < 1$, the temperature of the CE point is higher than that of the triple point, which now represents a coexistence of isotropic (vapor and liquid) and biaxial phases. For maximal biaxiality $\Delta = 1$, only isotropic and biaxial phases are stable, and ϕ-T phase diagrams are characterized by an ordinary vapor-liquid critical point, a Landau line, and, depending on the value of $U < 0$, a Landau tricritical point, as in Fig. 6(b), or a Landau end point, as in Fig. 6(a).

On the other hand, for $1 < \Delta < \Delta_1^- \approx 1.006$, the ϕ-T phase diagrams may exhibit uniaxial discotic phases, whose region of stability increases with Δ. In addition, we have CE points and vapor-liquid-biaxial triple points, producing the same topology as in Fig. 5(a). When $\Delta = \Delta_1^-$, the lines of CE and triple points meet at the temperature $T_1^- \approx 0.7322$. For $\Delta_1^- < \Delta < \Delta_{MCE} \approx 1.063$, the ϕ-T phase diagrams also present CE points and vapor-liquid-biaxial triple points

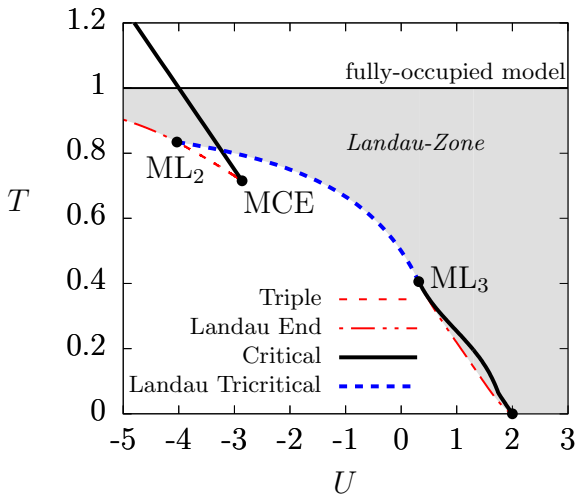

FIG. 7. Lines of multicritical points in the U-T plane for the case of maximal biaxiality parameter $\Delta = 1$. The gray region marked as a "Landau zone" consists of Landau points associated with different concentrations. ML_2 and ML_3 are higher-order Landau multicritical points. MCE is a higher-order multicritical end point.

whose temperature approaches that of the vapor-liquid critical point as $\Delta \to \Delta_{\rm MCE}$. For biaxiality degree $\Delta = \Delta_{\rm MCE}$, the vapor-liquid-biaxial triple point and the ordinary vapor-liquid critical point meet at the temperature $T_{\rm MCE} = 3/4$, and we cannot distinguish isotropic vapor and liquid phases. For nematic systems with $\Delta_{\rm MCE} < \Delta < 3$, the topology of the ϕ-T phase diagrams is the same as the one shown in Fig. 1(b), the only multicritical point being a CE point separating regions of coexistence between the low-concentration isotropic phase and the high-concentration biaxial (at low temperatures) or uniaxial (at higher temperatures) phases. For the intrinsically uniaxial cases $\Delta = 0$ or $\Delta = 3$, the phase diagrams exhibit only isotropic and uniaxial phases, as exemplified in Sec. IV A.

B. Case with $U > 0$

Now, by considering repulsive isotropic interactions with $(A, U) = (1, 1)$, we obtain the multicritical lines shown in Fig. 8(b). Here lines of CE, tricritical, and triple points meet at multicritical points $M_2^{\pm}$. We also have the multicritical points $M_3^{\pm}$, where lines of CE, triple, and ordinary critical points meet. The topology of the ϕ-T phase diagrams is essentially symmetric with respect to the axis $\Delta = 1$, except for the change in character of the uniaxial phases, from calamitic (for $0 \leqslant \Delta < 1$) to discotic (for $1 < \Delta \leqslant 3$).

In the ranges $0 < \Delta < \Delta_2^+ \approx 0.525$ or $\Delta_2^- \approx 1.3743 < \Delta < 3$, where $\Delta_i^{\pm}$ is the biaxiality parameter at $M_i^{\pm}$, the topology of the ϕ-T phase diagrams is the same as the one shown in Fig. 1(b), and the temperature of the CE point increases as the value of Δ becomes closer to 1. For biaxiality in the ranges $\Delta_2^+ < \Delta < \Delta_3^+ \approx 0.872$ or $\Delta_3^- \approx 1.115 < \Delta < \Delta_2^-$, there exist isotropic-uniaxial and uniaxial-biaxial coexistence regions, as well as a tricritical (TC) point, as illustrated in Fig. 5(b). Finally, for $\Delta_3^+ < \Delta < \Delta_3^-$, the TC point is replaced by a low-concentration CE point (or a Landau end point if $\Delta = 1$) and an ordinary critical point associated with a biaxial-biaxial coexistence region, a topology exemplified in Fig. 6(c). For biaxiality exactly equal to Δ_3^+ or Δ_3^-, the lines of critical and CE points meet the line of TC points and the biaxial-biaxial coexistence region is absent.

VI. CONCLUSIONS

We considered a lattice-gas version of the Maier-Saupe model for biaxial nematics with discrete orientations, in addition to an energetic term that described an isotropic interaction. The model is investigated in mean-field theory through a fully connected spinlike system with inclusion of dilution effects. The free energy functional, and the mean-field equations were obtained exactly.

For systems without isotropic interactions, $U = 0$, we have drawn phase diagrams in terms of temperature and concentration of nematogens, with fixed value of Δ. The case $\Delta = 1$ is particularly interesting due to the absence of a nematic uniaxial phase, and we find a line of Landau points which is limited by a Landau tricritical point (LTC). In the cases $\Delta = 0$ or 3 the nematogens are intrinsically uniaxial, so that the phase diagrams show no biaxial nematic phase. Any other value of Δ leads to a diagram which presents a critical end point (CE) at high concentration.

Systems with $U \neq 0$ present a great variety of multicritical points depending on the character of the isotropic interaction and the biaxiality degree of the nematogens. To clarify this idea, diagrams of multicritical points were constructed in the U-T plane for some values of Δ, and these diagrams show the different multicritical points that can be found in the phase diagrams.

Although our calculations are of a mean-field nature, we do not anticipate much qualitative difference between our results and those which would be obtained from improved approximations or from Monte Carlo simulations. Our basis for this is twofold. First, there is a general agreement between our results for limiting cases and those from previous work employing either improved off-lattice approximations (see, e.g., Refs. [39] and [40]) or Monte Carlo simulations (see, e.g., Refs. [12] and [33]). Second, mean-field calculations for dilute lattice systems are especially sensitive to effects related to percolation, as the infinite range of mean-field interactions leads to a percolation threshold at an infinitesimal particle concentration, in sharp contrast to the finite percolation threshold of three-dimensional lattices with nearest-neighbor interactions. Therefore, we expect predictions of ordered phases at low concentration to be mean-field artifacts. However, except for very strong repulsive isotropic interactions, our calculations do not lead to such predictions. Monte Carlo simulations focusing on both these exceptional cases as well as on the predicted multicritical points would be most welcome.

It would be also interesting to extend the present work to deal with the limit in which the orientational interactions are described by the potential in Eq. (1) with $\zeta = 0$ and $\lambda \neq 0$. This would allow comparison with the results obtained by Skutnik *et al.* [53] for a three-dimensional model with short-range interactions via constant-pressure Monte Carlo simulations. Such a comparison would point to possible

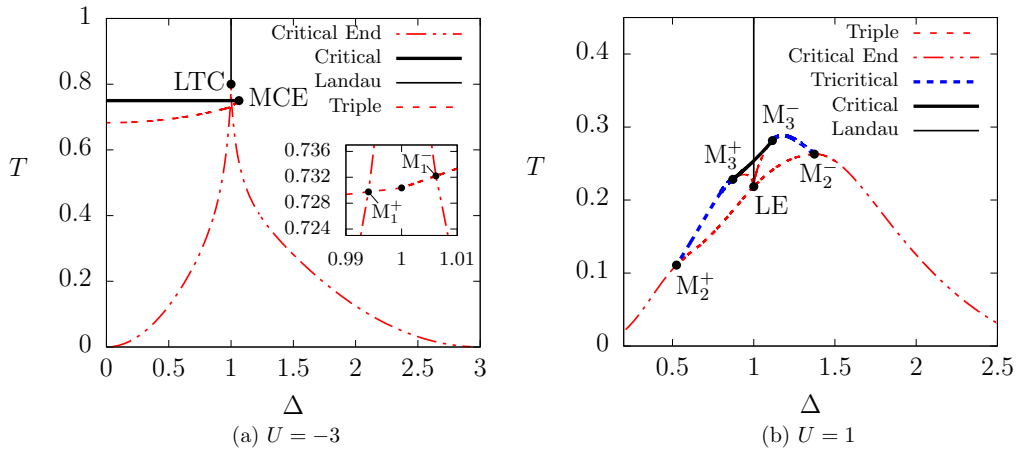

(a) $U = -3$ (b) $U = 1$

FIG. 8. Lines of multicritical points in the Δ-T plane. MCE: higher-order critical end point. $M_1^{\pm}$, $M_2^{\pm}$, and $M_3^{\pm}$ are higher-order multicritical points.

multicritical phenomena which could be further investigated via simulations.

Finally, we point out that our model could in principle be used to fit experimental data from lyotropic systems, providing estimates of coupling energies and biaxiality parameters, if we allow for variation of the parameter Δ with both temperature and concentration of components in a lyotropic mixture. Models for this variation should be informed by calculations similar to those provided by Amaral *et al.* for the change in micelle form induced by cosurfactant addition [54].

ACKNOWLEDGMENTS

This work was funded by CNPq, FAPESP, INCT/FCx, NAP/FCx, and Coordenação de Aperfeiçoamento de Pessoal de Nível Superior–Brasil (CAPES), Finance Code 001.

APPENDIX A: MEAN-FIELD CALCULATIONS FOR LGMSZ MODEL

The mean-field version of the LGMSZ model is obtained by assuming a fully connected lattice Hamiltonian

$$\mathcal{H}_{\rm mf} = -\frac{A}{2N}\sum_{i,j}\gamma_i\gamma_j\mathbf{\Omega}_i{:}\mathbf{\Omega}_j + \frac{U}{2N}\sum_{i,j}\gamma_i\gamma_j, \tag{A1}$$

where the sums now run over all lattice sites. The grand partition function is

$$\Xi = \sum_{\{\gamma_i\}}\sum_{\{\mathbf{\Omega}_i\}}\exp\left(\frac{\beta A}{2N}\sum_{i,j}\gamma_i\gamma_j\mathbf{\Omega}_i{:}\mathbf{\Omega}_j - \frac{\beta U}{2N}\sum_{i,j}\gamma_i\gamma_j + \beta\mu\sum_i\gamma_i\right). \tag{A2}$$

In order to obtain an integral representation of the grand partition function in the mean-field limit, we introduce the concentration of nematogens as

$$\phi = \frac{1}{N}\sum_{i=1}^{N}\gamma_i, \tag{A3}$$

and use the integral representation of the Dirac δ function,

$$\delta\left(N\phi - \sum_{i=1}^{N}\gamma_i\right) = \frac{1}{2\pi i}\int_{-i\infty}^{+i\infty}\exp\left[-\hat{\phi}\left(N\phi - \sum_{i=1}^{N}\gamma_i\right)\right]d\hat{\phi}, \tag{A4}$$

where $i = \sqrt{-1}$ represents the imaginary unit. We also have the Gaussian identity

$$\exp\left(\frac{\beta A}{2N}\sum_{i,j}\gamma_i\gamma_j\mathbf{\Omega}_i{:}\mathbf{\Omega}_j\right) \propto \int\exp\left(-\frac{\beta AN}{2}\|\mathbf{Q}\|^2 + \beta A\sum_i\gamma_i\mathbf{Q}{:}\mathbf{\Omega}_i\right)d[\mathbf{Q}], \tag{A5}$$

where the constant of proportionality is irrelevant, and $\|\cdot\|$ is the Frobenius norm. Using the identities in Eqs. (A4) and (A5) and performing the partial trace over the occupation variables $\{\gamma_i\}$, we can write the grand partition function in the form

$$\Xi \propto \int \mathrm{I}(\mathbf{Q},\phi)e^{-N\beta\Gamma(\mathbf{Q},\phi)}\,d\phi\,d[\mathbf{Q}], \tag{A6}$$

where

$$\Gamma(\mathbf{Q},\phi)=\frac{A}{2}\|\mathbf{Q}\|^2+\frac{U}{2}\phi^2-\mu\phi, \tag{A7}$$

$$\mathrm{I}(\mathbf{Q},\phi)=\frac{N}{2\pi i}\int_{-i\infty}^{+i\infty}e^{Nf(\mathbf{Q},\phi,\hat{\phi})}\,d\hat{\phi}, \tag{A8}$$

and

$$f(\mathbf{Q},\phi,\hat{\phi})=-\hat{\phi}\phi+\ln\left(6+e^{\hat{\phi}}\sum_{\mathbf{\Omega}}e^{\beta A\mathbf{Q}:\mathbf{\Omega}}\right). \tag{A9}$$

In the thermodynamic limit $N\gg 1$, we expect the integral in Eq. (A8) to be dominated by the highest stationary point of $f(\mathbf{Q},\phi,\hat{\phi})$ with respect to $\hat{\phi}$. As for a complex function the only stationary points are saddle points, the integral is therefore dominated by the highest saddle point. The saddle point, $\hat{\phi}_o$, can be determined by the condition $f'(\mathbf{Q},\phi,\hat{\phi}_o)=0$, where the derivative is taken with respect to $\hat{\phi}$. Then

$$\hat{\phi}_o=\ln\left(\frac{6\phi}{1-\phi}\right)+\ln\left(\sum_{\mathbf{\Omega}}e^{\beta A\mathbf{Q}:\mathbf{\Omega}}\right), \tag{A10}$$

where $\hat{\phi}_o\in\mathbb{R}$, because $0<\phi<1$. In a neighborhood of $\hat{\phi}_o$ we can write

$$f(\mathbf{Q},\phi,\hat{\phi})\approx f(\mathbf{Q},\phi,\hat{\phi}_o)+\tfrac{1}{2}f''(\mathbf{Q},\phi,\hat{\phi}_o)(\hat{\phi}-\hat{\phi}_o)^2, \tag{A11}$$

so that the integral $\mathrm{I}(\mathbf{Q},\phi)$ takes the form

$$\mathrm{I}(\mathbf{Q},\phi)\approx\frac{N}{2\pi i}e^{Nf(\mathbf{Q},\phi,\hat{\phi}_o)}\times\int_{-i\infty}^{+i\infty}\exp\left[\frac{N}{2}f''(\mathbf{Q},\phi,\hat{\phi}_o)(\hat{\phi}-\hat{\phi}_o)^2\right]d\hat{\phi}. \tag{A12}$$

The integral in Eq. (A12) can be solved by the method of steepest descents. For $\phi\approx\hat{\phi}_o$, we write

$$\hat{\phi}-\hat{\phi}_o=\rho e^{i\varphi}, \tag{A13}$$

in which φ is the angle according to which the integration contour passes through the saddle point $\hat{\phi}_o$ so that, in the complex plane defined by $\hat{\phi}$, $f''(\mathbf{Q},\phi,\hat{\phi}_o)$ is a real number. Taking into account that in this particular problem $f''(\mathbf{Q},\phi,\hat{\phi}_o)=\phi(1-\phi)$, implying $\varphi=\pi/2$ (see Ref. [55], p. 491), we obtain

$$\mathrm{I}(\mathbf{Q},\phi)\approx\sqrt{\frac{N}{2\pi}}\frac{e^{Nf(\mathbf{Q},\phi,\hat{\phi}_o)}}{\sqrt{\phi(1-\phi)}}. \tag{A14}$$

Finally we get an integral representation of the grand partition function,

$$\Xi\propto\int R(\phi)e^{-N\beta\psi(\phi,\mathbf{Q})}\,d\phi\,d[\mathbf{Q}], \tag{A15}$$

where

$$\psi(\phi,\mathbf{Q})=\frac{A}{2}\|\mathbf{Q}\|^2+\frac{U}{2}\phi^2-\mu\phi-\frac{f(\mathbf{Q},\phi,\hat{\phi}_o)}{\beta}, \tag{A16}$$

with

$$f(\mathbf{Q},\phi,\hat{\phi}_o)=-\phi\ln\phi-(1-\phi)\ln\left(\frac{1-\phi}{6}\right)+\phi\ln\left[\sum_{\mathbf{\Omega}}\exp\left(\beta A\mathbf{Q}:\mathbf{\Omega}\right)\right]. \tag{A17}$$

The symmetric traceless tensor $\mathbf{Q}$ can be parameterized by the scalar quantities S and η as

$$\mathbf{Q}=\frac{1}{2}\begin{pmatrix}-S-\eta & 0 & 0\\ 0 & -S+\eta & 0\\ 0 & 0 & 2S\end{pmatrix}. \tag{A18}$$

In terms of these parameters, the isotropic phase is characterized by $S=\eta=0$, the uniaxial phase by $S\neq 0$ and $\eta=0$ (or $\eta=\pm 3S$), and the biaxial phase by $\eta\neq 0$. Using this parametrization in Eq. (A16), we obtain the free-energy functional $\psi(S,\eta,\phi)$ in Eq. (8).

APPENDIX B: LOW-TEMPERATURE ANALYSIS

Let us consider a diluted liquid crystal whose constituent units interact via the Hamiltonian of the LGMSZ model, which was presented in Sec. II. Investigating the low-temperature limit $T\to 0$ amounts to comparing the internal energy of the different phases, as minimizing this quantity for a given choice of the Hamiltonian parameters determines the stable phase. We must also consider the possibility that the internal energy is minimized under phase coexistence.

In the isotropic phase, the energy is minimized by having $\mathbf{\Omega}_i{:}\mathbf{\Omega}_j=0$ for any pair of particles (i,j), so the internal energy as a function of ϕ is given by

$$E_{\mathrm{I}}(\phi)=\frac{UN}{2}\phi^2. \tag{B1}$$

On the other hand, for $T\to 0$, $\mathbf{\Omega}_i{:}\mathbf{\Omega}_j=(1+\Delta^2)/2$ in the fully occupied nematic phase (biaxial if $0<\Delta<3$ or uniaxial if $\Delta=0$ or $\Delta=3$) for any pair (i,j). The internal energy of the nematic phase is

$$E_{\mathrm{N}}(\phi)=-\frac{AN}{4}(3+\Delta^2)\phi^2+\frac{UN}{2}\phi^2. \tag{B2}$$

As for the coexistence between an isotropic phase with $\phi=0$ and a nematic phase with $\phi\neq 0$, the lever rule gives an internal energy

$$E_{\mathrm{I\text{-}N}}=(1-\phi)E_{\mathrm{I}}(0)+\phi E_{\mathrm{N}}(1)=\phi E_{\mathrm{N}}(1). \tag{B3}$$

The sign of the energy difference $E_{\mathrm{I\text{-}N}}-E_{\mathrm{N}}=\phi(1-\phi)E_{\mathrm{N}}(1)$ determines the stability of the nematic phase towards phase coexistence as $T\to 0$. Just when $E_{\mathrm{N}}(1)=0$ the nematic phase becomes metastable with respect to isotropic-nematic coexistence. This corresponds to

$$E_{\mathrm{N}}(1)=0\quad\Rightarrow\quad U=\frac{A}{2}(3+\Delta^2). \tag{B4}$$

Therefore, if $U/A>(3+\Delta^2)/2$ the nematic phase is stable, otherwise there appears an isotropic-nematic coexistence region.

[1] P. de Gennes and J. Prost, *The Physics of Liquid Crystals*, International Series of Monographs on Physics (Clarendon Press, Oxford, 1993).

[2] A. M. Figueiredo Neto and S. R. A. Salinas, *The Physics of Lyotropic Liquid Crystals* (Oxford University Press, Oxford, 2005).

[3] S. Singh, Phys. Rep. **324**, 107 (2000).

[4] P. Palffy-Muhoray, Phys. Today **60**(9), 54 (2007).

[5] M. J. Freiser, Phys. Rev. Lett. **24**, 1041 (1970).

[6] L. J. Yu and A. Saupe, Phys. Rev. Lett. **45**, 1000 (1980).

[7] A. Jákli, O. D. Lavrentovich, and J. V. Selinger, Rev. Mod. Phys. **90**, 045004 (2018).

[8] G. Luckhurst and T. Sluckin, *Biaxial Nematic Liquid Crystals: Theory, Simulation and Experiment* (Wiley, Chichester, 2015).

[9] E. Akpinar and A. M. Figueiredo Neto, Crystals **9**, 158 (2019).

[10] E. F. Gramsbergen, L. Longa, and W. H. de Jeu, Phys. Rep. **135**, 195 (1986).

[11] P. A. Lebwohl and G. Lasher, Phys. Rev. A **6**, 426 (1972).

[12] M. A. Bates, Phys. Rev. E **64**, 051702 (2001).

[13] M. A. Bates, Phys. Rev. E **65**, 041706 (2002).

[14] G. Luckhurst and S. Romano, Mol. Phys. **40**, 129 (1980).

[15] W. Maier and A. Saupe, Z. Naturforsch. A **13**, 564 (1958).

[16] L. Longa and G. Pająk, Liq. Cryst. **32**, 1409 (2005).

[17] F. Biscarini, C. Chiccoli, P. Pasini, F. Semeria, and C. Zannoni, Phys. Rev. Lett. **75**, 1803 (1995).

[18] J. P. Straley, Phys. Rev. A **10**, 1881 (1974).

[19] A. M. Sonnet, E. G. Virga, and G. E. Durand, Phys. Rev. E **67**, 061701 (2003).

[20] R. A. Horn and C. R. Johnson, *Matrix Analysis*, 2nd ed. (Cambridge University Press, Cambridge, 2013).

[21] E. S. Nascimento, E. F. Henriques, A. P. Vieira, and S. R. Salinas, Phys. Rev. E **92**, 062503 (2015).

[22] R. Zwanzig, J. Chem. Phys. **39**, 1714 (1963).

[23] M. J. de Oliveira and A. M. Figueiredo Neto, Phys. Rev. A **34**, 3481 (1986).

[24] E. do Carmo, D. B. Liarte, and S. R. Salinas, Phys. Rev. E **81**, 062701 (2010).

[25] E. do Carmo, A. P. Vieira, and S. R. Salinas, Phys. Rev. E **83**, 011701 (2011).

[26] D. B. Liarte and S. R. Salinas, Braz. J. Phys. **42**, 261 (2012).

[27] R. A. Sauerwein and M. J. de Oliveira, J. Chem. Phys. **144**, 194904 (2016).

[28] E. S. Nascimento, A. P. Vieira, and S. R. Salinas, Braz. J. Phys. **46**, 664 (2016).

[29] A. Petri and S. R. Salinas, Liq. Cryst. **45**, 980 (2018).

[30] D. D. Rodrigues, A. P. Vieira, and S. R. Salinas, Crystals **10**, 632 (2020).

[31] C. T. G. dos Santos, A. P. Vieira, S. R. Salinas, and R. F. S. Andrade, Phys. Rev. E **103**, 032111 (2021).

[32] S. R. Salinas and E. S. Nascimento, Mol. Cryst. Liq. Cryst. **657**, 27 (2017).

[33] M. J. Blair and G. N. Patey, Phys. Rev. E **57**, 5682 (1998).

[34] P. I. C. Teixeira, Phys. Rev. E **59**, 1280 (1999).

[35] D. I. Uzunov, *Introduction to the Theory of Critical Phenomena* (World Scientific, Singapore, 1993).

[36] M. J. de Oliveira, *Equilibrium Thermodynamics* (Springer-Verlag, Berlin, 2013).

[37] C. M. Knobler and R. L. Scott, in *Phase Transitions and Critical Phenomena*, Vol. 9, edited by C. Domb and J. L. Lebowitz (Academic Press, London, 1984), pp. 164–231.

[38] D. Luders, G. Arcolezi, M. Pereira, W. Braga, O. Santos, M. Simões, N. Kimura, A. Sampaio, and A. Palangana, Liq. Cryst. **48**, 974 (2021).

[39] P. I. C. Teixeira, Liq. Cryst. **25**, 721 (1998).

[40] P. Teixeira and M. Telo da Gama, Mol. Phys. **86**, 1537 (1995).

[41] H. Lekkerkerker and A. Stroobants, Nuovo Cimento D **16**, 949 (1994).

[42] P. Palffy-Muhoray, J. J. de Bruyn, and D. A. Dunmur, Mol. Cryst. Liq. Cryst. **127**, 301 (1985).

[43] A. Khokhlov and A. Semenov, J. Stat. Phys. **38**, 161 (1985).

[44] P. G. Bolhuis, A. Stroobants, D. Frenkel, and H. N. W. Lekkerkerker, J. Chem. Phys. **107**, 1551 (1997).

[45] H. Zhang and M. Widom, Phys. Rev. E **49**, R3591 (1994).

[46] E. Lomba, J.-J. Weis, N. G. Almarza, F. Bresme, and G. Stell, Phys. Rev. E **49**, 5169 (1994).

[47] J. M. Tavares, M. M. Telo da Gama, P. I. C. Teixeira, J. J. Weis, and M. J. P. Nijmeijer, Phys. Rev. E **52**, 1915 (1995).

[48] J. M. Tavares, P. I. C. Teixeira, and M. M. Telo da Gama, Phys. Rev. E **58**, 3175 (1998).

[49] A. Oukouiss and M. Baus, Phys. Rev. E **55**, 7242 (1997).

[50] T. G. Sokolovska, Physica A **253**, 459 (1998).

[51] L.-S. Li, L. Li, and X.-S. Chen, Commun. Theor. Phys. **51**, 287 (2009).

[52] B. Groh and S. Dietrich, Phys. Rev. E **50**, 3814 (1994).

[53] R. A. Skutnik, I. S. Geier, and M. Schoen, Mol. Phys. **118**, e1726520 (2020).

[54] L. Q. Amaral, O. Santin Filho, G. Taddei, and N. Vila-Romeu, Langmuir **13**, 5016 (1997).

[55] G. Arfken and H. J. Weber, *Mathematical Methods for Physicists*, 6th ed. (Elsevier Academic Press, London, 2005).

Bibliography

[1] Pierre-Gilles De Gennes and Jacques Prost. *The physics of liquid crystals*. Number 83 in The International series of monographs on physics. Oxford University Press, 1993.

[2] Antônio M Figueiredo Neto and Silvio RA Salinas. *The physics of lyotropic liquid crystals: phase transitions and structural properties*, volume 62. OUP Oxford, 2005.

[3] Shri Singh. Phase transitions in liquid crystals. *Physics Reports*, 324(2-4):107–269, 2000.

[4] Peter Palffy-Muhoray. Orientationally ordered soft matter: The diverse world of liquid crystals. *Electronic-Liquid Crystal Communications (e-LC)*, 2007.

[5] MJ Freiser. Ordered states of a nematic liquid. *Physical Review Letters*, 24(19):1041, 1970.

[6] Wilhelm Maier and Alfred Saupe. Eine einfache molekulare theorie des nematischen kristallinflüssigen zustandes. *Zeitschrift für Naturforschung A*, 13(7):564–566, 1958.

[7] Richard Alben. Phase transitions in a fluid of biaxial particles. *Physical Review Letters*, 30(17):778, 1973.

[8] Richard Alben. Liquid crystal phase transitions in mixtures of rodlike and platelike molecules. *The Journal of Chemical Physics*, 59(8):4299–4304, 1973.

[9] Chuen-Shyr Shih and Richard Alben. Lattice model for biaxial liquid crystals. *The Journal of Chemical Physics*, 57(8):3055–3061, 1972.

[10] Richard Alben. Possible phase diagrams for mixtures of 'positive'and 'negative'nematic liquid crystals. *Liquid Crystals and Ordered Fluids: Volume 2*, pages 81–84, 1974.

[11] LJ Yu and Alfred Saupe. Observation of a biaxial nematic phase in potassium laurate-1-decanol-water mixtures. *Physical Review Letters*, 45(12):1000, 1980.

[12] AM Figueiredo Neto, AM Levelut, L Liébert, and Y Galerne. Biaxial nematic lyomesophase studied by x-ray diffraction. *Molecular Crystals and Liquid Crystals*, 129(1-3):191–198, 1985.

[13] Y Galerne, AM Figueiredo Neto, and L Liébert. Microscopical structure of the uniaxial and biaxial lyotropic nematics. *The Journal of chemical physics*, 87(3):1851–1856, 1987.

[14] EA Oliveira, L Liebert, and AM Figueiredo Neto. A new soap/detergent/water lyotropic liquid crystal with a biaxial nematic phase. *Liquid Crystals*, 5(6):1669–1675, 1989.

[15] E Akpinar, D Reis, and AM Figueiredo Neto. Lyotropic mixture made of potassium laurate/1-undecanol/k 2 so 4/water presenting high birefringences and large biaxial nematic phase domain: a laser conoscopy study. *The European Physical Journal E*, 35(6):1–9, 2012.

[16] Louis A Madsen, Theo J Dingemans, Michi Nakata, and Edward T Samulski. Thermotropic biaxial nematic liquid crystals. *Physical review letters*, 92(14):145505, 2004.

[17] Bharat R Acharya, Andrew Primak, and Satyendra Kumar. Biaxial nematic phase in bent-core thermotropic mesogens. *Physical review letters*, 92(14):145506, 2004.

[18] EF Henriques, CB Passos, VB Henriques, and LQ Amaral. Mixture of changing uniaxial micellar forms in lyotropic biaxial nematics. *Liquid Crystals*, 35(5):555–568, 2008.

[19] E Do Carmo, Danilo Barbosa Liarte, and SR Salinas. Statistical models of mixtures with a biaxial nematic phase. *Physical Review E*, 81(6):062701, 2010.

[20] E Do Carmo, AP Vieira, and SR Salinas. Phase diagram of a model for a binary mixture of nematic molecules on a bethe lattice. *Physical Review E*, 83(1):011701, 2011.

[21] Danilo Barbosa Liarte and Silvio Roberto Salinas. Enhancement of nematic order and global phase diagram of a lattice model for coupled nematic systems. *Brazilian Journal of Physics*, 42(3-4):261–266, 2012.

[22] ES Nascimento, EF Henriques, André de Pinho Vieira, and SR Salinas. Maier-saupe model for a mixture of uniaxial and biaxial molecules. *Physical Review E*, 92(6):062503, 2015.

[23] ES Nascimento, André de Pinho Vieira, and SR Salinas. Lattice statistical models for the nematic transitions in liquid-crystalline systems. *Brazilian Journal of Physics*, 46(6):664–671, 2016.

[24] Ricardo A Sauerwein and Mário J de Oliveira. Lattice model for biaxial and uniaxial nematic liquid crystals. *The Journal of chemical physics*, 144(19):194904, 2016.

[25] Daniel D Rodrigues, André P Vieira, and Silvio R Salinas. Magnetic field and dilution effects on the phase diagrams of simple statistical models for nematic biaxial systems. *Crystals*, 10(8):632, 2020.

[26] Hao Qi and Torsten Hegmann. Formation of periodic stripe patterns in nematic liquid crystals doped with functionalized gold nanoparticles. *Journal of Materials Chemistry*, 16(43):4197–4205, 2006.

[27] Yukihide Shiraishi, Naoki Toshima, Kenji Maeda, Hiroaki Yoshikawa, Jun Xu, and Shunsuke Kobayashi. Frequency modulation response of a liquid-crystal electro-optic device doped with nanoparticles. *Applied Physics Letters*, 81(15):2845–2847, 2002.

[28] Shunsuke Kobayashi and Naoki Toshima. Nanoparticles and lcds: it's a surprising world. *Information Display*, 23(9):26, 2007.

[29] S Kaur, SP Singh, AM Biradar, Amit Choudhary, and K Sreenivas. Enhanced electro-optical properties in gold nanoparticles doped ferroelectric liquid crystals. *Applied physics letters*, 91(2):023120, 2007.

[30] A Kumar, J Prakash, DS Mehta, AM Biradar, and W Haase. Enhanced photoluminescence in gold nanoparticles doped ferroelectric liquid crystals. *Applied Physics Letters*, 95(2):023117, 2009.

[31] Hao Qi, Brandy Kinkead, and Torsten Hegmann. Effects of functionalized metal and semiconductor nanoparticles in nematic liquid crystal phases. In *Emerging Liquid Crystal Technologies III*, volume 6911, pages 38–48. SPIE, 2008.

[32] Lena M Lopatina and Jonathan V Selinger. Theory of ferroelectric nanoparticles in nematic liquid crystals. *Physical review letters*, 102(19):197802, 2009.

[33] Lena M Lopatina and Jonathan V Selinger. Maier-saupe-type theory of ferroelectric nanoparticles in nematic liquid crystals. *Physical Review E*, 84(4):041703, 2011.

[34] Maxim V Gorkunov and Mikhail A Osipov. Mean-field theory of a nematic liquid crystal doped with anisotropic nanoparticles. *Soft Matter*, 7(9):4348–4356, 2011.

[35] Akihiko Matsuyama and Ryota Hirashima. Phase separations in liquid crystal-colloid mixtures. *The Journal of chemical physics*, 128(4):044907, 2008.

[36] AN Zakhlevnykh, MS Lubnin, and DA Petrov. On a simple molecular–statistical model of a liquid-crystal suspension of anisometric particles. *Journal of Experimental and Theoretical Physics*, 123:908–917, 2016.

[37] Silvia Orlandi, Erika Benini, Isabella Miglioli, Dean R Evans, Victor Reshetnyak, and Claudio Zannoni. Doping liquid crystals with nanoparticles. a computer simulation of the effects of nanoparticle shape. *Physical Chemistry Chemical Physics*, 18(4):2428–2441, 2016.

[38] Grigoriy Kimaev. Coarse-grained molecular Monte Carlo simulations of liquid crystal-nanoparticle mixtures. Master's thesis, University of Waterloo, 2015.

[39] Grzegorz Pawlik, Antoni C Mitus, and Andrzej Miniewicz. Modelling of enhanced photoinduced reorientation of nematic liquid crystal molecules in twisted geometry: Monte carlo approach. *Molecular Crystals and Liquid Crystals*, 554(1):56–64, 2012.

[40] MSS Pereira, AA Canabarro, IN De Oliveira, ML Lyra, and LV Mirantsev. A molecular dynamics study of ferroelectric nanoparticles immersed in a nematic liquid crystal. *The European Physical Journal E*, 31:81–87, 2010.

[41] Robert Zwanzig. First-order phase transition in a gas of long thin rods. *The Journal of Chemical Physics*, 39(7):1714–1721, 1963.

[42] Roger A Horn, and Charles R Johnson. *Topics in matrix analysis*. Cambridge University Press, 1994.

[43] MJ De Oliveira and AM Figueiredo Neto. Reentrant isotropic-nematic transition in lyotropic liquid crystals. *Physical Review A*, 34(4):3481, 1986.

[44] N David Mermin and Herbert Wagner. Absence of ferromagnetism or antiferromagnetism in one or two-dimensional isotropic Heisenberg models. *Physical Review Letters*, 17(22):1133, 1966.

[45] Egbert F Gramsbergen, Lech Longa, and Wim H de Jeu. Landau theory of the nematic-isotropic phase transition. *Physics Reports*, 135(4):195–257, 1986.

[46] N Boccara, R Mejdani, and L De Seze. Solvable model exhibiting a first-order phase transition. *Journal de Physique*, 38(2):149–151, 1977.

[47] Joseph P Straley. Ordered phases of a liquid of biaxial particles. *Physical Review A*, 10(5):1881, 1974.

[48] André M Sonnet, Epifanio G Virga, and Georges E Durand. Dielectric shape dispersion and biaxial transitions in nematic liquid crystals. *Physical Review E*, 67(6):061701, 2003.

[49] Martin A Bates. Computer simulation study of the phase behavior of a nematogenic lattice-gas model. *Physical Review E*, 64(5):051702, 2001.

[50] Martin A Bates. Phase behavior and free interfaces of a lattice-gas nematic-liquid-crystal model. *Physical Review E*, 65(4):041706, 2002.

[51] A Petri and SR Salinas. Field-induced uniaxial and biaxial nematic phases in the maier–saupe–zwanzig (msz) lattice model. *Liquid Crystals*, 45(7):980–992, 2018.

[52] SR Salinas and ES Nascimento. Elementary lattice models for the nematic transitions in liquid-crystalline systems. *Molecular Crystals and Liquid Crystals*, 657(1):27–33, 2017.

[53] George B Arfken and Hans J Weber. Mathematical methods for physicists 6th ed. *Mathematical methods for physicists 6th ed. by George B. Arfken and Hans J. Weber. Published: Amsterdam; Boston: Elsevier*, 2005.

[54] MJ Blair and GN Patey. Gas-liquid coexistence and demixing in systems with highly directional pair potentials. *Physical Review E*, 57(5):5682, 1998.

[55] PIC Teixeira. Comment on "gas-liquid coexistence and demixing in systems with highly directional pair potentials". *Physical Review E*, 59(1):1280, 1999.

[56] Dimo I Uzunov. *Introduction to the theory of critical phenomena: mean field, fluctuations and renormalization*. World Scientific, 1993.

[57] Mário J De Oliveira. *Equilibrium thermodynamics*. Springer, 2013.

[58] DD Luders, GM Arcolezi, MLG Pereira, WS Braga, OR Santos, M Simões, NM Kimura, AR Sampaio, and AJ Palangana. Conoscopic image of a biaxial negative in a reentrant discotic–biaxial nematic phase transition. *Liquid Crystals*, 48(7):974–979, 2021.

[59] PIC Teixeira. An old model for magnetic nematics. *Liquid crystals*, 25(6):721–726, 1998.

[60] PIC Teixeira and MM Telo da Gama. A model nematic liquid crystal revisited: some new phase diagrams from density-functional theory. *Molecular Physics*, 86(6):1537–1543, 1995.

[61] HNW Lekkerkerker and A Stroobants. Phase behaviour of rod-like colloid+ flexible polymer mixtures. *Il Nuovo Cimento D*, 16(8):949–962, 1994.

[62] P Palffy-Muhoray, JJ De Bruyn, and DA Dunmur. Mean field theory of binary mixtures of nematic liquid crystals. *Molecular Crystals and Liquid Crystals*, 127(1):301–319, 1985.

[63] AR Khokhlov and AN Semenov. On the theory of liquid-crystalline ordering of polymer chains with limited flexibility. *Journal of Statistical Physics*, 38(1):161–182, 1985.

[64] Peter G Bolhuis, Alain Stroobants, Daan Frenkel, and Henk NW Lekkerkerker. Numerical study of the phase behavior of rodlike colloids with attractive interactions. *The Journal of chemical physics*, 107(5):1551–1564, 1997.

[65] H Zhang and M Widom. Global phase diagrams for dipolar fluids. *Physical Review E*, 49(5):R3591, 1994.

[66] Enrique Lomba, Jean-Jacques Weis, Noe G Almarza, Fernando Bresme, and George Stell. Phase transitions in a continuum model of the classical Heisenberg magnet: The ferromagnetic system. *Physical Review E*, 49(6):5169, 1994.

[67] JM Tavares, MM Telo Da Gama, PIC Teixeira, JJ Weis, and MJP Nijmeijer. Phase diagram and critical behavior of the ferromagnetic Heisenberg fluid from density-functional theory. *Physical Review E*, 52(2):1915, 1995.

[68] JM Tavares, PIC Teixeira, and MM Telo da Gama. Stability of the order-order critical points of Heisenberg and nematic model fluids. *Physical Review E*, 58(3):3175, 1998.

[69] Abdelkarim Oukouiss and Marc Baus. Phase diagrams of the classical Heisenberg fluid within the extended van der Waals approximation. *Physical Review E*, 55(6):7242, 1997.

[70] Tetjana Georhiïvna Sokolovska. Phase diagram in a continuum model of the classical Heisenberg ferromagnet: mean spherical approximation. *Physica A: Statistical Mechanics and its Applications*, 253(1-4):459–472, 1998.

[71] Li Liang-Sheng, Li Li, and Chen Xiao-Song. Characterization of phase transition in Heisenberg fluids from density functional theory. *Communications in Theoretical Physics*, 51(2):287, 2009.

[72] B Groh and S Dietrich. Ferroelectric phase in Stockmayer fluids. *Physical Review E*, 50(5):3814, 1994.

[73] Philippe Poulin, Holger Stark, TC Lubensky, and DA Weitz. Novel colloidal interactions in anisotropic fluids. *Science*, 275(5307):1770–1773, 1997.

[74] Yuedong Gu and Nicholas L Abbott. Observation of Saturn-ring defects around solid microspheres in nematic liquid crystals. *Physical Review Letters*, 85(22):4719, 2000.

[75] Holger Stark. Physics of colloidal dispersions in nematic liquid crystals. *Physics Reports*, 351(6):387–474, 2001.

[76] Makoto Yada, Jun Yamamoto, and Hiroshi Yokoyama. Direct observation of anisotropic interparticle forces in nematic colloids with optical tweezers. *Physical review letters*, 92(18):185501, 2004.

[77] Ivan I Smalyukh, OD Lavrentovich, AN Kuzmin, AV Kachynski, and PN Prasad. Elasticity-mediated self-organization and colloidal interactions of solid spheres with tangential anchoring in a nematic liquid crystal. *Physical Review Letters*, 95(15):157801, 2005.

[78] Igor Musevic, Miha Skarabot, Uros Tkalec, Miha Ravnik, and Slobodan Zumer. Two-dimensional nematic colloidal crystals self-assembled by topological defects. *Science*, 313(5789):954–958, 2006.

[79] Fenghua Li, Oleksandr Buchnev, Chae Il Cheon, Anatoliy Glushchenko, Victor Reshetnyak, Yuri Reznikov, Timothy J Sluckin, and John L West. Orientational coupling amplification in ferroelectric nematic colloids. *Physical Review Letters*, 97(14):147801, 2006.

[80] Y Lin, R Douali, F Dubois, A Segovia-Mera, and A Daoudi. On the phase transitions of $8\mathrm{CB}/\mathrm{Sn_2P_2S_6}$ liquid crystal nanocolloids. *The European Physical Journal E*, 38(9):1–8, 2015.

[81] O Kurochkin, H Atkuri, O Buchnev, A Glushchenko, O Grabar, R Karapinar, V Reshetnyak, J West, and Yu Reznikov. Nano-colloids of $\mathrm{Sn_2P_2S_6}$ in nematic liquid crystal pentylcianobiphenile. *Condensed Matter Physics*, 2010.

[82] E Ouskova, O Buchnev, V Reshetnyak, Yu Reznikov, and H Kresse. Dielectric relaxation spectroscopy of a nematic liquid crystal doped with ferroelectric $\mathrm{Sn_2P_2S_6}$ nanoparticles. *Liquid Crystals*, 30(10):1235–1239, 2003.

[83] MR Hakobyan, RB Alaverdyan, RS Hakobyan, and Yu S Chilingaryan. Enhanced physical properties of nematics doped with ferroelectric nanoparticles. *Armenian Journal of Physics*, 7(1), 2014.

[84] Martin Čopič, Alenka Mertelj, Olexandr Buchnev, and Yuri Reznikov. Coupled director and polarization fluctuations in suspensions of ferroelectric nanoparticles in nematic liquid crystals. *Physical Review E*, 76(1):011702, 2007.

[85] Jung Y Huang, Liu S Li, and Ming C Chen. Probing molecular binding effect from zinc oxide nanocrystal doping in surface-stabilized ferroelectric liquid crystal with two-dimensional infrared correlation technique. *The Journal of Physical Chemistry C*, 112(14):5410–5415, 2008.

[86] IP Pinkevich, YUA REZNIKOV, VYU RESHETNYAK, and OV Yaroshchuk. Nematic liquid crystals. *International Journal of Nonlinear Optical Physics*, 1(3):447–472, 1992.

[87] Oleksandr Buchnev, Andriy Dyadyusha, Malgosia Kaczmarek, Victor Reshetnyak, and Yuriy Reznikov. Enhanced two-beam coupling in colloids of ferroelectric nanoparticles in liquid crystals. *JOSA B*, 24(7):1512–1516, 2007.

[88] M Kaczmarek, O Buchnev, and I Nandhakumar. Ferroelectric nanoparticles in low refractive index liquid crystals for strong electro-optic response. *Applied Physics Letters*, 92(10):87, 2008.

[89] Jai Prakash, Sidra Khan, Shikha Chauhan, and AM Biradar. Metal oxide-nanoparticles and liquid crystal composites: A review of recent progress. *Journal of Molecular Liquids*, 297:112052, 2020.

[90] Yuriy Garbovskiy and Anatoliy Glushchenko. Ferroelectric nanoparticles in liquid crystals: recent progress and current challenges. *Nanomaterials*, 7(11):361, 2017.

[91] Yuriy Garbovskiy and Iryna Glushchenko. Nano-objects and ions in liquid crystals: ion trapping effect and related phenomena. *Crystals*, 5(4):501–533, 2015.

[92] R. Wong. *Asymptotic Approximations of Integrals*. Society for Industrial and Applied Mathematics, 2001. (See chapter IX).

[93] MV Fedoryuk. Asymptotic methods in analysis. In *Analysis I*, pages 83–191. Springer, 1989.

[94] William GC Oropesa, Eduardo S Nascimento, and André P Vieira. Phase behavior of a lattice-gas model for biaxial nematics. *Physical Review E*, 105(4):044705, 2022.

[95] Aristoula Selevou, George Papamokos, Martin Steinhart, and George Floudas. 8ocb and 8cb liquid crystals confined in nanoporous alumina: Effect of confinement on the structure and dynamics. *The Journal of Physical Chemistry B*, 121(30):7382–7394, 2017.

[96] N Tomašovičová, M Timko, N Éber, T Tóth-Katona, K Fodor-Csorba, A Vajda, V Gdovinová, X Chaud, and Peter Kopčanskỳ. Magnetically induced shift of the isotropic–nematic phase transition temperature in a mixture of bent-core and calamitic liquid crystals doped with magnetic particles. *Liquid Crystals*, 42(7):959–963, 2015.

[97] Thermal Vimal, DP Singh, SK Gupta, S Pandey, K Agrahari, and R Manohar. Thermal and optical study of semiconducting cnts-doped nematic liquid crystalline material. *Phase Transitions*, 89(6):632–642, 2016.

[98] Mukesh Mishra, Roman S Dabrowski, Jagdish K Vij, Avneesh Mishra, and Ravindra Dhar. Electrical and electro-optical parameters of 4′-octyl-4-cyanobiphenyl nematic liquid crystal dispersed with gold and silver nanoparticles. *Liquid Crystals*, 42(11):1580–1590, 2015.

[99] William. G. C. Oropesa. Perturbative calculation for the N_U-N_B second-order phase transition. `https://drive.google.com/file/d/17hMe-eJv-aWoSFUM5K4JnXZM9rAuME4L/view?usp=sharing`. [Accessed: 03-14-2023].